PNNL-11348
UC-2010

Pacific Northwest
National Laboratory

Operated by Battelle for the
U.S. Department of Energy

Numerical Analysis of the In-Well Vapor-Stripping System Demonstration at Edwards Air Force Base

M. D. White
T. J Gilmore

October 1996

PNNL-11348

Prepared for the U.S. Department of Energy
under Contract DE-AC06-76RLO 1830

DISCLAIMER

PACIFIC NORTHWEST NATIONAL LABORATORY
operated by
BATTELLE
for the
UNITED STATES DEPARTMENT OF ENERGY
under Contract DE-AC06-76RLO 1830

Printed in the United States of America

Available to DOE and DOE contractors from the Office of Scientific and Technical Information, P.O. Box 62, Oak Ridge, TN 37831; prices available from (615) 576-8401.

Available to the public from the National Technical Information Service, U.S. Department of Commerce, 5285 Port Royal Rd., Springfield, VA 22161

The document was printed on recycled paper.

PNNL-11348
UC-2010

Numerical Analysis of the In-Well Vapor-Stripping System Demonstration at Edwards Air Force Base

M. D. White
T. J Gilmore

October 1996

Prepared for the U.S. Department of Energy
under Contract DE-AC06-76RLO 1830

This work is funded by the Office of Science and Technology, within the U.S. Department of Energy's Office of Environmental Management, under the Plumes Focus Area.

Pacific Northwest National Laboratory
Richland, Washington 99352

DISCLAIMER

Summary

In-well vapor stripping is a remediation technology designed to remove dissolved volatile organic compounds from groundwater. The in-well vapor-stripping system comprises an engineered and a hydrologic component that operate in unison to form an in situ recirculation pattern. The engineered system is driven with compressed air, utilizing an air-lift pumping scheme that volatilizes dissolved organic compounds. The volatile vapors are removed from the gas stream above the ground surface and pumped water is infiltrated into the hydrologic system below the ground surface. This technology was demonstrated at Edwards Air Force Base (AFB), near Mojave, California, by collaborating researchers from Pacific Northwest National Laboratory(a) and Stanford University as part of the interim cleanup activities at the base. Preliminary results on the performance of the demonstration system have been reported and indicate a significant reduction in the concentration of contaminant, dissolved trichloroethylene (TCE), around the demonstration well.

Numerical simulations and analyses were applied to the design, operational visualization, and performance prediction activities of the Edwards AFB in-well vapor-stripping demonstration. These numerical analyses were conducted to demonstrate and assess the utility of numerical simulation in the field installation and operation of in-well vapor-stripping technologies. All simulations were executed with the STOMP simulator, which was developed by the Pacific Northwest National Laboratory for the U.S. Department of Energy under the Arid Soils Integration Demonstration Program. Steady-flow simulations prior to the field design and installation were used to assess design concepts for the vapor-stripping well, to compute preliminary operational parameters, to locate monitoring equipment, and to predict system performance. These design simulations were based on a conceptual model of the hydrologic system, which was generated from core samples and laboratory analyses. Besides providing quantitative data on pumping/infiltration rates, zones of influence, water table mounding heights, recirculation flow rates, ponding heights, and equilibrium reduction rates, numerical simulations additionally provide a window to the subsurface through visualization of the recirculating flow fields, saturation mounds, and dissolved solute concentrations.

Infiltration field tests and preliminary operational field tests provided an assessment of the accuracy of the design conceptual model for the hydrologic system and the numerical model of the combined engineered and hydrologic systems. Calibration of hydraulic conductivities to achieve close agreement between numerical and field results, in terms of pressure and water-level measurements, required adjustments of 0.189/0.189 and 2.84/1.89 to the horizontal/vertical components in the vadose and saturated strata, respectively. Redevelopment activities at

---

(a) Pacific Northwest National Laboratory is operated by Battelle for the U.S. Department of Energy.

Edwards AFB site to flocculate the dispersive clays and improve the hydraulic conductivity necessitated a second calibration of the conceptual model parameters. For these calibrations, the hydraulic conductivities were adjusted from the design conceptual model values by 0.560/0.560 and 2.82/1.89 for the horizontal/vertical components of the vadose and saturated strata, respectively. These modifications to the hydraulic conductivities are relatively minor for properties generated strictly from grain size distributions and bulk and grain density measurements.

Numerical simulations to predict operational performance of the in-well vapor-stripping system at Edwards AFB were executed based solely on field data for ponding heights and air to water volumetric flow rate ratios. Redevelopment activities at the demonstration site to flocculate dispersive clays increased hydraulic conductivities of the vadose zone strata three fold between the period from January to April 1996. Three simulations of a continuous operational field test between January 16 and March 19, 1996 (63 days) were executed that differed in hydraulic conductivities for the vadose zone strata. These simulations were designed to bracket the operational performance of the demonstration system. Simulation results using low-permeability isotropic hydrologic properties showed close agreement in the timing sequencing of TCE concentration reductions at the monitoring wells and demonstrated the field observation that shallower zones displayed significantly lower dissolved TCE concentrations. Simulation results using high-permeability isotropic and anisotropic hydrologic properties showed advanced timing on the sequencing of TCE concentration reductions at the monitoring wells when compared against the field data. Both simulations predicted lower dissolved TCE concentrations within the recirculation zone, which indicates incomplete or nonequilibrium stripping of dissolved TCE during the air-lift pumping. Stripping rates of TCE from field results were estimated to be between 80% and 90%.

Acknowledgments

This work was prepared with the support of the following contributors:

Headquarters:	U.S. Department of Energy Office of Science and Technology David L. Biancosino
Focus Area/Program:	Plumes Focus Area James A. Wright
Operations Office:	Richland Science and Technology Programs Division Jeffrey A. Frey, Technical Program Officer
Contractor:	Pacific Northwest National Laboratory Environmental Management Technology Development Program Steven C. Slate, Manager

Contributors

Mr. David Steckel and the Environmental Management Office at Edwards Air Force Base are recognized for their steadfast support of the field demonstration. Osman Taban, Massen Kassar, and others at Earth Technology Corporation, the primary environmental contractor at Edwards Air Force Base are recognized for their diligent assistance in data collection and field operations. Odile François, Mike Pinto, and Steve Gorelick from Stanford University are recognized for their contributions to the system design, field operations, and laboratory testing of the air-lift pumping. EG&G Environmental is recognized for granting an educational license of the in-well vapor-stripping system to allow this demonstration to proceed. Sandy Ballard from Sandia National Laboratories is recognized for providing the in situ flow-measuring devices and data. Bruce Bjornstad from Pacific Northwest National Laboratory is recognized for his divers contributions to the field operations and data-collection activities.

Contents

Figures

Tables

1.0 Introduction

Numerical simulations, with the Subsurface Transport Over Multiple Phases (STOMP) simulator, were applied to the field demonstration of an in-well vapor-stripping system at Edwards Air Force Base (AFB), near Mojave, California. The demonstration field site on the Edwards AFB was previously contaminated from traversing groundwater that was contained a varied composition of volatile organic compounds (VOCs), which primarily includes trichloroethylene (TCE). Contaminant TCE originated from surface basin that had been used to collect runoff during the cleaning of experimental rocket powered planes in the 1960s and 1970s. This report documents those simulations and associated numerical analyses. A companion report [Gilmore et al. 1996] documents the in-well vapor-stripping demonstration from a field perspective.

The numerical simulations given herein were used to evaluate system design options, devise the monitoring equipment layout, predict system performance, visualize subsurface flow fields and contaminant concentrations, and assess remediation effectiveness. System design evaluations and monitoring equipment layouts were completed prior to the operational field tests, based on numerical simulations using estimates of hydrologic properties from grain-size distributions, porosity measurements, and permeability tests. These hydrologic properties were combined with stratigraphic information from the demonstration site to develop a conceptual model of the hydrologic system surrounding the vapor-stripping well. The in-well vapor-stripping system comprises an engineered and a hydrologic component, where the engineered component primarily refers to the vapor-stripping well and associated aboveground equipment. During operation the two components work in unison to effect the in situ vapor-stripping processes. These simulations additionally provided visualizations of the subsurface flow and dissolved contaminant concentrations during steady operation of the demonstration system. The conceptual model for the hydrologic system was calibrated using infiltration and preliminary operational field tests. Simulations to model these field tests were executed with a matrix of hydraulic conductivities. Those simulations yielding the closest agreement in hydraulic pressure responses to the field data were used to calibrate hydraulic conductivities of soil strata within the vadose and saturated zones. Preliminary operational field tests induced a degradation in the permeability of the vadose zone strata through release of dispersive clays. Permeabilities for the vadose zone strata were reclaimed through redevelopment activities that involved the addition of soluble calcium carbonate to the vapor-stripping well. These redevelopment activities were continued through the operational field test, which necessitated using three conceptual models for the hydrologic properties to bracket the system performance. These conceptual models were calibrated primarily from infiltration tests conducted before and after the operational test period. Normally, hydrologic properties determined from laboratory analysis of core samples and calibrated with preliminary operational field tests would be sufficient to generate a conceptual model for the hydrologic system for the purpose of numerical analysis.

The following chapters give an overview of the technology and field site (Chapters 2.0 and 3.0); describe the numerical models, solution schemes, and numerical analysis procedures (Chapter 4.0); the hydrologic conceptual models (Chapter 5.0); the engineered system model and design options (Chapter 6.0); calibrations with field test (Chapter 7.0); and actual system performance (Chapter 8.0). The conclusions are given in Chapter 9.0, followed by the references cited in the text in Chapter 10.0. Numerical simulation provides a window to the subsurface environment that complements field data and provides interpretations of observed processes. Therefore, this report relies heavily on graphical presentation to communicate numerical results. The supporting graphics are given in Appendices A through F.

2.0 Technology Overview

The in-well vapor-stripping technology is an in situ method for removing volatile organic compounds (VOCs) from contaminated groundwater, whose feasibility was first analyzed by Gvirtzman and Gorelick [1992]. The technology involves pumping water contaminated with VOCs from below the water table to a point above the water table using air-lift pumping (Figure 2.1). Air-lift pumping is accomplished by injecting compressed air into a well with the injection point positioned beneath the water table. When applied in conjunction with the in-well vapor-stripping technology, air injection typically occurs through a diffuser. Air injection causes water to be lifted through buoyancy body forces, contaminated water to be drawn toward the well inlet, and provides large interfacial areas between the uncontaminated air and contaminated water streams. Concentration differences of the VOC between the water and air cause mass transfer of the VOC between phases during the air-lift process. At the top of the air-lift column the air and water phases are separated. The water that has been reduced in dissolved VOC concentration is infiltrated into the hydrologic system and the contaminated air is treated above the ground surface. Water infiltration occurs beneath the ground surface, thus avoiding the removal of groundwater from the hydrologic system. Infiltration of water from above the water table creates a recirculation pattern, where the concentration of VOC in the groundwater is reduced on each pass through the in-well vapor-stripping system. The effectiveness of the in-well vapor-stripping system is largely dependent on the solubility characteristics of the contaminating VOCs, the system design, and the operational characteristics.

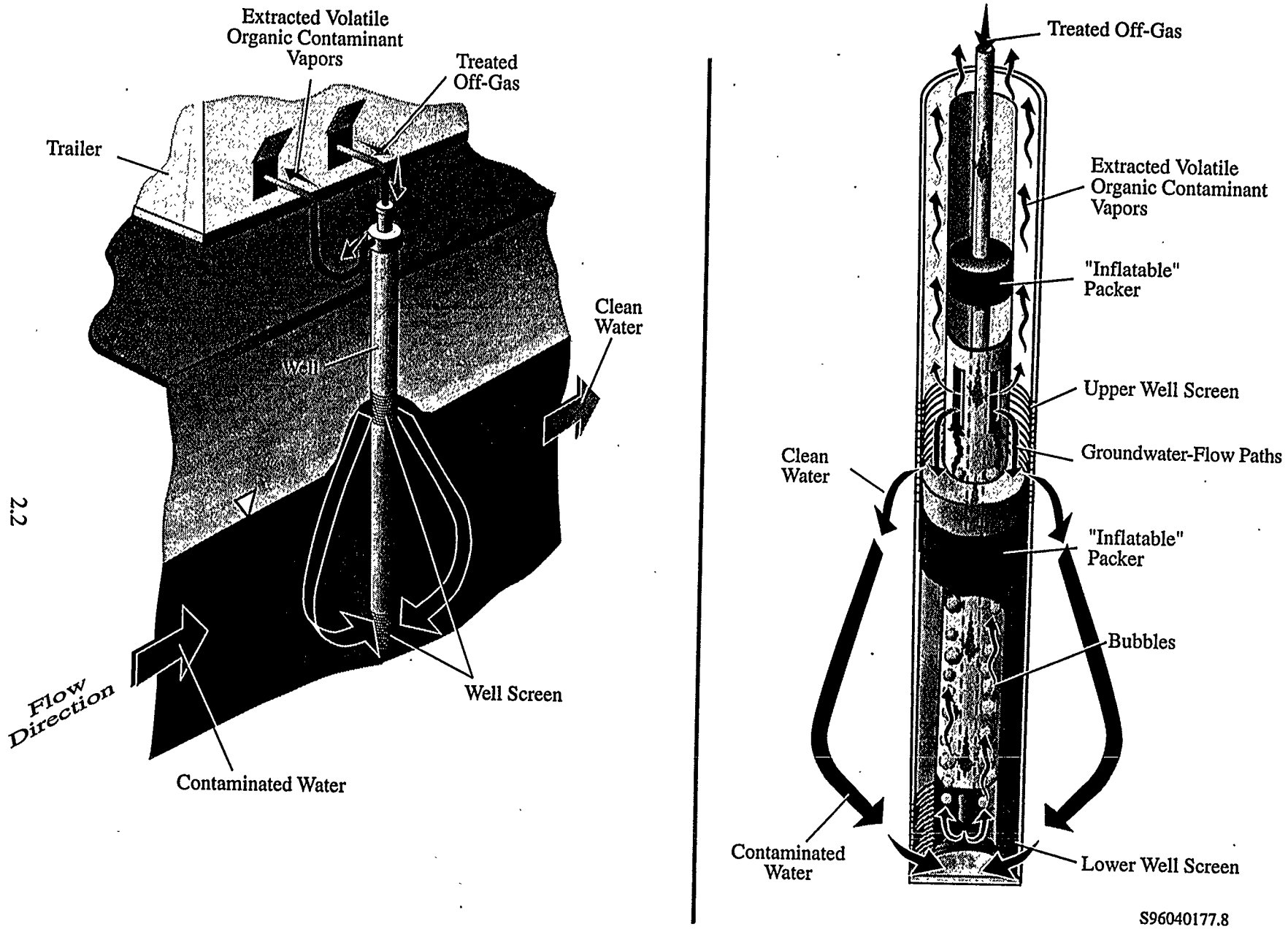

Figure 2.1. Schematic of the In-Well Vapor-Stripping System

3.0 Field Site Overview

The Edwards AFB site used for the demonstration of the in-well vapor-stripping system is located within one of ten operable units, which have been identified on the base. Edwards AFB has been included on the National Priorities List for cleanup under the Comprehensive Environmental Response, Compensation, and Liability Act of 1980 (CERCLA). This site has been designated by the base as Site 19 within Operable Unit 1 (Figure 3.1). The groundwater moving beneath this site had been previously contaminated with a varied composition of VOCs, which primarily included trichloroethylene (TCE). This contamination is believed to have occurred through the disposal of liquid TCE into surface basins. TCE had been used as a cleaning agent for experimental rocket powered planes in the 1960s and 1970s.

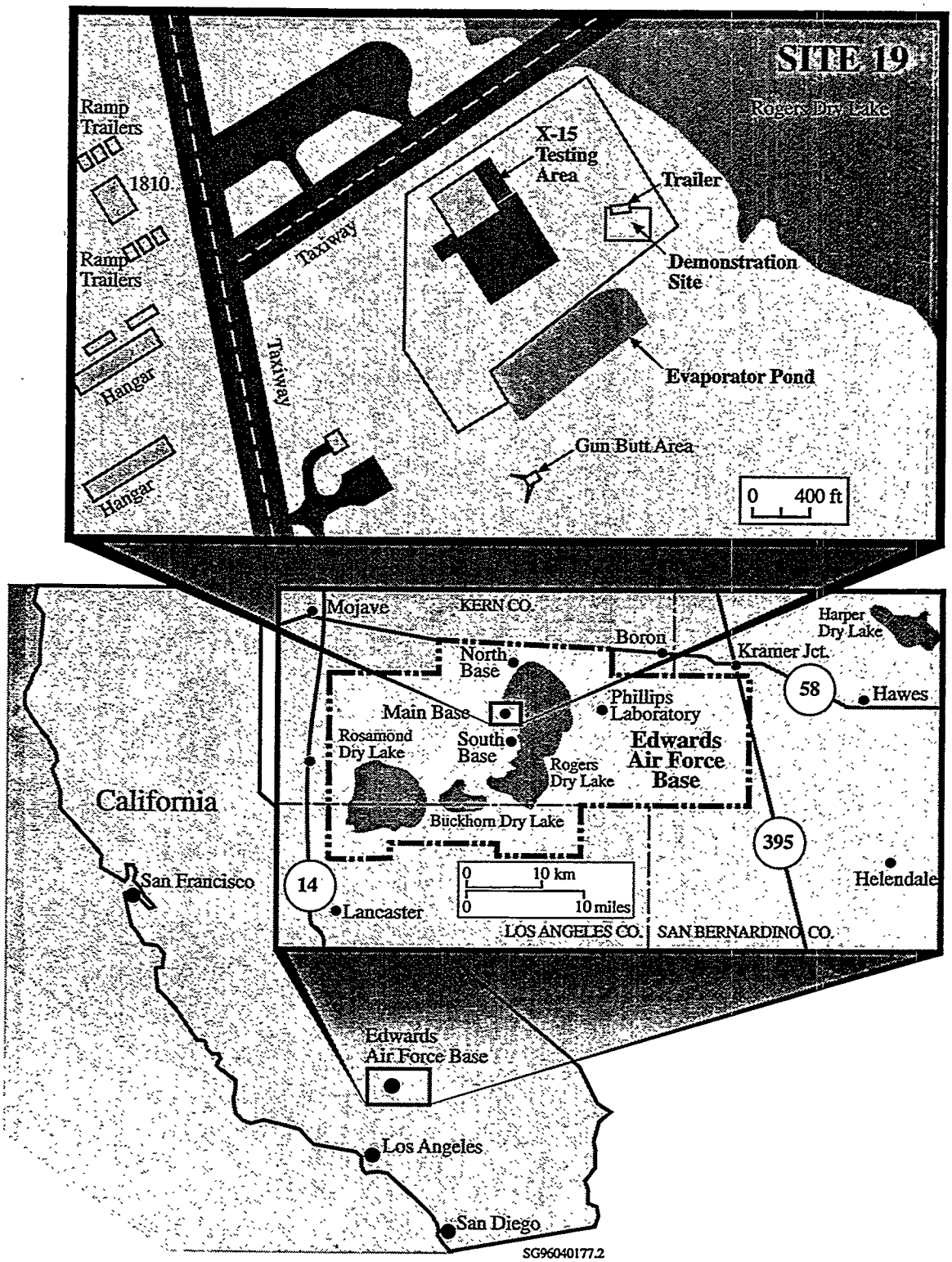

Figure 3.1. Edwards AFB Demonstration Site Location

4.0 Numerical Simulator

This numerical analysis of the in-well vapor-stripping system at Edwards AFB comprised, in part, numerical simulations with the STOMP simulator [White and Oostrom 1996] developed for the U.S. Department of Energy's Office of Environmental Restoration and Waste Management in conjunction with the Volatile Organic Compounds - Arid Soils Integrated Demonstration Program (VOC-Arid ID). The VOC-Arid ID, which has been concluded, was directed toward the remediation of sites where the subsurface environment had been contaminated with VOCs and/or radioactive material.

The STOMP engineering simulator provides a variety of capabilities to evaluate subsurface remediation technologies. Specifically the engineering simulator has been designed to provide engineers and scientists with multidimensional analysis capabilities of subsurface flow and transport phenomena for multiple phase and nonisothermal systems in saturated or partially saturated environments. The engineering simulator offers a variable source code configuration, which allows the user to optimize the source code, in terms of execution speed and memory, to the specifics of the subsurface system under consideration. Construction of the variable source code and input files may be performed through an associated interactive graphical user interface, sTeP.

The engineering simulator employs an integrated-volume finite-difference approach for the physical domain and a backward Euler approach for the time domain to discretize the governing partial differential conservation equations. Coupled solutions of component mass and energy conservation equations over four immiscible phases (aqueous, gas, ice, and nonaqueous liquid) are possible. Simulation of freezing conditions is currently limited to air-water systems. The simulator provides two solute transport options (coupled and uncoupled). Coupled solute transport concerns brine solutions, where phase properties (e.g., viscosity, density, enthalpy) are dependent on the solute concentration. Uncoupled solute transport concerns the dilute concentrations or tracers. Dilute solute transport problems with equilibrium partitioning between four phases (aqueous, gas, nonaqueous liquid, and solid) may be solved for multiple dilute solutes with radioactive decay. These solute transport equations are solved sequentially to the coupled flow and heat transport equations. Nonlinearities in the discretized coupled flow and heat transport equations are resolved with a Newton-Raphson iteration scheme. Phase appearances and transitions are handled through variable switching schemes. The saturation-relative permeability-pressure constitutive theory for describing both two-phase (water-air) and three-phase (water-oil-air) systems includes fluid entrapment and hysteretic effects. The simulator allows a variety of boundary conditions, both internally and externally with respect to the computational domain. The simulator allows computation domains with both permanent and dynamically defined inactive nodes. The simulator currently provides two linear system solvers, a directed banded scheme and an iterative conjugate gradient algorithm.

4.1 Governing Equations

The in-well vapor-stripping system at Edwards AFB was numerically simulated as an air-water system with a passive gas. Because of the low concentrations of TCE, the contaminant was modeled as a tracer solute. This approach allowed the governing equations for the conservation of water mass and solute mass to be decoupled and solved sequentially. The passive gas assumption implies that the gas phase within the hydrologic system would not participate in liberating volatile TCE. The governing equation for conservation of water mass solved in these simulations balances the accumulation of water mass against the advective flux of liquid water, according to Equation (4.1)

$$\frac{\partial}{\partial t}\left(n_D s_\ell \rho_\ell \omega_\ell^w\right) - \dot{m}^w = -\nabla \mathbf{V}_\ell = -\nabla\left[\frac{\omega_\ell^w \rho_\ell k_{r\ell} \mathbf{k}}{\mu_\ell}\left(\nabla P_\ell + \rho_\ell g \mathbf{z}_g\right)\right] \tag{4.1}$$

where t = time

n_D = diffusive porosity

s_ℓ = aqueous saturation

ρ_ℓ = aqueous density

ω_ℓ^w = mass fraction of water in the aqueous phase

$\dot{m}^w$ = mass source of water

$\mathbf{V}_\ell$ = Darcy velocity

$k_{r\ell}$ = aqueous relative permeability

$\mathbf{k}$ = intrinsic permeability

μ_ℓ = aqueous dynamic viscosity

P_ℓ = aqueous pressure

g = acceleration of gravity

$\mathbf{z}_g$ = gravitational unit vector.

This equation is nonlinear, primarily through the dependencies of the aqueous saturation on the aqueous pressure and the aqueous relative permeability on the aqueous saturation. The Brooks and Corey [1964] soil-moisture retention function was used to describe the functional relation between the aqueous saturation and gas-aqueous capillary pressure, according to Equation (4.2)

$$\bar{s}_\ell = \left[\frac{\left(\frac{P_g - P_\ell}{\bar{\rho}_\ell g}\right)}{\psi}\right]^{-\lambda} \quad for\ P_g - P_\ell > \psi$$

$$\bar{s}_\ell = 1 \quad for \quad P_g - P_\ell \leq 0 \tag{4.2}$$

where $\bar{s}_\ell$ = effective aqueous saturation
ψ = Brooks and Corey air entry pressure head
λ = parameter for the Brooks and Corey function
P_g = gas pressure
$\bar{\rho}_\ell$ = aqueous density at reference conditions.

The Burdine [1953] porosity distribution function was used in combination with the Brooks and Corey soil-moisture retention function to describe the functional relation between the aqueous relative permeability and saturation, according to Equation (4.3)

$$k_{r\ell} = \bar{s}_\ell^{(3+2/\lambda)} \tag{4.3}$$

The governing equation for conservation of solute mass (TCE) solved in these simulations balances the accumulation of solute mass against the advective, diffusive, and dispersive fluxes of the solute through water, according to Equation (4.4)

$$\frac{\partial C}{\partial t} = -\nabla(C_\ell \mathbf{V}_\ell) + \nabla\left[\left(\tau_\ell s_\ell n_D D_\ell^C + s_\ell n_D D_{h\ell}\right)\nabla C_\ell\right] + \dot{m}^C \tag{4.4}$$

where C = total molar solute concentration
C_ℓ = aqueous molar solute concentration
$\mathbf{V}_\ell$ = aqueous flux vector
τ_ℓ = aqueous tortuosity
n_D = diffusive porosity
D_ℓ^C = molecular solute diffusion coefficient through pure water
$D_{h\ell}$ = aqueous hydraulic dispersion coefficient
$\dot{m}^C$ = solute source rate.

The governing equations and associated constitutive equations were solved in a sequential process, the water mass conservation equation followed by the solute mass conservation equation. Solution of the water mass conservation equation yields Darcy velocity components, which are then used for advective transport of the dissolved solute. The STOMP simulator solves the governing equations numerically using the integrated-finite-difference scheme [Patankar 1980] for spatial discretization and backward Euler differencing for temporal discretization. The

system of algebraic equations that result from the discretization of the governing equations and constitutive relations for the flow solution is nonlinear. The nonlinearities were resolved using the Newton-Raphson [Kreyszig 1979] iterative solution scheme. The governing equations for solute transport were solved using the flux limiter algorithm (i.e., Leonard's third order scheme) of Gupta et al. [1991]. Flux limiter algorithms split the advective and diffusive/dispersive components of solute transport. First, an explicit scheme is used to advectively transport solute through the flux limiting scheme, yielding an intermediate solute concentration field. Second an implicit scheme is used to transport the intermediate solute concentration field through diffusion and dispersion to yield the final solute concentration field. Solution of the algebraic equations that result from discretizing the governing equations for solute transport is direct and follows that of the flow solution.

4.2 Equilibrium Model for Vapor Stripping

The engineered component (i.e., air-lift pumping well) of the in-well vapor-stripping system was treated numerically in the STOMP simulator as a linked solute source model. In this model, a zone of surfaces is defined within the computational grid over which inlet fluxes of solute are summed. In the physical domain, this would represent the lower screened interval of the vapor-stripping well. Solute concentrations of the incoming water are reduced according to the thermodynamic equilibrium conditions at the separator plate. The fundamental assumption associated with this model is that sufficient interphase mass transport of the VOC has occurred between the water and air during the air-lift pumping to achieve nearly equilibrium conditions at the separator plate. The zone of surfaces is then linked to a zone of nodes in the computational domain that receives the solute at reduced concentration levels. In the physical domain, this would be equivalent to the separator plate and upper screened interval where water of lower dissolved TCE concentration is infiltrated into the hydrologic system.

Thermodynamic equilibrium of the VOC between the aqueous and gas phases during air-lift pumping is assumed to depend on the air-to-water volumetric flow ratio, well-head pressure, temperature, and solubility of the dissolved VOC. The mole fraction of dissolved solute in the returning water stream can be computed from a conservation equation for solute between the inlet and outlet of the vapor-stripping well, according to Equation (4.5).

$$\dot{C} = \frac{\chi_g^C \rho_g \dot{q}_g}{M_g} + \frac{\chi_\ell^C \rho_\ell \dot{q}_\ell}{M_\ell} \tag{4.5}$$

where $\dot{C}$ = molar flux of solute at the well inlet

χ_g^C = mole fraction of solute in the gas phase at the separator plate

χ_ℓ^C = mole fraction of solute in the aqueous phase at the separator plate

ρ_g = gas-phase density at the separator plate

ρ_ℓ = aqueous-phase density at the separator plate

$\dot{q}_g$ = volumetric gas-phase flow rate

$\dot{q}_\ell$ = volumetric aqueous-phase flow rate

M_g = gas-phase molecular weight at the separator plate

M_ℓ = aqueous-phase molecular weight at the separator plate.

With the assumption of low VOC concentrations the gas and aqueous molecular weights can be expressed as functions of the water and air mole fractions, according to Equations (4.6)

$$M_g = \chi_g^a M^a + \chi_g^w M^w$$

$$M_\ell = M^w \tag{4.6}$$

where, χ_g^a = mole fraction of air in the gas phase

χ_g^w = mole fraction of water vapor in the gas phase

M^a = molecular weight of air

M^w = molecular weight of water.

Phase partitioning of the VOC between the aqueous and gas phases is expressed using Henry's Law, according to Equation (4.7)

$$\chi_g^C = \frac{\chi_\ell^C H_{g\ell}^C}{P_g} \tag{4.7}$$

The mole fraction of dissolved VOC at the water-separator plate is computed by combining Equations (4.5) through (4.7), according to Equation (4.8).

$$\chi_\ell^C = \frac{\dot{C}}{\dot{q}_\ell \left[\frac{H_{g\ell}^C \rho_g \left(\dot{q}_g / \dot{q}_\ell \right)}{P_g M_g} + \frac{\rho_\ell}{M_\ell} \right]} \tag{4.8}$$

5.0 Hydrologic Conceptual Model

Numerical analysis of the in-well vapor-stripping system requires a conceptual model that completely describes the engineered component, terrestrial component, and operational parameters. The engineered component comprises the well, screen intervals, and the air-lift pumping system. The terrestrial component comprises the stratigraphy, hydrologic properties, and ambient water table depths and flow rates. Operational parameters comprise the air-injection rates, air-injection submergence, lift heights, and pumping flow rates. The objective of numerical analysis during the design period of an in-well vapor-stripping system is to generate predictions of operational performance of the coupled engineered and terrestrial components subjected to various operational parameters. Primary design objectives for in-well vapor-stripping systems are the determination of return heights above the upper screened interval and zones of influence. The return height is a critical parameter in defining the zone of influence for an in-well vapor-stripping system. Return heights are strongly dependent on the hydrologic properties of the terrestrial component along with the lift height and pumping rate of the engineered system. Optimization of the system design for remediation effectiveness and zone of influence requires accurate predictions of return height. System design involves four processes: 1) development of a hydrologic conceptual model, 2) development of an engineered component model, 3) numerical simulation of the coupled conceptual models to predict system performance, and 4) modification of the engineered components to optimize performance. Steps three and four represent an iterative process.

5.1 Stratigraphy

The hydrologic conceptual model comprises the subsurface stratigraphy and hydrologic parameters for each distinct soil component. A preliminary stratigraphy was generated for the field demonstration site from a visual inspection of core samples obtained from the two characterization wells. A schematic of this geologic stratigraphy is show in the first column of Figure 5.1. Core samples, taken from the characterization wells, were analyzed in the laboratory to determine porosity, grain density, grain size distributions, liquid permeability, and gas permeability. Core samples used for hydrostatic and hydrodynamic parameters are shown in reference to the visual inspection stratigraphy in Figure 5.1 under the columns labeled Grain-Size Cores and Permeability Cores, respectively.

The American Society for Testing and Materials standards [ASTM 1993] prescribe a system for designating soil types based on grain-size distributions. The soils collected from the Edwards AFB site were considered as coarse-grained soils having more than 50% of the grains retained on the No. 200 (75-μm) sieve. Within this classification, the soils were subclassified as sands with more than 50% of the coarse fraction passing the No. 4 (4.75-mm) sieve. Further

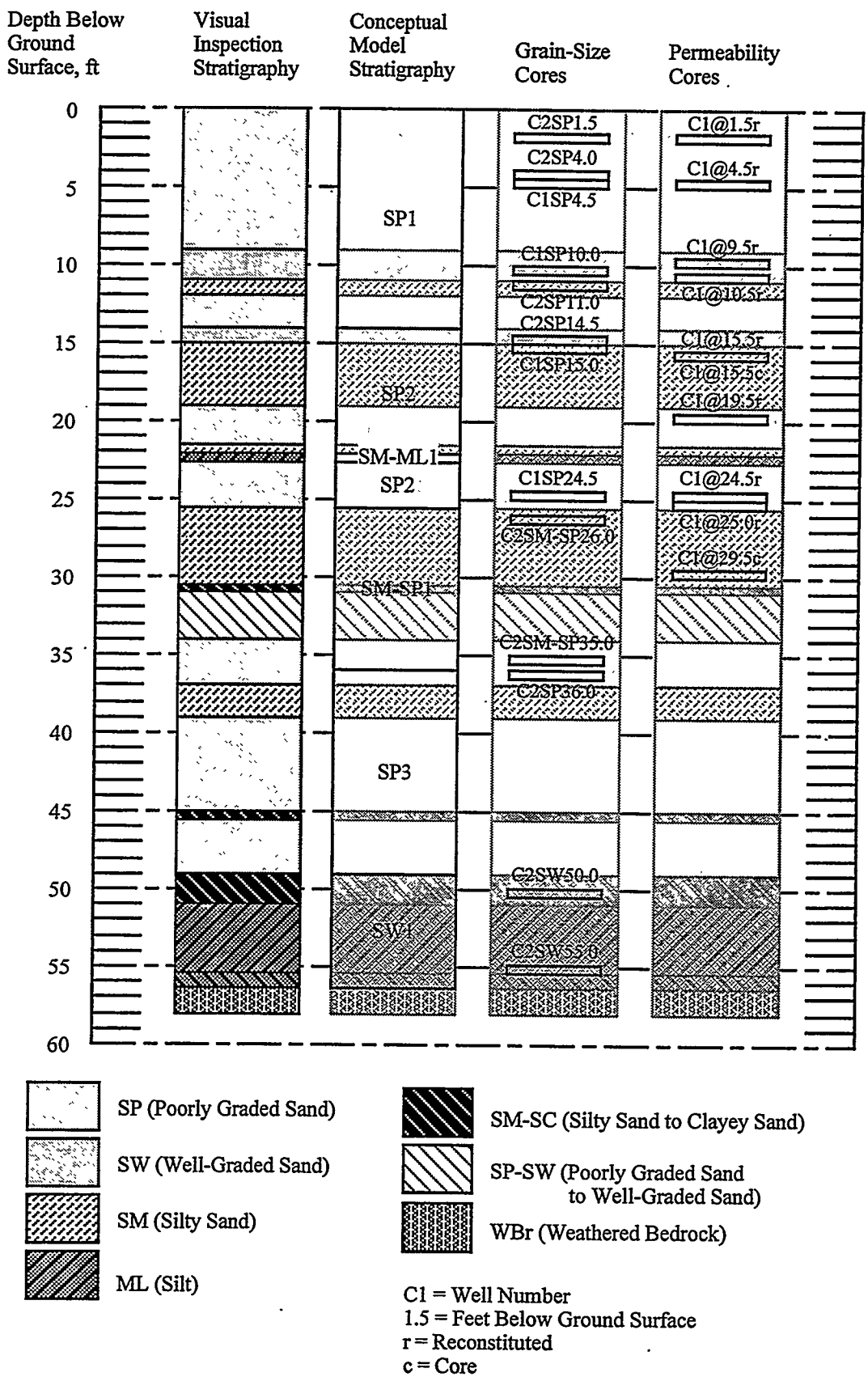

Figure 5.1. Field Site and Conceptual Model Stratigraphy and Core Sample Locations

subclassification of the soils required determination of two parameters (the coefficient of uniformity, *Cu,* and the coefficient of curvature, *Cc*) from a plot of the cumulative particle size distribution. The coefficients of uniformity and curvature are computed according to Equations (5.1) and (5.2)

$$Cu = \frac{D_{60}}{D_{10}} \tag{5.1}$$

$$Cc = \frac{(D_{30})^2}{(D_{10} D_{60})} \tag{5.2}$$

where D_{10}, D_{30}, and D_{60} are the particle-size diameters corresponding to 10%, 30%, and 60% passing, respectively, on the cumulative particle-size distribution curves, Figures 5.2 through 5.4. Grain-size distribution plots are shown graphically for soil samples C2SP1.5, C2SP4.0, C1SP4.5, and C2SW10.0 in Figure 5.2; for soil samples C2SM11.0, C2SW14.5, C1SM15.0, and C1SP24.5 in Figure 5.3; and for soil samples C2SM26.0, C2SP35.0, C2SP36.0, C2SM-SC50.0, and C2ML55.0 in Figure 5.4.

Following the ASTM [1993] classification standards, the collected soil samples were reclassified from the original visual classifications, as shown in Table 5.1. These ASTM classifications were then used to define the conceptual model for the soil stratigraphy. Soil layers between 0 and 14 ft below ground surface (BGS) were classified as a homogeneous layer of poorly graded sand, indicated as SP1 in the Conceptual Model Stratigraphy column in Figure 5.1. Continuing down the soil column, layers between 14 and 25.5 ft BGS were classified as a homogeneous layer of poorly graded sand (indicated as SP2), layers between 25.5 and 35.5 ft BGS were classified as a homogeneous layer of silt to poorly graded sand (indicated as SM-SP1), layers between 35.5 and 49 ft BGS were classified as a homogeneous layer of poorly graded sand (indicated as SP3), and layers between 49 and 56.5 ft BGS were classified as a homogeneous layer of well graded sand (indicated as SW1). A critical layer of soil between 22 and 22.5 ft BGS, visually classified as silt, was without a representative core sample. A homogeneous layer of soil with a silty-sand to silt particle-size distribution was included in the conceptual model (indicated as SM-ML1). The particle-size distribution for this layer of soil was generated by reducing the particle size distributions of the adjacent soil layers until a particle-size distribution of silt was obtained.

A composite grain-size distribution for each conceptual model soil (CMS) designation was generated from the core samples taken from within that soil strata. For example, the grain-size distribution for the SP1 soil was generated from the distributions in the following core samples: C2SP1.5, C2SP4.0, C1SP4.5, C1SP10.0, and C2SP11.0. These composite grain-size

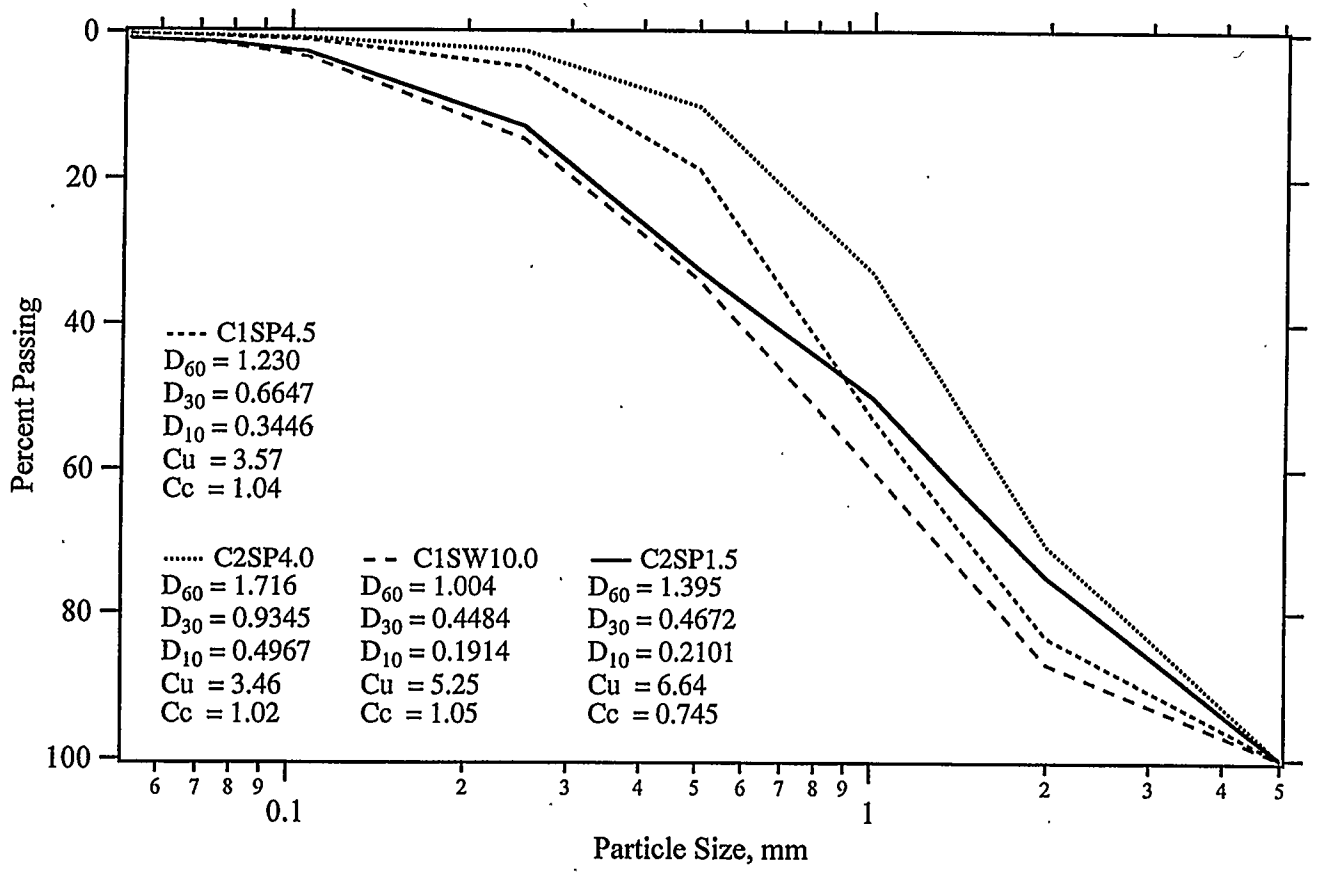

Figure 5.2a. Particle Size Distributions (C1SP4.5, C2SP4.0, C1SW10.0, C2SP1.5)

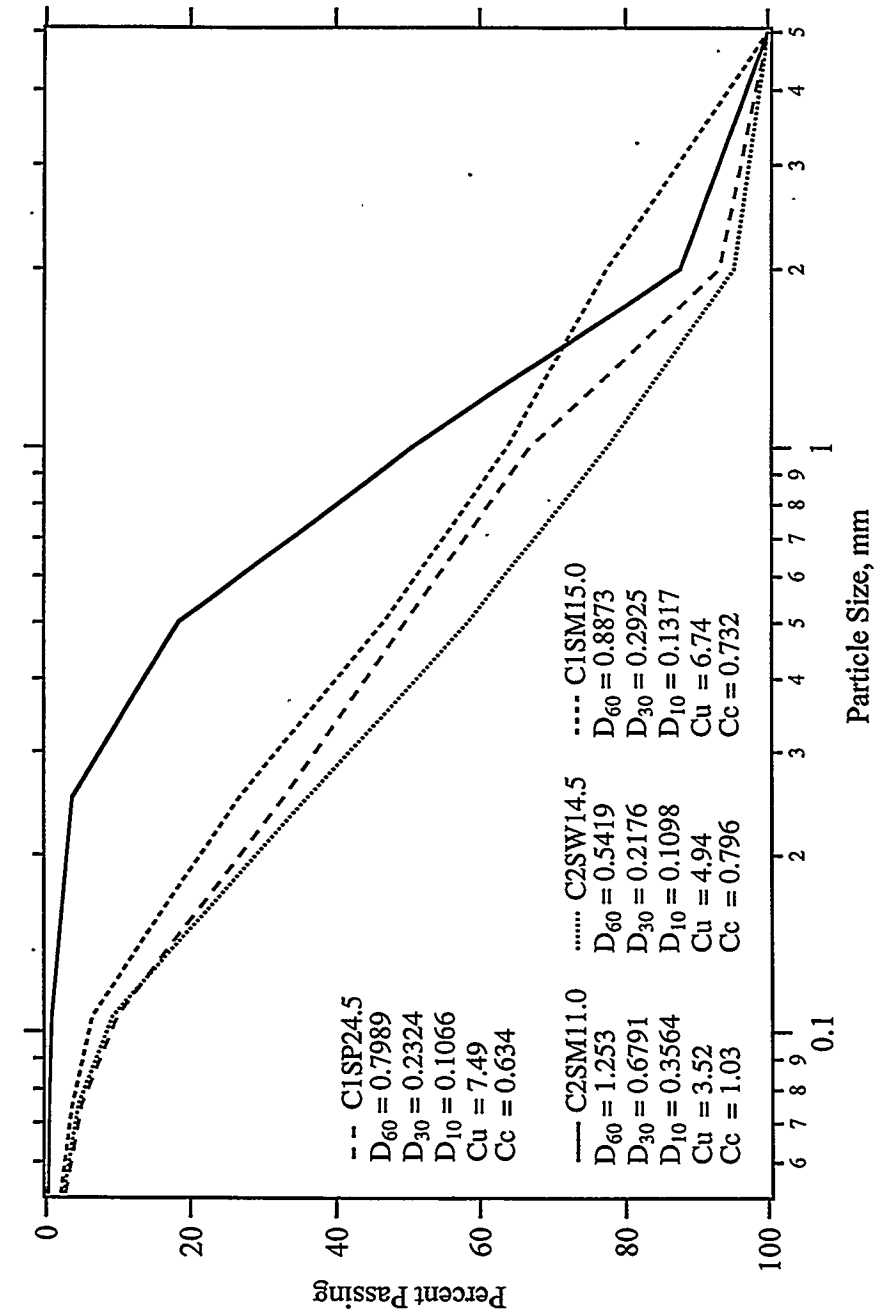

Figure 5.2b. Particle Size Distributions (C1SP24.5, C2SM11.0, C2SW14.5, C1SM15.0)

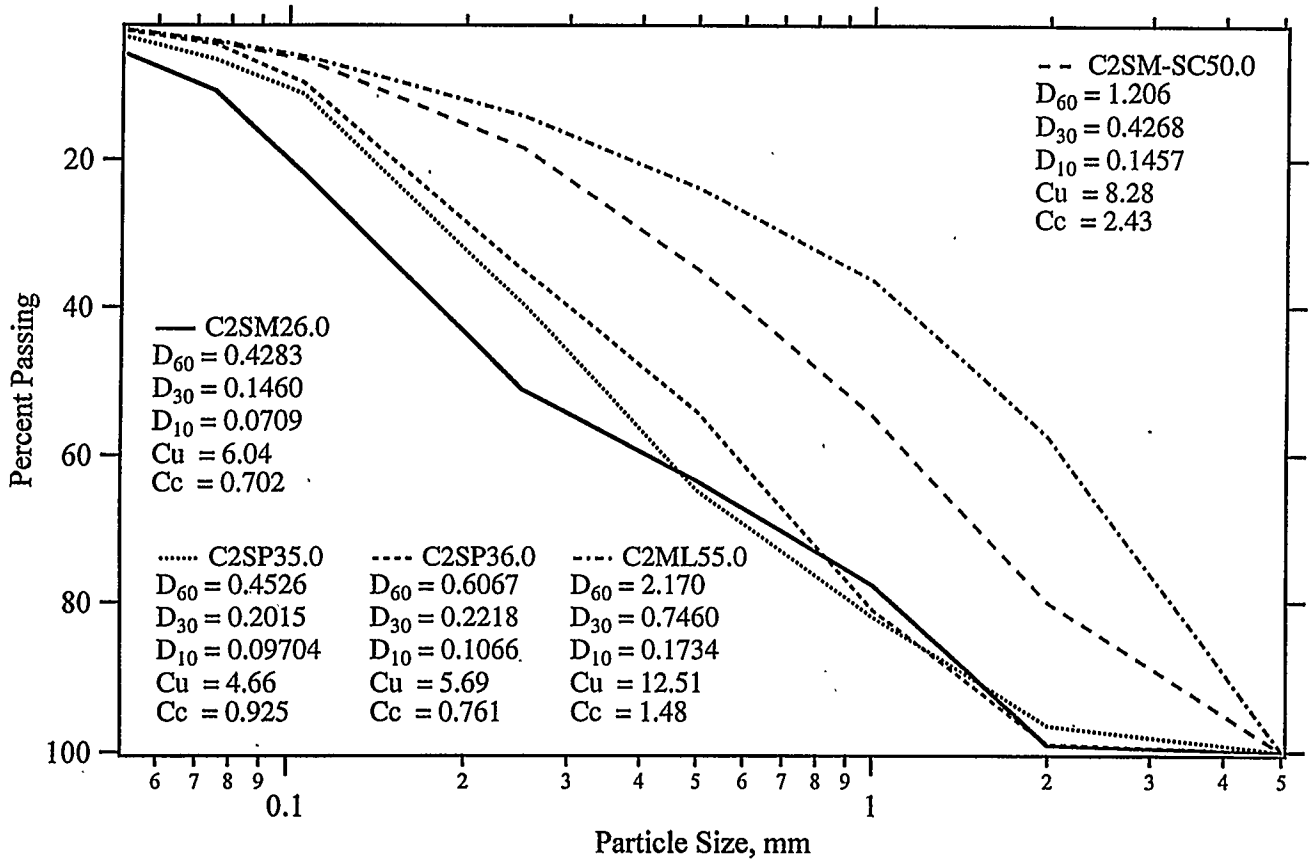

Figure 5.2c. Particle Size Distributions (C2SM26.0, C2SP35.0, C2SP36.0,C2ML55.0, C2SM-SC50.0)

distributions for the CMS designations are given in Table 5.2. It should be noted that the grain-size distribution measurements taken on the cores extracted from the characterization wells were limited to a No. 270 sieve, which retains particles greater than 0.053 mm. Therefore, no distinction between silt and clay size particles was possible. Clay and silt fractions for the CMS s were assumed to be 1/3 and 2/3, respectively, of the percent passing the No. 270 sieve. Because of the small percentages of clay- and silt-sized particles, the distinction between these two sizes has an inconsequential effect on the static and dynamic hydrologic properties.

Table 5.1 ASTM [1993] Soil Core Classifications

Soil Core	ASTM Soil Designation
C2SP1.5	SP -- poorly graded sand
C2SP4.0	SP -- poorly graded sand
C1SP4.5	SP -- poorly graded sand
C2SW10.0	SP -- poorly graded sand
C2SM11.0	SP -- poorly graded sand
C2SW14.5	SP -- poorly graded sand
C1SM15.0	SP -- poorly graded sand
C1SP24.5	SP -- poorly graded sand
C2SM26.0	SM-SP -- silty sand to poorly graded sand
C2SP35.0	SM-SP -- silty sand to poorly graded sand
C2SP36.0	SP -- poorly graded sand
C2SM-SC50.0	SW -- well-graded sand
C2ML55.0	SW -- well-graded sand

Table 5.2. Grain-Size Distributions for the Conceptual Model Soils

		Weight Percent					
Particle Size	mm	SP1	SP2	SM-ML1	SM-SP1	SP3	SW1
Clay	0.0015	0.173	0.79	2.67	1.63	0.93	0.9
Silt	0.026	0.347	1.58	5.33	3.27	1.87	1.8
Very fine sand	0.075	1.22	6.13	17.0	11.7	7.0	3.8
Fine sand	0.175	5.94	23.24	25.9	28.85	25.0	9.75
Medium sand	0.375	15.14	19.81	16.8	18.7	19.4	13.0
Coarse sand	0.75	26.54	17.91	14.2	15.75	26.7	16.3
Very coarse sand	1.5	31.42	19.11	16.1	17.85	18.0	23.25
Fine gravel	7.0	19.22	11.40	2.0	2.2	1.0	31.2

5.2 Hydrologic Properties

Soil porosity was measured in the laboratory on four core samples using soil clods to determine bulk and particle density. These results are summarized in Table 5.3. Minimum values for soil porosity were also estimated from the water content measurements made on the grain-size cores, by assuming an average grain density of 2.63 g/cm^3. These results are summarized in Table 5.4. Porosity values for the CMS s were assigned according to the data reported in Tables 5.3 and 5.4, and are given in Table 5.5.

Table 5.3. Bulk Density, Particle Density, and Porosity for Core Samples

Soil Sample	Bulk Density	Particle Density	Porosity
C1SP4.5	2.20	2.612	0.155
C1SP10.0	2.130	2.622	0.188
C2SP14.5	1.980	2.630	0.247
C1SP15.0	1.813	2.637	0.313

Table 5.4. Weight Percent Water and Minimum Porosity for Core Samples

Soil Sample	Weight% Water	Minimum Porosity
C2SP1.5	0.0643	0.025
C2SP4.0	0.1193	0.263
C1SP4.5	0.0795	0.185
C1SP10.0	0.2459	0.110
C2SP11.0	0.1297	0.282
C2SP14.5	0.1107	0.247
C1SP15.0	0.1027	0.231
C2SM-SP26.0	0.1786	0.364
C2SM-SP35.0	0.1892	0.380
C2SP36.0	0.1217	0.267
C2SW50.0	0.1441	0.306
C2SW55.0	0.1192	0.263

Soil moisture retention characteristics for the CMS s were computed from the particle-size distribution and porosity data shown in Tables 5.2 and 5.5, respectively, using SOILPROP [Mishra et al. 1989]. SOILPROP is a commercially available program for estimating unsaturated soil hydraulic properties from particle-size distribution data. Using particle-size distribution and porosity data, the code generates parameters for the van Genuchten [1980] and Brooks and Corey [1964] functions, which relate soil saturation to capillary head. Results are summarized in Table 5.6.

Table 5.5. Porosity for the Conceptual Model Soils

Model Soil	Porosity
SP1	0.19
SP2	0.24
SM-ML1	0.35
SM-SP1	0.37
SP3	0.27
SW1	0.28

Table 5.6. van Genuchten [1980] Retention Parameters for the Conceptual Model Soils

Model Soil	van Genuchten α Parameter, 1/m	van Genuchten n Parameter	Brooks/Corey Ψ Parameter, m	Brooks/Corey λ Parameter
SP1	14.8	1.63	0.0432	0.528
SP2	10.6	1.47	0.0641	0.415
SM-ML1	6.95	1.42	0.100	0.383
SM-SP1	7.47	1.49	0.0900	0.430
SP3	6.07	1.58	0.107	0.494
SW1	61.9	1.38	0.0117	0.346

Saturated soil hydraulic conductivity for the CMS s was computed using the Kozeny-Carman equation [Koltermann and Gorelick 1995], according to Equation (5.3)

$$K_\ell = \left(\frac{\overline{\rho}_\ell g}{\overline{\mu}_\ell} \right) \frac{d^2 \phi^3}{180(1-\phi)^2} \tag{5.3}$$

where K_ℓ =e saturated hydraulic conductivity

$\overline{\rho}_\ell$ = aqueous density at reference conditions

$\overline{\mu}_\ell$ = aqueous dynamic viscosity at reference conditions

d = representative grain diameter

ϕ = sediment porosity.

Representative grain diameters were computed from the particle-size distributions as the harmonic mean grain diameter according to Equation (5.4)

$$\frac{1}{d} = \sum \frac{1}{d_i f_i} \tag{5.4}$$

where d_i is the particle size diameter and f is the fraction of particles. Hydraulic conductivity and intrinsic permeability computed from Equations (5.3) and (5.4) are shown in Table 5.7 for the CMS s.

Table 5.7. Saturated Hydraulic Conductivity for the Conceptual Model Soils

Model Soil	Hydraulic Conductivity, m/s	Intrinsic Permeability, m^2
SP1	7.21×10^{-5}	7.50×10^{-12}
SP2	1.60×10^{-5}	1.67×10^{-12}
SM-ML1	9.16×10^{-6}	9.51×10^{-13}
SM-SP1	2.61×10^{-5}	2.71×10^{-12}
SP3	1.87×10^{-5}	1.94×10^{-12}
SW1	3.12×10^{-5}	3.24×10^{-12}

A portion of the core samples taken from the characterization wells were analyzed for liquid and gas permeability. Core samples subjected to permeability analysis are identified in the Permeability Core column of Figure 5.1. Plots of liquid permeability versus liquid saturation and gas permeability versus liquid saturation for these core samples are shown in Figures 5.5 and 5.6, respectively, as unconnected markers. All but two of the samples analyzed used recomposited soils. The two samples that used subcores were those identified as C1@15.5c and C1@25.5c. Aqueous permeability data from laboratory measurements, shown in Figure 5.5, were significantly lower than that predicted using the correlations of Kozeny-Carman, Brooks-Corey, and Burdine [1953]. Conversely, gas permeability data from laboratory measurements, shown in Figure 5.6, were significantly higher than those predicted using the empirical correlations. Clearly, the laboratory data are inconsistent between aqueous and gas permeabilities. Aqueous permeabilities were determined using an ultracentrifuge technique [Khaleel et al. 1995], whereas gas permeability was measured using a more conventional steady-state head control method. One possible rationale for this discrepancy between measured permeabilities is that dispersive clays were released during the centrifuge test which effectively clogged the aqueous flow. When the soil samples were then transferred to the gas permeability equipment, these mobilized clay fractions remained on ultracentrifuge sample holders. Therefore, dispersive clay released during the aqueous permeability test were not present during the gas permeability tests. Because of this discrepancy in permeability measurements, comparisons of numerical simulations and field measurements were used to determine the permeabilities for the CMS s.

5.3 Computational Domain

The computational domain for numerical simulations of the in-well vapor-stripping system at Edwards AFB used a two-dimensional cylindrical grid comprised of 52 radial direction

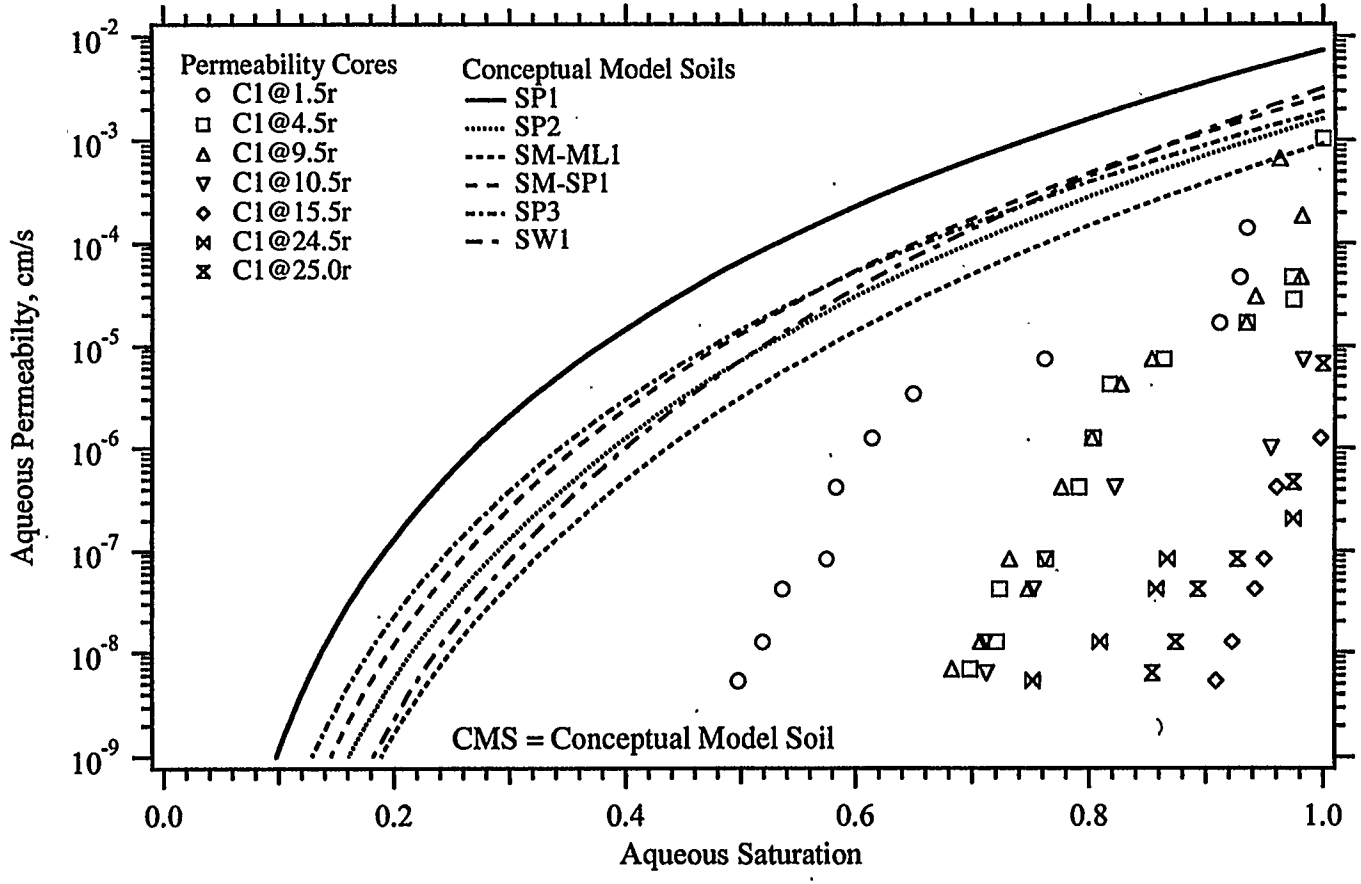

Figure 5.3. Aqueous Permeability Versus Aqueous Saturation from Core Measurements and CMS Functions

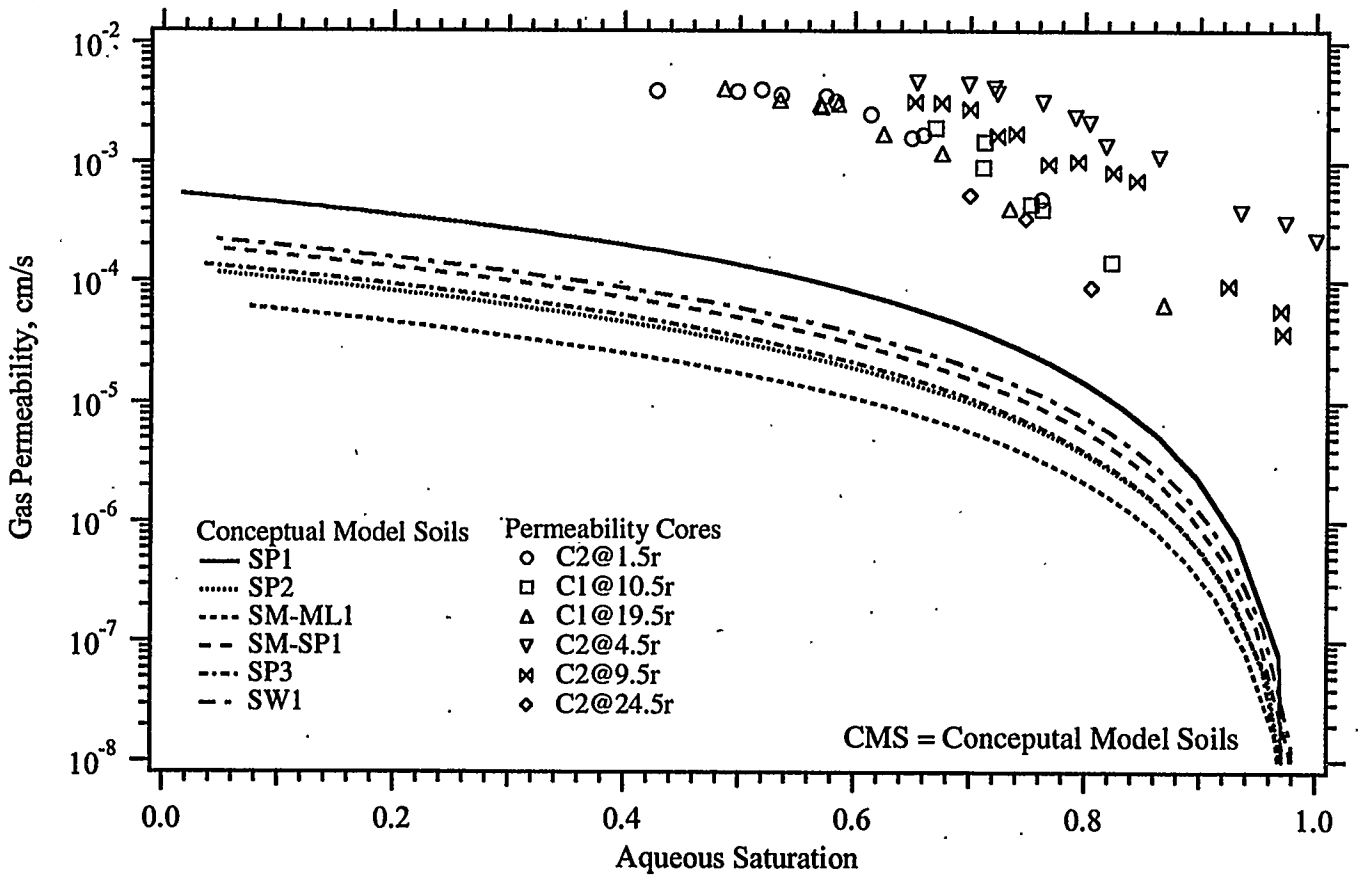

Figure 5.4. Gas Permeability Versus Aqueous Saturation from Core Measurements and CMS Functions

nodes and 113 vertical direction nodes, as represented in Figure 5.7. Nodes in the vertical direction were uniform with a spacing of 6 in. Nodes in the radial direction increased in width with distance from the center with the following spacings: 3.125 in., 2 in., 2.875 in., 4 in., 18 @ 6 in., 10 @ 1 ft, 10 @ 2 ft, and 10 @ 4 ft. Soil strata were defined according to conceptual model soil stratigraphy shown in Figure 5.1: SW1 spanning layers 1 to 15, SP3 spanning layers 16 to 45, SM-SP1 spanning layers 46 to 62, SP3 spanning layers 63 to 68 and 70 to 85, SM-ML1 at layer 69, and SP1 spanning layers 86 to 113. A special soil type was created to model the upper screened interval, which spanned the domain from (2,71) to (2,100), where the indices are denoted (radial,vertical). Inactive nodes (i.e., noncomputational) were defined for the vapor-stripping well, which spanned the domains from (1,14) to (1,113) and from (2,101) to (2,113). An inactive node was defined at (2,70) to model the bentonite seal beneath the upper screened interval. A domain of inactive nodes was defined over (2,14) to (2,33) to model the riprap around the lower screened interval. Injection of water and TCE into the hydrologic system was modeled with an injection source at node (2,71), located at the bottom of the upper screened well nodes. Removal of water and TCE from the hydrologic system was modeled with boundary conditions applied on the surfaces between the active and inactive nodes along the lower screened surface, from (3,14) to (3,33).

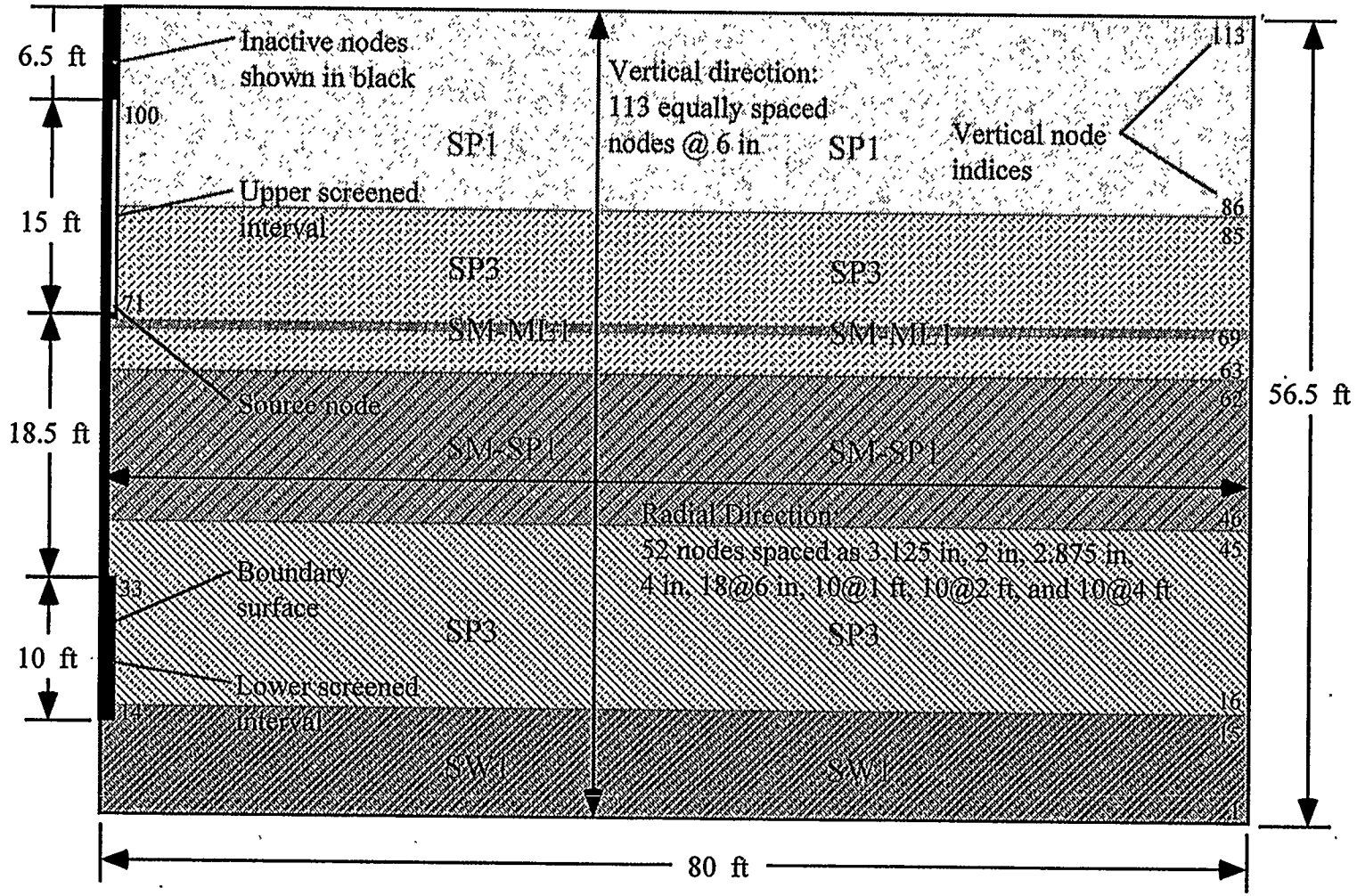

Figure 5.5. Computational Grid

6.0 System Design

The pumping capacity of an in-well vapor-stripping system depends on the performance of the air-lift process of the engineered component and the infiltration capacity of the terrestrial component. The air-lift operation and performance vary with total lift and submergence of the air line below the pumping level. The well design for in-well vapor-stripping requires that the liquid-gas separator plate be above the top of the upper screened interval of well casing and that the air injection diffuser be mounted either above the top of the lower screened interval or above the bottom of an eductor pipe within the lower screened interval. Infiltration capacity of the terrestrial system is dependent on the stratigraphy and saturated conductivity of the soil layers between the screened intervals and the position of the screened interval above the static water table height. A principal design parameter for the in-well vapor-stripping system, therefore, is the length and spacing of the upper and lower screened intervals. Five design options were considered for the Edwards AFB field demonstration, shown in Figure 6.1 as wells designs A through E. Pumping/infiltration capacity predictions were generated for each well design using the STOMP simulator with the conceptual model.

The pumping/infiltration capacity problem was conceptualized as a source/sink driving function imposed on the conceptual model for the terrestrial environment. The model used a two-dimensional cylindrical coordinate system centered on the air-lift pumping well. The inner radius of nodes from the bottom of the well to the ground surface was inactive nodes (noncomputational). Inlet flow across the lower screened interval was modeled as uniformly distributed water sink. The surfaces between the inner radius of inactive nodes and the next radial column of active nodes over the lower screened interval had a uniform water removal rate, whose volumetric sum equaled the pumping rate. This driving function was imposed by applying a uniform-steady Neumann boundary condition on these surfaces. Outlet flow across the upper screened interval was modeled using a source node at the bottom of a column of special well nodes. In the Edwards AFB in-well vapor-stripping system design, the outer well casing diameter increases from 6 to 10 in. (inside diameter) at the bottom of the upper screened interval. The 6-in. casing continues to the separator plate, positioned some height above the screened interval, forming an annular space.

Water pumped from the lower screened interval strikes the separator plate, cascades down the annular space, and ponds within the annular space prior to infiltrating into the ground. Water ponding within the annular space can occur within and above the upper screened interval, but should not exceed the height of the separator plate. The height between the dynamic water table level and the separator plate represents the total lift for the air-lift pumping system. The annular space between the 6- and 10-in. well casings within the upper screened interval was modeled as special well nodes. A volumetric water source equivalent to the pumping rate was imposed on the lowest node of this column of special well nodes. The saturation and relative

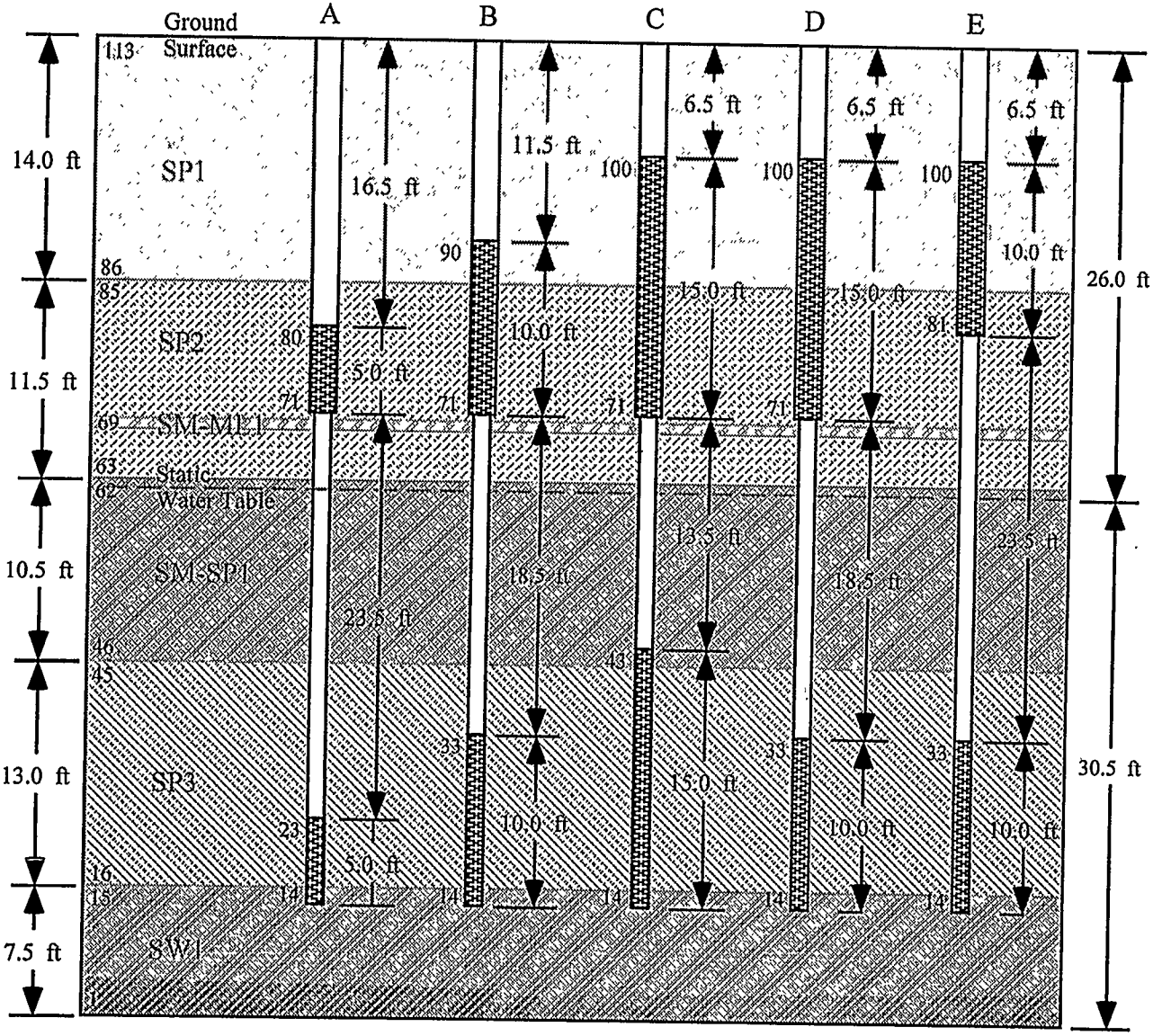

Figure 6.1. Vapor-Stripping Well Design Options

permeability of a special well node equaled the fractional height of ponded water within the node. Flow resistances within the well nodes were assigned to be negligible.

Simulations to determine pumping/infiltration capacity were initialized with a static hydraulic gradient for zero-recharge conditions and executed for a simulation period of 100 days, sufficient time to reach steady-state conditions. Steady-state results from the pumping/infiltration capacity simulations for the five system designs are summarized in Figure 6.2. These results show two regimes for the ponding height versus pumping rate relation. For ponding heights within the upper screened interval, a nonlinear relation occurs between the ponding height and the pumping rate. This nonlinear relation results from the proportional change in infiltration area from the upper screened interval with ponding height. For ponding heights greater than the upper screened interval, a nearly linear relation occurs between the ponding height and pumping rate. This linear relation results because the infiltration area from the upper screened interval is fixed by the screened height. Comparison of designs C and D demonstrates that for the Edwards AFB stratigraphy differences in the lower screened interval height are insignificant unless pumping rates cause soil desaturation to occur near the well inlet. For Edwards AFB, pumping/infiltration capacity appears generally to be limited by ponding heights. Comparison of designs B and E demonstrates the benefit of raising the height of the upper screened interval above the static water table level in terms of ponding. Simulation results in terms of lift height are summarized in Figure 6.3, where lift height is computed as the difference between the design lift and static water table elevations. The design lift elevation equals the top of the upper screened interval for ponding heights within the screened interval or the top of the ponded water for ponding height above the screened interval and represents the minimum lift required for a particular design and pumping/infiltration rate. Design E shows an advantage over design B in terms of ponding height for all pumping/infiltration rates. In terms of lift heights, however, design B is more efficient than design E for pumping rates below 10.5 gpm.

Banded gray-scaled images of the steady-state saturation fields for the pumping/infiltration capacity simulations are given in Appendix A, for the five design options. Each figure in Appendix A depicts the saturation field for the maximum pumping/infiltration rate simulated. The lightest shade on these figures indicates fully saturated conditions. The initial saturation field would appear as the vertical profile shown along the right-hand side of the images, with the static water level at 26 ft BGS. The recirculation pattern of the in-well vapor-stripping system comprises a saturated zone above the static water table level, which is bell shaped in homogeneous soils. Because of the heterogeneities in hydrologic properties between soil strata, the saturated region above the static water table appears as a distorted bell. The steady-state condition represents a more saturated state than the initial hydrologic condition. The additional water used to saturate the bell-shaped regions is pulled in from outside the domain during the startup transient and would be released during a shutdown of the recirculation system. The width of the bell-shaped saturated zone is a function of the pumping/infiltration rate and the

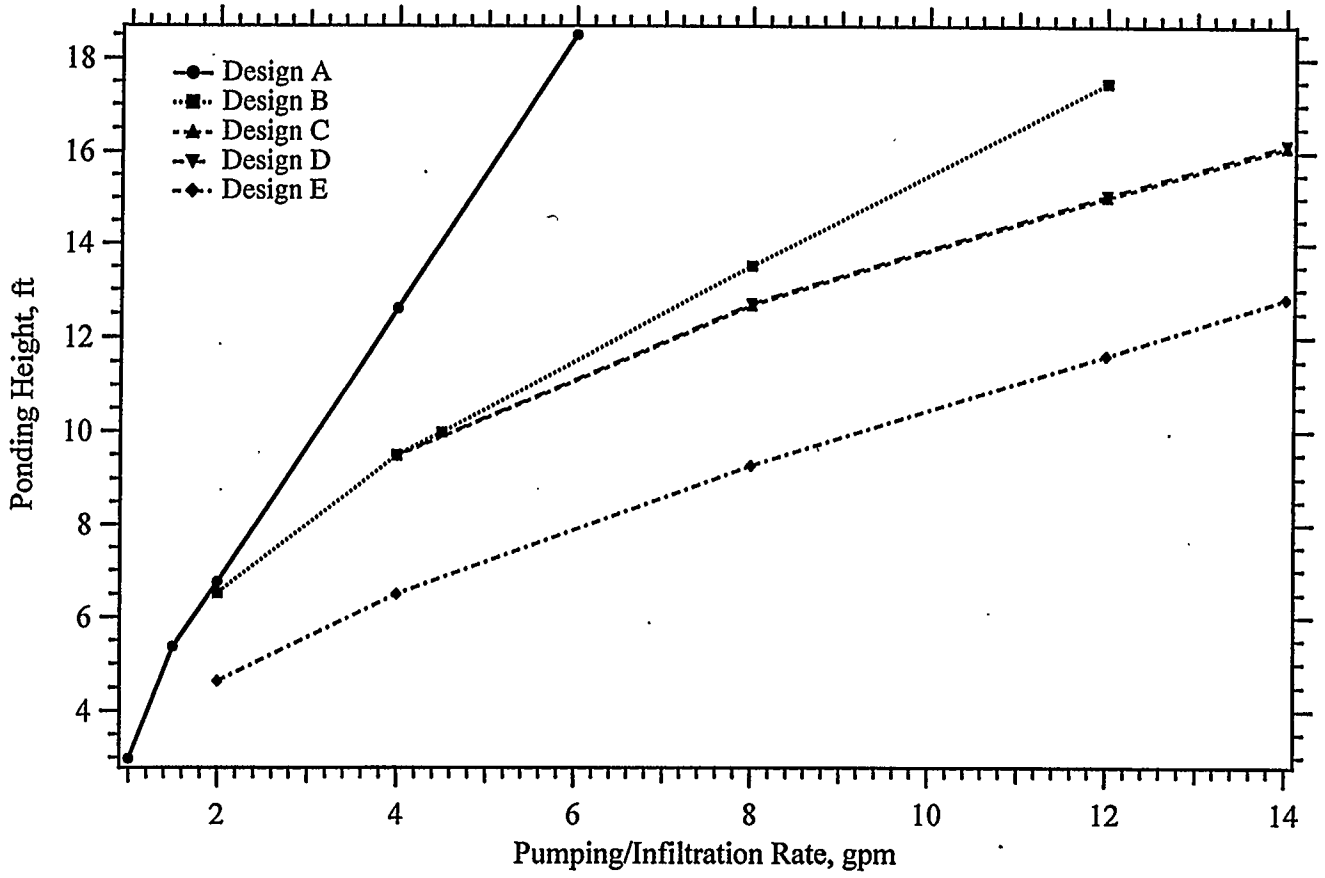

Figure 6.2. Ponding Height Versus Pumping/Infiltration Rate for the Vapor-Stripping Well Design Options

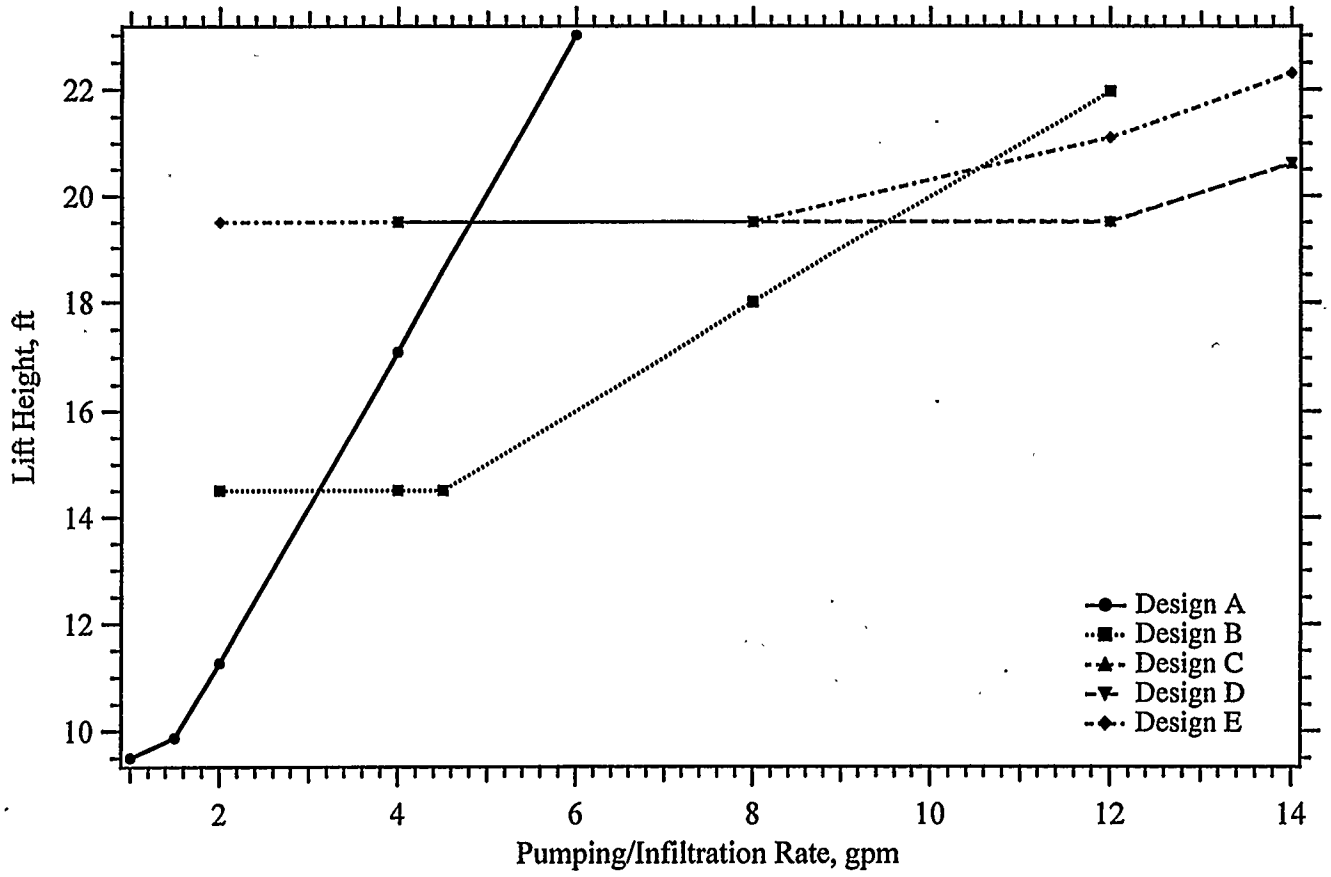

Figure 6.3. Lift Height Versus Pumping/Infiltration Rate for the Vapor-Stripping Well Design Options

height of the upper screened interval above the static water table. Increasing either the pumping rate or upper screened interval height will increase both the water table and the zone of influence. Saturation profiles provide a visual indication of the system performance within the vadose zone, but provide no information about the zone of influence within the saturated zone.

Zone of influence has no formal definition but loosely refers to the region within which in-well vapor-stripping could potentially remove the dissolved VOCs. For design purposes, the zone of influence was determined from steady-state simulations of the in-well vapor-stripping system that included dissolved trichlorethylene (TCE) in the aqueous phase. These simulations were initialized with a uniform distribution of dissolved TCE in vadose and saturated zone pore water. The in-well vapor-stripping system was assumed to have complete stripping effectiveness such that the reinjected water was void of TCE. Concentrations of dissolved TCE on the outer perimeter of the simulation were maintained at the initial concentration. These types of simulations provide a quantitative measure of the zone of influence; therefore, they are beneficial in making comparisons between designs and operational parameters. Banded gray-scale images of the steady-state fields of dissolved TCE concentrations for the pumping/infiltration capacity simulations are shown for the five designs options in Appendix B. An additional simulation was executed on Design D using a pumping/infilitration rate of 2.5 gpm, shown in Figure B.6. The solid dark gray regions in these images indicate the zone of influence, negligible concentrations of dissolved TCE. In all simulations, the low-permeability layer SM-ML1 diverted the mounded water from the upper screened interval yielding a larger zone of influence with the saturated zone than within the vadose zone. These simulations further indicate that the zone of influence is most sensitive to the pumping/infiltration flow rate, as evidenced by comparing Figures B.4 and B.6. At a flow rate of 14 gpm, as shown in Figure B.4, the zone of influence extends radially within the saturated region to nearly 40 ft. At a flow rate of 2.5 gpm for the same well design, as shown in Figure B.6, the zone of influence is reduced to a radial extent of 25 ft. Design D was chosen for the field demonstration at the Edwards AFB site.

7.0 Field Test Calibration

Soil properties for the conceptual model were developed from ex situ laboratory measurements and empirical correlations. These properties were used during the design process for the field demonstration at Edwards AFB. In situ results from the field test, however, allow some calibration of the CMS properties. Calibration of the conceptual model parameters with field test results were limited to those field tests occurring after redevelopment of the infiltration capacity. Two different field tests were used to calibrate the conceptual model parameters to field measurements from the infiltration field tests and operational field test #12. The infiltration test used an external water source to measure infiltration capacity under steady-flow conditions. Operational field test #12 involved operating the in-well vapor-stripping system under nearly steady pumping/infiltration rates during the period from December 13 to January 9, 1996.

7.1 Infiltration Field Tests

Two infiltration field tests were performed following the redevelopment process at the Edwards AFB demonstration site. Specific information on the justification and approach taken for the redevelopment of the demonstration site is reported by Gilmore et al. [1996]. The first infiltration field test was conducted in January 1996 prior to the operational field test #12 and the second in April following operational field test #13. These field experiments were designed to measure infiltration rates from the vapor-stripping well under saturated conditions in the vadose zone. Both infiltration tests were conducted following an extended period of continuous operation of the in-well vapor-stripping system to ensure saturated conditions above the water table. During these tests, the air-lift pumping system was inactive and water from an external source was pumped into the upper screened interval of the vapor-stripping well. After steady-flow conditions had been achieved the ponding height and volumetric flow rate were measured, where the ponding height refers to the depth of water in the vapor-stripping well from the base of the upper screened interval. Results from the January test were a flow rate of 2.5 gpm at 16 ft of ponding height and from the April test, a flow rate of 10 gpm at 18 ft. The increase in infiltration rate from January to April was due, in part, to the ongoing redevelopment activities.

Because infiltration rates under steady-flow conditions from the upper screened interval are primarily dependent on the saturated hydraulic conductivity of the strata above the water table, these infiltration tests were used as a calibration mark for the saturated hydraulic conductivities of the CMS types designated SP1, SP2, and SM-ML1, see Figure 5.1. Numerical simulations were executed with the STOMP simulator of these infiltration experiments. In each simulation, a constant volumetric flow rate was imposed on the upper screened interval of the vapor-stripping well. Simulations were then executed until steady-flow conditions were obtained, and the resulting ponding height was recorded. Different ponding heights were achieved by modifying the saturated hydraulic conductivities of the vadose zone strata of the conceptual

model. The resulting relation between the normalized hydraulic conductivity and ponding height are shown in Figures 7.1 and 7.2 for the January and April infiltration field tests, respectively. Normalized hydraulic conductivities are based on the saturated conductivities for the CMSs reported in Table 5.7. The January infiltration field test results were matched by multiplying the saturated hydraulic conductivities of the vadose zone strata (i.e., CMS types SP1, SP2, and SM-ML1) by a factor of 0.189. The April field test results were duplicated using both isotropic and anisotropic soil properties. For the anisotropic soils, the horizontal conductivities were a factor of 1.5 higher than their vertical counterparts. With the isotropic soils, a normalized hydraulic conductivity of 0.560 yielded a ponding height of 18 ft at a steady flow rate of 10 gpm. With the anisotropic soils, a normalized hydraulic conductivity of 0.591 horizontal and 0.394 vertical yielded the field data ponding height and flow rate. These field experiments only provide an integrated measure of the response of the terrestrial system to a certain imposed infiltration rate. No specific information can be extracted that pertains to a particular soil layer or type; therefore, this calibration mark only provides a gross correction to the saturated hydraulic conductivity of the CMSs.

7.2 Operational Field Test #12

The infiltration field tests were used as calibration marks for the saturated hydraulic conductivity of the CMSs above the ambient water table (i.e., SP1, SP2, and SM-ML1). Operational field test #12 was used to calibrate the saturated hydraulic conductivity of the CMSs below the ambient water table (i.e., SM-SP1, SP3, SW-1). Operational field test #12 involved steady operation of the in-well vapor-stripping system over a six-day period (from 14:19 January 3, 1996 to 09:19 January 8, 1996) following the redevelopment activities. Ponding heights during the test generally ranged between 15.025 and 19.025 ft, with an average height of 16.509 ft and a standard deviation of 0.402 ft. Actual pumping rate data were unavailable from the field test; therefore, pumping/infiltration flow rates were estimated from steady-state flow simulations with the STOMP simulator using saturated hydraulic conductivity values for the vadose zone soils that were calibrated with the January infiltration field test data. The resulting relation between ponding height and pumping/infiltration flow rate is shown in Figure 7.3.

Field data from operational field test #12 included hydraulic pressure measurements to determine ponding height at the upper screened interval, differential hydraulic pressure measurements for the deep monitoring wells (i.e., M3D, M4D, and M5D), and water table level measurements for the tape piezometers (i.e., P1, P2, and P3). Monitoring wells M3, M4, and M5 are located crossgradient from the central vapor-stripping well at distances of 10, 30, and 50 ft, respectively. The tape piezometers (P1, P2, and P3), for measuring the water table mound, were located radially at distances of 5, 10, and 5 ft, respectively. Data from the tape piezometers were taken manually and recorded approximately on daily intervals. The ponding height data were converted to simulation input data for the upper and lower screened intervals through a

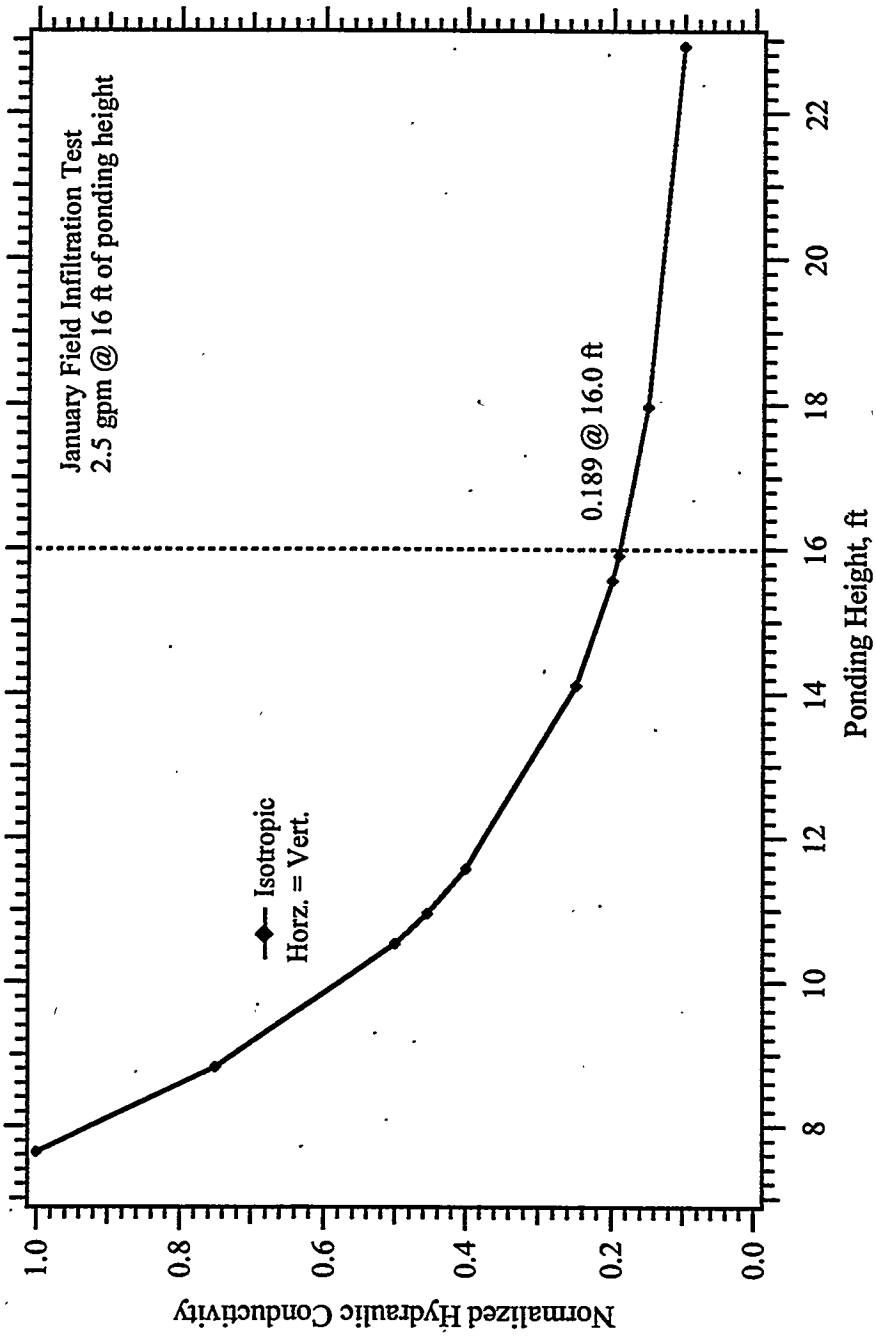

Figure 7.1. Normalized Hydraulic Conductivity Versus Ponding Height for the January Infiltration Test

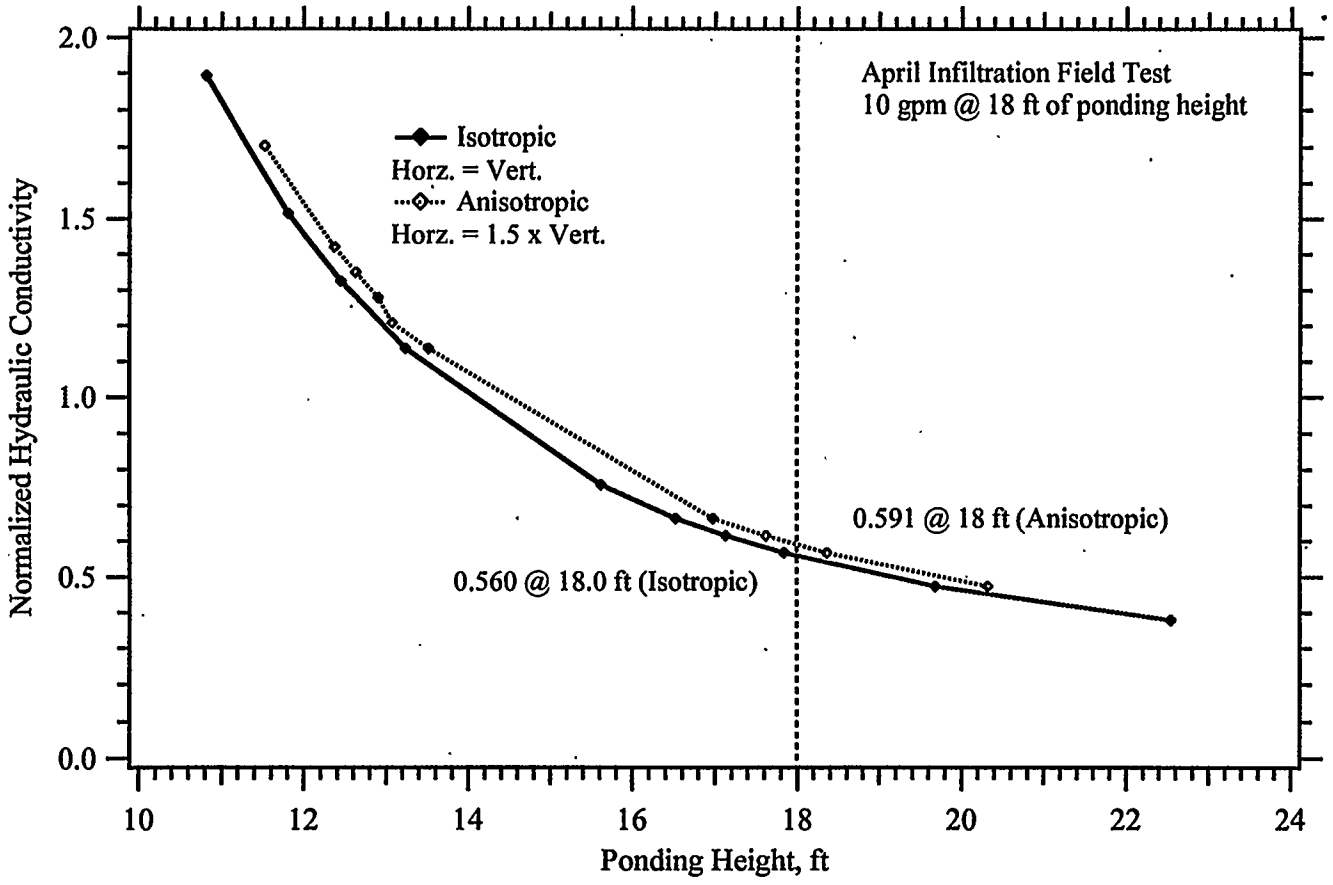

Figure 7.2. Normalized Hydraulic Conductivity Versus Ponding Height for the April Infiltration Test

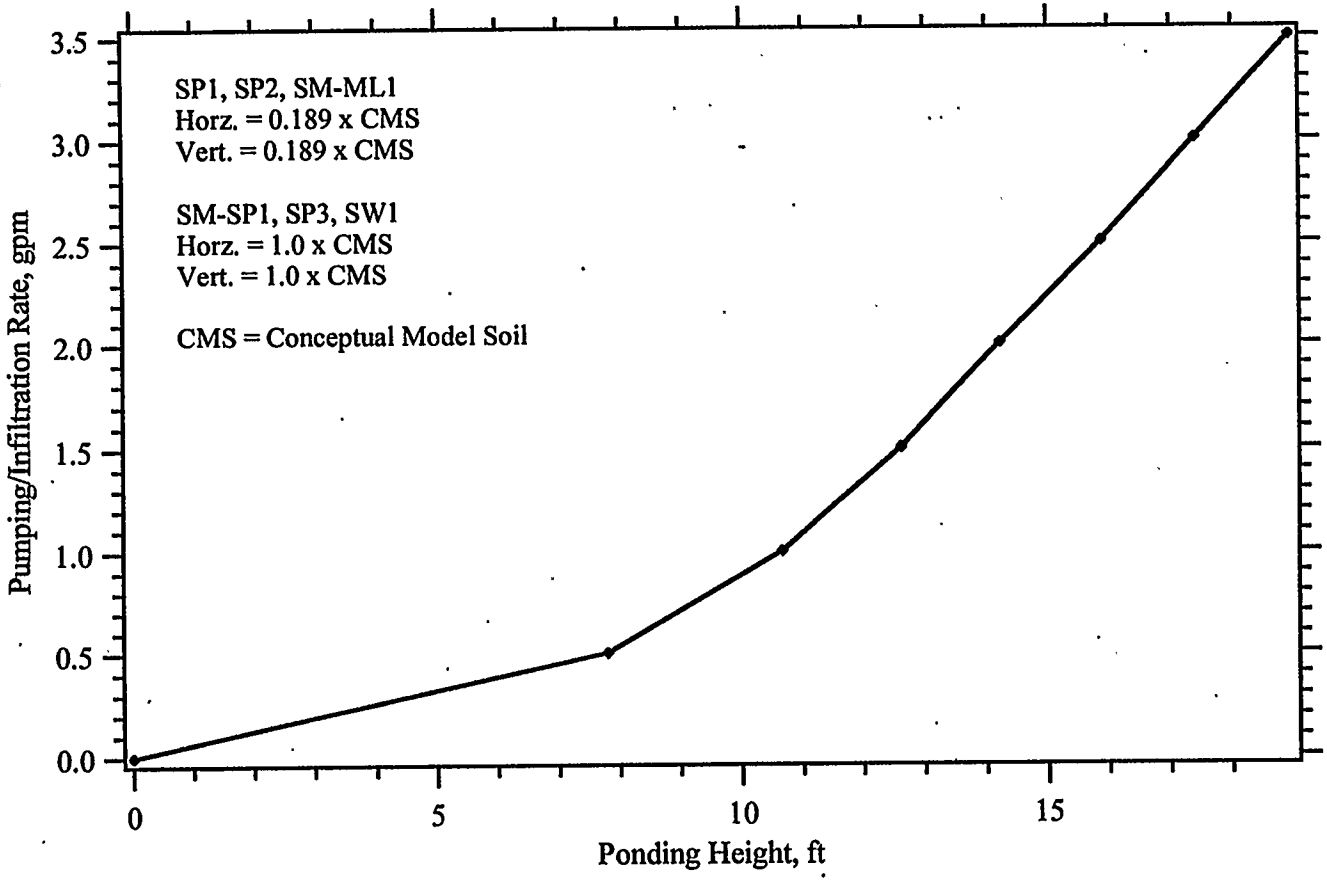

Figure 7.3. Pumping/Infiltration Rate Versus Ponding Height (Operational Field Test #12)

two-step process. The ponding height and deep monitoring well measurements were recorded every 10 minutes (1150 points) during the test period. These ponding height data were first reduced to 183 evenly spaced time points using cubic spline interpolation with natural end points. Pumping/infiltration rates were then computed by linear interpolation using the relation shown in Figure 7.3. The reduced data for ponding height and pumping/infiltration flow rates are shown in Figure 7.4.

Field data for ponding height and for differential hydraulic pressure from the three deep monitoring wells are shown for the test period in Figures 7.5 and 7.6, where each figure depicts a 3-day time sequence. The pressure plots shown in Figures 7.5 and 7.6 were referenced to a value of zero at 23:58 January 1, 1996, prior to system startup at 14:19 January 3, 1996. The system was briefly started at 12:37 January 3, 1996, however, this portion of the operational test was not simulated. Large spikes in the pressure measurements during steady operation of the in-well vapor-stripping system generally indicate a failure of the data acquisition system. Data collected after some failures often required offset corrections to be recalibrated. A total failure of the data acquisition system to record data for the three monitoring wells occurred shortly after 14:00 January 7, 1996. During the core of the field test period (i.e., from 15:08 January 3, 1996 to 12:18 January 17, 1996) the ponding height had an average value of 16.45 ft and monitoring wells M3D, M4D, and M5D had average drawdowns of 0.33, 0.21, and 0.19 ft, respectively.

Field data for the water table mound were taken manually and recorded daily as shown in Figure 7.7. These groundwater level measurements indicate that the water table mound was asymmetrical. The two piezometers located at a radial distance of 5 ft, P1 and P3, displayed markedly different responses (see Figure 7.7). Piezometer P1 indicated an increase of over 2 ft, whereas piezometer P3 only indicated a mounding of 0.5 ft, followed with a decrease in mounding. Piezometer P2, located at a radial distance of 10 ft, showed an initial depression followed with a slight mounding of 0.18 ft. These field data for differential hydraulic head and water table mound were used to calibrate the saturated hydraulic conductivities of CMSs in the saturated zone.

A matrix of simulations was executed using the pumping/infiltration rates shown in Figure 7.4 as the driving function for the in-well vapor-stripping system. The simulations differed in saturated hydraulic conductivity and flow rate as shown in Table 7.1. Modifications to the horizontal and vertical components were considered. The simulation yielding the closest agreement in ponding height, differential hydraulic pressure at the monitoring wells, and water table mounding was used to define the saturated hydraulic properties of the CMSs below the ambient water table. Simulation results for ponding height, differential hydraulic pressure in the monitoring wells, and water table mounding at the piezometers is shown in Appendix C for simulations numbered 1 through 17.

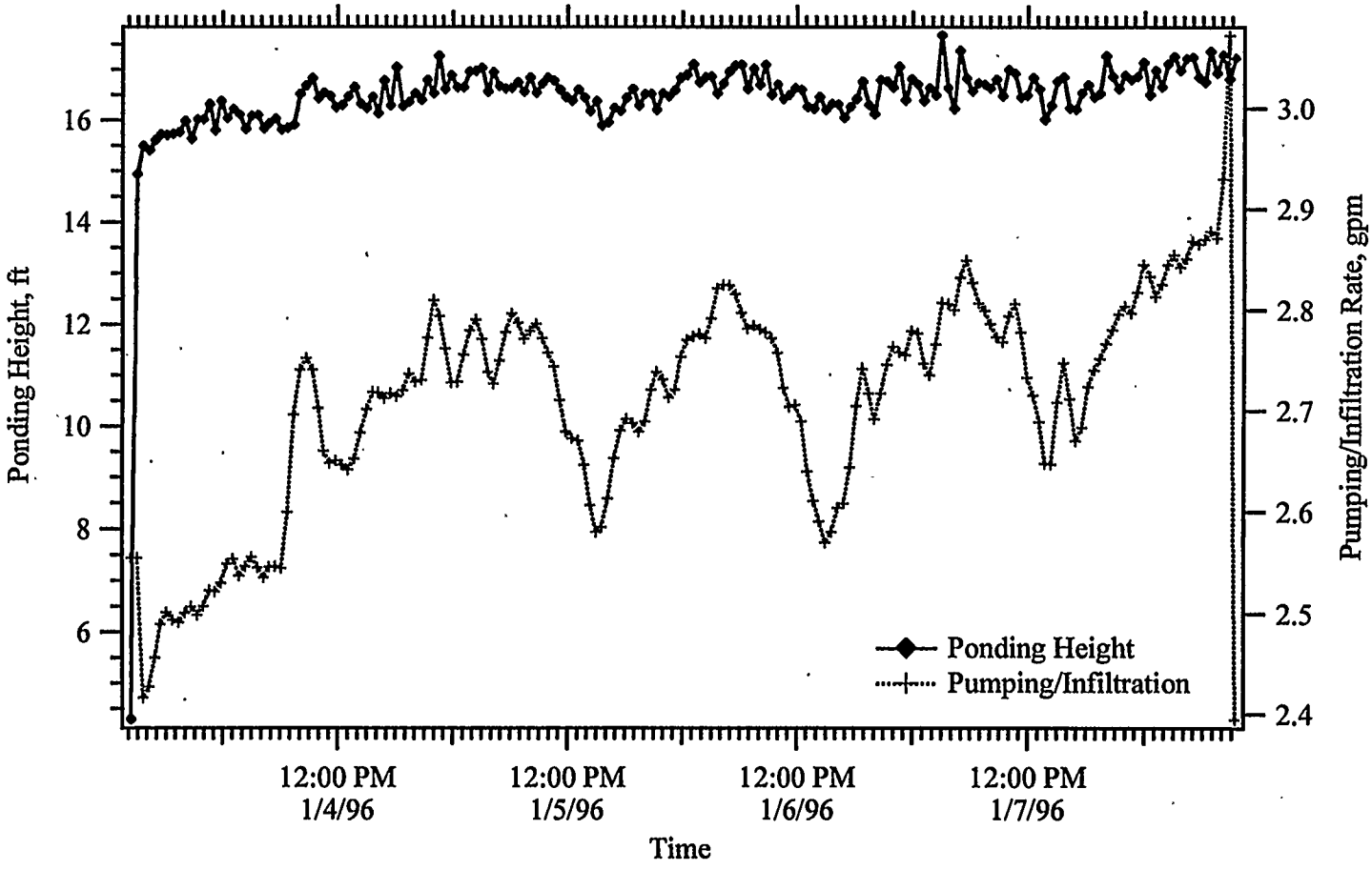

Figure 7.4. Ponding Height Versus Time (Field Test #12)

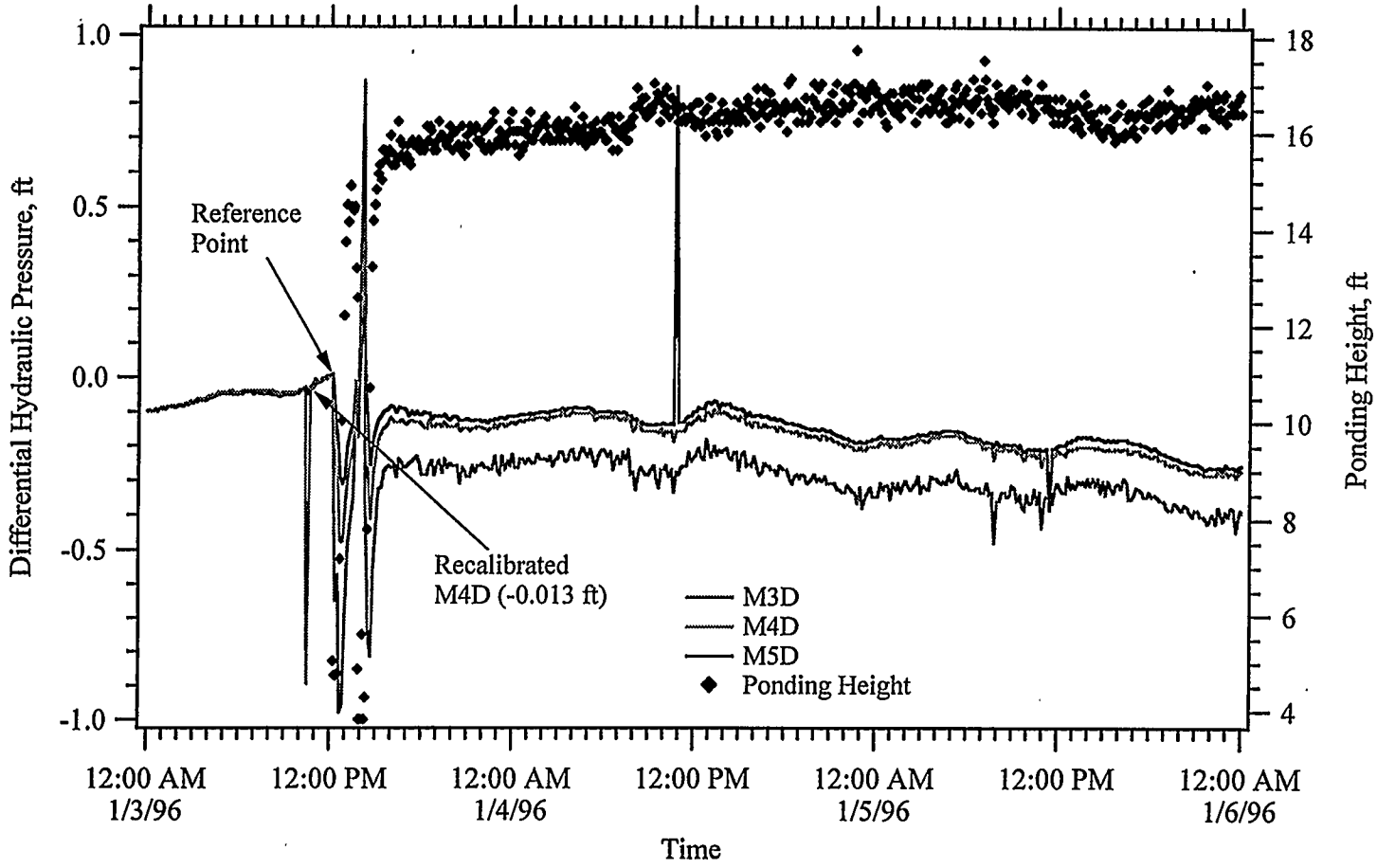

Figure 7.5a. Differential Hydraulic Pressure Versus Time, Field Data (Field Test #12, 1/3/96-1/6/96)

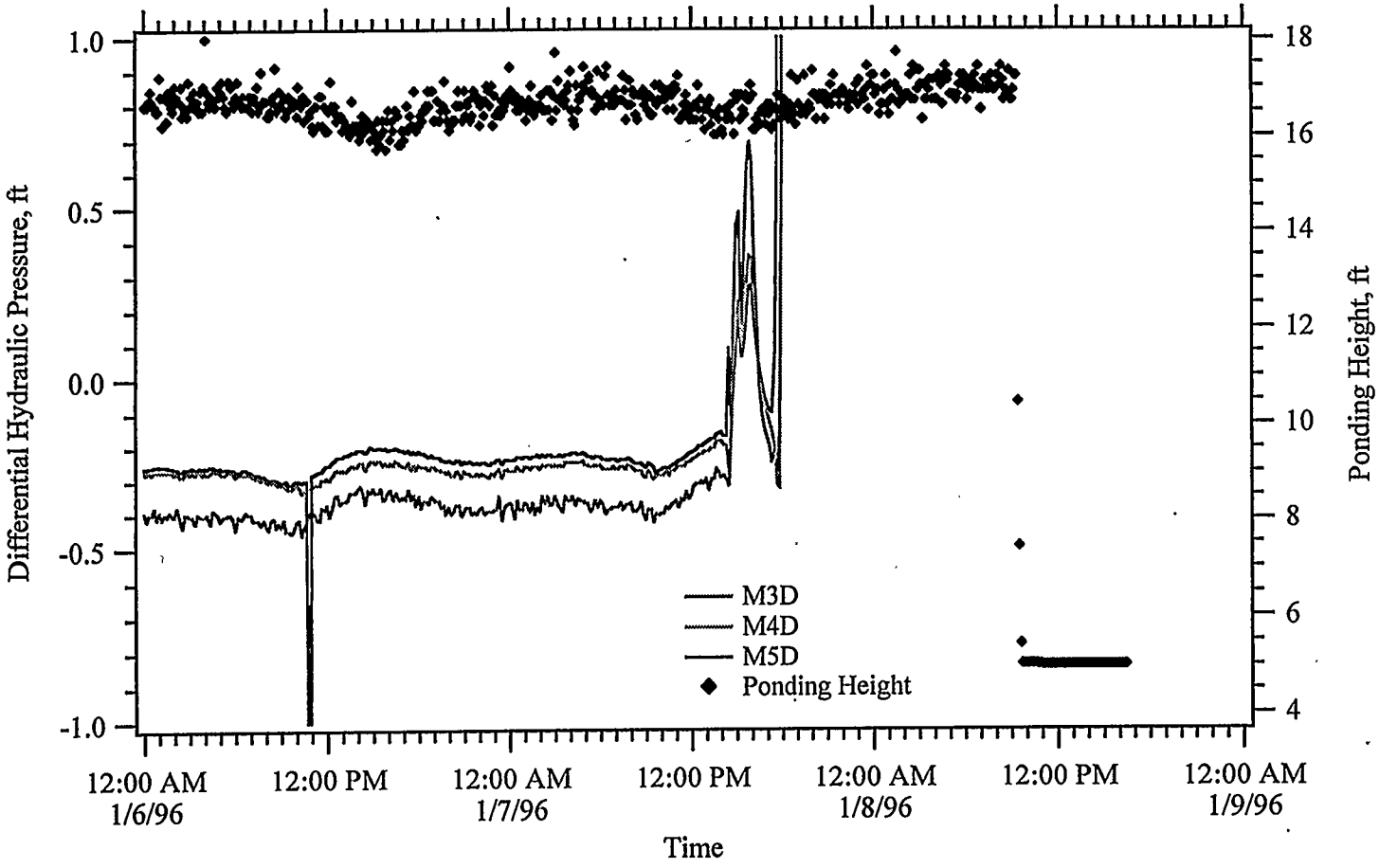

Figure 7.5b. Differential Hydraulic Pressure Versus Time, Field Data (Field Test #12, 1/6/96-1/9/96)

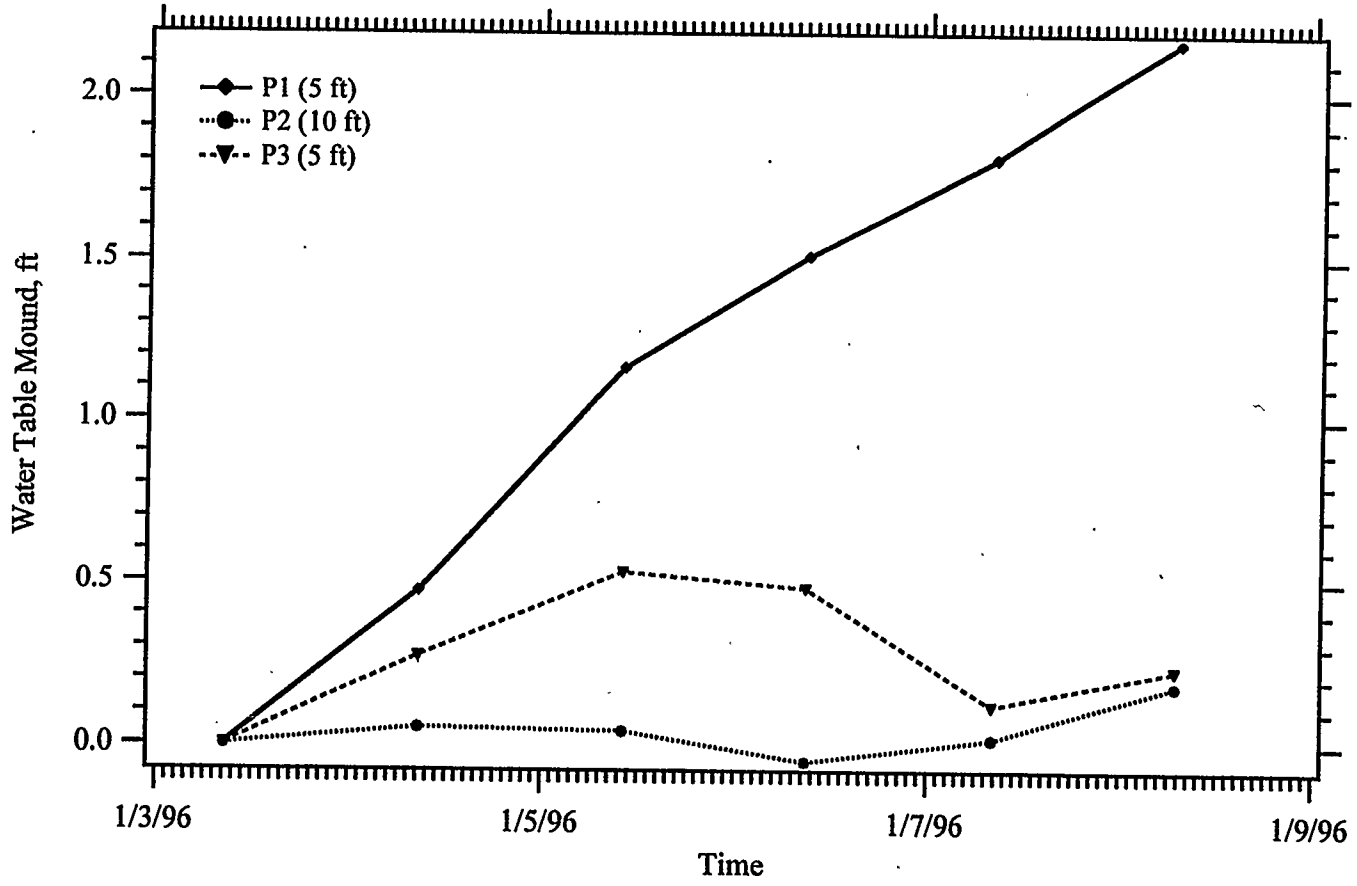

Figure 7.6. Water Table Mound Versus Time, Field Data (Field Test #12, 1/3/96-1/9/96)

Table 7.1 Matrix of Simulations for Operational Field Test #12

Simulation Number	Flow Rate Fraction	SP1, SP2, SM-ML1 Horizontal Conductivity	SP1, SP2, SM-ML1 Vertical Conductivity	SM-SP1, SP3, SW1 Horizontal Conductivity	SM-SP1, SP3, SW1 Vertical Conductivity
1	1.0	0.189 x CMS	0.189 x CMS	0.189 x CMS	0.189 x CMS
2	1.0	1.89 x CMS	1.89 x CMS	1.89 x CMS	1.89 x CMS
3	1.0	1.89 x CMS	0.189 x CMS	0.189 x CMS	0.189 x CMS
4	1.0	0.189 x CMS	1.89 x CMS	0.189 x CMS	0.189 x CMS
5	1.0	1.89 x CMS	1.89 x CMS	0.189 x CMS	0.189 x CMS
6	1.0	0.189 x CMS	0.189 x CMS	1.89 x CMS	0.189 x CMS
7	1.0	0.189 x CMS	0.189 x CMS	0.189 x CMS	1.89 x CMS
8	1.0	0.189 x CMS	0.189 x CMS	1.89 x CMS	1.89 x CMS
9	0.5	0.189 x CMS	0.189 x CMS	0.189 x CMS	0.189 x CMS
10	0.1	0.189 x CMS	0.189 x CMS	0.189 x CMS	0.189 x CMS
11	0.5	0.0945 x CMS	0.0954 x CMS	0.0945 x CMS	0.0945 x CMS
12	0.1	0.0189 x CMS	0.0189 x CMS	0.0189 x CMS	0.0189 x CMS
13	0.5	0.0945 x CMS	0.0954 x CMS	0.945 x CMS	0.945 x CMS
14	0.1	0.0189 x CMS	0.0189 x CMS	0.189 x CMS	0.189 x CMS
15	1.0	0.189 x CMS	0.189 x CMS	2.84 x CMS	0.378 x CMS
16	1.0	0.189 x CMS	0.189 x CMS	1.89 x CMS	0.945 x CMS
17	1.0	0.189 x CMS	0.189 x CMS	2.84 x CMS	1.89 x CMS

CMS = Conceptual model soil

Simulation #1 used hydraulic conductivities for the CMSs (CMSs) that were calibrated from the January infiltration field test (a correction factor of 0.189). Responses of the monitoring wells, see Figure C.1, were nearly an order of magnitude greater than measured during the field test. This result suggested that the hydraulic conductivities of the soils strata beneath the water table were low. Simulation #2 used hydraulic conductivities that were 10 times greater than those for the calibrated CMSs. This simulation showed improved responses, see Figure C.2, in the monitoring wells; however, the ponding height within the vapor-stripping well was nearly three times lower than that measured during the field test. This result demonstrated that the ponding height was primarily dependent on the pumping/infiltration rate and hydraulic conductivities of the soil strata above the ambient water table; whereas, the pressure reductions in the deep monitoring wells were primarily dependent on the pumping/infiltration rate and hydraulic conductivities of the soil strata below the ambient water table.

Simulations #3 through #5 considered anisotropic and isotropic hydraulic conductivities for the soil strata in the vadose zone. In each simulation, either the vertical, horizontal, or both hydraulic conductivity components were 10 times greater than those for the calibrated CMSs,

whereas the other hydraulic conductivity components were at the calibrated CMS values. These simulations, see Figures C.3 through C.5, showed either lower-than-measured ponding heights or higher-than-measured water table mounding. In all simulations, the pressure responses of the deep monitoring wells were elevated above the measured values. These results suggest that increasing the horizontal component of hydraulic conductivity in the vadose zone strata lowers the ponding height by increasing the cross-sectional area for imbibition from the upper screened zone and that increasing the vertical component slightly lowers the ponding height but increases the water table mounding by reducing the cross-sectional area for imbibition.

Simulations #6 through #8 considered anisotropic and isotropic hydraulic conductivities for the soil strata in the saturated zone. In each simulation, either the vertical, horizontal, or both hydraulic conductivity components were 10 times greater than those for the calibrated CMSs, whereas the other hydraulic conductivity components were at the calibrated CMS values. An increase in only the horizontal or vertical components of the saturated zone conductivities, see Figures C.6 and C.7, was insufficient in lowering the pressure response of the deep monitoring wells. A combined increase in the saturated zone hydraulic conductivities, see Figure C.8, however, yielded reasonable agreement between the simulation results and field measurements for ponding height, water table mounding, and deep monitoring well pressures.

Simulations #9 through #14 considered alterations in both the pumping/infiltration rate and hydraulic conductivities. Reducing the flow rate to 0.5 or 0.1 times the values computed from the relation shown in Figure 7.1, in conjunction with the hydraulic conductivities at the calibrated CMS values, yielded decreases in the response of all critical parameters, see Figures C.9 and C.10. Although these simulations produced pressure responses in the deep monitoring wells closer in agreement with the field measurements, the reduced flow rates also lowered the simulated ponding heights away from the measured field values. Reducing the flow rate and hydraulic conductivities to 0.5 and 0.1 times the calibrated CMSs and corresponding pumping/infiltration rate values, yielded elevated pressure responses in the deep monitoring wells, see Figures C.11 and C.12. The ponding heights in these simulations generally showed reasonable agreement with the field measurements, thus confirming the nearly proportional relationship between pumping/infiltration flow rates and the vadose zone hydraulic conductivities for constant ponding heights. Simulations #13 and #14 were executed to investigate lowering the pumping/infiltration rate and hydraulic conductivities, in proportion to those of simulation #8, which had yielded close agreement with all the critical field measurements. Whereas, both simulations yielded responses in ponding heights and deep monitoring well pressures that agreed with the field measurements, neither simulation shows agreement in water table mounding with the field data, see Figures C.13 and C.14. These simulation results lend strong support to the pumping/infiltration rates shown in Figure 7.1.

Simulations #15 through #17 were modifications to simulation #8 with respect to the hydraulic conductivities for the saturated zone strata, see Figures C.15 through C.17. The closest

agreement between simulation results and field measurements in terms of ponding height, water table mounding, and deep monitoring well pressure was obtained in simulation #17, where the horizontal and vertical components of hydraulic conductivity for the saturated zone strata were 15 and 10 times the CMS values. This result suggests a 1.5 ratio in horizontal to vertical hydraulic conductivity, which is characteristic of depositional hydrologic systems. This series of simulations on operational field test #12, confirmed the hydrologic properties for the vadose zone strata, which had been determined from the simulations of the January infiltration test, and provided estimates of the hydrologic properties for the saturated zone strata. The simulations also support the pumping/infiltration rates reported in Figure 7.1.

8.0 Operational Field Test #13

The January infiltration field test and operational field test #12 were used primarily to calibrate the hydrologic properties of the soils at the Edwards AFB site and to establish a functional relation between ponding height and pumping/infiltration rate. Under normal field test conditions, the pumping/infiltration rate would have been an important field measurement. The loss of the downhole weir and problems with calibrating the orifice plates eliminated the possibility for recording accurate field measurements of pumping/infiltration rates. Therefore, ponding height measurements became the principal indicator of flow rate. Because of the redevelopment activities, which primarily involved injecting dissolved calcium carbonate into the vadose zone, the pumping/infiltration and ponding height functional relationship changed between the January and April infiltration field tests. The January infiltration field test indicated significantly lower permeabilities in the vadose zone strata than did the April test; an indication of the success of the redevelopment activities.

Operational field test #13 involved steady operation of the in-well vapor-stripping system over a 63-day period (from 10:17 January 16, 1996 to 06:27 March 19, 1996) following operational field test #12. Simulations of field test #13 were designed to demonstrate the capabilities of the STOMP simulator to predict system performance for the in-well vapor-stripping system in terms of hydrologic and contaminant concentration responses. Because the only field measurements of pumping/infiltration rates were derived from ponding heights and the redevelopment activities at the field site changed this relation over the test period, multiple simulations of operational field test #13 were executed. The objective for these simulations was to bound the performance of the in-well vapor-stripping system using hydrologic properties and pumping/infiltration rates from both the January and April infiltration field tests. Three simulations were executed of operational field test #13. The first simulation, referred to as the low-permeability isotropic hydrologic properties, used results from the January infiltration field test. The second and third simulations, referred to as the high-permeability isotropic and high-permeability anisotropic hydrologic properties, used results from the April infiltration field test. For the anisotropic simulations, the horizontal conductivities of the vadose zone strata were a factor of 1.5 higher than their vertical counterparts. In all simulations, the horizontal conductivities of the saturated zone strata were 1.5 times higher than the vertical components.

Field data from operational field test #13 included hydraulic pressure measurements to determine ponding height at the upper screened interval, differential hydraulic pressure measurements for the deep monitoring wells (i.e., M3D, M4D, and M5D), and water table level measurements for the tape piezometers (i.e., P1, P2, and P3). The ponding height and deep monitoring well measurements were recorded every 6 and 10 minutes (13316 and 9051), respectively, during the test period. Data from the tape piezometers were taken manually and recorded approximately once a day. Ponding height and deep monitoring well data from

operational field test #13 are shown in Figures 8.1 through 8.3, where the figures are sequential and each displays 21 days of data. These data show disruptions and significant daily fluctuations. The ponding height and deep monitoring well data were collected on different data acquisition systems. The ponding height data have numerous gaps, which may or may not correspond with system failures. The deep monitoring well data end at 13:30 February 28, 1996, prior to the end of the field test. Ponding height data from the field were converted to 1332 evenly spaced time points using cubic spline interpolation with natural end points as shown in Figure 8.4 for the entire test period. This reduced data set for ponding height was used to generated pumping/infiltration flow rate input data for the numerical simulations. Water table mounding data were collected manually from the field piezometers and are shown in Figure 8.5 for the entire test period. Consistent with the previous operational field test, these measurements indicate that the water table mound was asymmetrical. The two piezometers located at a radial distance of 5 ft, P1 and P3, displayed markedly different responses (see Figure 7.7). Piezometer P1 indicated an increase of over 4 ft, whereas piezometer P3 only indicated a mounding of 0.9 ft, followed with a decrease in mounding. Piezometer P2, located at a radial distance of 10 ft, showed an initial depression, followed with a slight mounding of 0.4 ft.

8.1 Low-Permeability Isotropic Simulation

The low-permeability isotropic (LPI) simulation of operational field test #13 used soil hydraulic conductivities, pumping/infiltration rates, and air-to-water volumetric flow ratios determined from the January infiltration field test and calibration with operational field test #12. The pumping/infiltration versus ponding height curve, shown in Figure 8.6, was developed by simulating the in-well vapor-stripping system to steady-flow conditions under a constant pumping/infiltration rate. This curve was then combined with the ponding height time history, shown in Figure 8.4, to generate the pumping/infiltration flow rate input shown in Figure 8.7. Volumetric air flow data collected from the field test were converted to 1332 evenly spaced time points using cubic spline interpolation with natural end points. These data were then combined with the pumping/infiltration flow rate data to generate air-to-water volumetric flow ratios, shown in Figure 8.8. Because of the sampling techniques used to reduce the number of field data points to 1332 evenly spaced time points, several anomalous values of the air-to-water volumetric flow ratio occurred in the data set around system shutdown times. These anomalous data were modified to match neighboring data points.

The pumping/infiltration rate data, shown in Figure 8.7, were converted into a time-varying Neumann boundary condition, applied to the lower screened interval, and a time-varying volumetric water source for the upper screened interval. The air-to-water volumetric flow ratio data, shown in Figure 8.8, were converted into linked solute source (see Section 4.2) for the upper screened interval. As with the boundary conditions, the linked solute source input varied with time. Initial conditions for the aqueous saturation field assumed hydrostatic conditions with the water table located at 26 ft BGS. Initial dissolved TCE molar concentrations

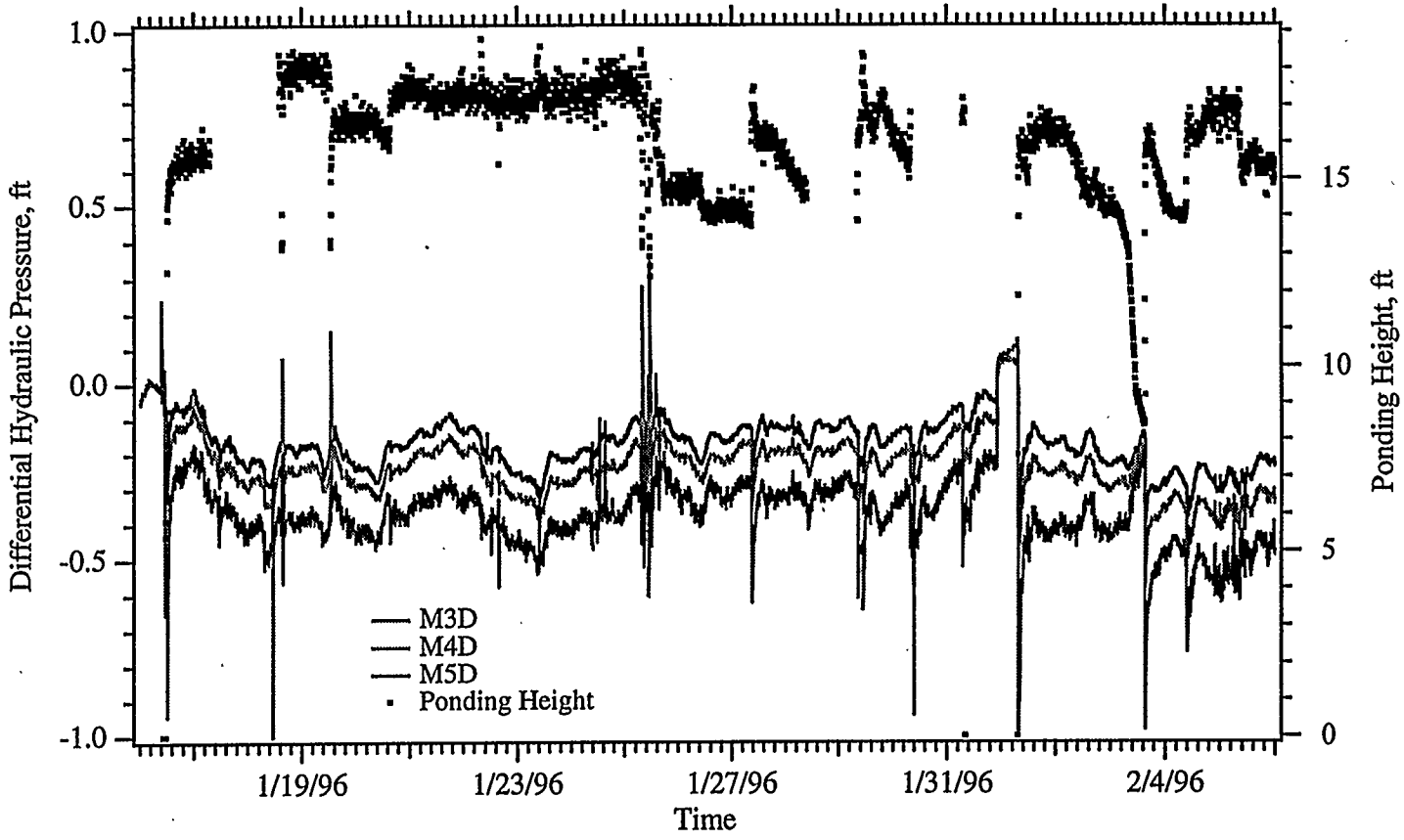

Figure 8.1a. Differential Hydraulic Pressure and Ponding Height Versus Time, Field Data (Field Test #13, 1/16/96-2/6/96)

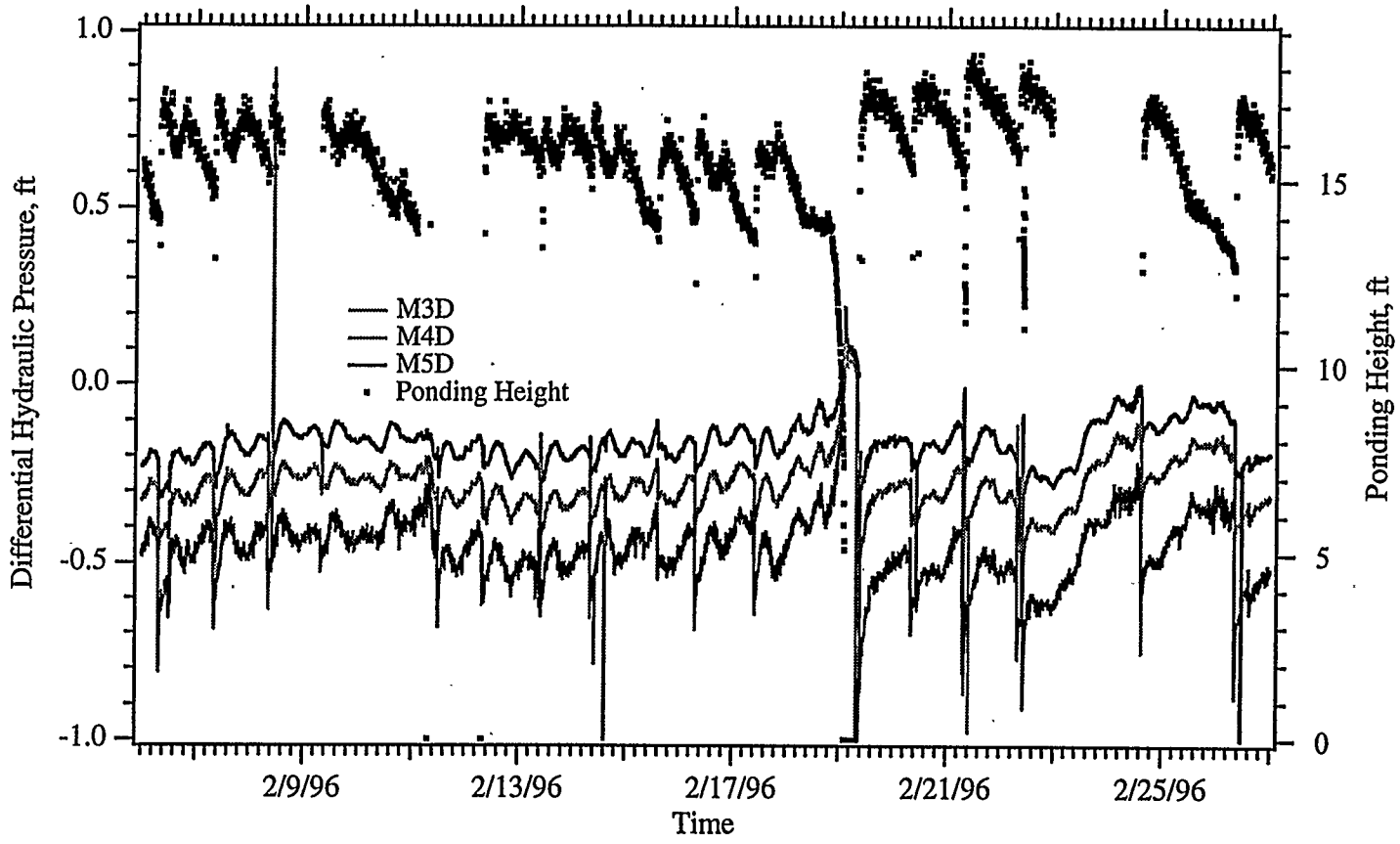

Figure 8.1b. Differential Hydraulic Pressure and Ponding Height Versus Time, Field Data (Field Test #13, 2/6/96-2/27/96)

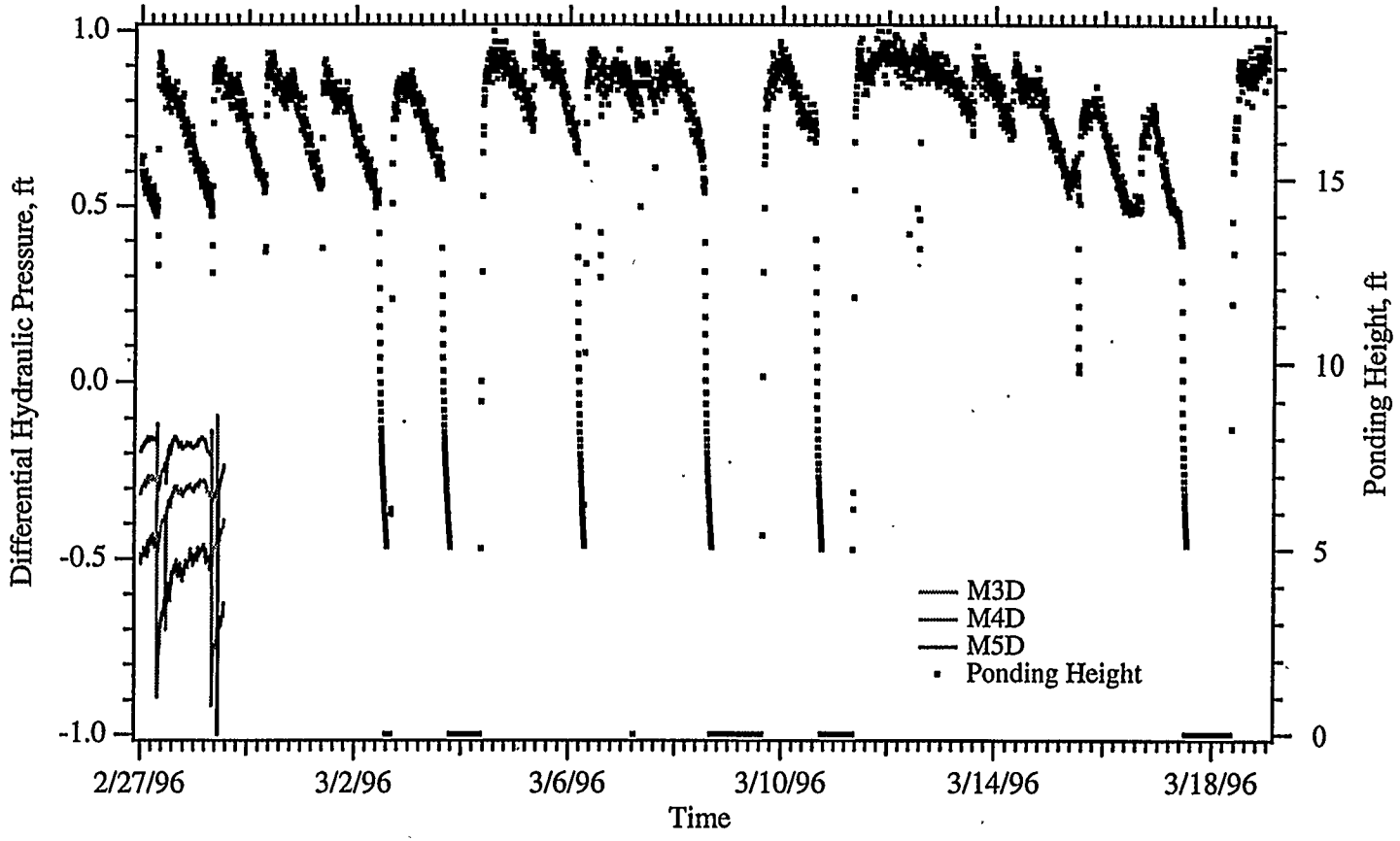

Figure 8.1c. Differential Hydraulic Pressure and Ponding Height Versus Time, Field Data (Field Test #13, 2/27/96-3/19/96)

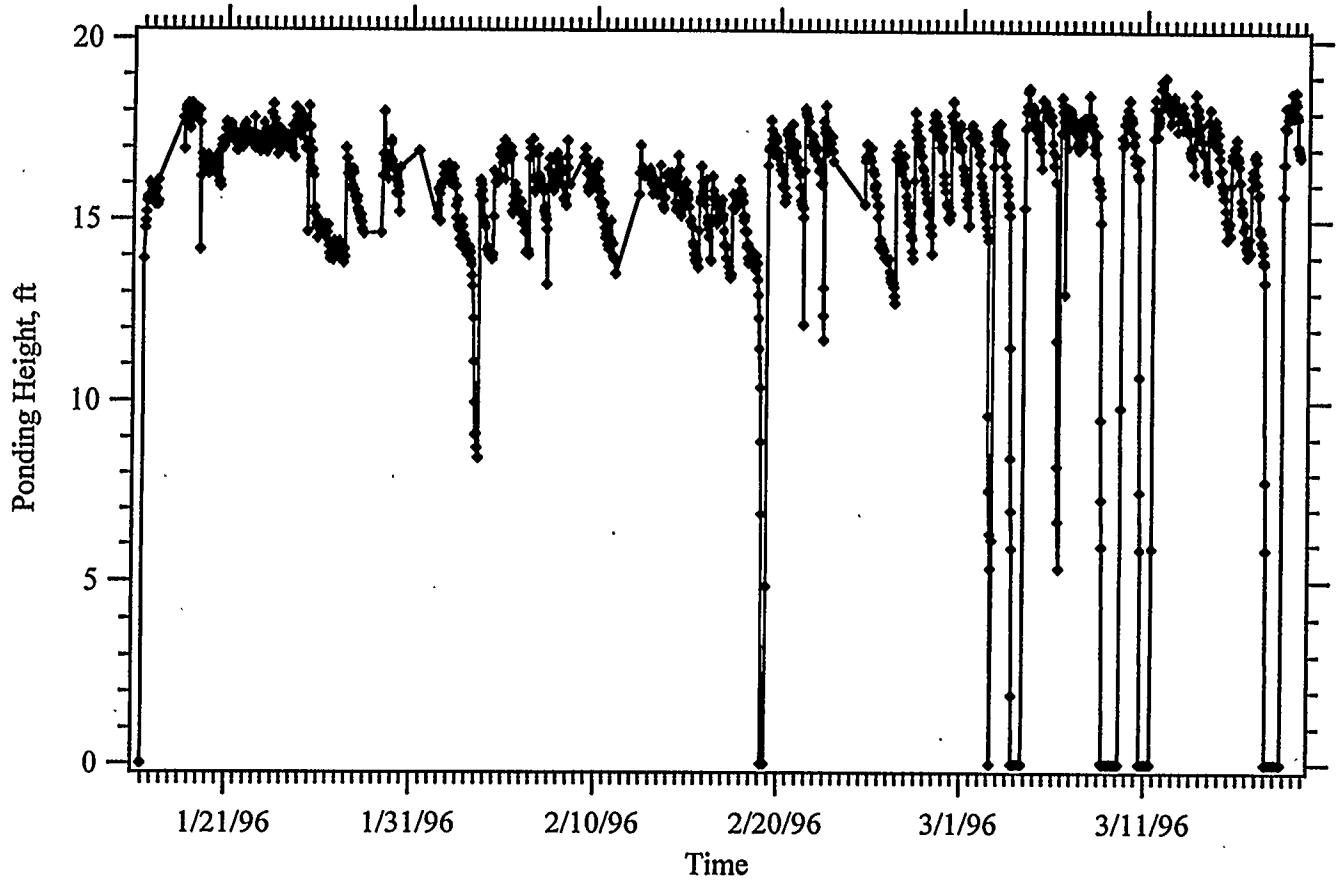

Figure 8.2. Ponding Height Versus Time, Reduced Field Data (Field Test #13, 1/16/96-3/19/96)

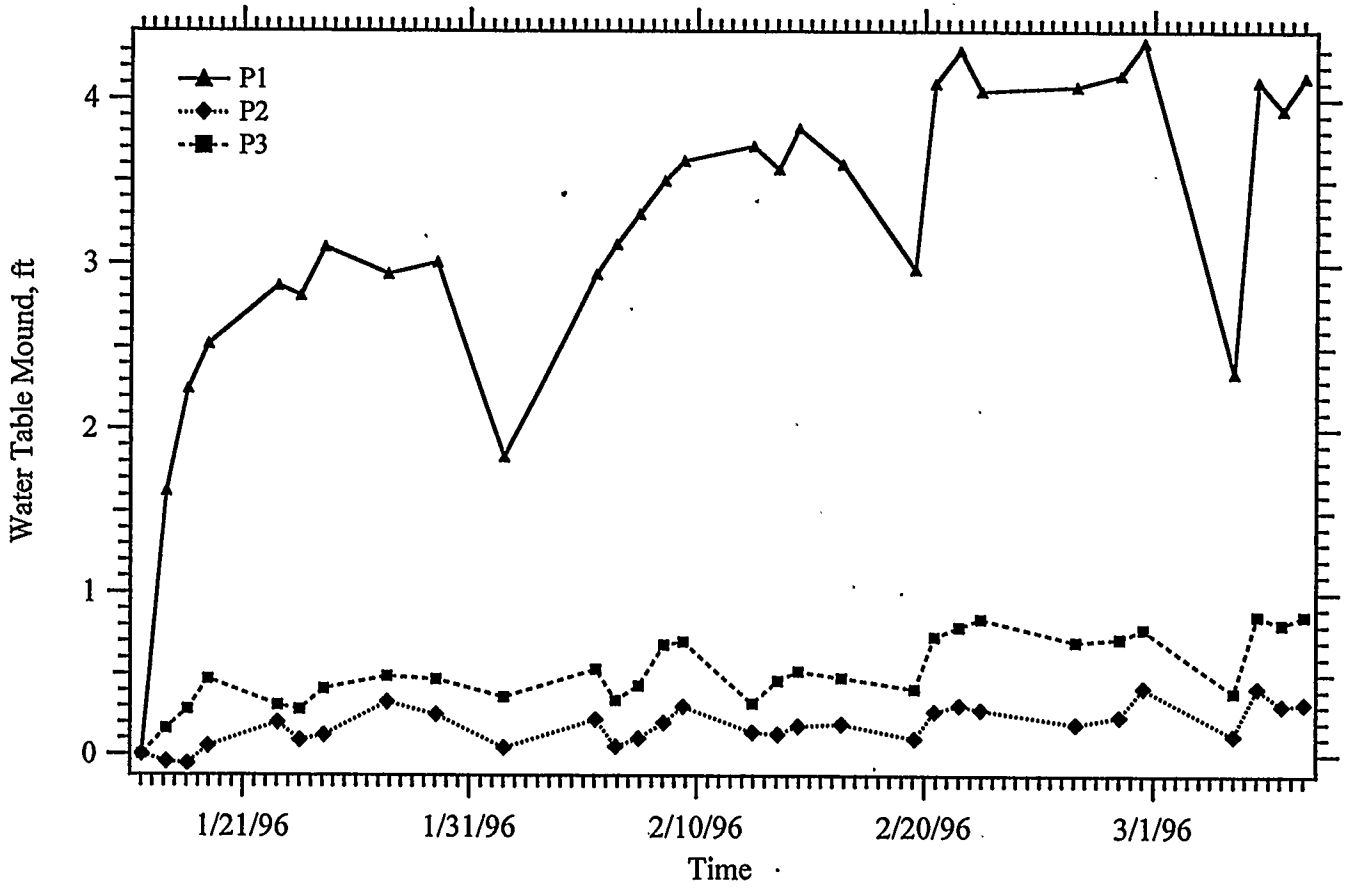

Figure 8.3. Water Table Mound Versus Time, Field Data (Field Test #13, 1/16/96-3/19/96)

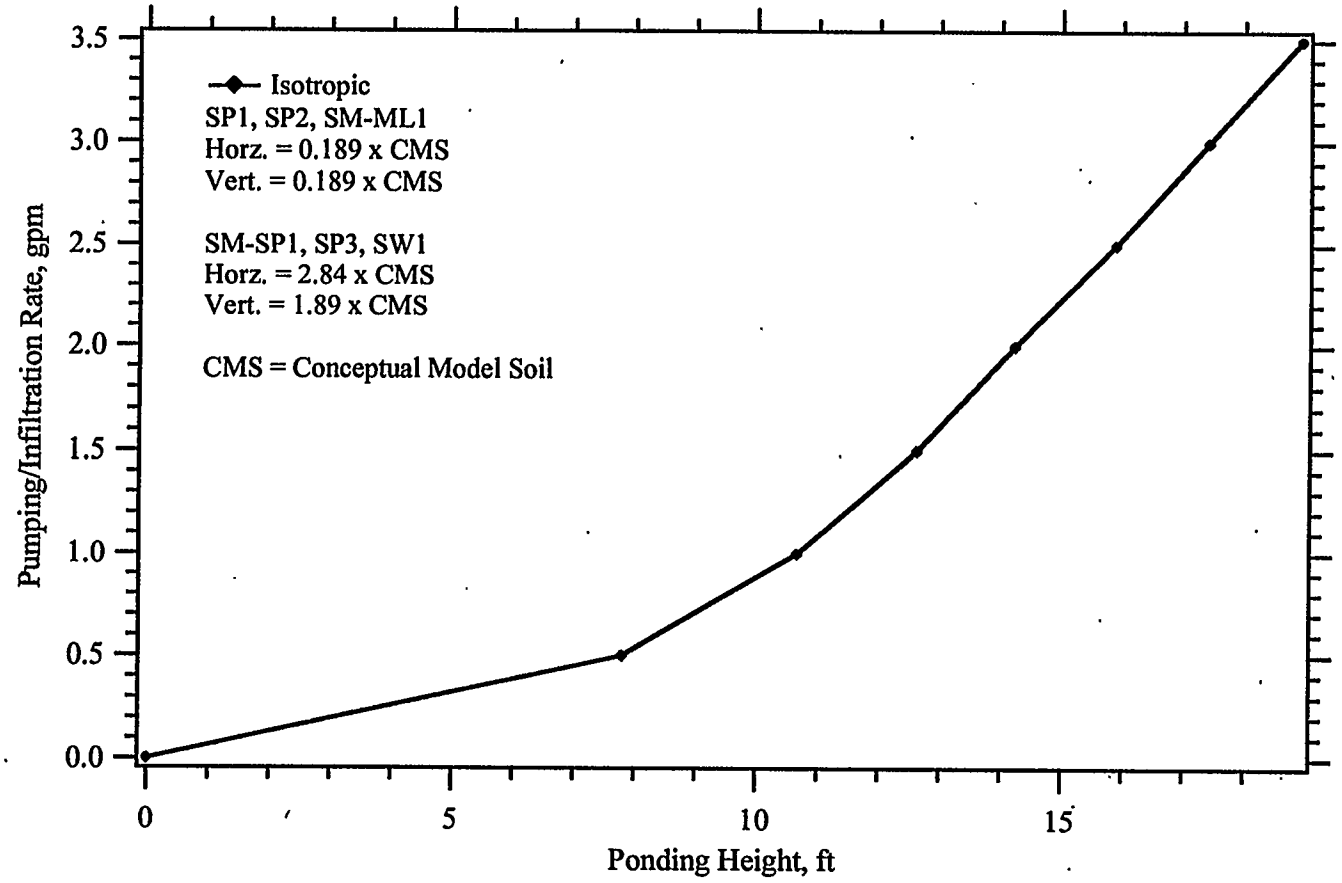

Figure 8.4. Pumping/Infiltration Rate Versus Ponding Height, LPI Simulation

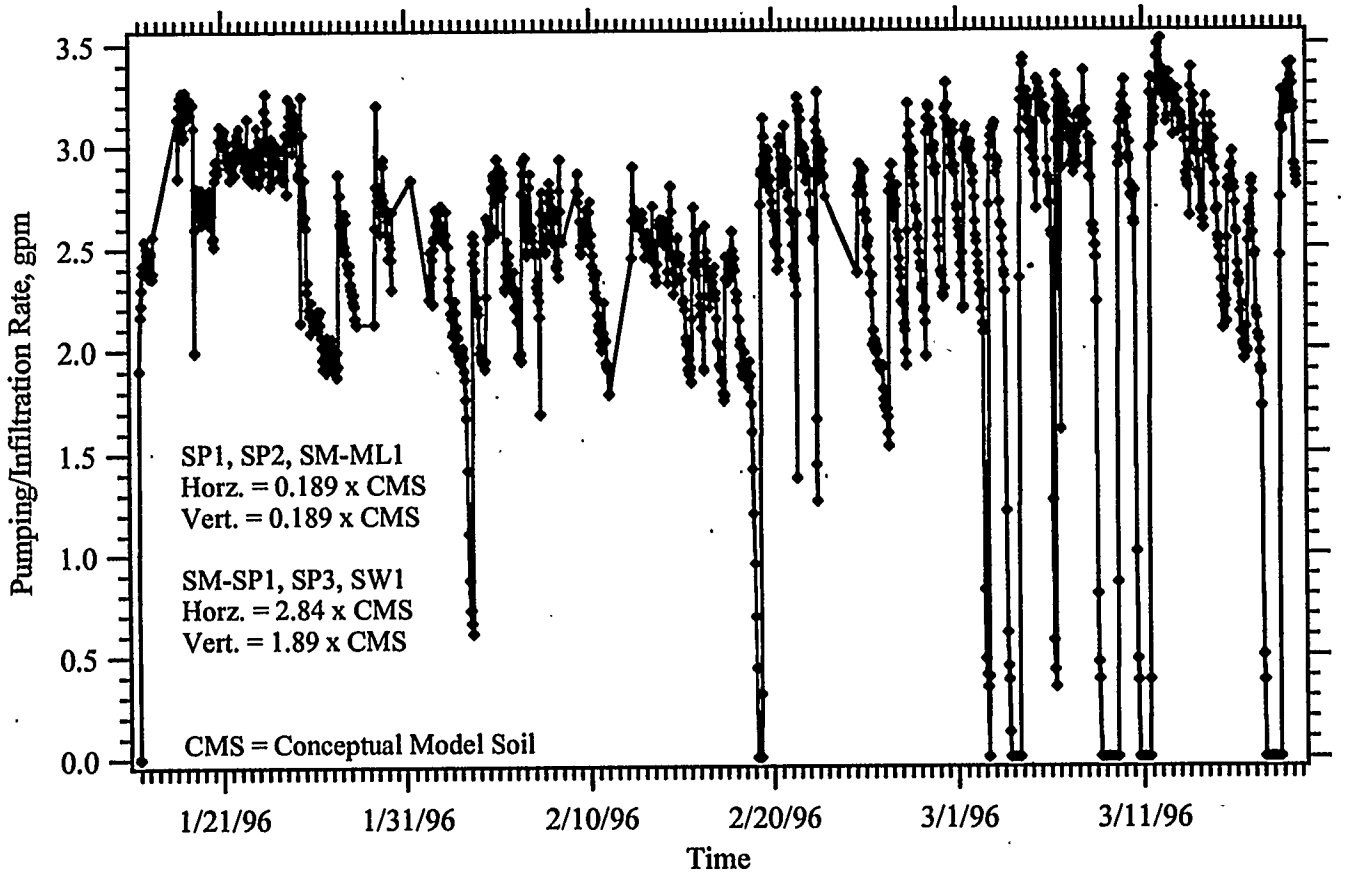

Figure 8.5. Pumping/Infiltration Rate Versus Time, LPI Simulation (Field Test #13, 1/16/96-3/19/96)

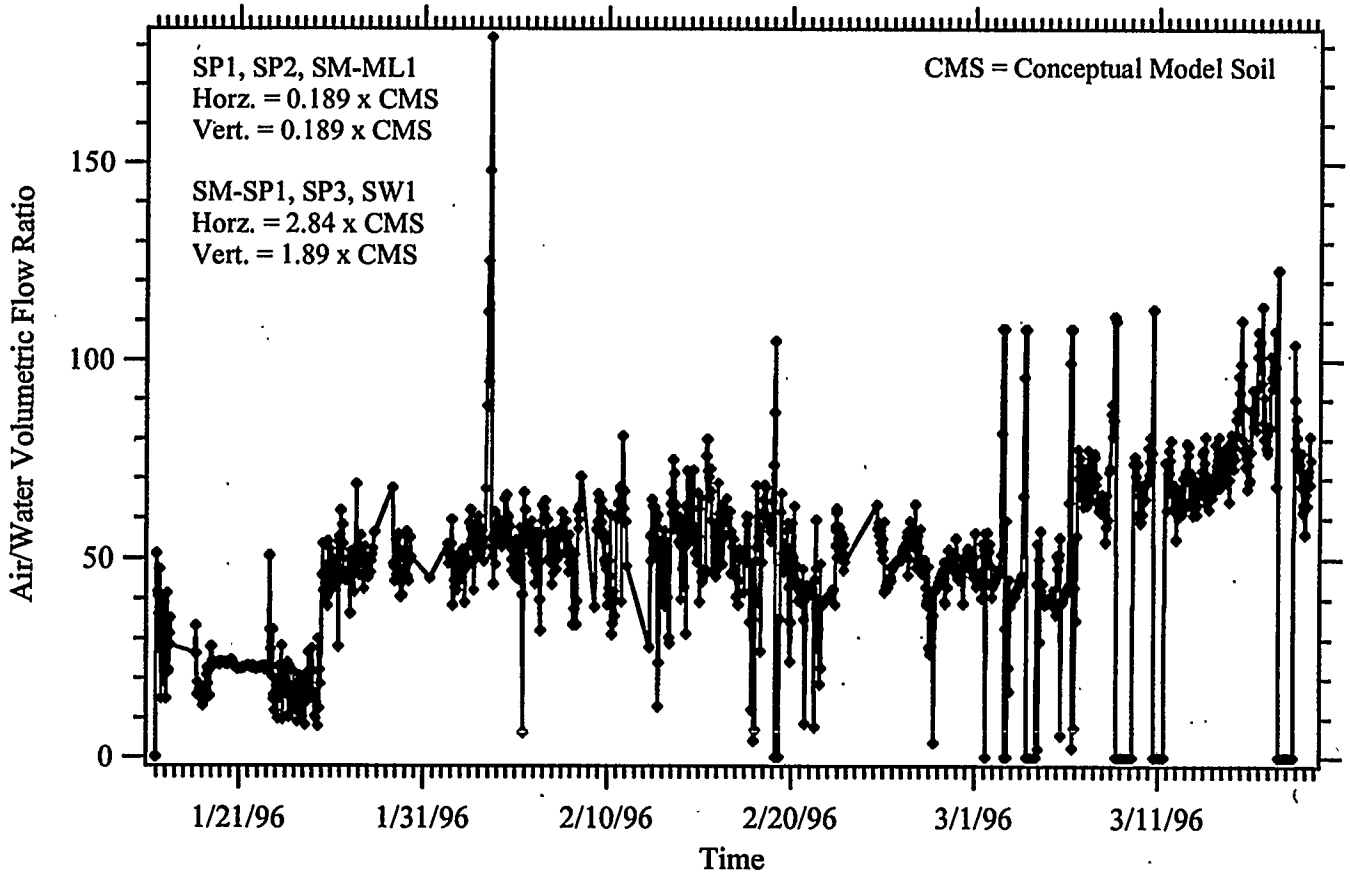

Figure 8.6. Air/Water Volumetric Flow Ratio Versus Time, LPI Simulation (Field Test #13, 1/16/96-3/19/96)

were set to a normalized value of 1 in the saturated zone and linearly decreased in concentration with height above the water table. Normalized molar concentrations of dissolved TCE were assumed to be 0 at the ground surface. Using these boundary conditions and sources as drivers with the computational grid described in Section 5.3, the operational field test was simulated using maximum time steps of 20 minutes. The LPI simulation required 6,835 time steps to complete the 90,512-minute simulation period.

8.1.1 Hydrologic Response

The hydrologic response of the vadose zone strata are shown graphically in the time sequence of aqueous saturation profiles in Appendix D (Figures D.1 through D.7). This sequence of images indicates that the aqueous saturation plume that descends from the upper screened interval reaches the water table in approximately 1 day and that steady-flow conditions are achieved after approximately 8 days. Variations in the bell-shaped saturation mound occur at later times because of the fluctuations in pumping/infiltration rates, see Figures D.6 and D.7. Pumping rates at the lower screened interval, infiltration rates at the upper screened interval, and volumetric flow rates across the radial perimeter are shown sequentially in Figures D.8 through D.10, where each figure depicts a 21-day period. The negative pumping at the lower screened interval indicates flow into the well. Similarly, negative flow rates at the domain perimeter indicate flow into the domain. These plots show that the pumping and infiltration flow rates are equivalent and that on system startup water is drawn into the domain to create the bell-shaped saturation mound. Decreases in the pumping/infiltration rate produce net water losses from the domain as the saturation mound decays and vice versa.

The ponding height and water table mounding responses are shown sequentially in Figures D.11 through D.13, where each figure depicts a 21-day period. These figures show close agreement between the field data and numerical predictions of ponding heights. The water table mound responses from the numerical simulations generally agree with those for piezometers P2 and P3, but not piezometer P1. Hydraulic pressure responses at the deep monitoring wells are shown sequentially in Figures D.14 through D.16. The field values for hydraulic pressure in the deep monitoring wells generally show slightly greater pressure changes compared with the numerical results. Differences between the pressure response at wells M4D and M5D agree with the numerical predictions during the first 3 weeks, but show significantly larger differences during the second 3-week period. A distinct difference is noted in the field data after the system shutdown on February 2, 1996, which could indicate a shift in the pressure transducer or calibration. Overall, the pressure responses in the deep monitoring wells show reasonable agreements between the numerical predictions and field data.

Numerical predictions of horizontal and vertical components of aqueous Darcy velocity, at the radial positions of flow sensors F1, F2, and F3, are shown in Figures D.17 through D.22. As with the previous response histories, each figure depicts a 21-day period within the test

period and the figures are arranged sequentially, first showing the horizontal component sequence, followed with the vertical component sequence. The horizontal components show a strong negative component during the first 4 days that gradually decays, which corresponds with the net influx of water toward the vapor-stripping well until the bell-shaped saturation mound develops. Typical ratios for the horizontal Darcy velocity times the radial distances (i.e., the volumetric flow ratio) between flow senors F3/F2 and F3/F1 were 2.5 and 4.1, respectively. A ratio of 1.0 would indicate pure radial flow. These elevated ratios indicate a recirculating flow pattern that decreases radially. The vertical components, see Figures D.20 through D.22, indicate downward velocities at a depth of 47.5 ft BGS. At a particular position, the vertical velocity components are generally a fraction of the horizontal components. Field measurements of the horizontal and vertical Darcy velocities differ significantly from these numerical predictions. For the horizontal component, the field values are generally an order of magnitude lower than the numerical predictions and the volumetric flow ratios are approximately 1.0. Field values for the vertical components are generally negative and higher than the horizontal components for a given position, which is in direct contrast with the numerical results. Given pumping/infiltration rates of approximately 2.5 gpm, the magnitudes of the horizontal velocity components measured in the field would indicate either shortcircuiting between the upper and lower screened intervals or a more confined zone of influence than predicted from the numerical simulations. Shortcircuiting of water between the upper and lower screened intervals remains a possibility; however, bentonite seals were located between the intervals during the installation of the vapor-stripping well. The pressure responses in the deep monitoring wells and the water table mounding responses in the field indicate zones of influence and water flow paths as predicted by the numerical simulations.

8.1.2 Dissolved TCE Concentration Response

Characterization of the demonstration site for TCE concentrations prior to the operational field tests was limited to samples taken from the monitoring wells positioned around the vapor-stripping well. Because the subject numerical analysis was based on an azimuthally symmetric computational grid, no variations in aqueous flow patterns or TCE concentrations were considered around the vapor-stripping well. This numerical analysis, therefore, ignores the ambient hydraulic gradients and makes no distinction between upgradient, downgradient, and crossgradient locations. TCE removal was numerically simulated by assuming a normalized molar concentration of TCE beneath the water table and a linearly decreasing TCE concentration with height above the water table in the vadose zone. The molar concentration of TCE at the ground surface was assumed to be equal to zero.

Predictions of dissolved TCE molar concentrations for the LPI simulation are shown in a time sequence of gray-scaled images, (Appendix D, Figures D.23 through D.29). Dissolved TCE concentrations first decrease around the upper screened interval because of the reduced concentrations of dissolved TCE in the infiltrating water. Recirculation of water is predicted to occur after 8 days, where water of reduced TCE concentration contacts the lower screened

interval. As the circulation pattern develops, the zone of reduced TCE concentration spreads along the interface between the SP2 and SM-SP1 soil strata. This sharp spreading is partially an artifact of separating the hydraulic properties into saturated and unsaturated zones. The images do reveal unaltered regions of TCE concentration below the midpoint of the lower screened interval, which indicate dead spots in the circulation path. Cleanup of dissolved TCE within these regions would depend on diffusive processes if the system were operated under steady-flow conditions. Because the boundary conditions for TCE concentration along the radial perimeter of the computational grid maintained the normalized conditions, complete cleanup would not be predicted with these simulations.

Dissolved TCE concentration histories at the shallow and deep monitoring wells are shown sequentially in Figures D.30 through D.32, where each figure depicts a 21-day period. The initial molar reduction factor, which equals the ratio of dissolved TCE concentration between the upper and lower screened intervals, was approximately 0.01, indicating a significant vapor-stripping efficiency. These low molar reduction factors were partially due to the low solubility of TCE and the relatively high air-to-water volumetric flow ratios, see Figure 8.8. The concentration of dissolved TCE in the upper screened interval drops on 1/25/96 because infiltrated water from the upper-screened interval reached the lower screened interval, therefore, decreasing the quantity of dissolved TCE entering the vapor-stripping well. Monitoring well M3S, at a radial distance of 10 ft, shows the first indications of reduced dissolved TCE concentrations. At the end of the 63-day simulation period, dissolved TCE concentrations were reduced in the M3S, M4S, and M3D monitoring wells. The M3D well shows a decrease in dissolved molar concentration by 24%, which compares with the field value of 40%. Neither the field samples nor numerical predictions show declines in the TCE concentrations in the deep monitoring wells (M4D, at 30-ft radial distance, and M5D, at 50-ft radial distance). Dissolved TCE concentrations in the M4S monitoring well were predicted have been reduced by 43% by the end of the simulation. Predictions of the TCE molar reduction ratio are shown sequentially in Figures D.33 through D.35, where each figure depicts a 21-day period. The TCE molar reduction ratio was computed as the ratio of the total molar flux crossing the upper and lower screened intervals. The reduction ratio declines rapidly at the onset of recirculation, approximately after 8 days, and then slowly decays during the remainder of the simulation period. Spikes in the reduction ratio were primarily due to corresponding spikes in the air-to-water volumetric flow ratios.

8.2 High-Permeability Simulations

The high-permeability isotropic (HPI) and anisotropic (HPA) simulations of operational field test #13 used soil hydraulic conductivities, pumping/infiltration rates, and air-to-water volumetric flow ratios determined from the April infiltration field test and calibration with operational field test #12. The pumping/infiltration versus ponding height curve, shown in Figure 8.9, was developed by simulating the in-well vapor-stripping system to steady-flow

conditions under a constant pumping/infiltration rate. This curve was then combined with the ponding height time history, shown in Figure 8.4, to generate the pumping/infiltration flow rate input, shown in Figure 8.10. Volumetric air flow data collected from the field test were converted, as with the LPI simulation, and combined with the pumping/infiltration flow rate data to generate air-to-water volumetric flow ratios, shown in Figure 8.11. Because of the higher water flow rates, the air-to-water volumetric flow ratios for the HPI simulation were generally lower than those for the LPI simulations. Boundary and initial conditions for the simulations were developed in an identical manner to those for the LPI simulation and the computational grid remained unchanged. The only differences between the HPI and HPA simulations were the hydraulic conductivities for the saturated zone strata (i.e., CMS types SM-SP1, SP3, and SW1). Both simulations were executed using a maximum time step of 20 minutes. The HPI and HPA executions required 6,912 and 6,972 time steps, respectively, to complete the 90,512-minute simulation period.

8.2.1 Isotropic Simulation

The hydrologic response for the HPI simulation is documented graphically in Appendix E (Figures E.1 through E.22). The saturation plume from the upper screened interval, shown in Figures E.1 through E.7, develops slightly more rapidly for the HPI simulation compared with the LPI simulation; however, the fully developed plume shapes are generally similar. The higher pumping/infiltration rates, shown in Figures E.8 through E.10, of the HPI simulation are offset by the higher saturated hydraulic conductivities; therefore, yielding similar bell-shaped mounding profiles. Because the mounding profiles are similar in shape, the quantity of water drawn into the system during startup is comparable between simulations HPI and LPI. The HPI simulation, however, draws the water in more rapidly, reaching steady-flow conditions earlier. The ponding height response, shown in Figures E.11 through E.13, are practically identical to those predicted for the LPI simulation. As with the LPI simulation, this provides a check on the pumping/infiltration rate versus ponding height function, shown in Figure 8.9. Ponding heights predicted from the HPI simulation, Figures E.11 through E.13, are generally 1 ft higher than those from the LPI simulation and the field data. This result indicates a need to have the saturated zone hydraulic conductivities augmented in conjunction with the vadose zone properties. This also suggests that the vadose zone redevelopment activities additionally influenced the saturated zone. The pressure responses of the deep monitoring wells, shown in Figures E.14 through E.16, are also elevated in the HPI simulations compared with the LPI simulations, which tends to support the previous discussions on the saturated zone hydraulic conductivities. However, the predicted responses generally show good agreement with the field measurements during later periods of the operational tests. This implies that the redevelopment activities allowed increased pumping/infiltration rates at constant ponding heights over the course of the field test by modifying the permeability of the soil strata. Horizontal and vertical Darcy velocities, shown in

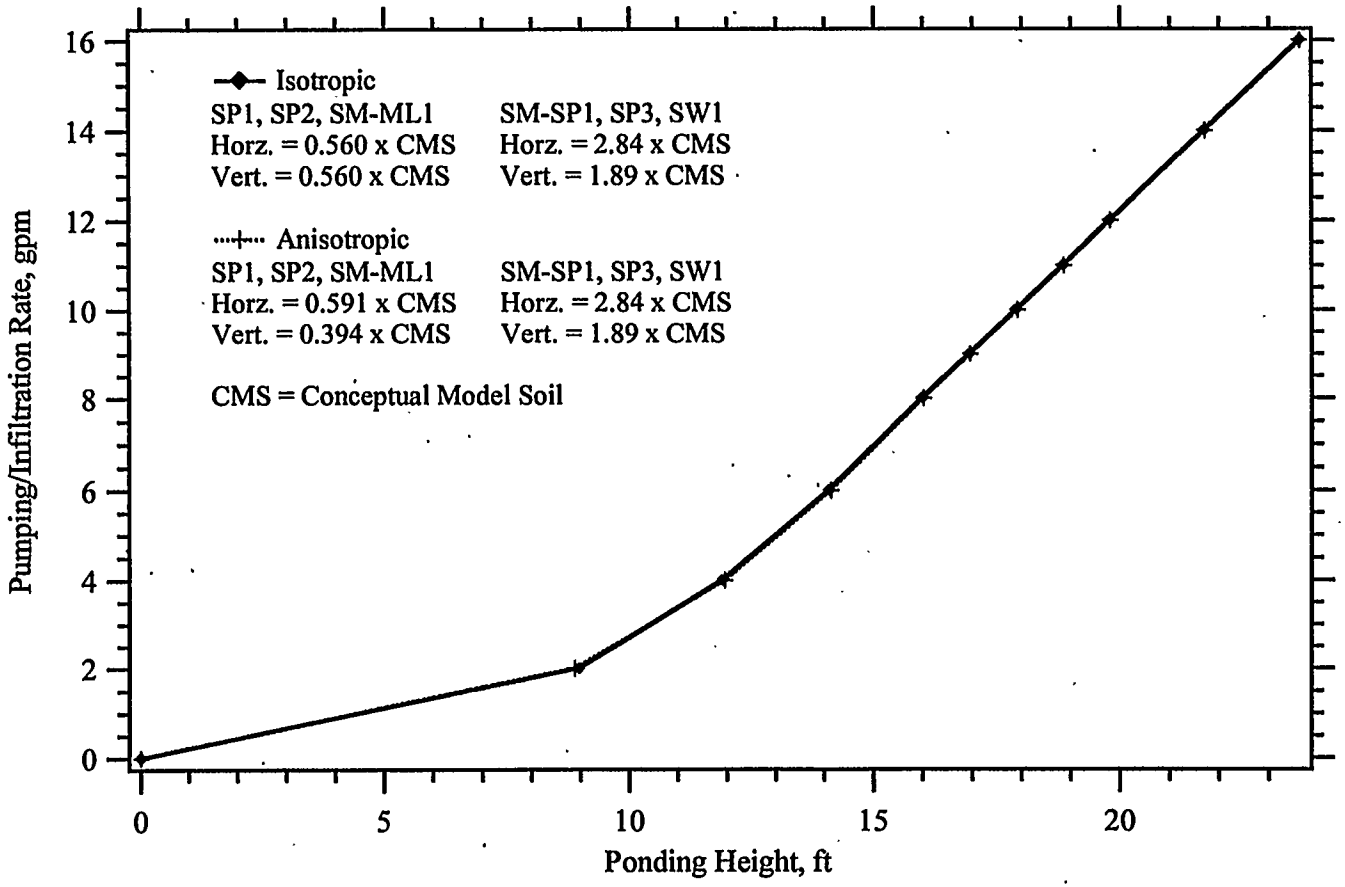

Figure 8.7. Pumping/Infiltration Rate Versus Ponding Height, HPI and HPA Simulations

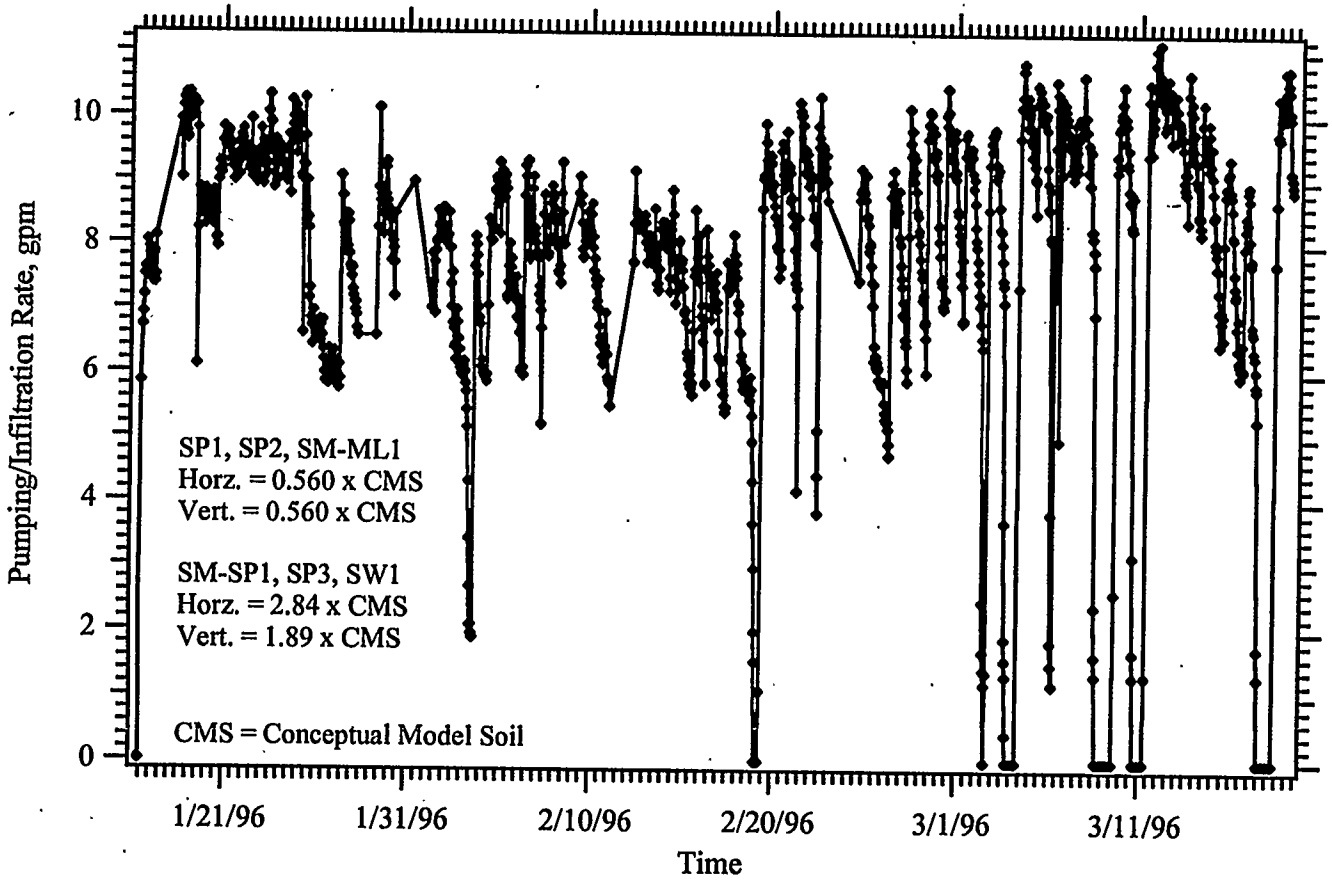

Figure 8.8. Pumping/Infiltration Rate Versus Time, HPI and HPA Simulations (Field Test #13, 1/16/96-3/19/96)

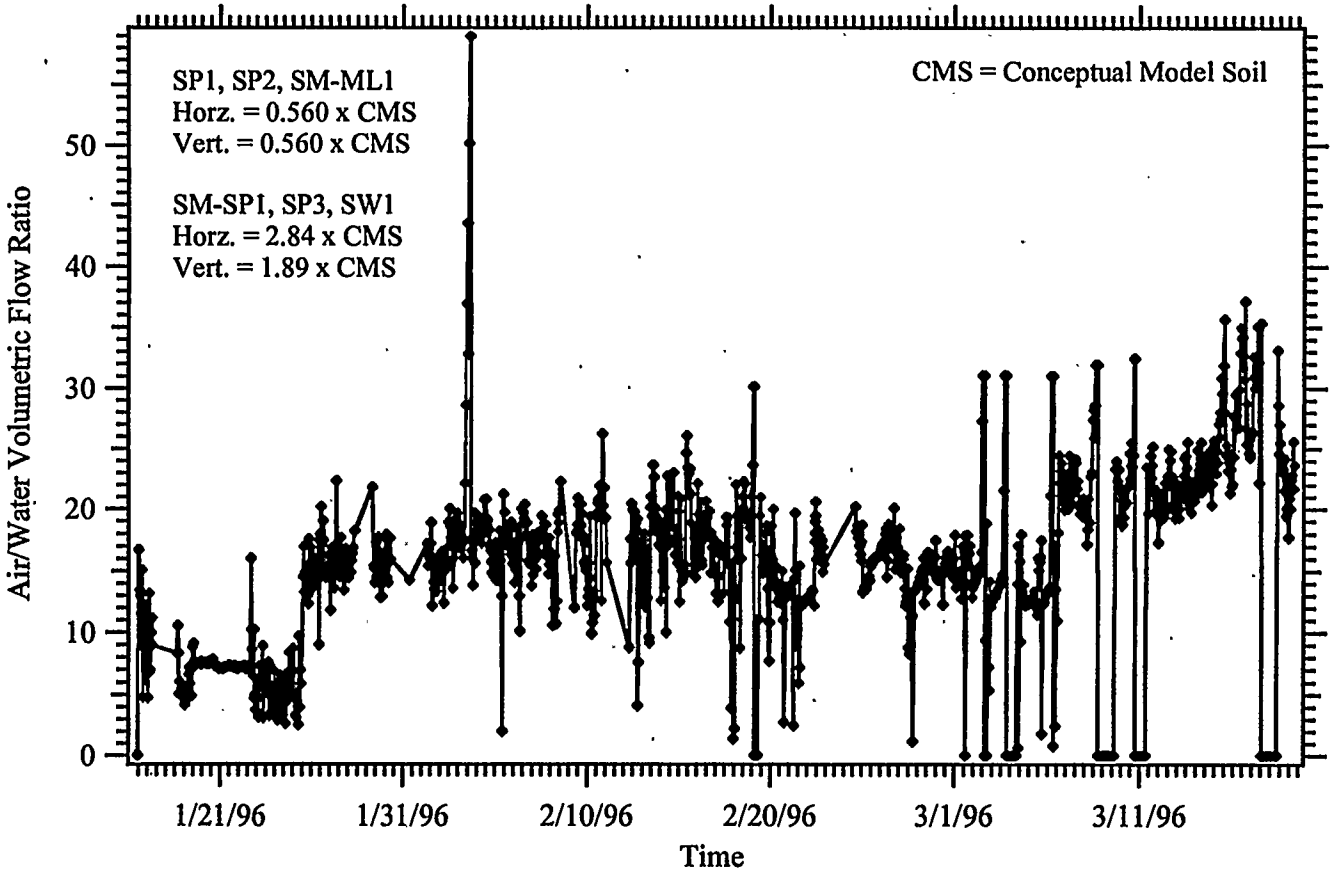

Figure 8.9. Air/Water Volumetric Flow Ratio Versus Time, HPI and HPA Simulations (Field Test #13, 1/16/96-3/19/96)

Figures E.17 through E.22, are approximately three times higher than those from the LPI simulation, which agrees with the ratio of pumping/infiltration rates between the two simulations.

The dissolved TCE concentration response for the HPI simulation is shown graphically in Figures E.23 through E.35. A time sequence of dissolved TCE concentration is shown using gray-scaled images in Figures E.23 through E.29. These images show significantly larger zones of influence for the higher pumping/infiltration rates of the HPI simulation compared to similar images from the LPI simulation, Figures D.23 through D.29. The region of zero influence below the lower screened interval has significantly broadened. Dissolved TCE concentration histories for the monitoring wells and upper screened intervals are shown in Figures E.30 through E.32. Compared with the LPI simulation, dissolved concentrations at the monitoring wells decrease earlier and more rapidly. By the end of the simulation period, TCE molar concentrations in monitoring wells M3S, M4S, M3D, M4D, and M5S had been reduced to normalized values of 0.0026, 0.0086, 0.016, 0.69, and 0.97, respectively. These reductions are significantly greater than those measured in the field and computed in the LPI simulation. Dissolved TCE concentrations in the upper screened interval are approximately double those from the LPI simulation, however, the recirculation point, marked by a sharp decline in concentration, occurs near the same time. Molar reduction ratios for TCE are shown in Figures E.33 through E.35 and are approximately three times greater than those for the LPI simulation. This results primarily from the reduced air-to-water volumetric flow ratios in the HPI simulation; therefore, water infiltrated into the hydrologic system had higher dissolved TCE concentrations in the HPI simulation.

8.2.2 Anisotropic Simulation

The hydrologic and dissolved TCE concentration responses for the HPA simulation are shown in Appendix F (Figures F.1 through F.35). Results for the HPA and HPI simulations were generally comparable, and this discussion will concentrate on specific differences between these two high permeability simulations. The saturation profiles, in Figures F.1 through F.7 show the influence of higher horizontal conductivities in the vadose zone strata, with broader bell-shaped saturation mounds. These broader profiles were also reflected in the slightly elevated ponding heights, Figures F.11 through F.13. As with the saturation profiles, the dissolved TCE concentration profiles, Figures F.23 through F.29, are slightly broader in the vadose zone; differences are less significant beneath the ambient water table. Reductions in dissolved TCE concentration at the monitoring well positions, Figures F.30 through F.32, were delayed for the M3S and M3D wells, but advanced for M4S and M4D wells. These results indicate that moderate anisotropies in the saturated conductivities for the vadose zone strata show little influence on the hydrologic and dissolved TCE concentration responses to the in-well vapor-stripping system.

9.0 Conclusions

The objectives for these numerical analyses were to demonstrate the utility and appropriateness of numerical simulations in the design, operational performance, and visualization of the in-well vapor-stripping system demonstration at Edwards AFB. Numerical simulations of the in-well vapor-stripping system were executed with the STOMP simulator, configured to solved decoupled two-phase flow and transport equations. Dissolved TCE was modeled as a tracer solute in the aqueous phase; the gas phase was considered passive for TCE transport. An equilibrium model for vapor-stripping of VOCs was incorporated into the STOMP simulator to model the engineered component of the in-well vapor-stripping system. This model partitions TCE into volatile and dissolved components according to thermodynamic equilibrium conditions and was used to compute TCE vapor-stripping ratios during air-lift pumping.

The objectives associated with system design were realized through development of a conceptual model for the hydrologic system and numerical simulation of the combined engineered and hydrologic components of the in-well vapor-stripping system under design operating conditions. The hydrologic conceptual model comprised the subsurface stratigraphy and mathematical descriptions of the hydrologic properties for each soil strata. Conceptual model soils were developed to represent the subsurface stratigraphy from visual inspection and grain-size distributions on core samples extracted from the field site. Hydrologic descriptions of the CMS types were developed from grain-size distributions, bulk density, and grain-density measurements. Hydrologic descriptions primarily comprised numerical values for diffusive porosity, saturated hydraulic conductivity, and parameters for the relative permeability-saturation-capillary pressure relations. The physical domain, which included the engineered and hydrologic components of the vapor-stripping system were modeled on an axialsymmetric computational domain with the well center-line aligned with the center of the computational grid. Design options for the vapor-stripping well were analyzed using numerical simulations to generate steady-flow fields. Results from these simulations provided design information on ponding height, water table mounding, zone of influence for TCE remediation, and subsurface flow rates and patterns. Field configuration of the vapor-stripping well and monitoring device locations were selected based on information provided from these design simulations.

Prior to estimating operational performance, numerical simulations were executed to calibrate critical parameters in the hydrologic conceptual model. Calibrations were conducted using data collected from three field tests, two infiltration tests, and one operational test. Because of its influence on saturation mounding, ponding height, and differential hydraulic pressure, the saturated hydraulic conductivity (intrinsic permeability) was the parameter of principal concern for these field calibrations. The infiltration tests were used to calibrate the hydraulic conductivities of the vadose zone strata, whereas the operational test was primarily

used to determine the hydraulic conductivities of the saturated zone strata. Redevelopment activities associated with the field operation to flocculate dispersive clays produced a three-fold increase in the vadose zone hydraulic conductivities between January and April 1996. Calibrating the saturated hydraulic conductivities for the soil strata was sufficient to yield close agreement between the simulated and field-measured responses in ponding height, water table mound, and differential hydraulic pressure at the monitoring well locations. These calibration tests additionally provided unavailable field data for pumping/infiltration rates and correlations with ponding heights. Calibration between the field data and simulation results required using anisotropic values for the hydraulic conductivities of the saturated zone strata. A horizontal-to-vertical ratio of 1.5 provided the closest agreement in the calibrated simulations. Poor agreement was found between the field measurements for horizontal and vertical Darcy velocity and the numerical predictions. The field results indicate either significant shortcircuit in the flow pattern or higher vertical flow rates in the vadose and saturated zone near the vapor-stripping well.

Predictions of operational performance were computed for operational field test #13, which had nearly continuous operation over a 63-day period, starting on January 16, 1996. This operational test continued beyond the 63-day period reported herein. Because of the continuous redevelopment activities associated with the Edwards AFB site, the hydraulic conductivities of at least the vadose zone soils increased three fold between January and April 1996. Instead of attempting to model these variations in hydraulic conductivities over time, performance predictions were made using calibrated permeabilities from the January and April infiltration tests, in an attempt to bracket the measured performance. Calibration of soil properties using the April infiltration test yielded both isotropic and anisotropic properties for the vadose zone strata that realized the calibration requirements. Performance predictions using both sets of permeability parameters yielded comparable responses in TCE concentration reductions. Performance predictions using the January infiltration test (the LPI simulation) showed good agreement in the hydrologic responses and timing of TCE concentration declines in the shallow and deep monitoring wells. Reduction ratios (approximately 0.01) and TCE concentrations within the cleaned plume were overestimated by the numerical simulator. These overestimates indicate nonequilibrium conditions at the water separator plate, which would be expected for the large air-to-water volumetric flow ratios, between 50 and 100, imposed during this simulation. The high-permeability simulations showed good predictions of hydrologic response when compared against data collected from the field toward the end of the 63-day operational period, specifically in the differential hydraulic pressures at the deep monitoring wells. The timing and magnitude of reductions (approximately 0.04) in dissolved TCE concentrations predicted by these simulations preceded and exceeded those collected in the field. The high-permeability simulations were designed to yield an upper bound for the zone of influence and concentration reduction rates. Both the high- and low-permeability simulations predicted and demonstrated the advanced remediation of monitoring wells within the shallow zone.

10.0 References

American Society for Testing and Materials (ASTM). 1993. "D 2487-93, Standard Classification of Soils for Engineering Purposes (Unified Soil Classification System)." *Annual Book of ASTM Standards.* Vol 04.08.

Burdine, N. T. 1953. "Relative Permeability Calculations from Pore-Size Distribution Data." *Petroleum Trans.* 198:71-77.

Brooks, R. H., and A. T. Corey. 1964. "Hydraulic Properties of Porous Media." *Hydrology Paper No. 3,* Colorado State University, Fort Collins, Colorado.

Comprehensive Environmental Response, Compensation and Liability Act of 1980, as amended. Public Law 96-510, 94 Stat. 2767, 42 USC 6901 et seq.

Gilmore, T. J, M. J. Pinto, M. D. White, S. Ballard, S. M. Gorelick, O. Teban, and F. A. Spane. 1996. *Preliminary Performance Assessment In-Well Vapor-Stripping System.* PNNL-xxxxx, Pacific Northwest National Laboratory, Richland, Washington.

Gupta, A. D., L. W. Lake, G. A. Pope, and K. Sepehrnoori. 1991. "High Resolution Monotonic Schemes for Reservoir Fluid Flow Simulation." *In Situ* 15(3):289-317.

Gvirtzman, H. and S. M. Gorelick. 1992. "The Concept of In-Situ Vapor Stripping for Removing VOCs from Groundwater." *Transport in Porous Media* 8:71-92.

Khaleel, R., J. F. Relyea, and J. L. Conca. 1995. "Evaluation of van Genuchten-Mualem Relationships to Estimate Unsaturated Hydraulic Conductivity at Low Water Contents." *Water Resources Research* 31(11):2659-2668.

Koltermann, C. E., and S. M. Gorelick. 1995. "Fractional Packing Model for Hydraulic Conductivity Derived from Sediment Mixtures." *Water Resources Research* 31(12):3283-3297.

Kreyszig, E. 1979. *Advanced Engineering Mathematics.* Fourth Edition. John Wiley & Sons, Inc., New York.

Mishra, S., J. C. Parker, and N. Singhal. 1989. "Estimation of Soil Hydraulic Properties and Their Uncertainty from Particle Size Distribution Data." *Journal of Hydrology* 108:1-18.

Patankar, S. V. 1980. *Numerical Heat Transfer and Fluid Flow.* Hemisphere Publishing Corporation, Washington, D.C.

van Genuchten, M. Th. 1980. "A Closed-Form Equation for Predicting the Hydraulic Conductivity of Unsaturated Soils." *Soil Sci. Soc. Am. J.* 44:892-899.

White, M. D., and M. Oostrom. 1996. *STOMP Subsurface Transport Over Multiple Phases, Theory Guide,* PNNL-11217, Pacific Northwest National Laboratory, Richland, Washington.

APPENDIX A

DESIGN SATURATION PROFILES

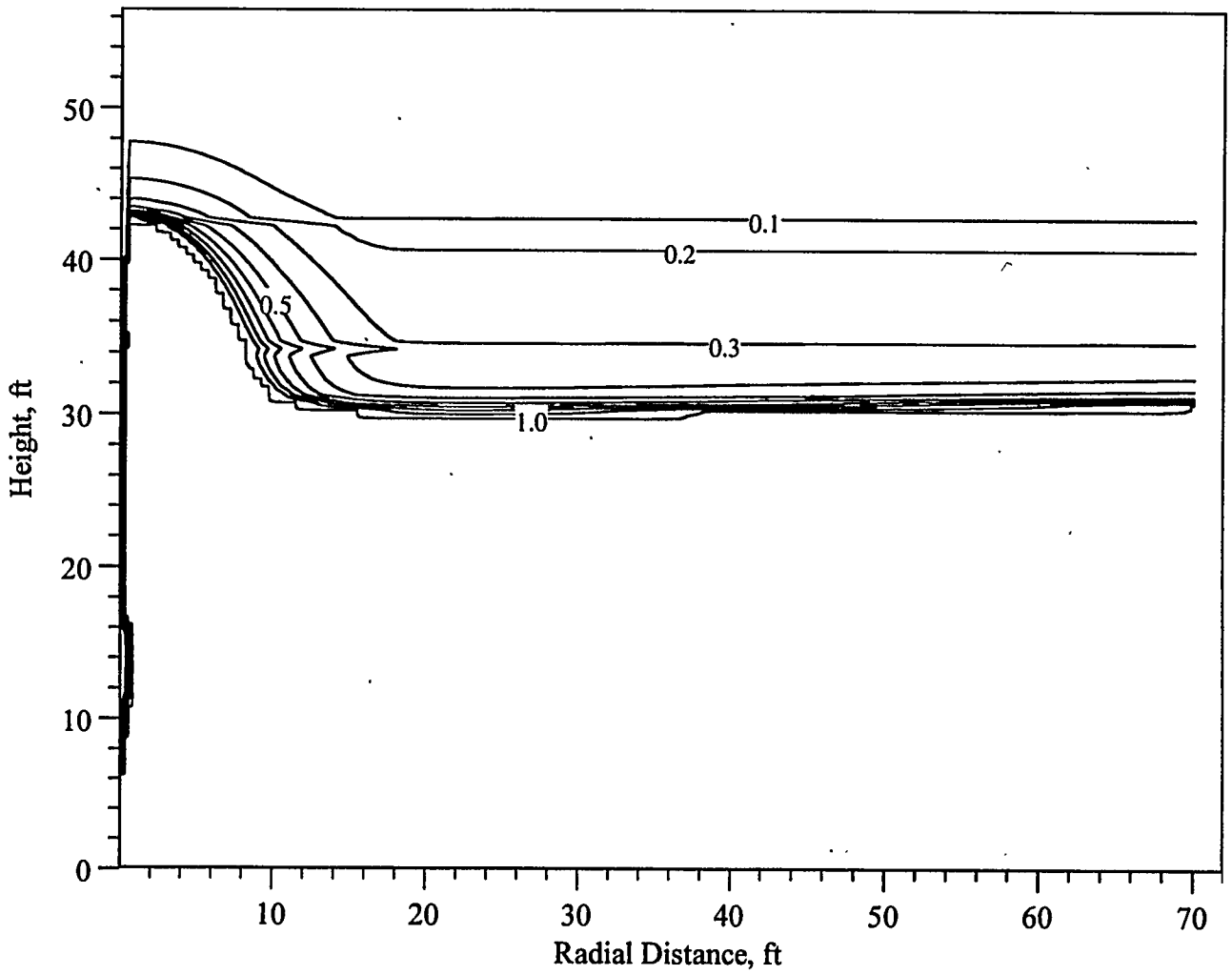

Figure A.1 Steady-State Saturation Profile, Design A

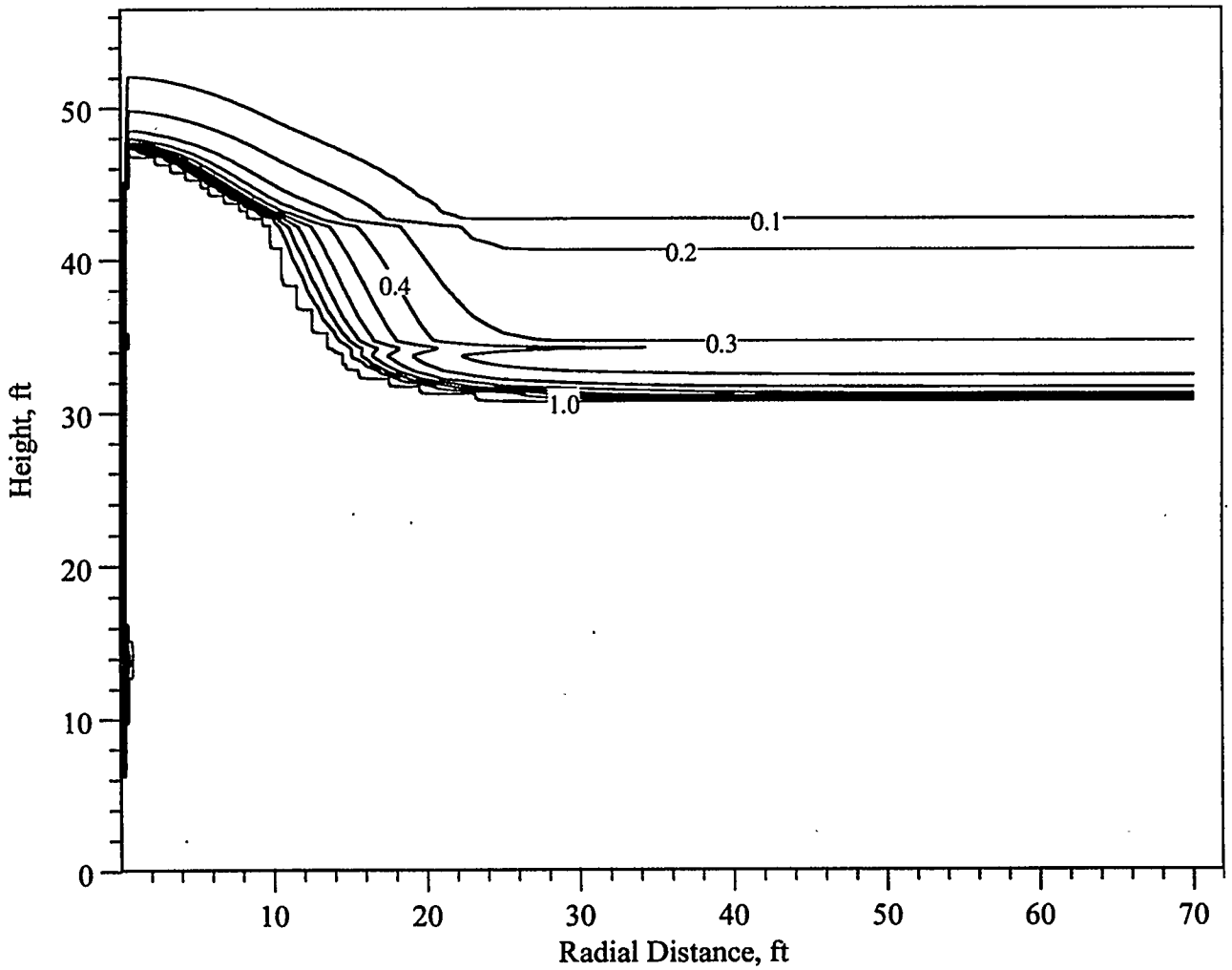

Figure A.2 Steady-State Saturation Profile, Design B

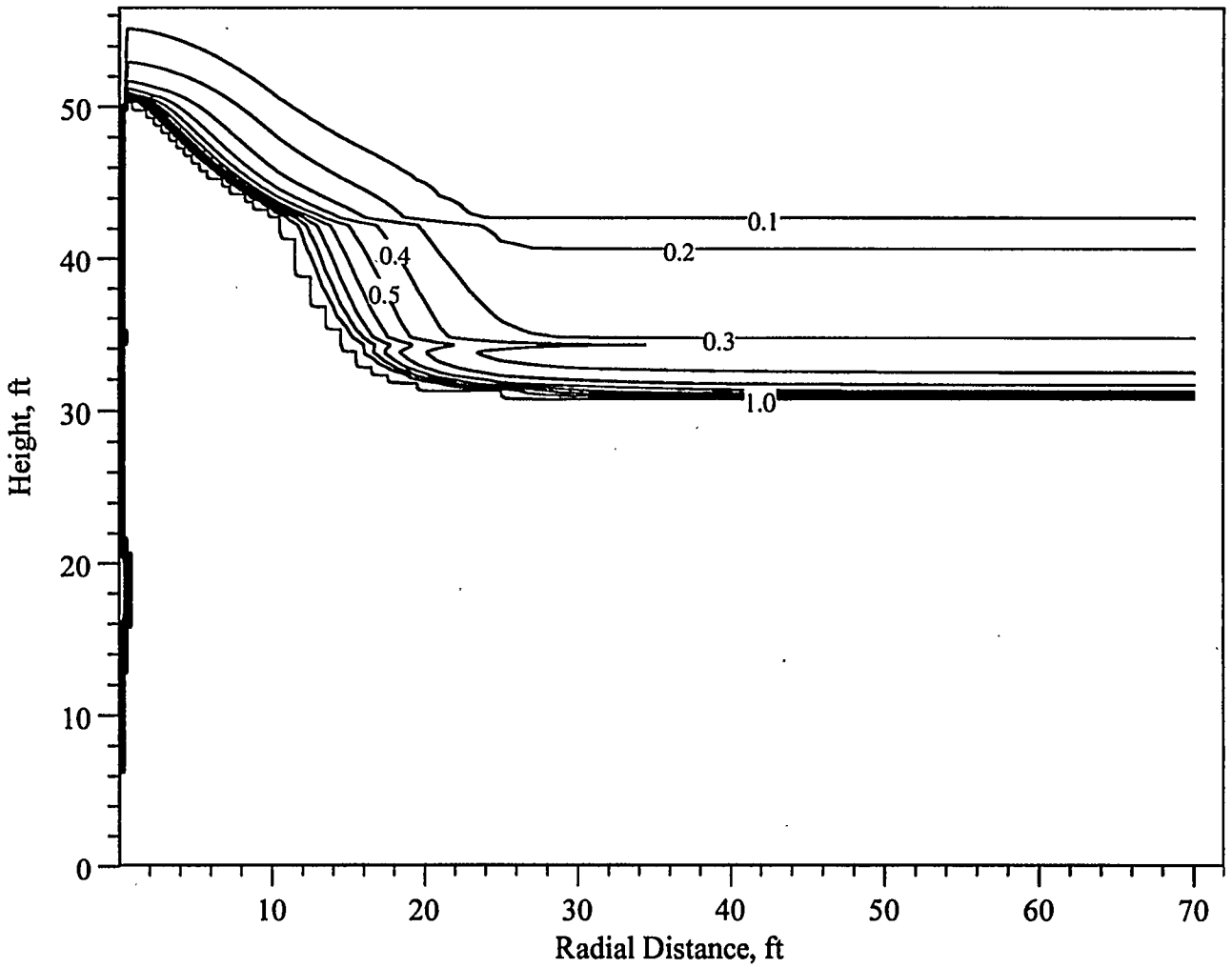

Figure A.3 Steady-State Saturation Profile, Design C

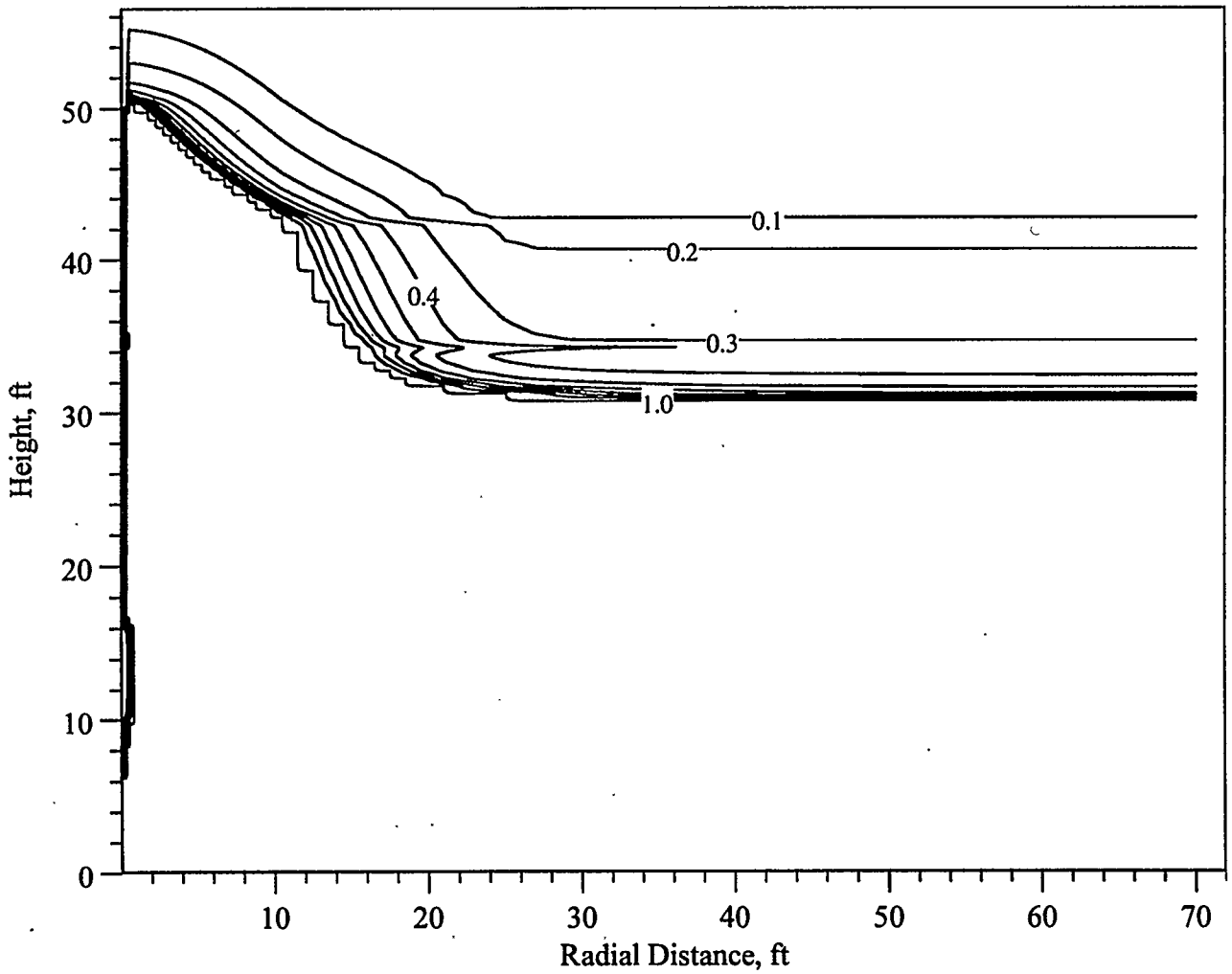

Figure A.4 Steady-State Saturation Profile, Design D

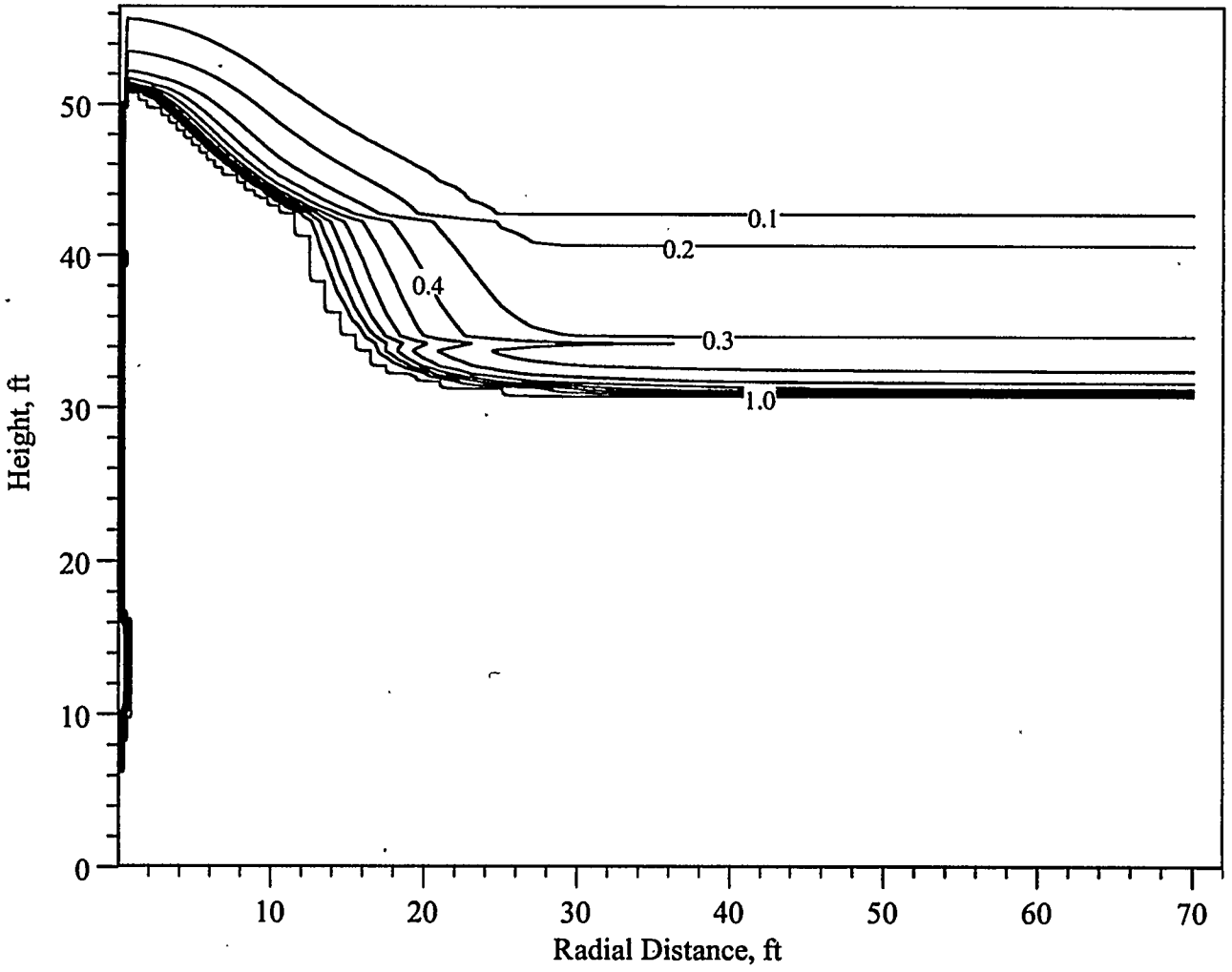

Figure A.5 Steady-State Saturation Profile, Design E

APPENDIX B

DESIGN TRICHLOROETHYLENE CONCENTRATION PROFILES

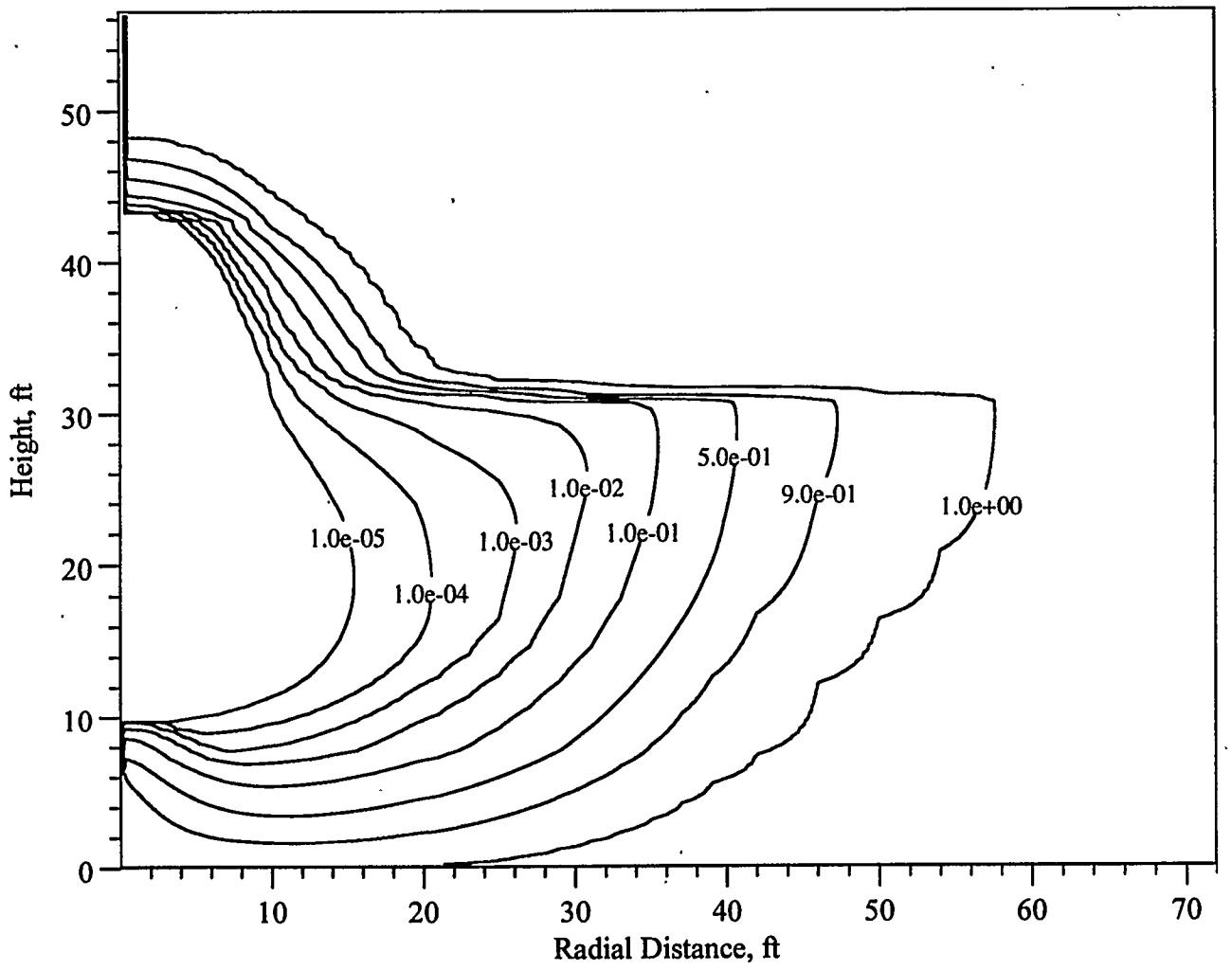

Figure B.1 Dissolved TCE Concentration Profile, Design A

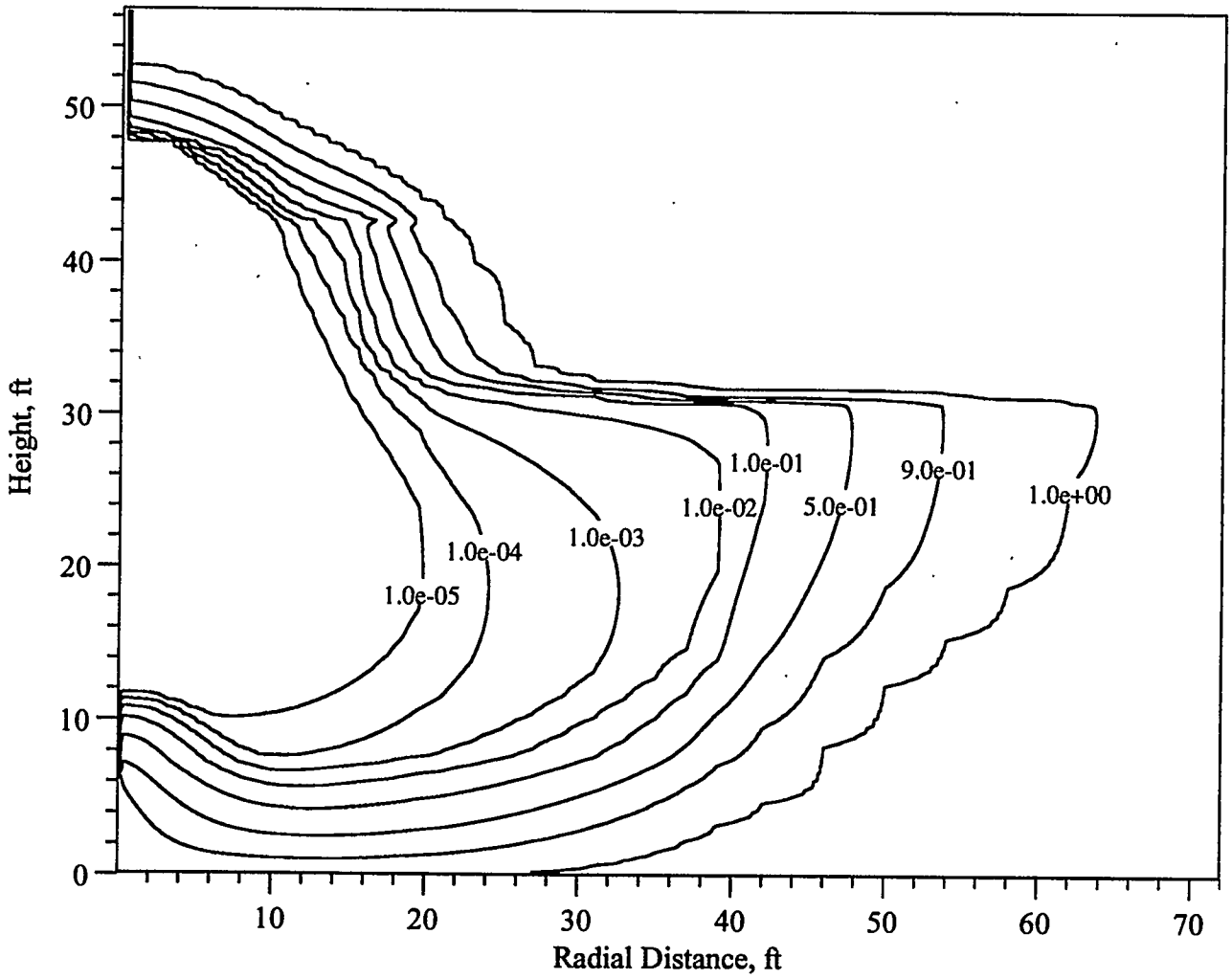

Figure B.2 Dissolved TCE Concentration Profile, Design B

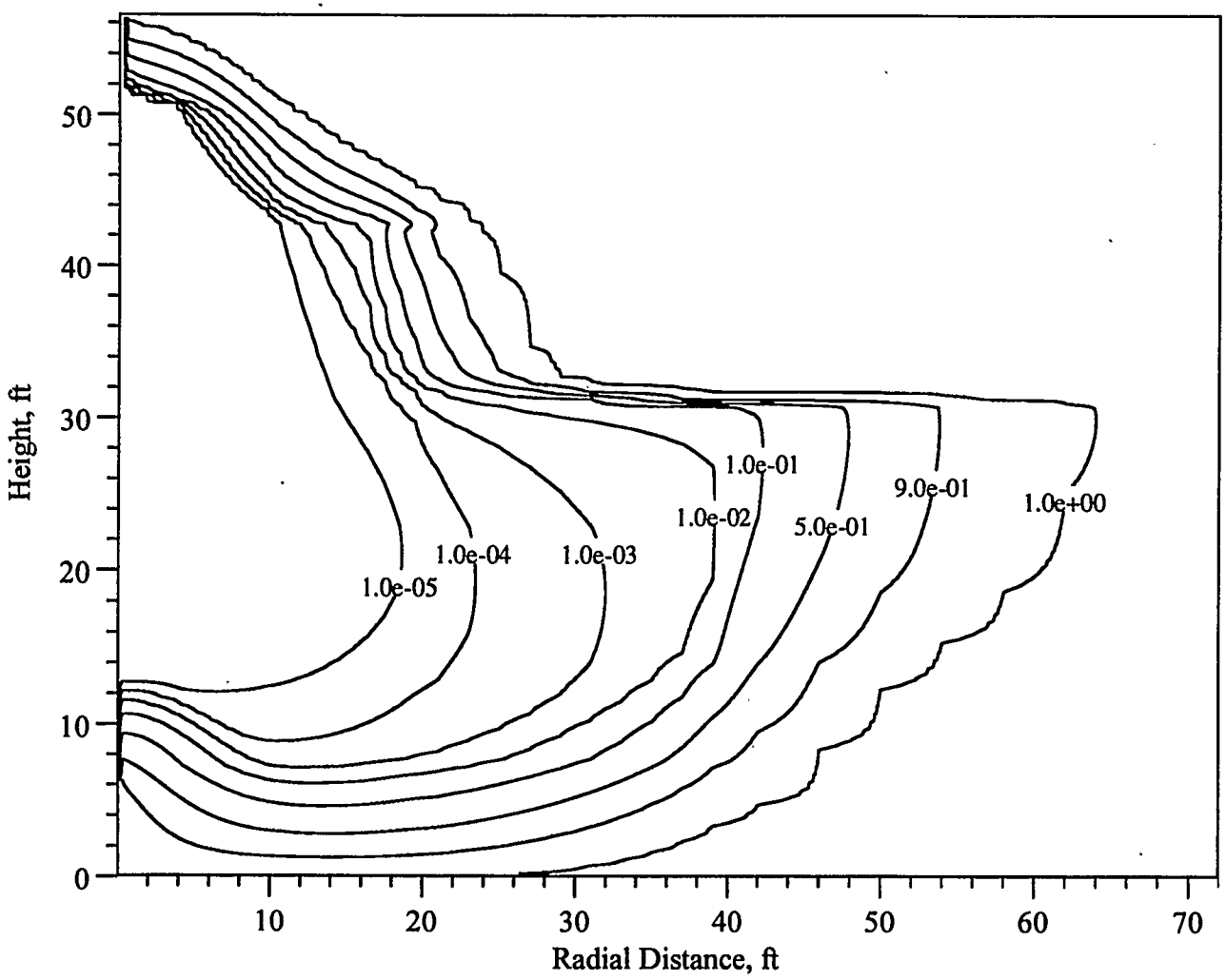

Figure B.3 Dissolved TCE Concentration Profile, Design C

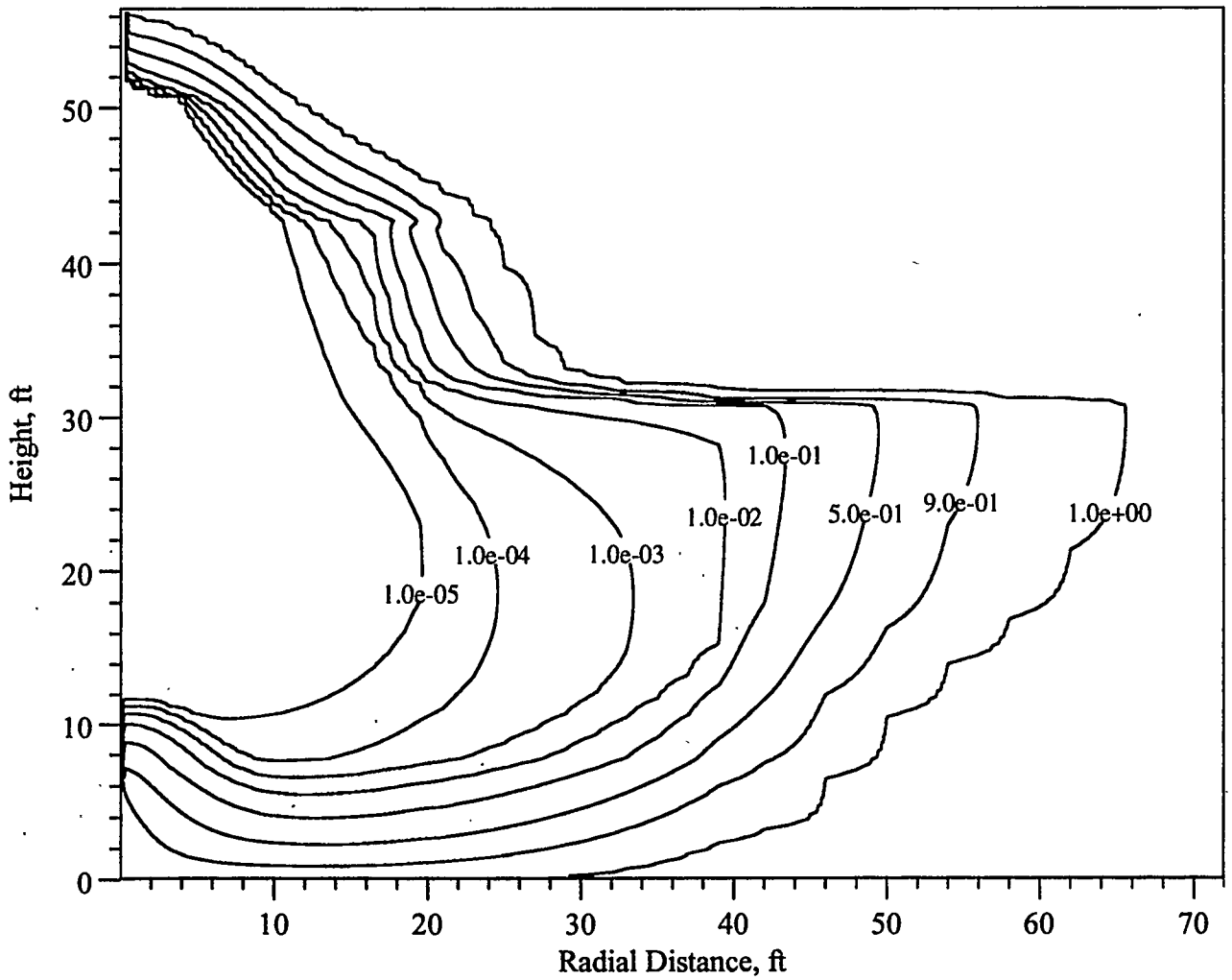

Figure B.4 Dissolved TCE Concentration Profile, Design D

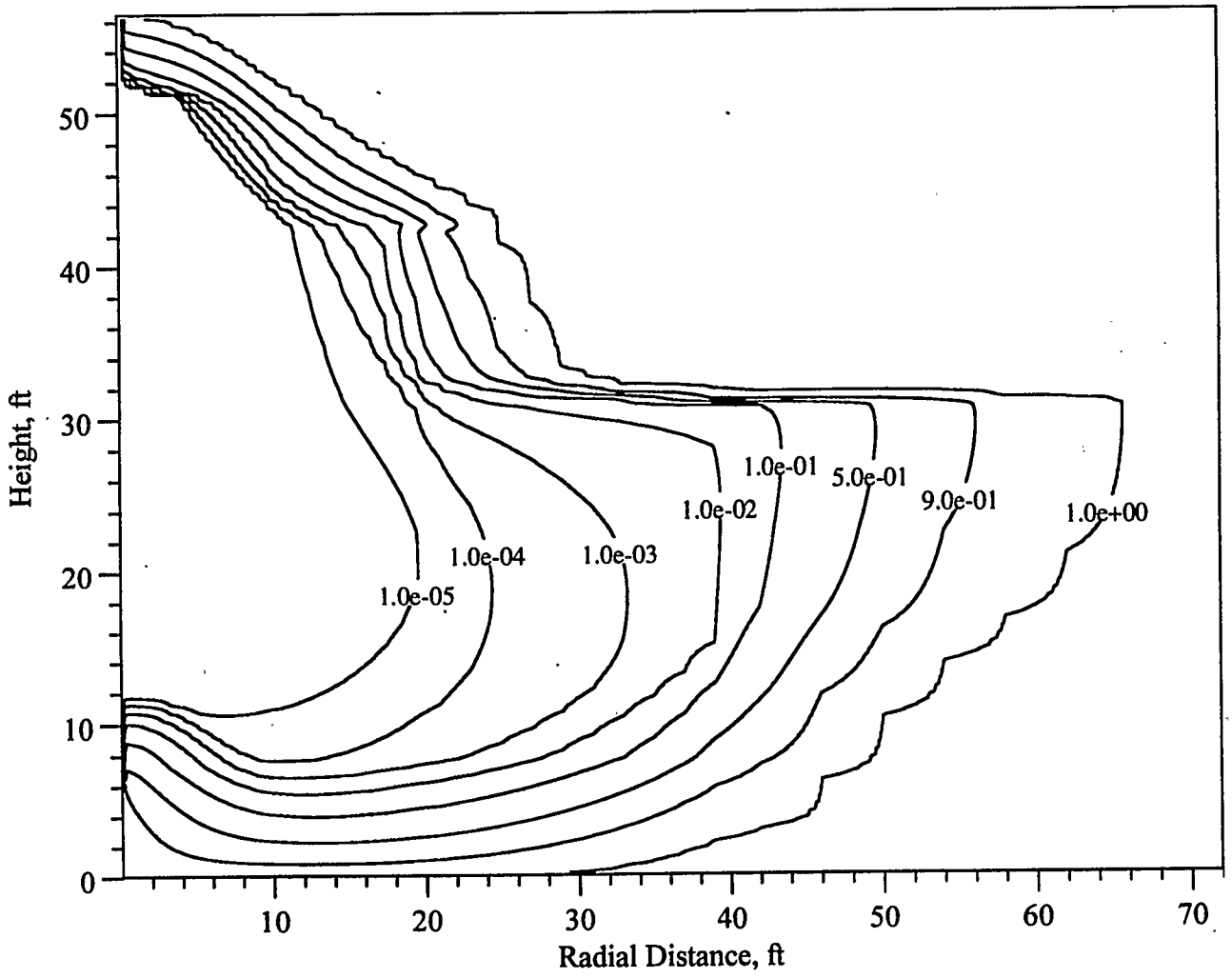

Figure B.5 Dissolved TCE Concentration Profile, Design E

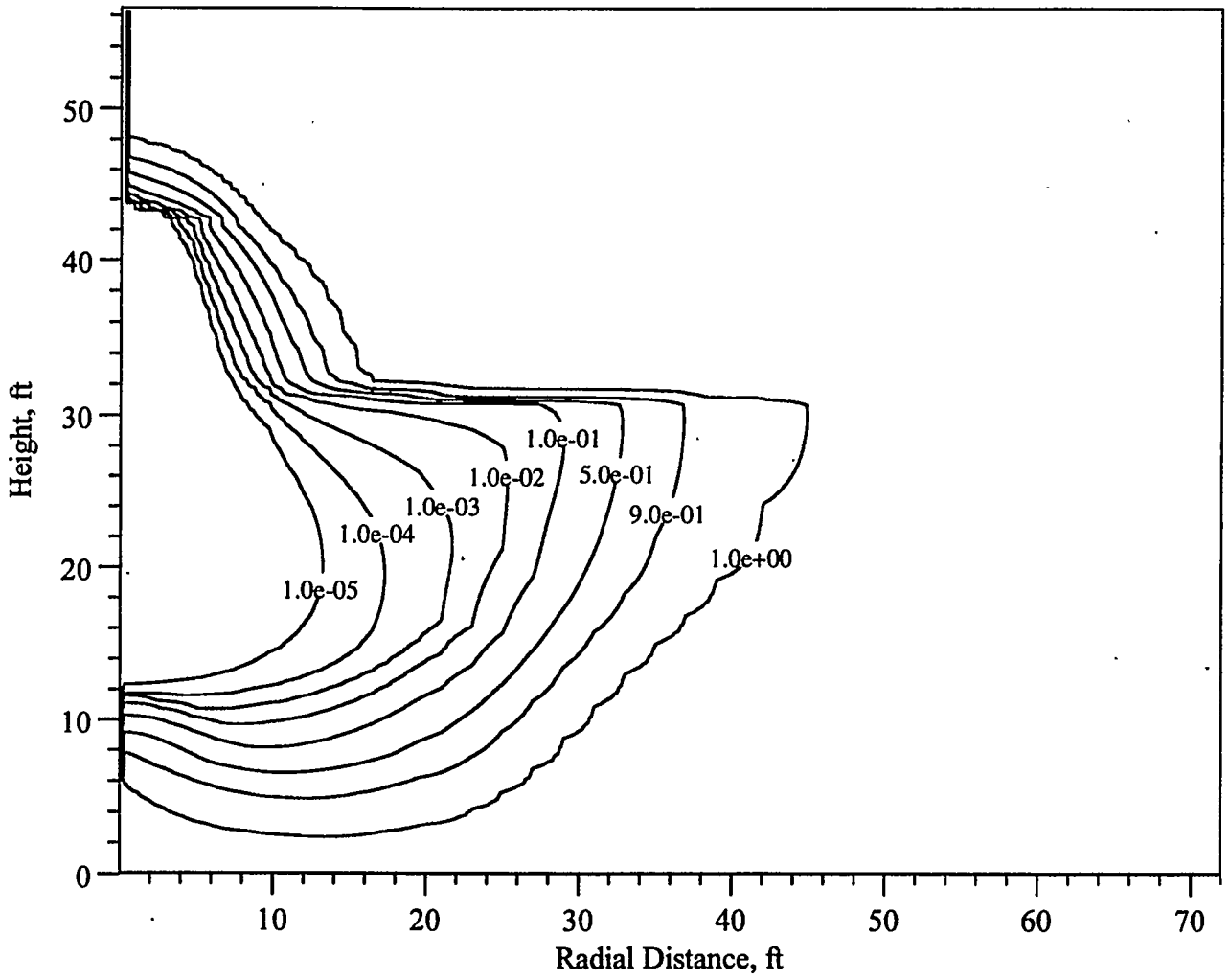

Figure B.6 Dissolved TCE Concentration Profile, Design D at 2.5 gpm

APPENDIX C

OPERATIONAL FIELD TEST #12 SIMULATION RESULTS

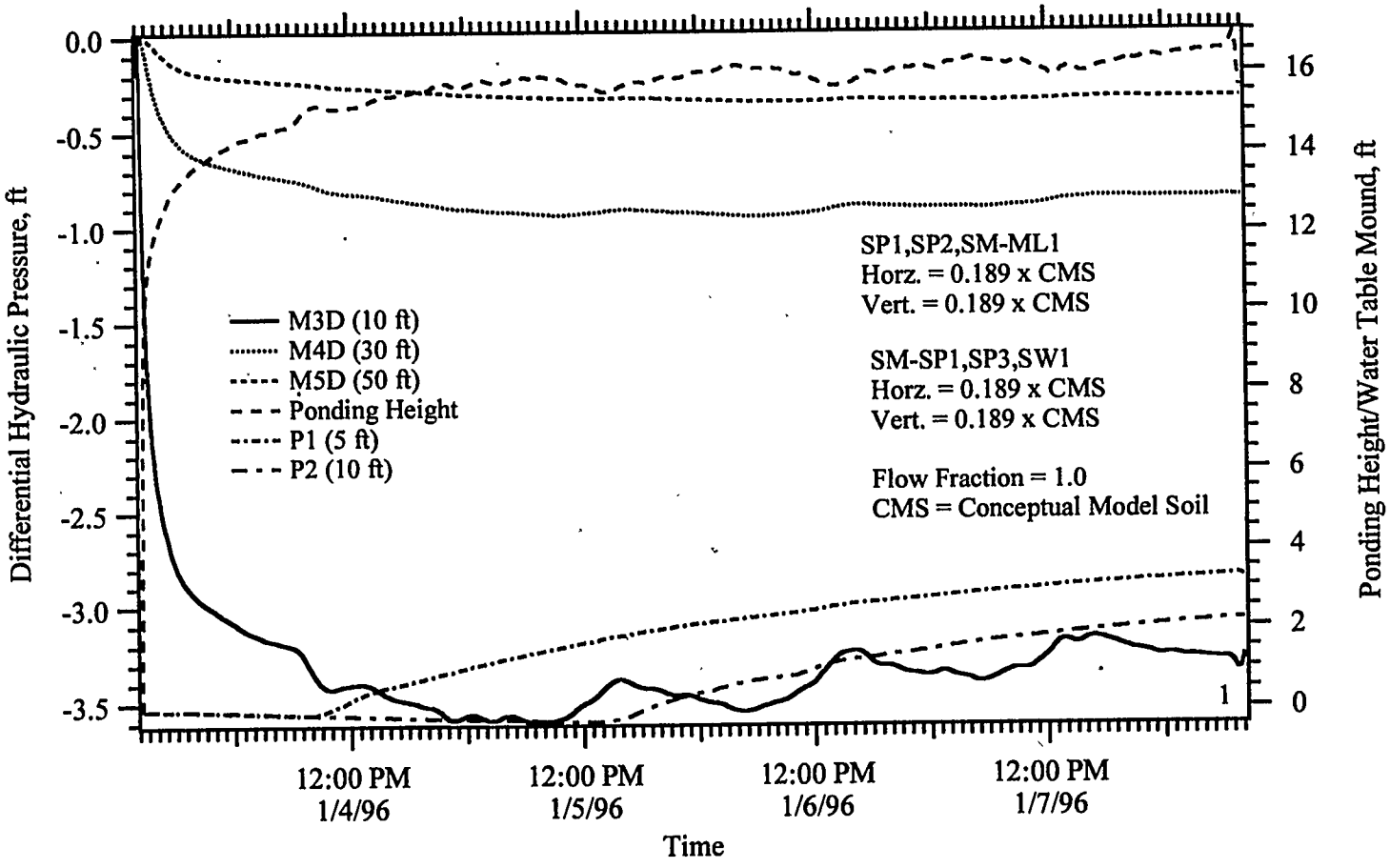

Figure C.1 Differential Hydraulic Pressure Versus Time, Simulation #1 of Operational Field Test #12

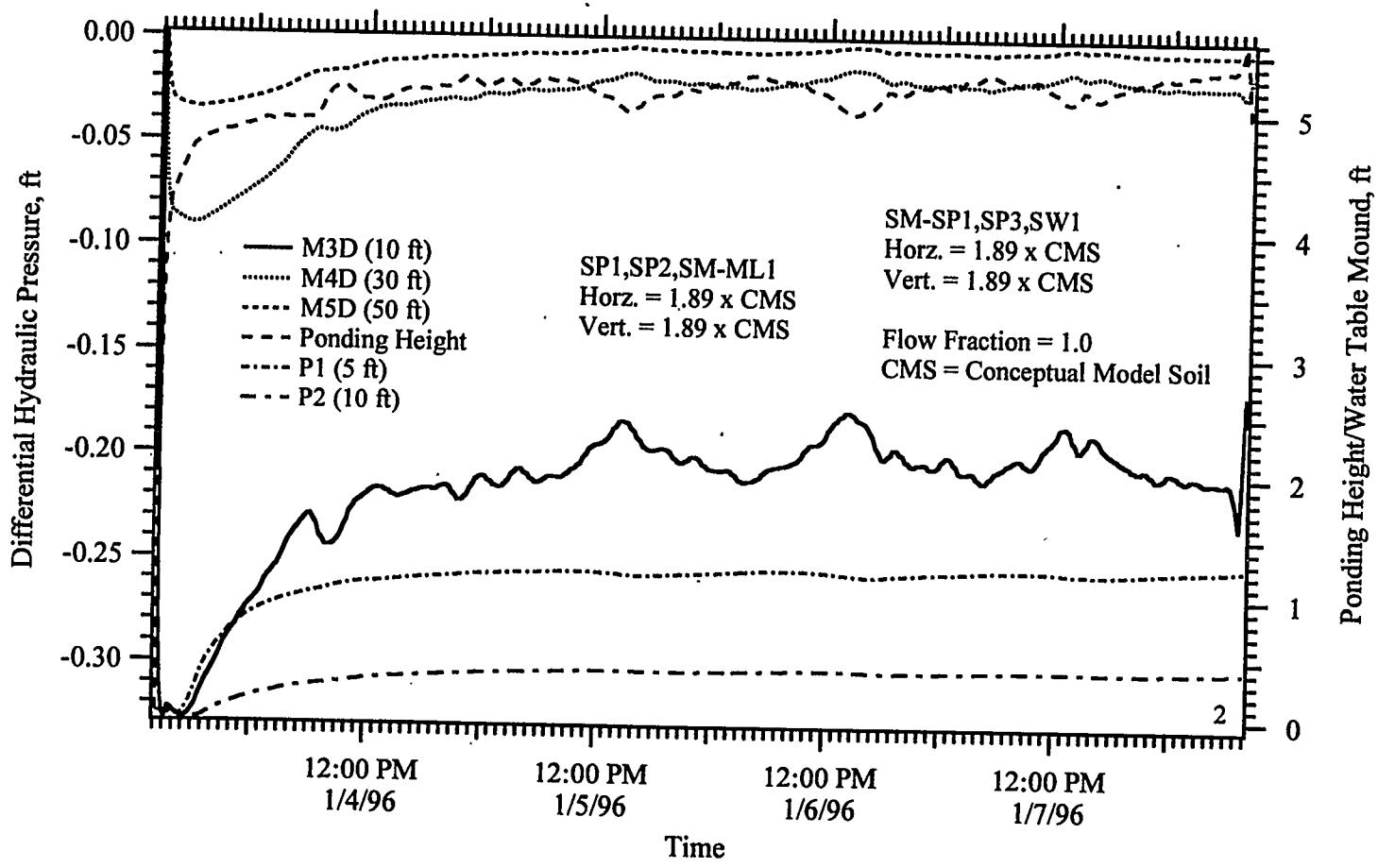

Figure C.2 Differential Hydraulic Pressure Versus Time, Simulation #2 of Operational Field Test #12

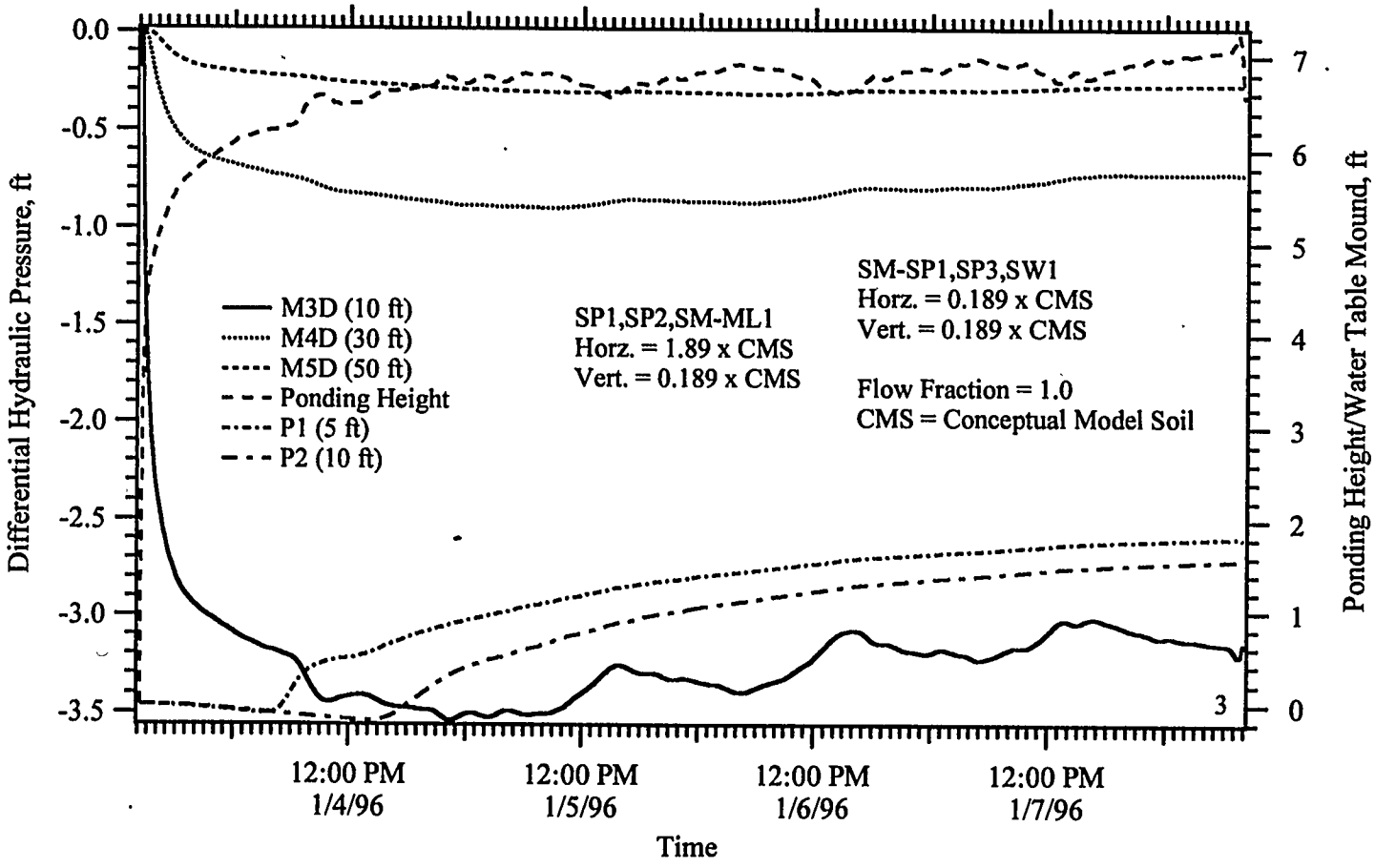

Figure C.3 Differential Hydraulic Pressure Versus Time, Simulation #3 of Operational Field Test #12

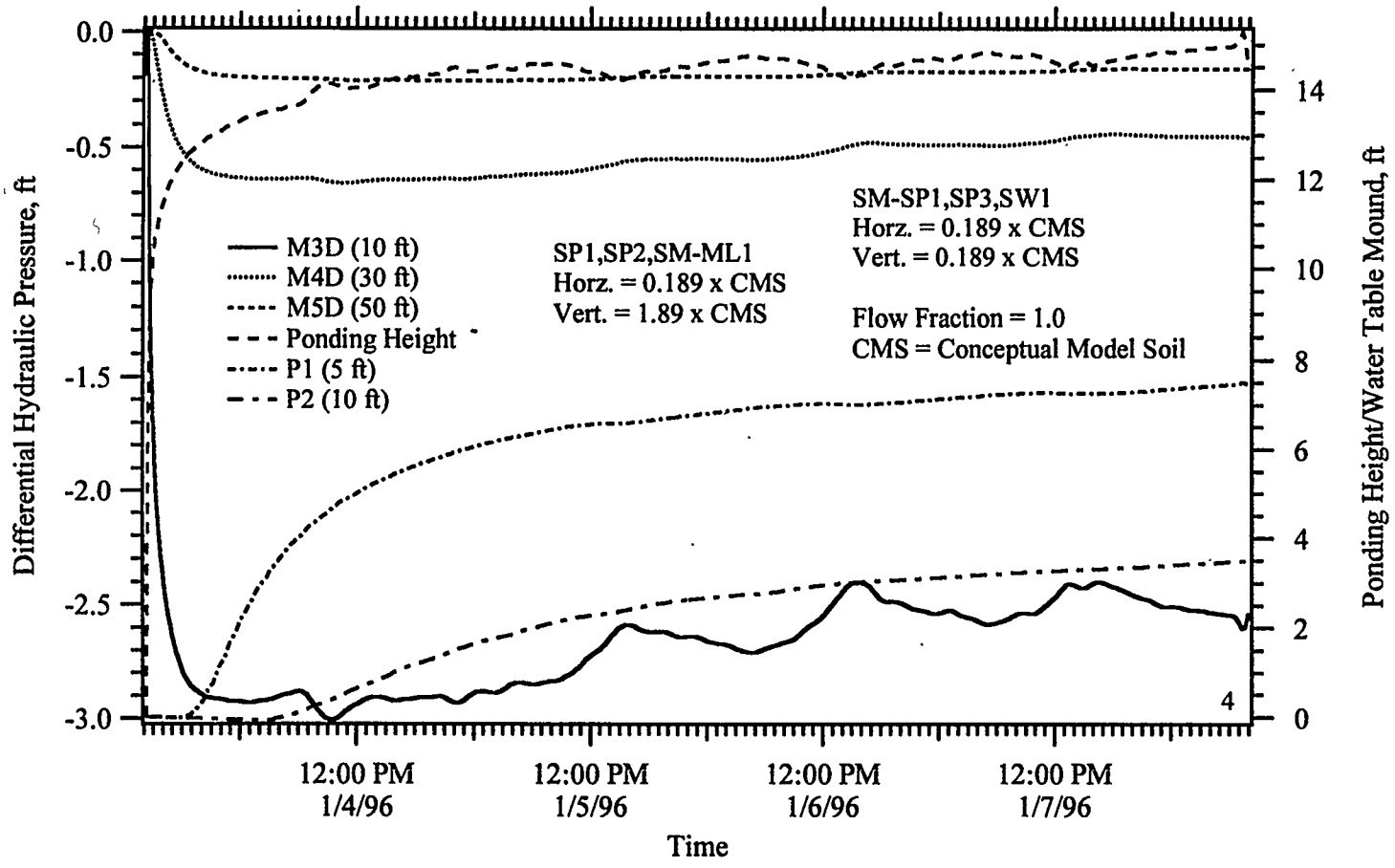

Figure C.4 Differential Hydraulic Pressure Versus Time, Simulation #4 of Operational Field Test #12

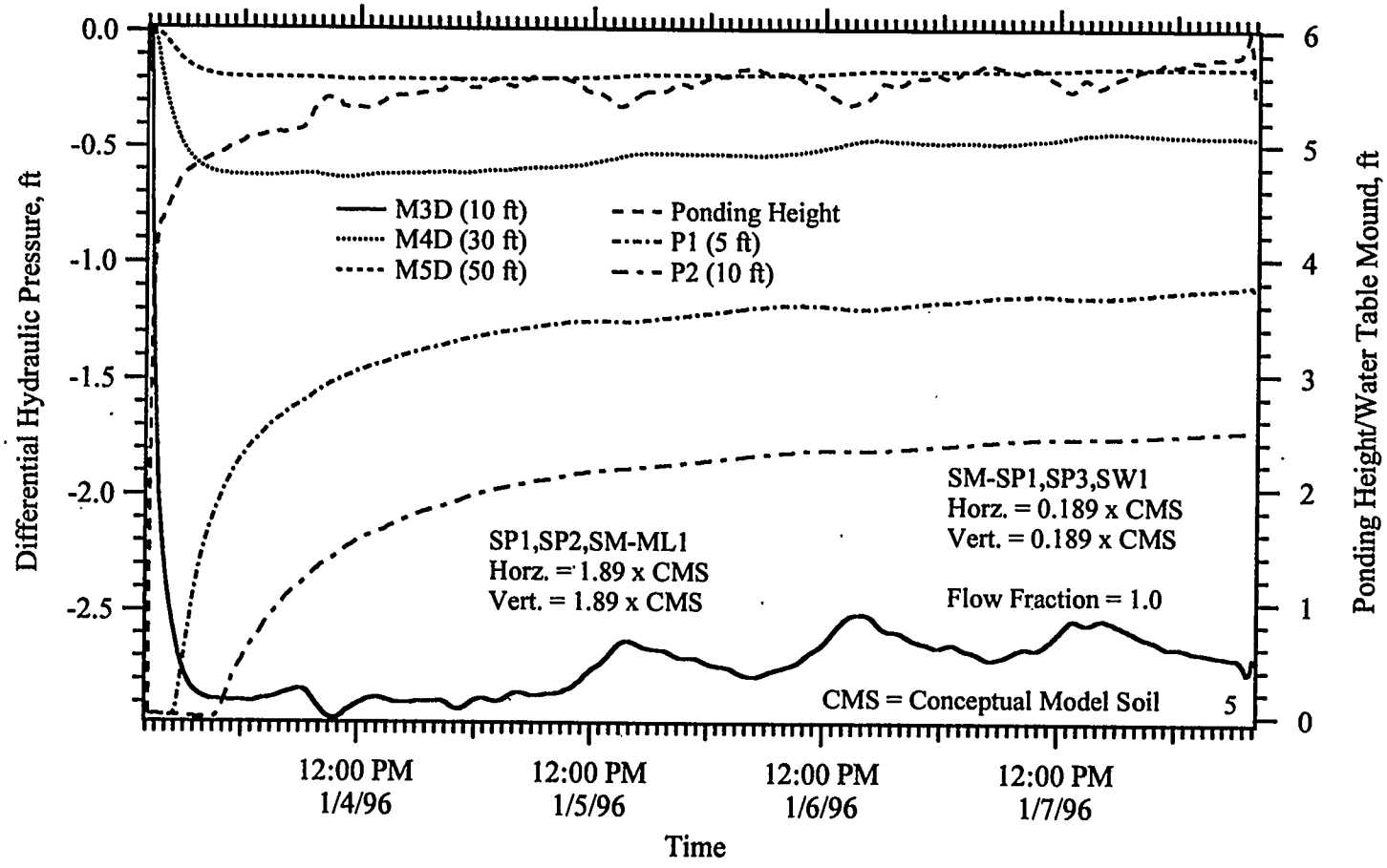

Figure C.5 Differential Hydraulic Pressure Versus Time, Simulation #5 of Operational Field Test #12

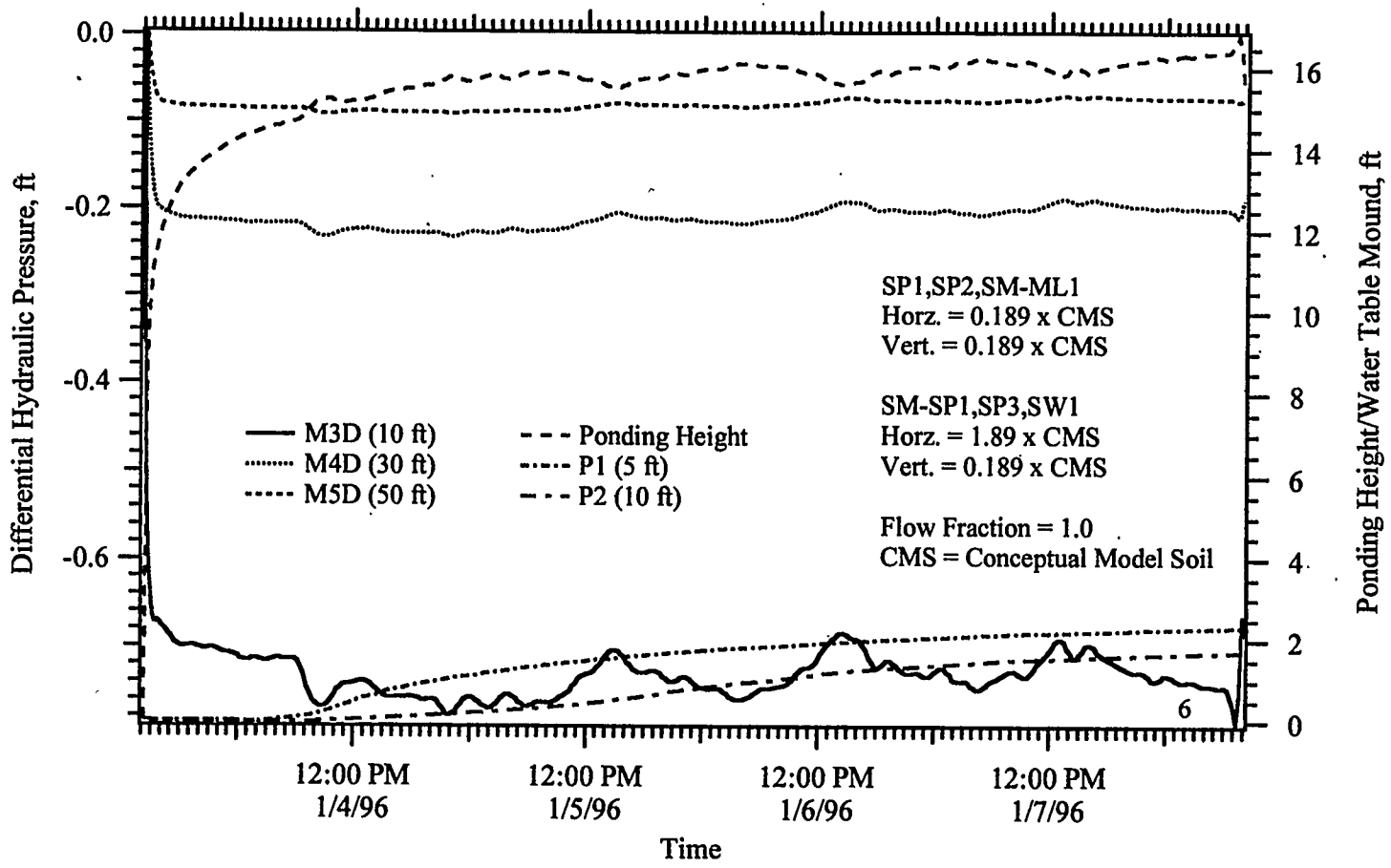

Figure C.6 Differential Hydraulic Pressure Versus Time, Simulation #6 of Operational Field Test #12

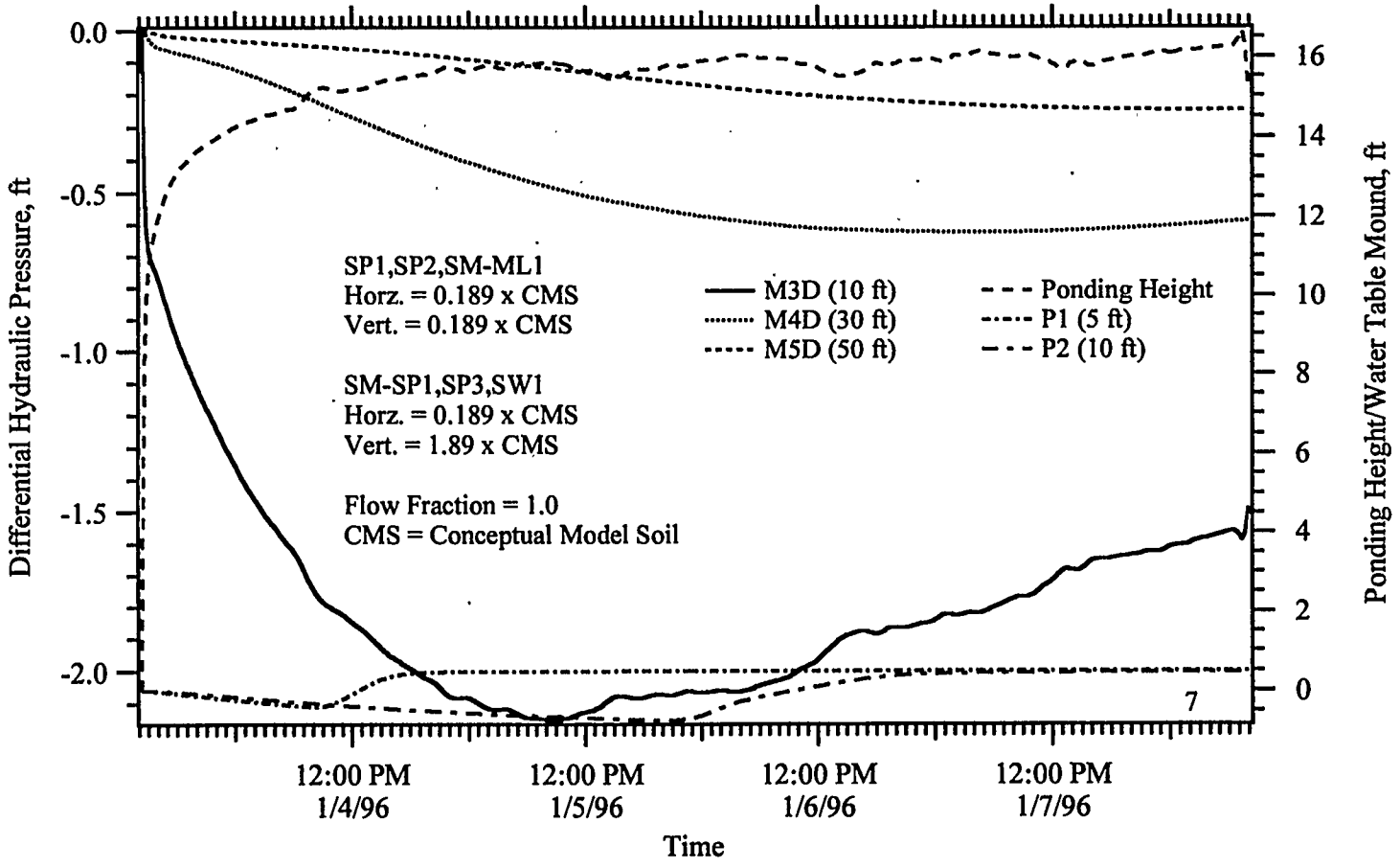

Figure C.7 Differential Hydraulic Pressure Versus Time, Simulation #7 of Operational Field Test #12

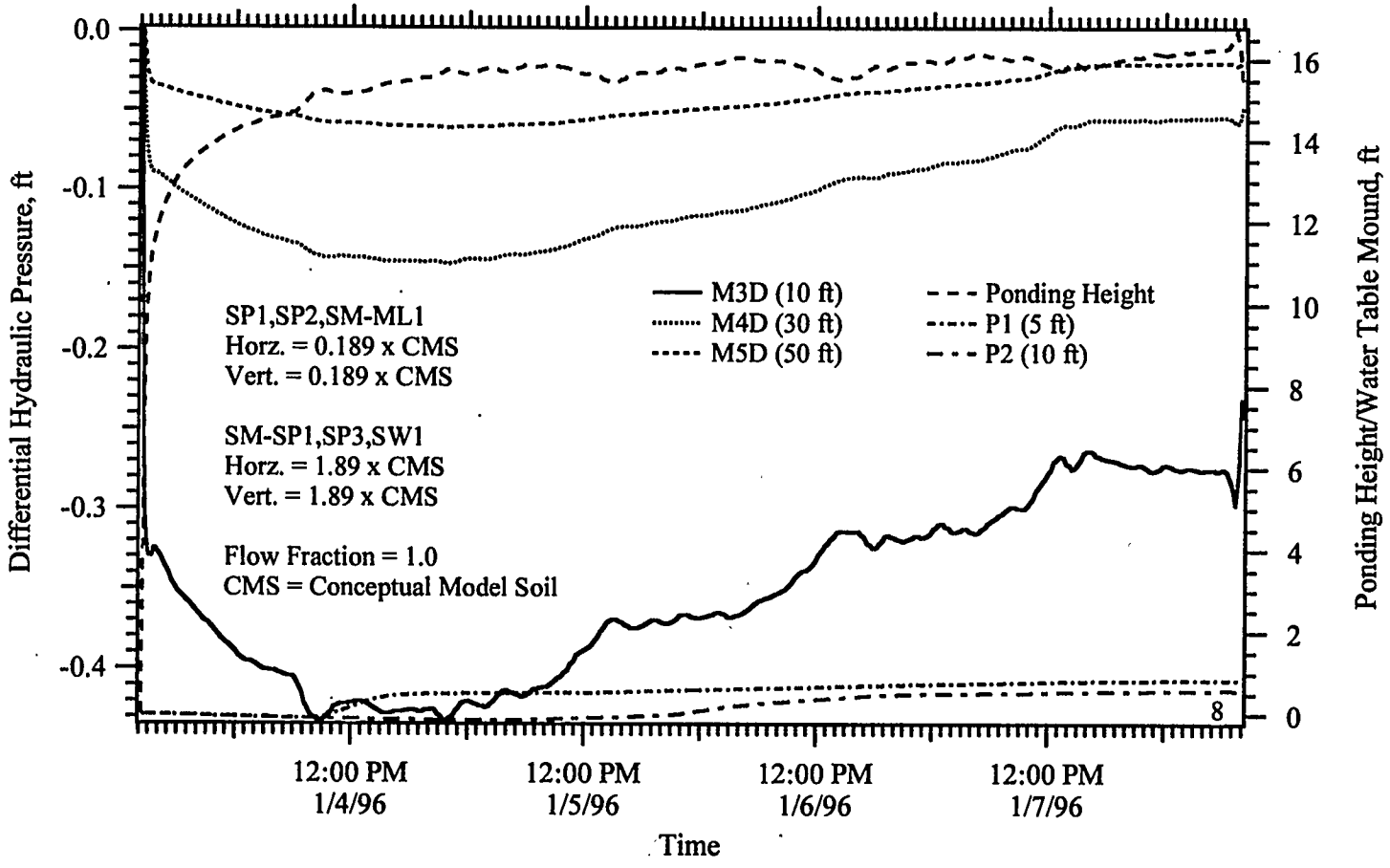

Figure C.8 Differential Hydraulic Pressure Versus Time, Simulation #8 of Operational Field Test #12

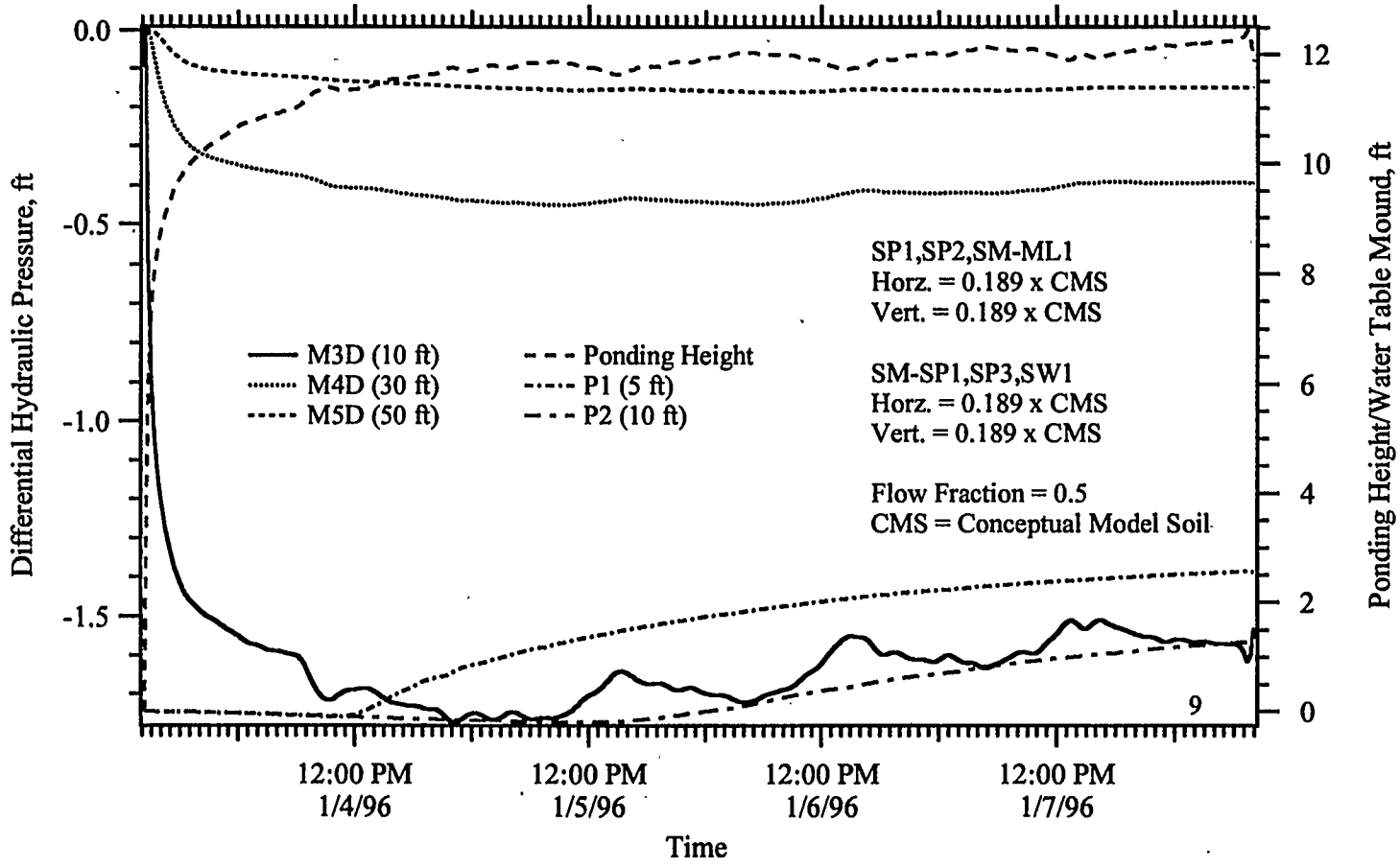

Figure C.9 Differential Hydraulic Pressure Versus Time, Simulation #9 of Operational Field Test #12

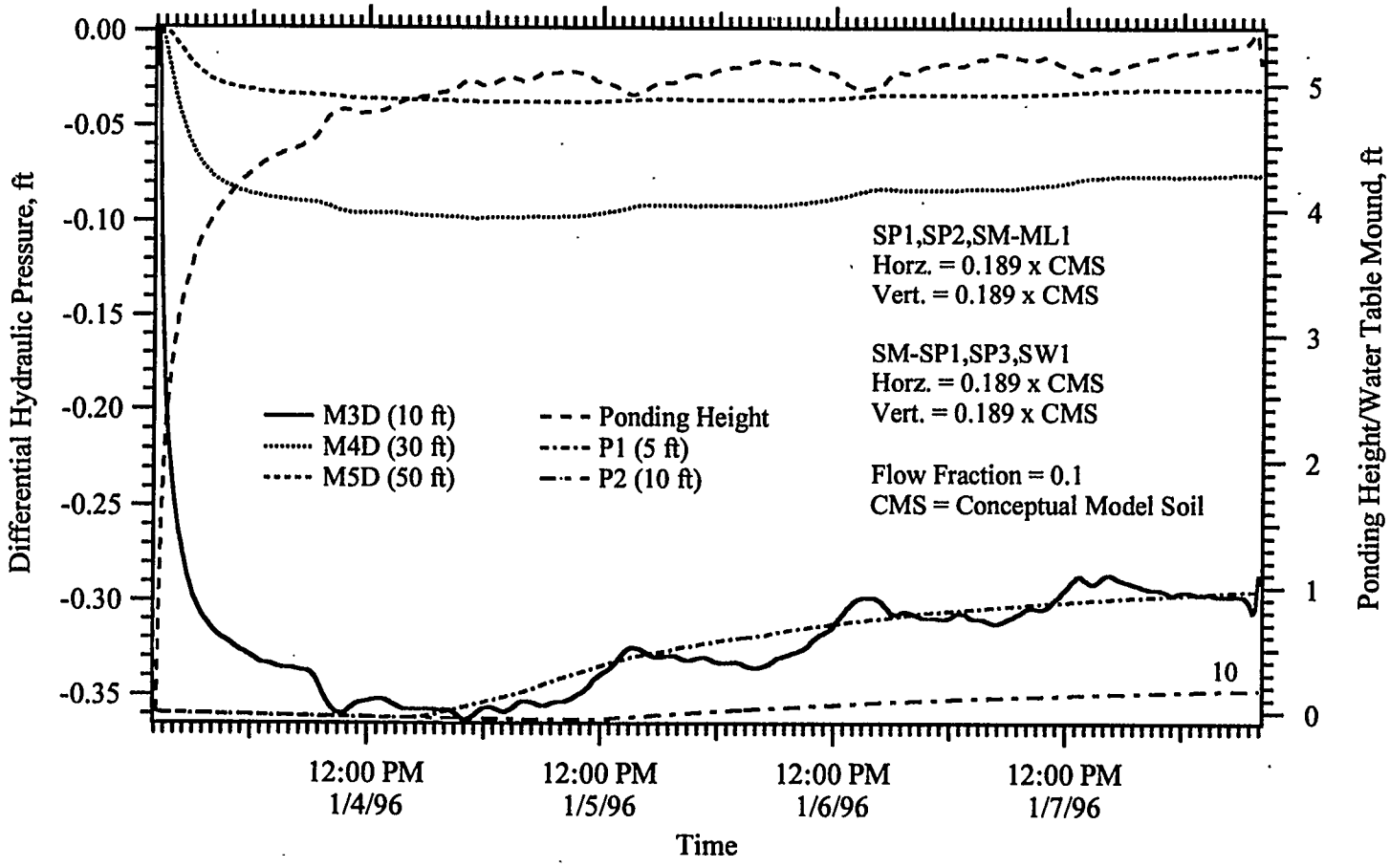

Figure C.10 Differential Hydraulic Pressure Versus Time, Simulation #10 of Operational Field Test #12

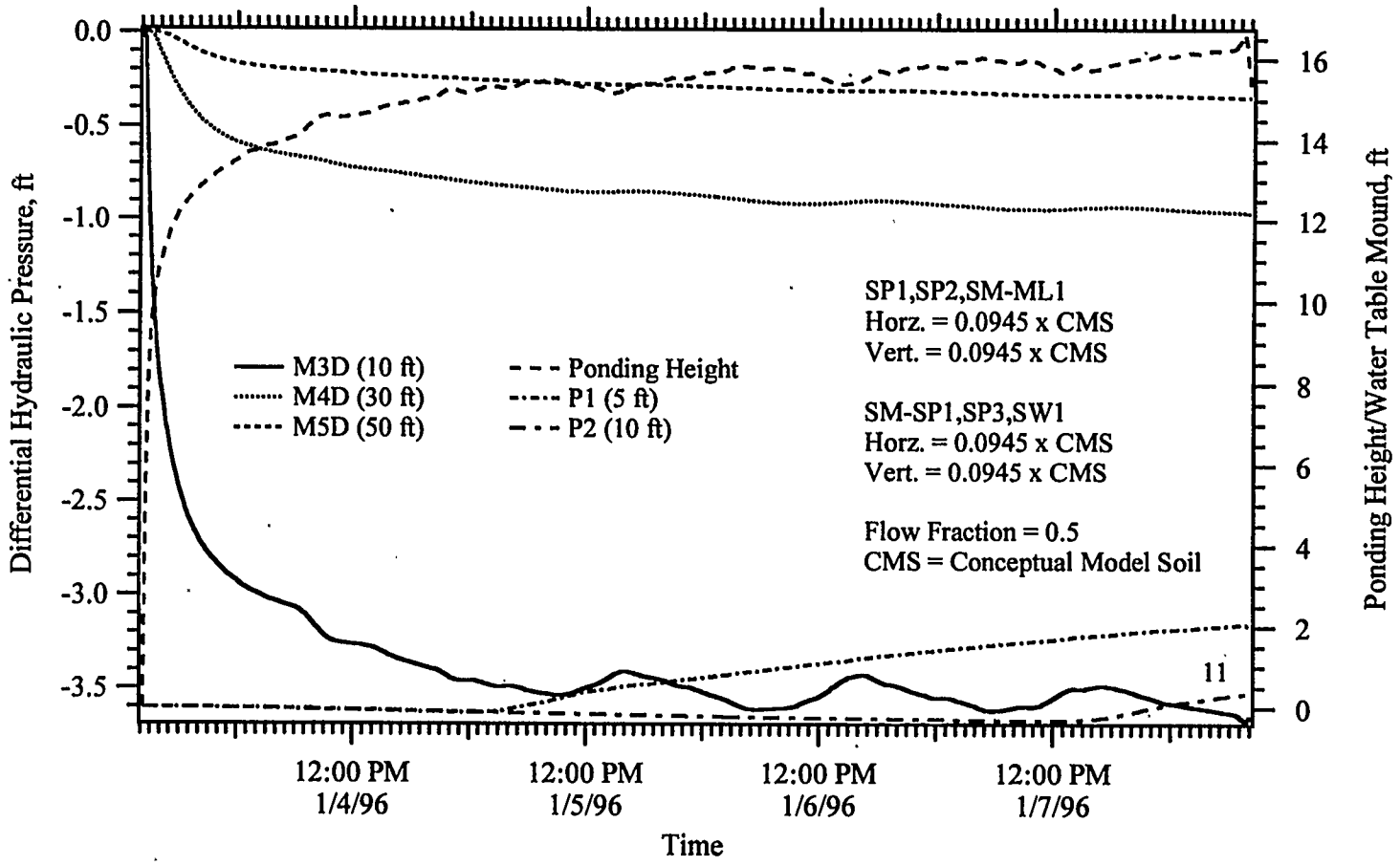

Figure C.11 Differential Hydraulic Pressure Versus Time, Simulation #11 of Operational Field Test #12

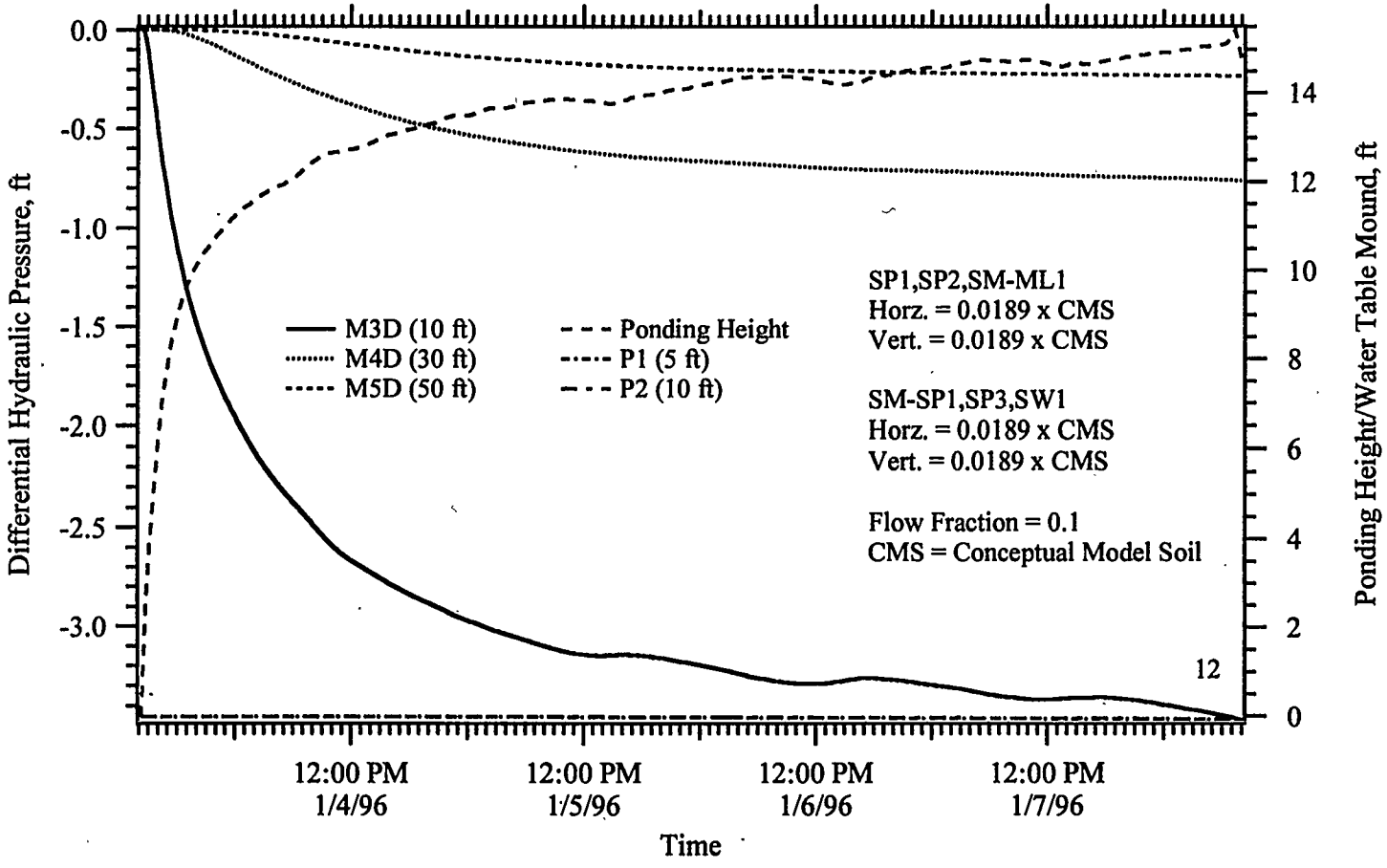

Figure C.12 Differential Hydraulic Pressure Versus Time, Simulation #12 of Operational Field Test #12

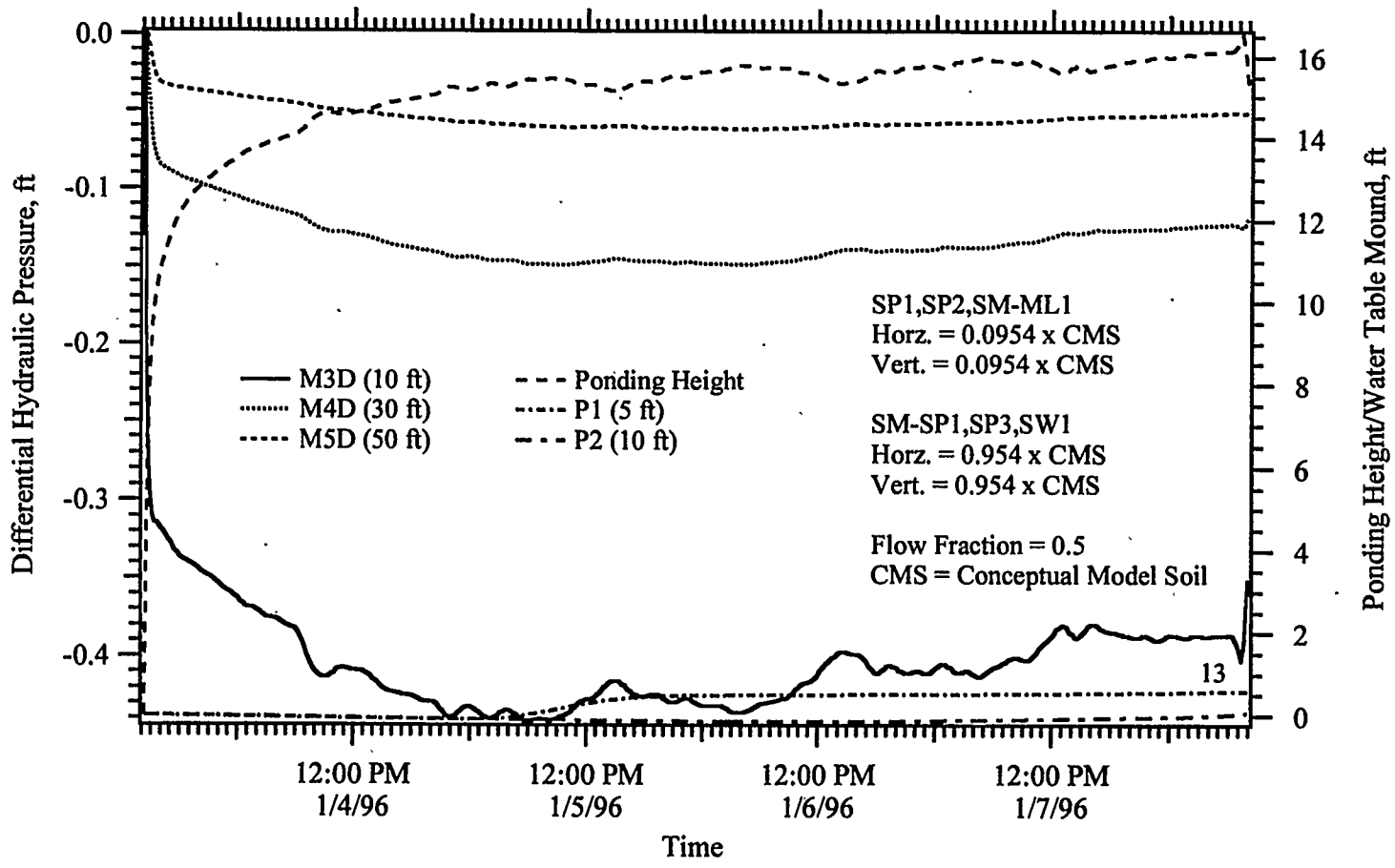

Figure C.13 Differential Hydraulic Pressure Versus Time, Simulation #13 of Operational Field Test #12

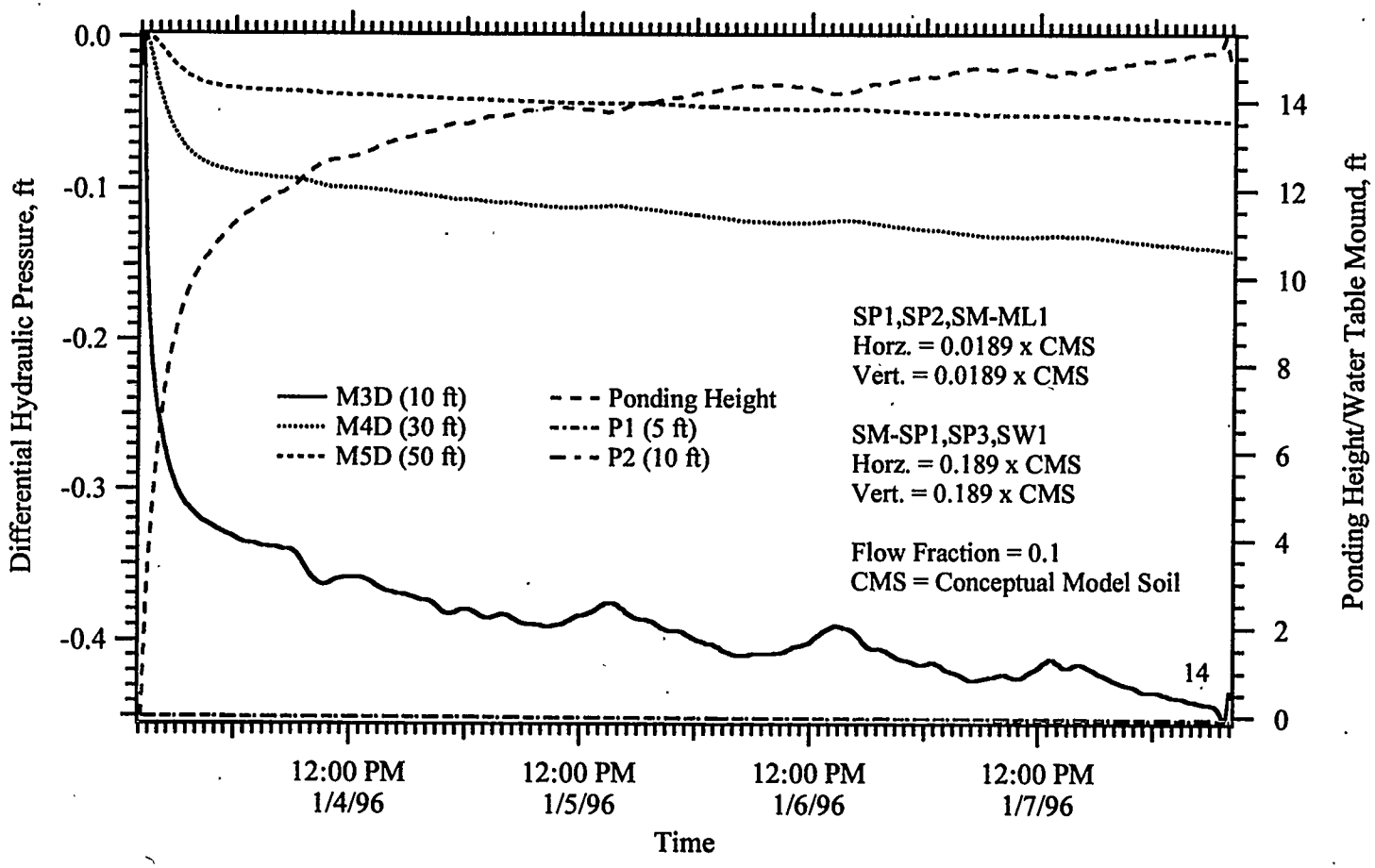

Figure C.14 Differential Hydraulic Pressure Versus Time, Simulation #14 of Operational Field Test #12

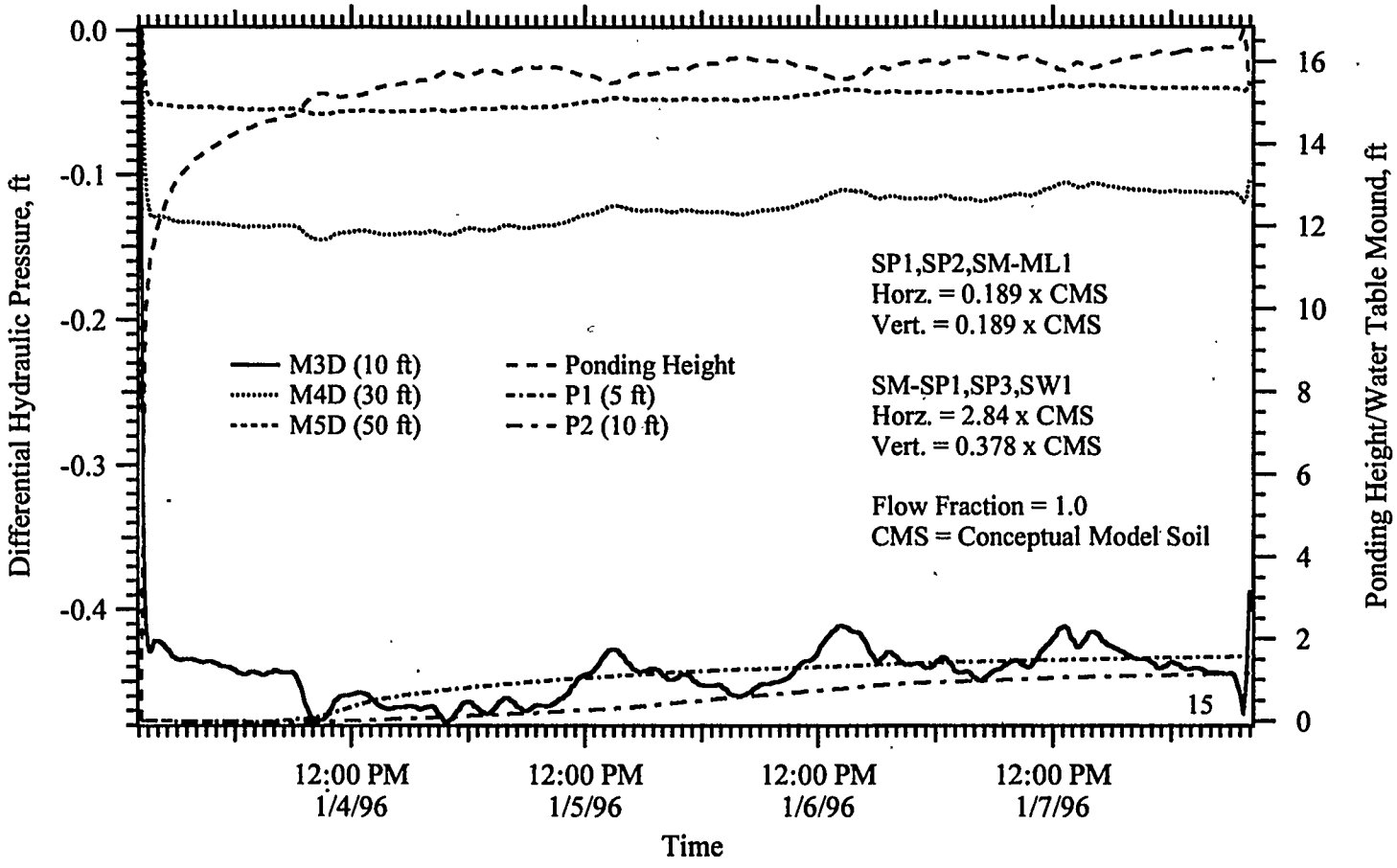

Figure C.15 Differential Hydraulic Pressure Versus Time, Simulation #15 of Operational Field Test #12

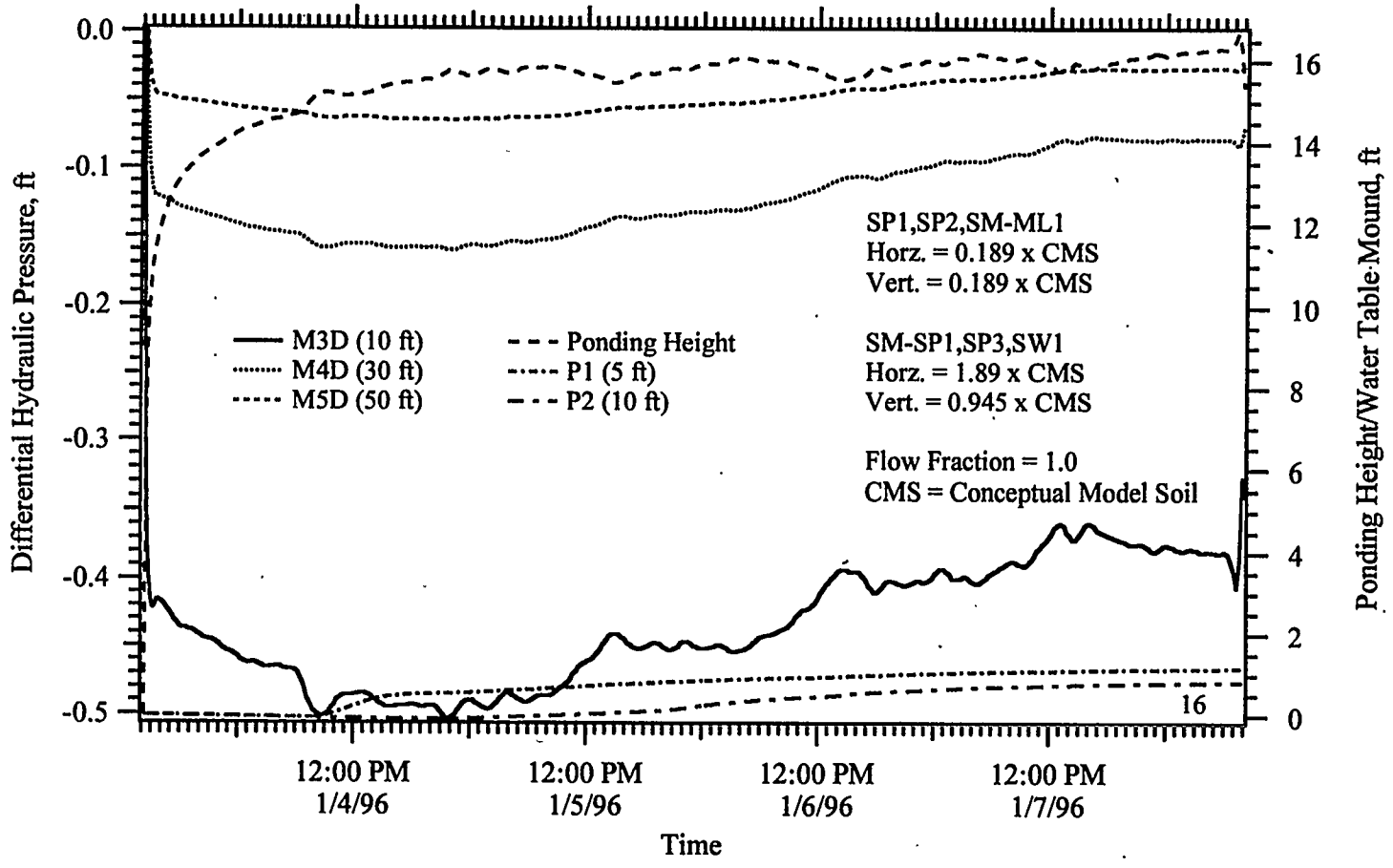

Figure C.16 Differential Hydraulic Pressure Versus Time, Simulation #16 of Operational Field Test #12

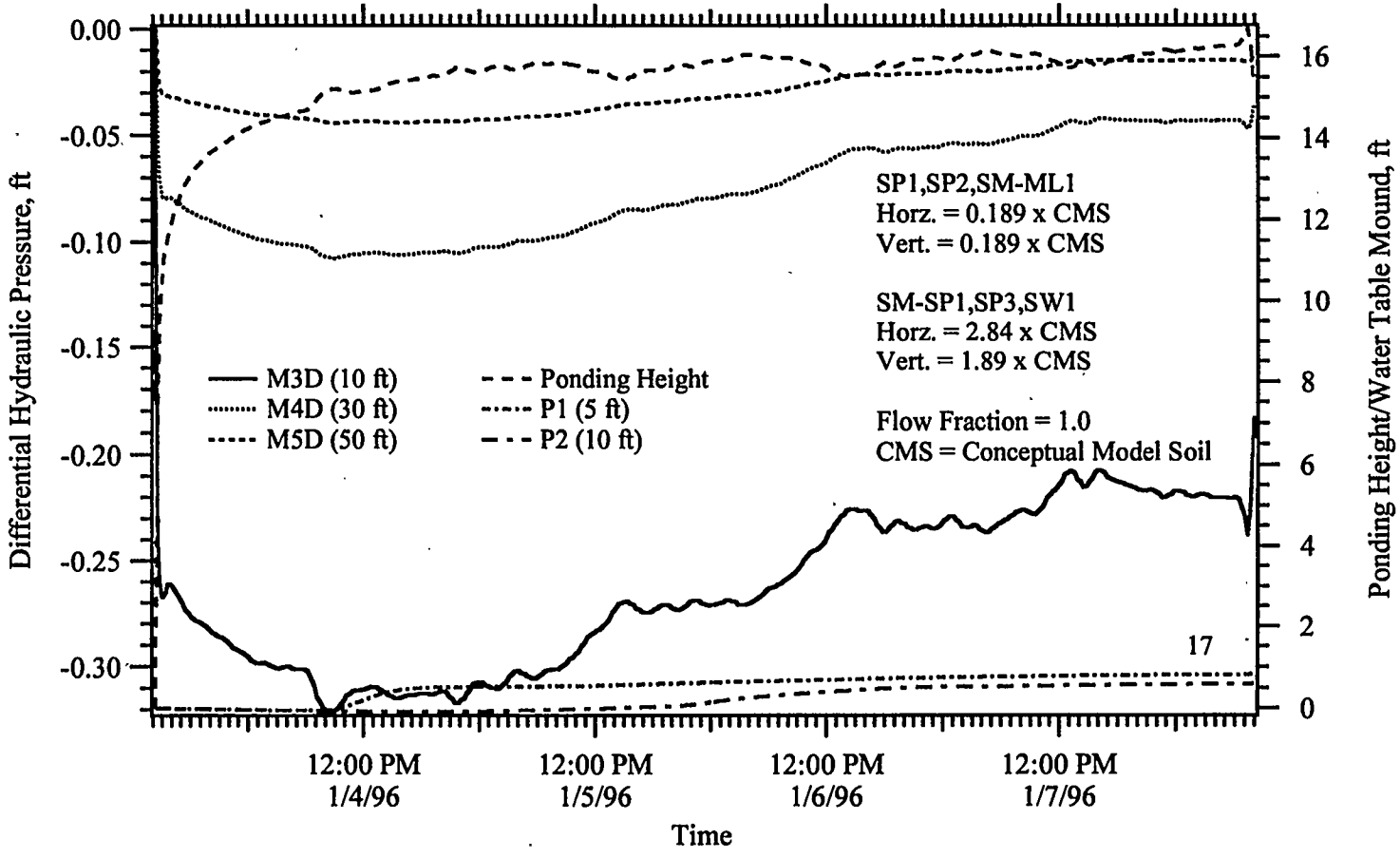

Figure C.17 Differential Hydraulic Pressure Versus Time, Simulation #17 of Operational Field Test #12

APPENDIX D

LOW-PERMEABILITY ISOTROPIC SIMULATION RESULTS

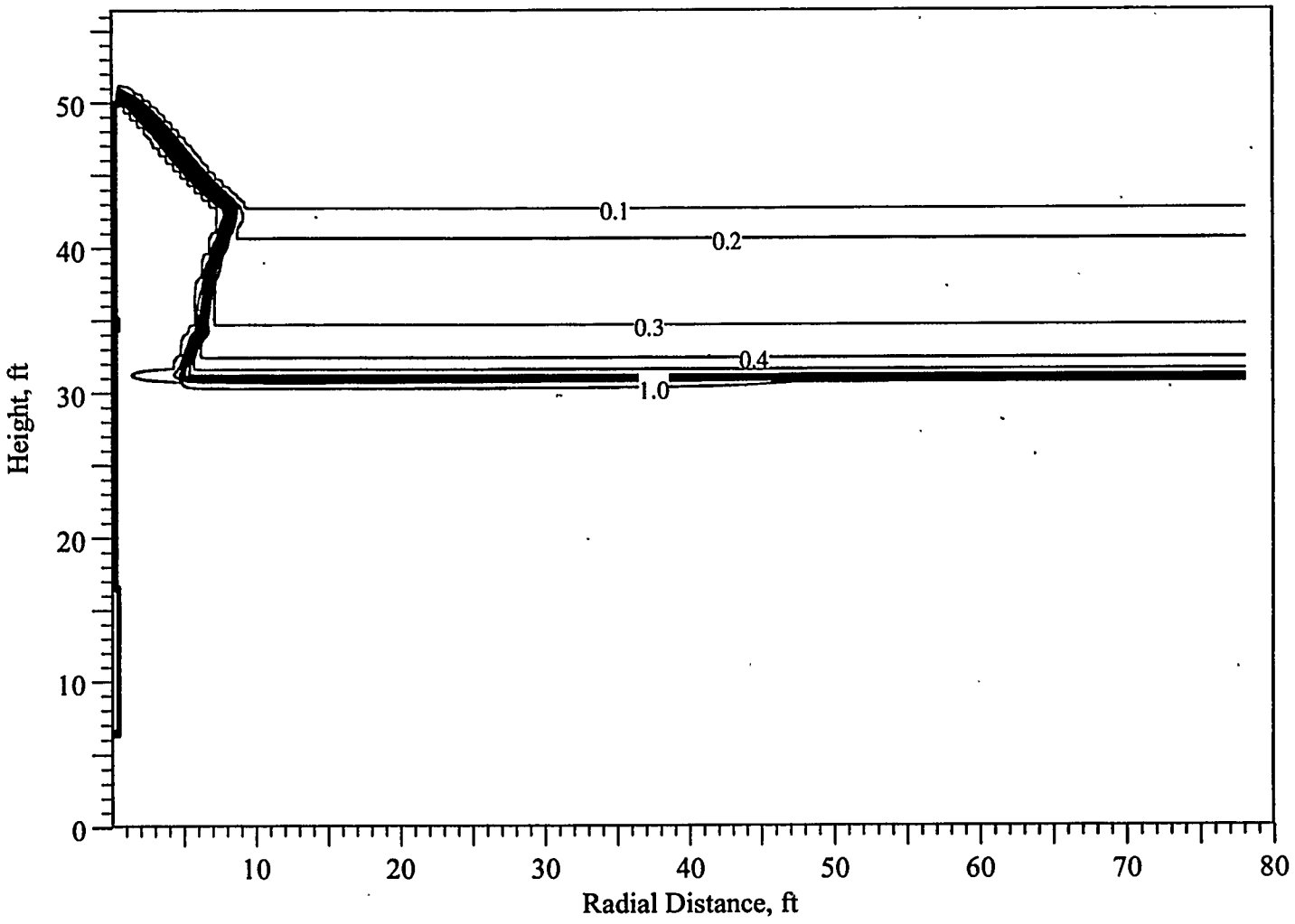

Figure D.1 Saturation Profile at 1 Day, Simulation LPI
(Operational Field Test #13, January 17, 1996)

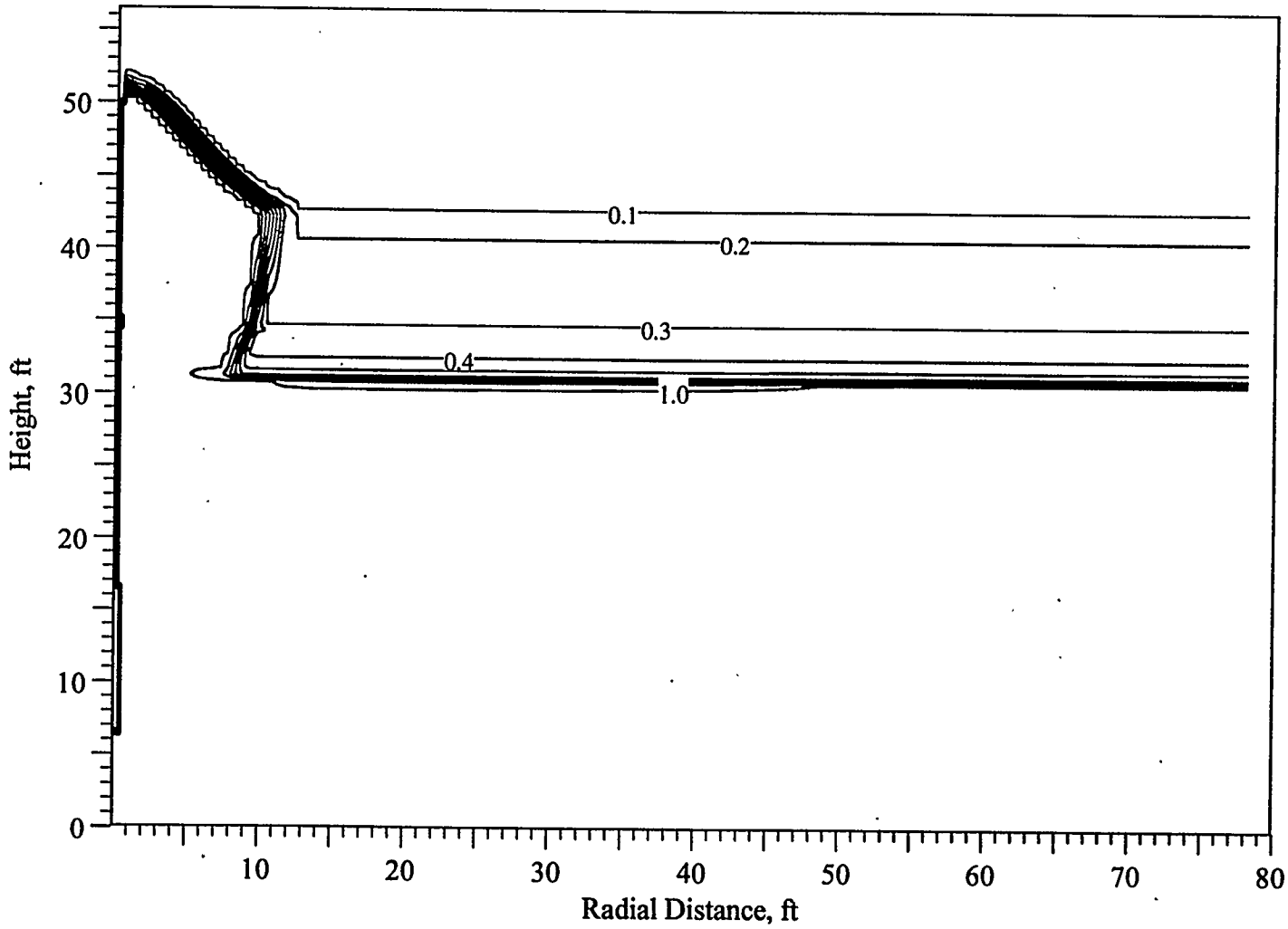

Figure D.2 Saturation Profile at 2 Days, Simulation LPI
(Operational Field Test #13, January 18, 1996)

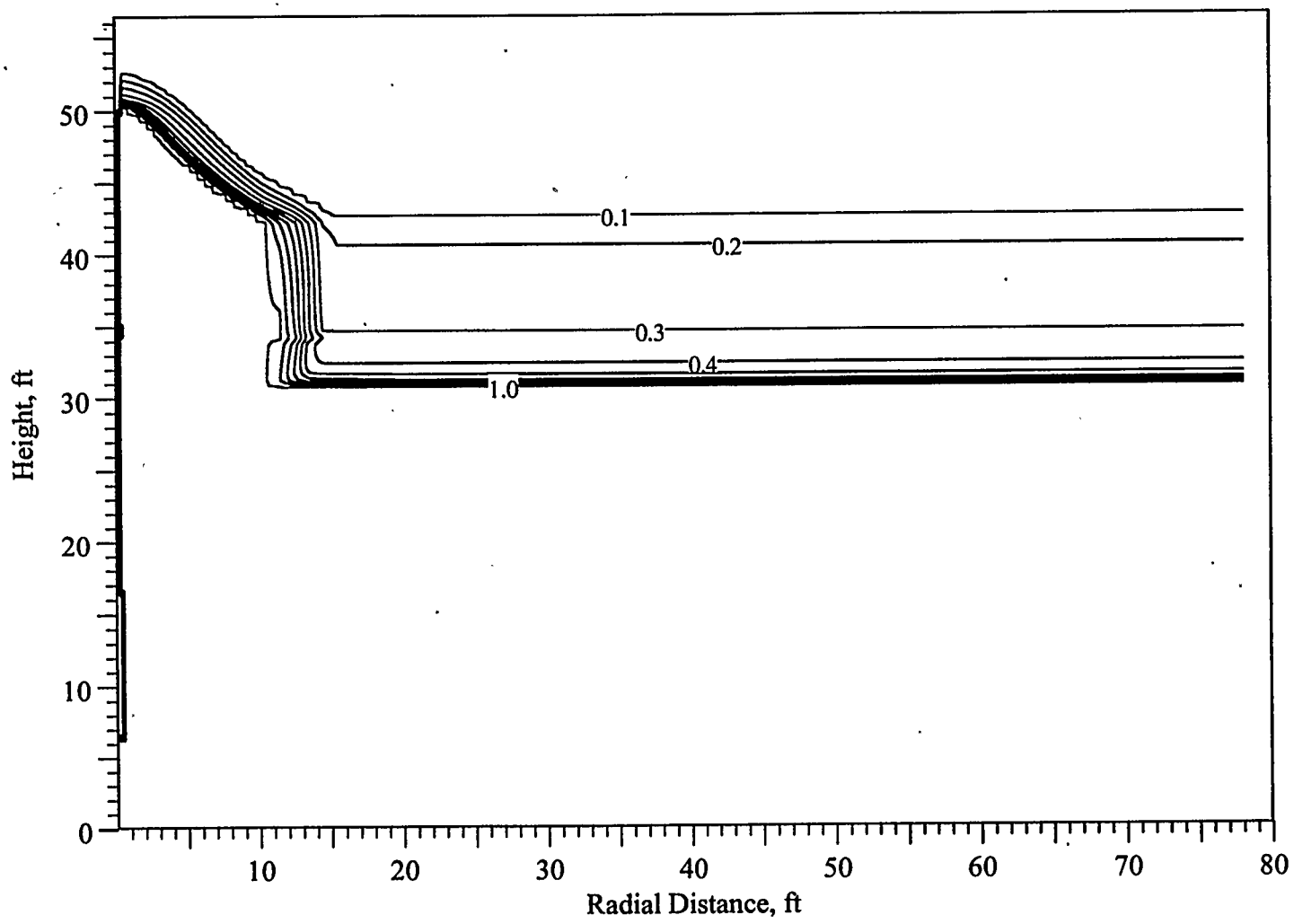

Figure D.3 Saturation Profile at 4 Days, Simulation LPI
(Operational Field Test #13, January 20, 1996)

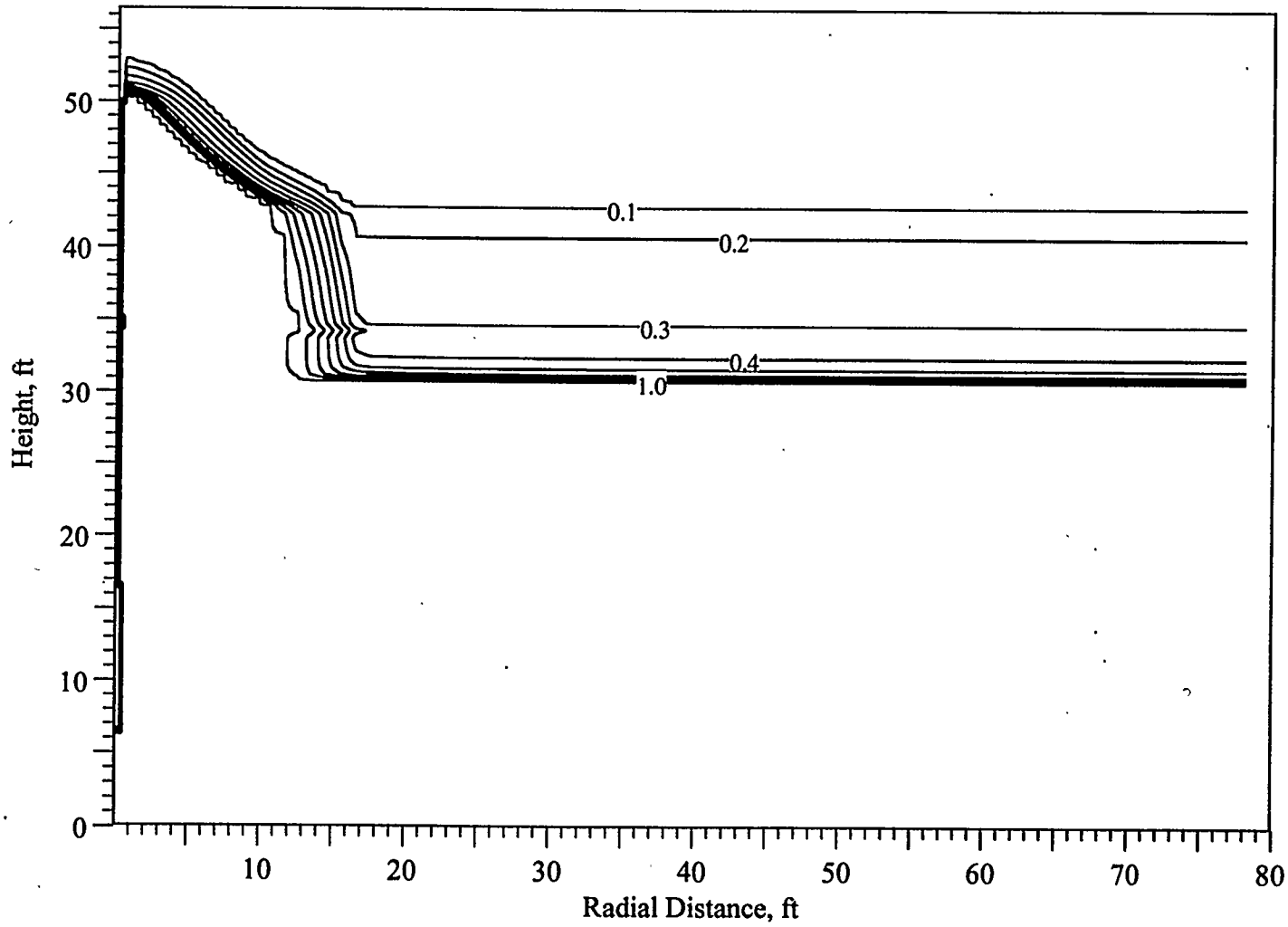

Figure D.4 Saturation Profile at 8 Days, Simulation LPI
(Operational Field Test #13, January 24, 1996)

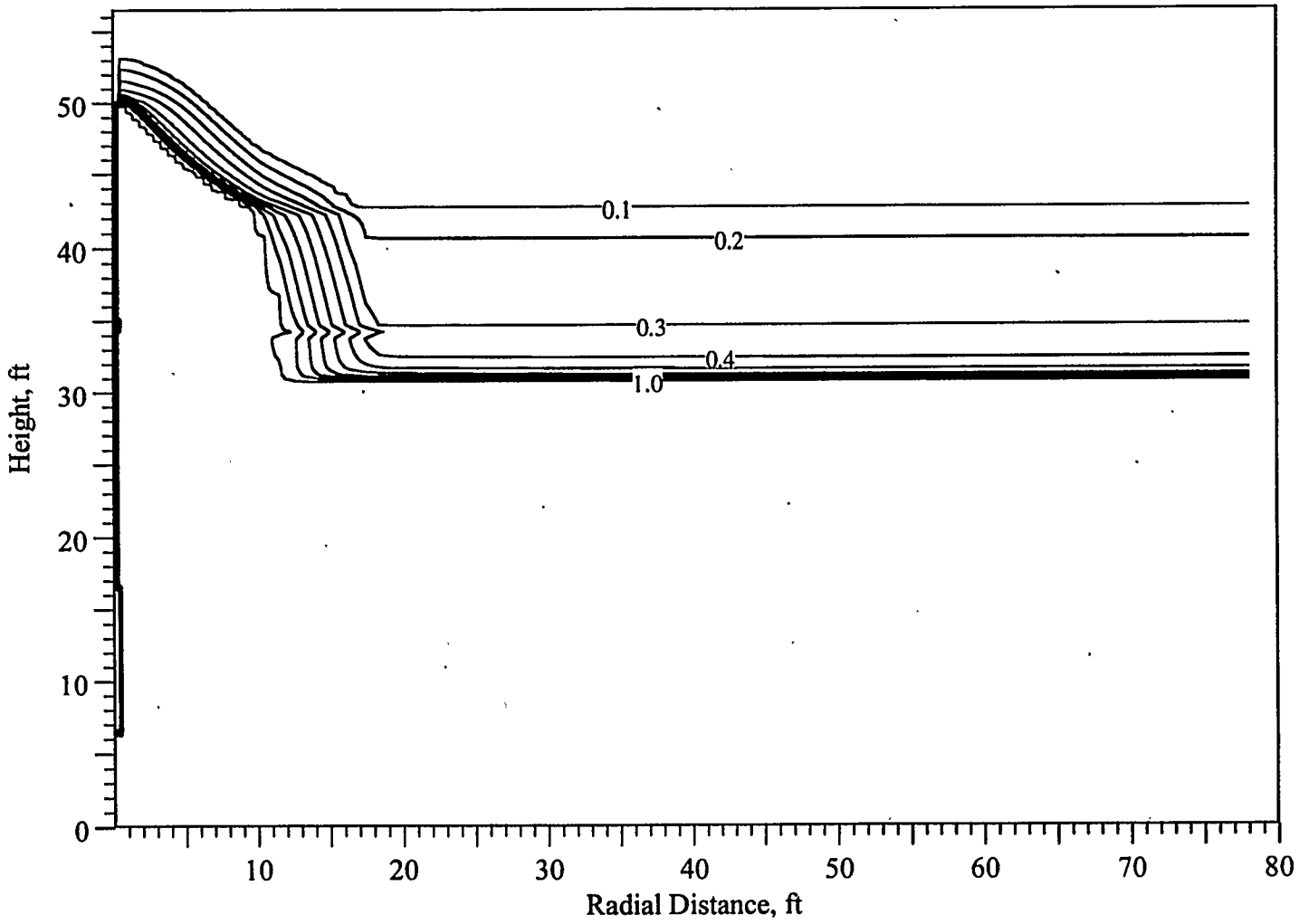

Figure D.5 Saturation Profile at 16 Days, Simulation LPI
(Operational Field Test #13, February 1, 1996)

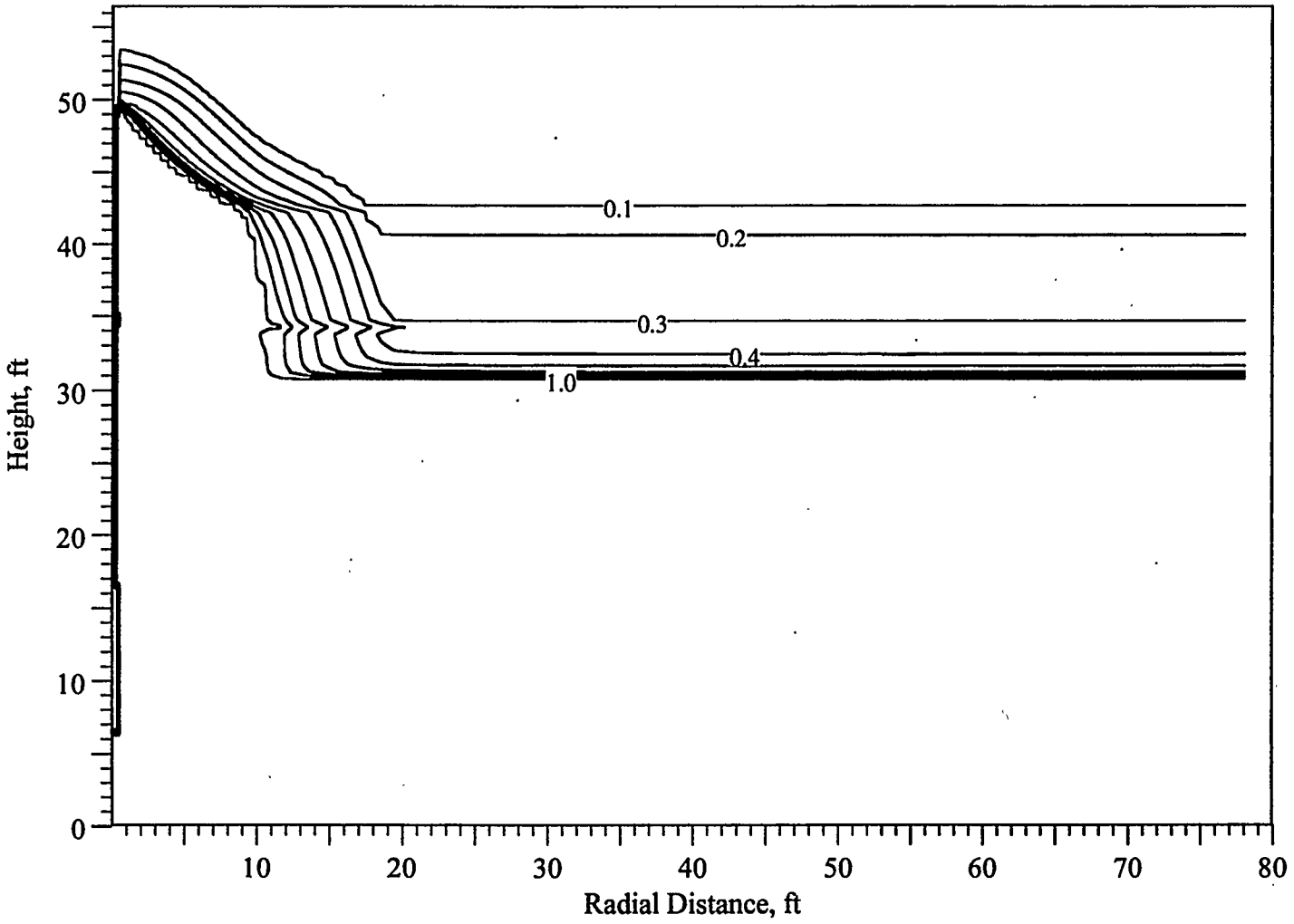

Figure D.6 Saturation Profile at 32 Days, Simulation LPI
(Operational Field Test #13, February 17, 1996)

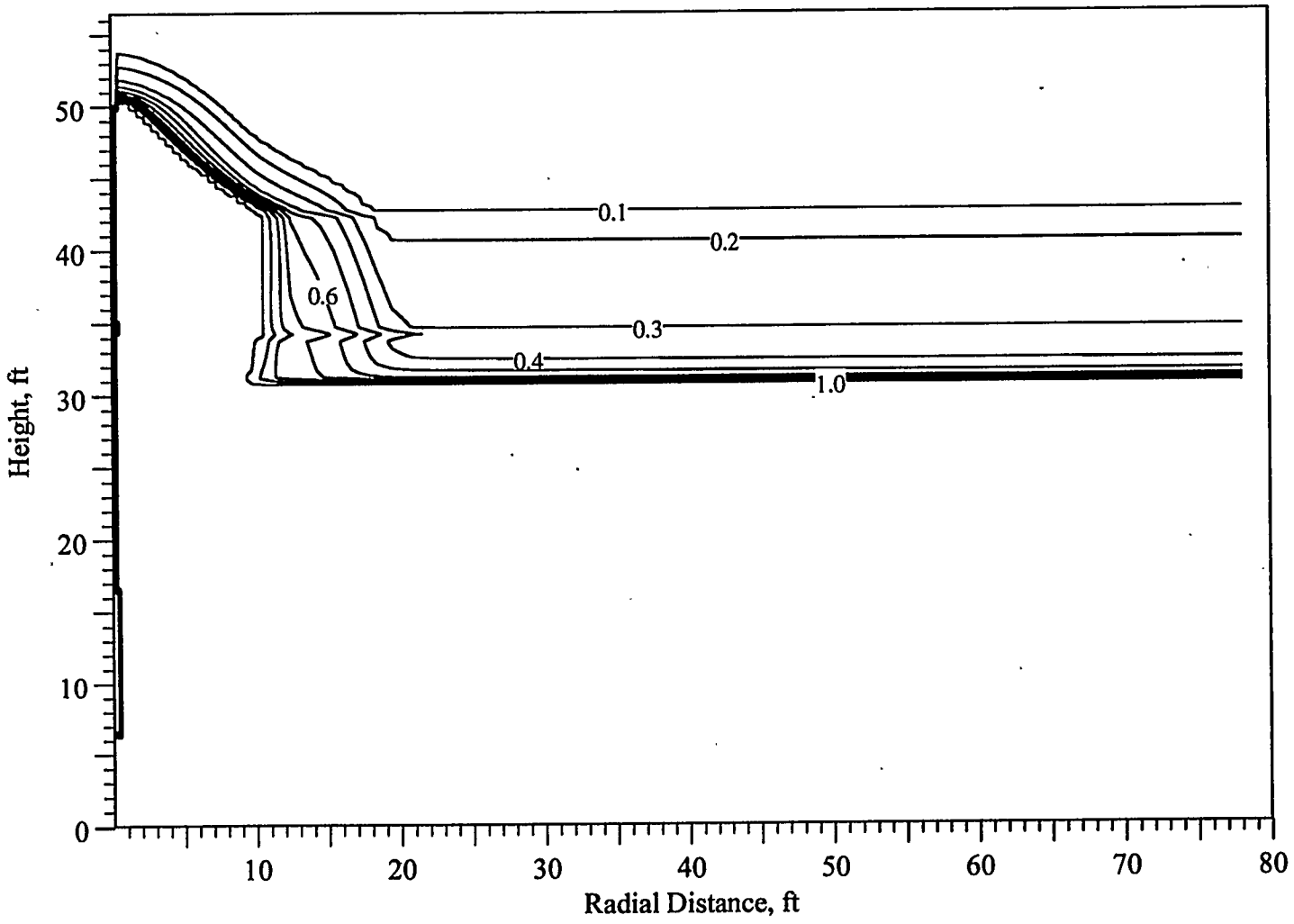

Figure D.7 Saturation Profile at 63 Days, Simulation LPI
(Operational Field Test #13, March 19, 1996)

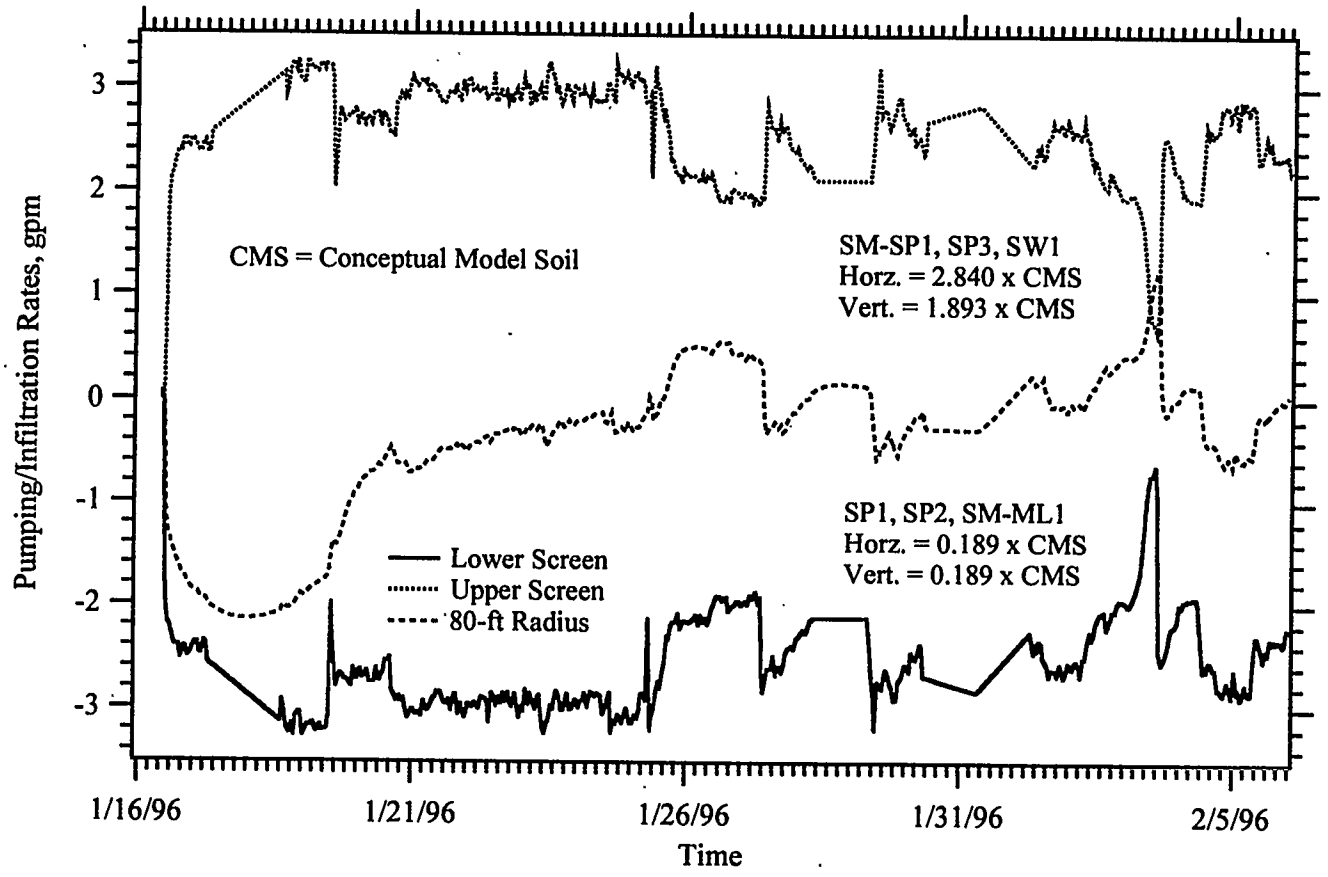

Figure D.8 Pumping/Infiltration Rates Versus Time, Simulation LPI
(Operational Field Test #13, January 16, 1996 - February 6, 1996)

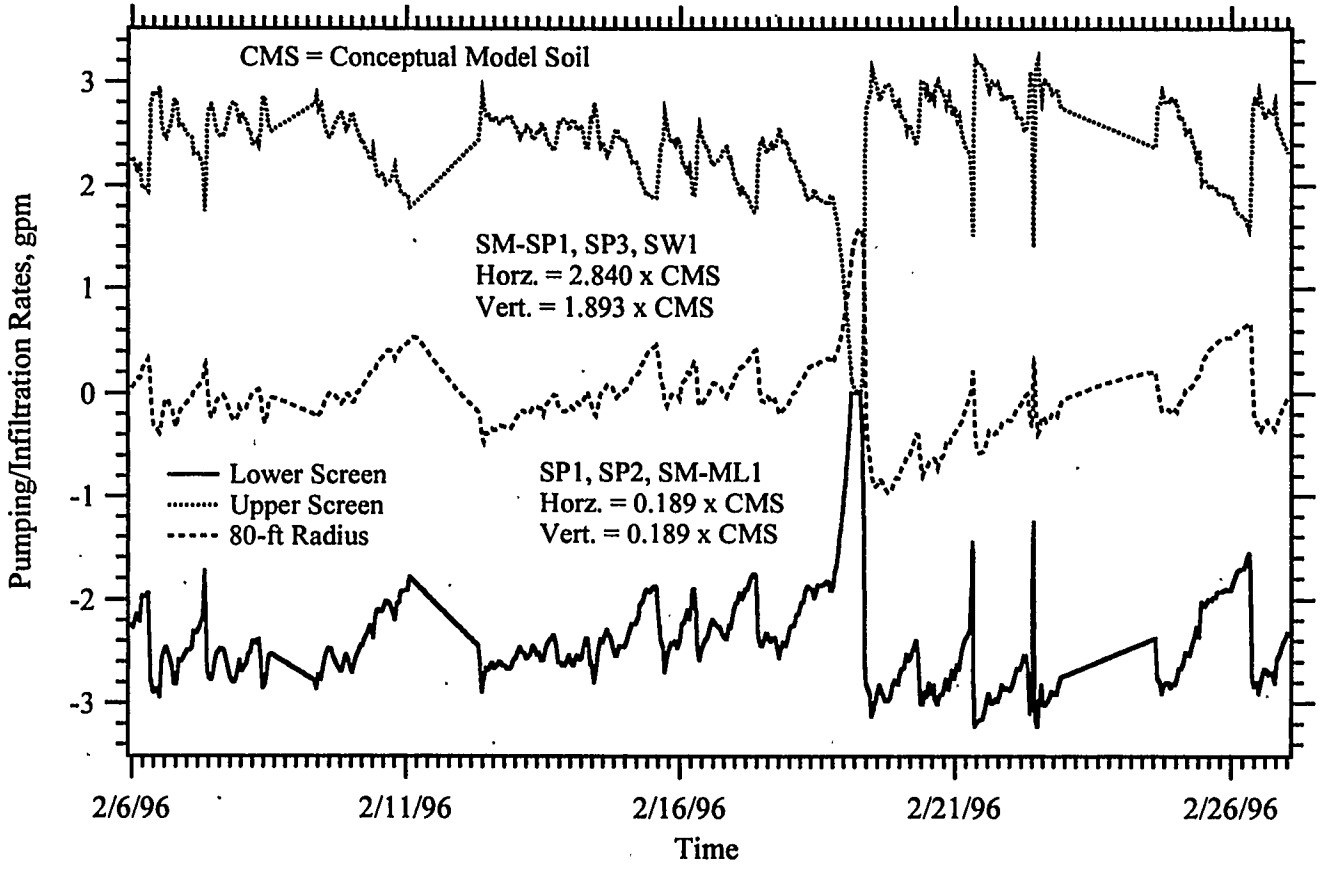

Figure D.9 Pumping/Infiltration Rates Versus Time, Simulation LPI
(Operational Field Test #13, February 6, 1996 - February 27, 1996)

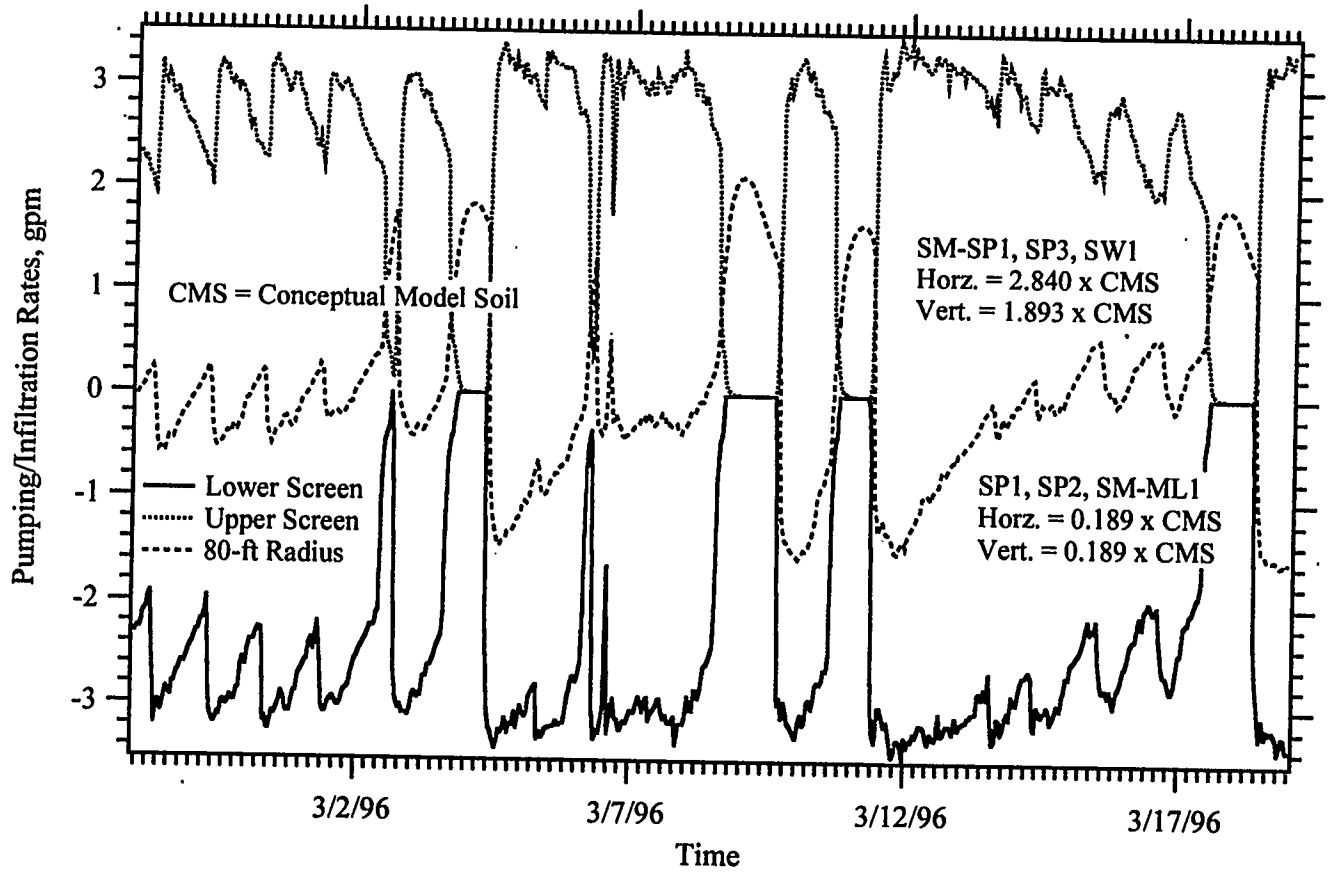

Figure D.10 Pumping/Infiltration Rates Versus Time, Simulation LPI
(Operational Field Test #13, February 27, 1996 - March 19, 1996)

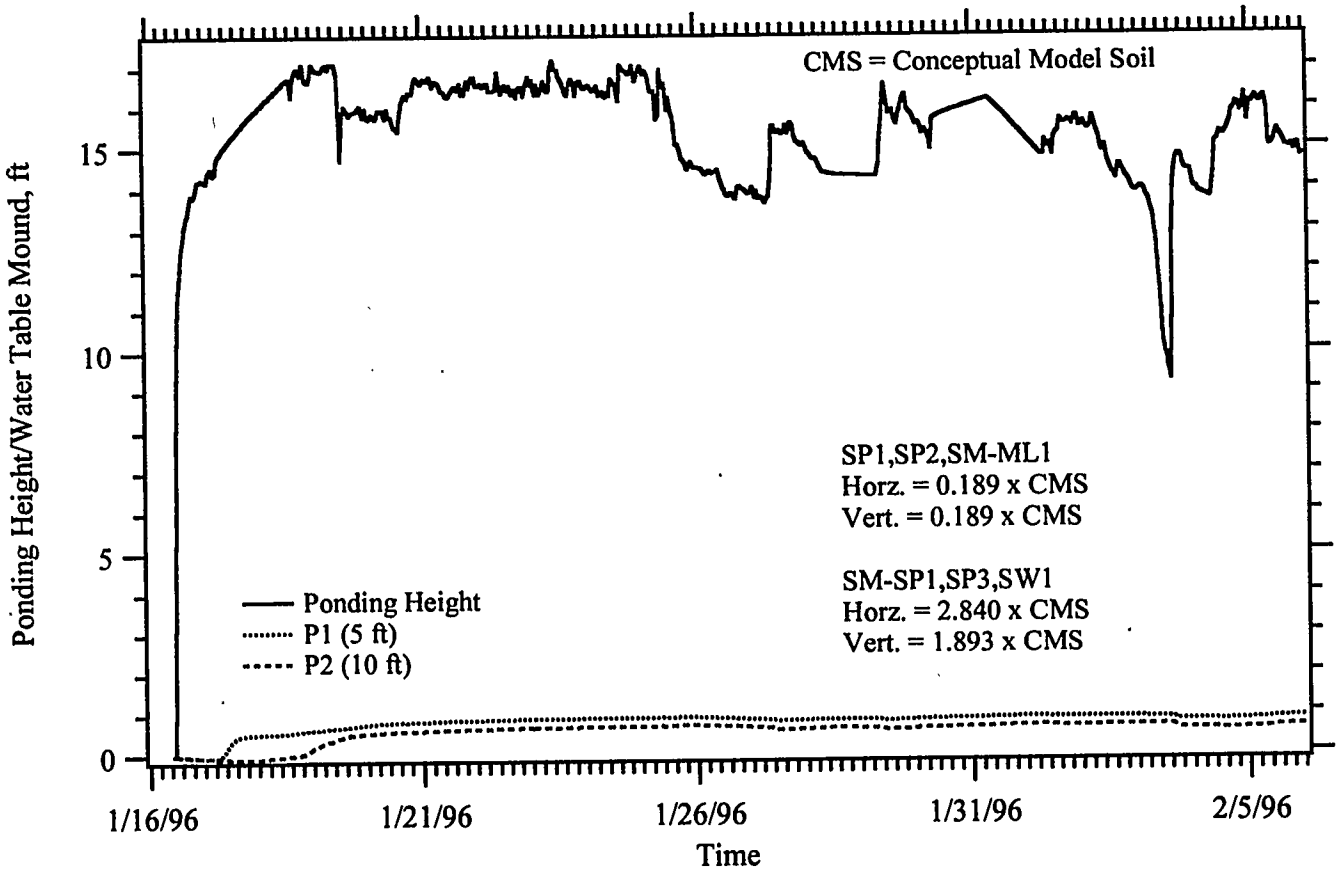

Figure D.11 Ponding Height/Water Table Mound Versus Time, Simulation LPI
(Operational Field Test #13, January 16, 1996 - February 6, 1996)

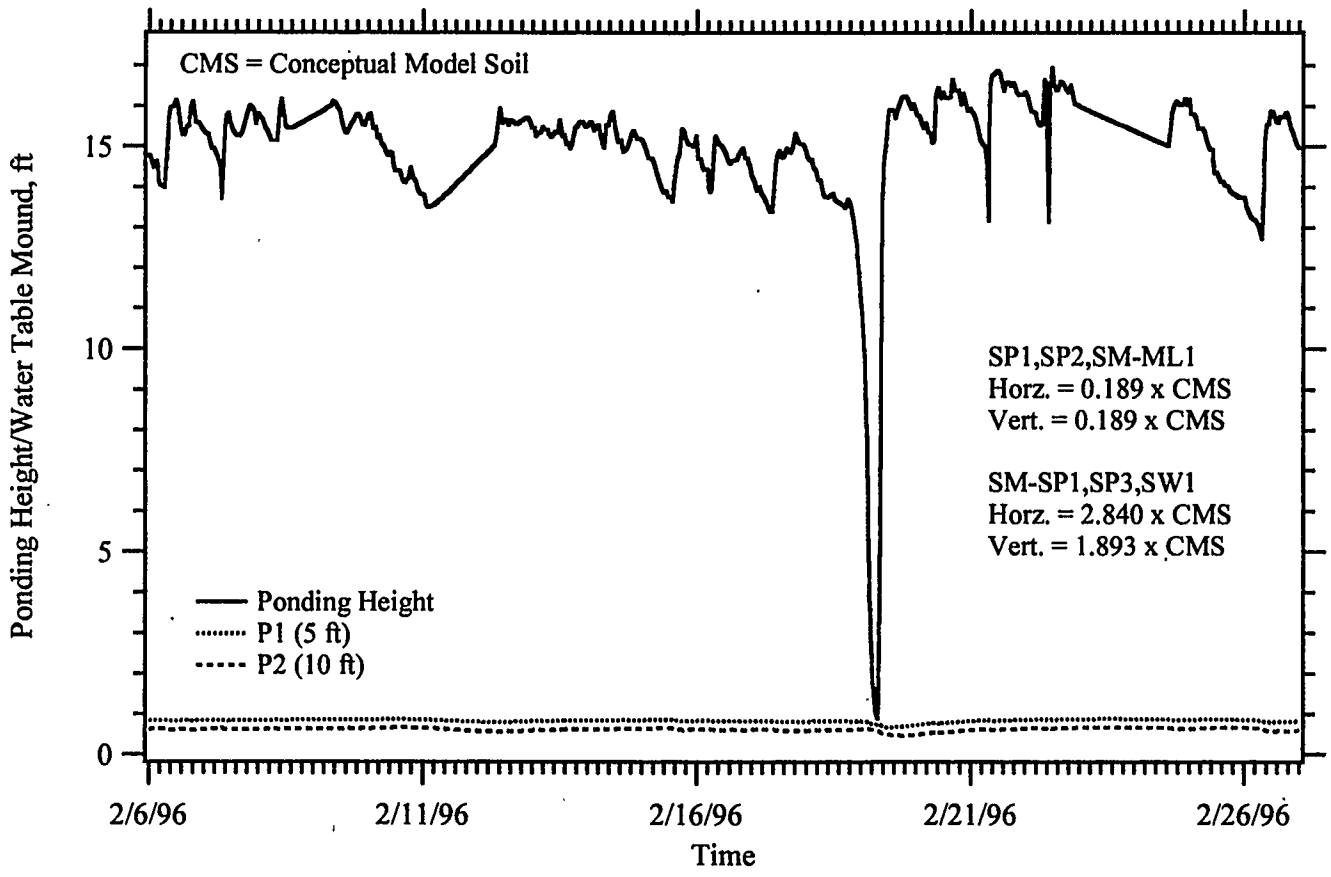

Figure D.12 Ponding Height/Water Table Mound Versus Time, Simulation LPI
(Operational Field Test #13, February 6, 1996 - February 27, 1996)

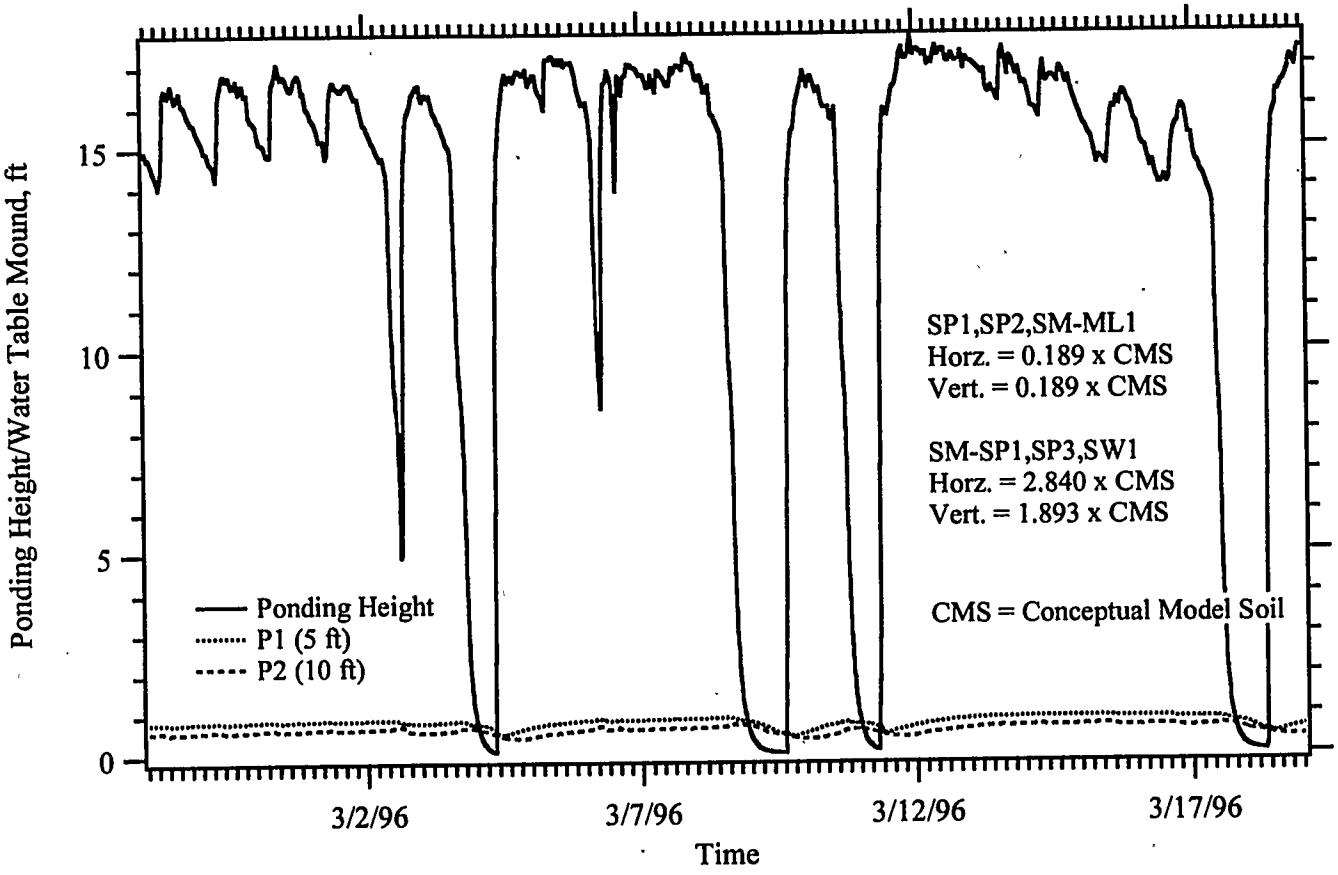

Figure D.13 Ponding Height/Water Table Mound Versus Time, Simulation LPI
(Operational Field Test #13, February 27, 1996 - March 19, 1996)

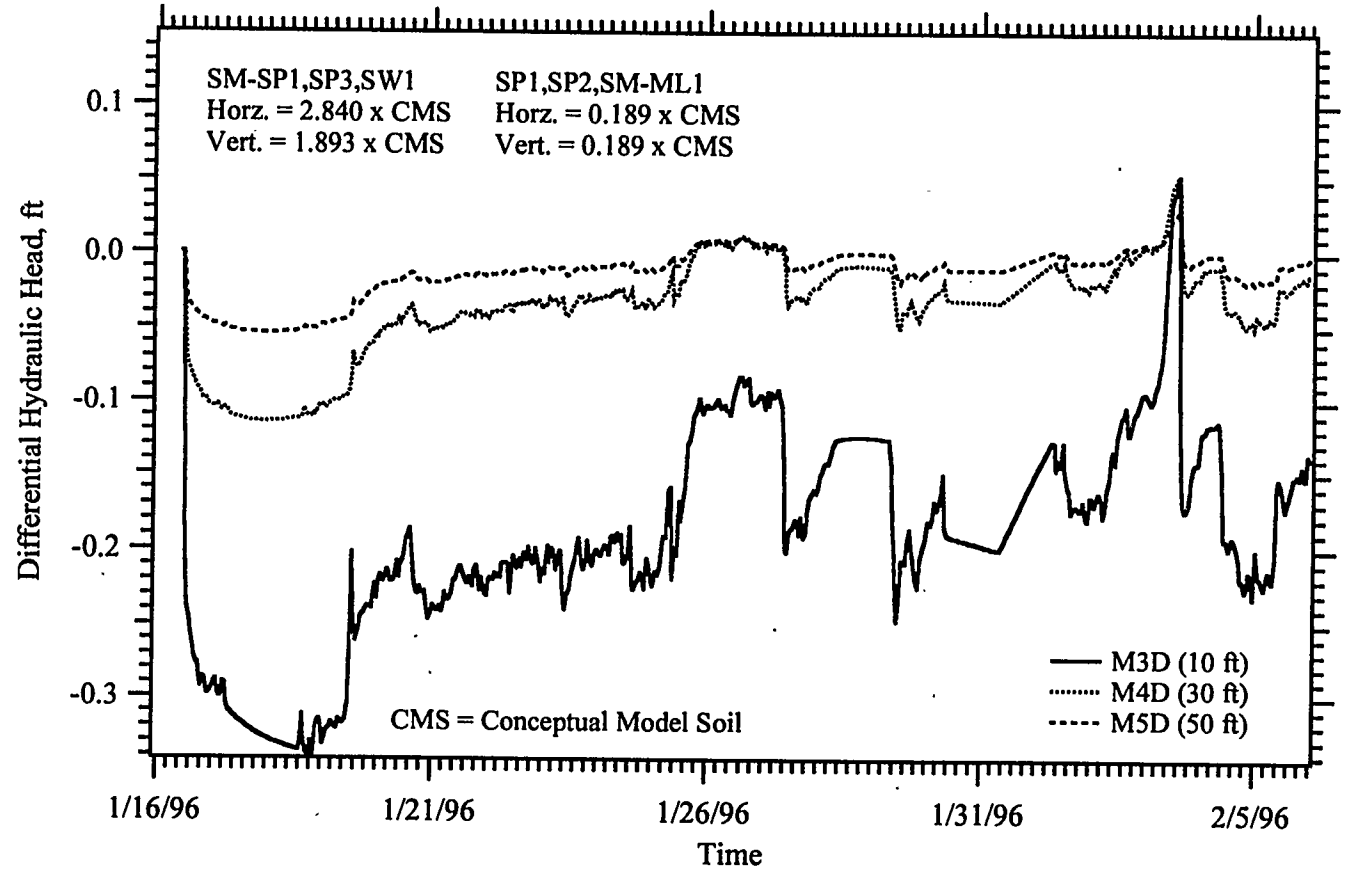

Figure D.14 Differential Hydraulic Pressure Versus Time, Simulation LPI
(Operational Field Test #13, January 16, 1996 - February 6, 1996)

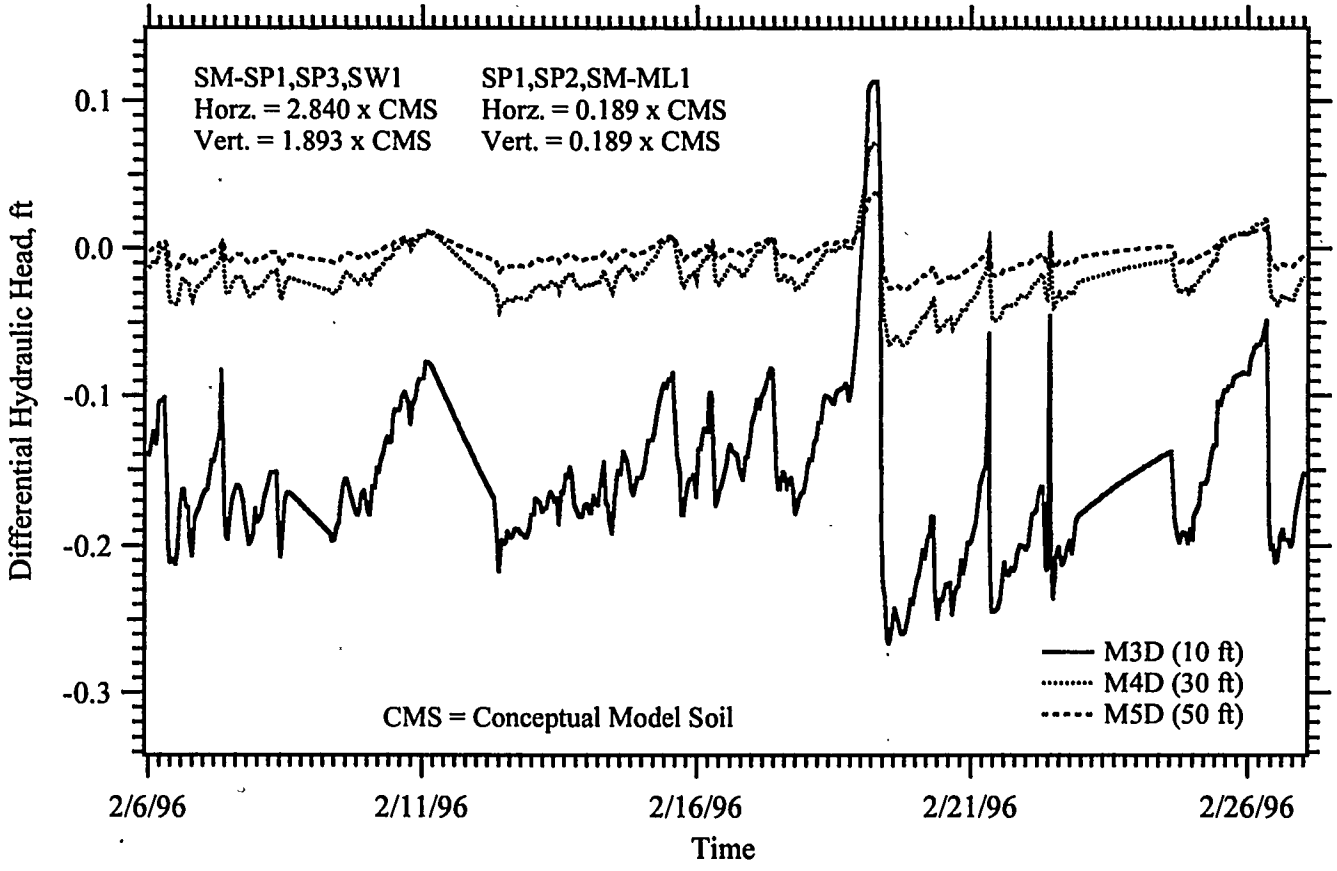

Figure D.15 Differential Hydraulic Pressure Versus Time, Simulation LPI
(Operational Field Test #13, February 6, 1996 - February 27, 1996)

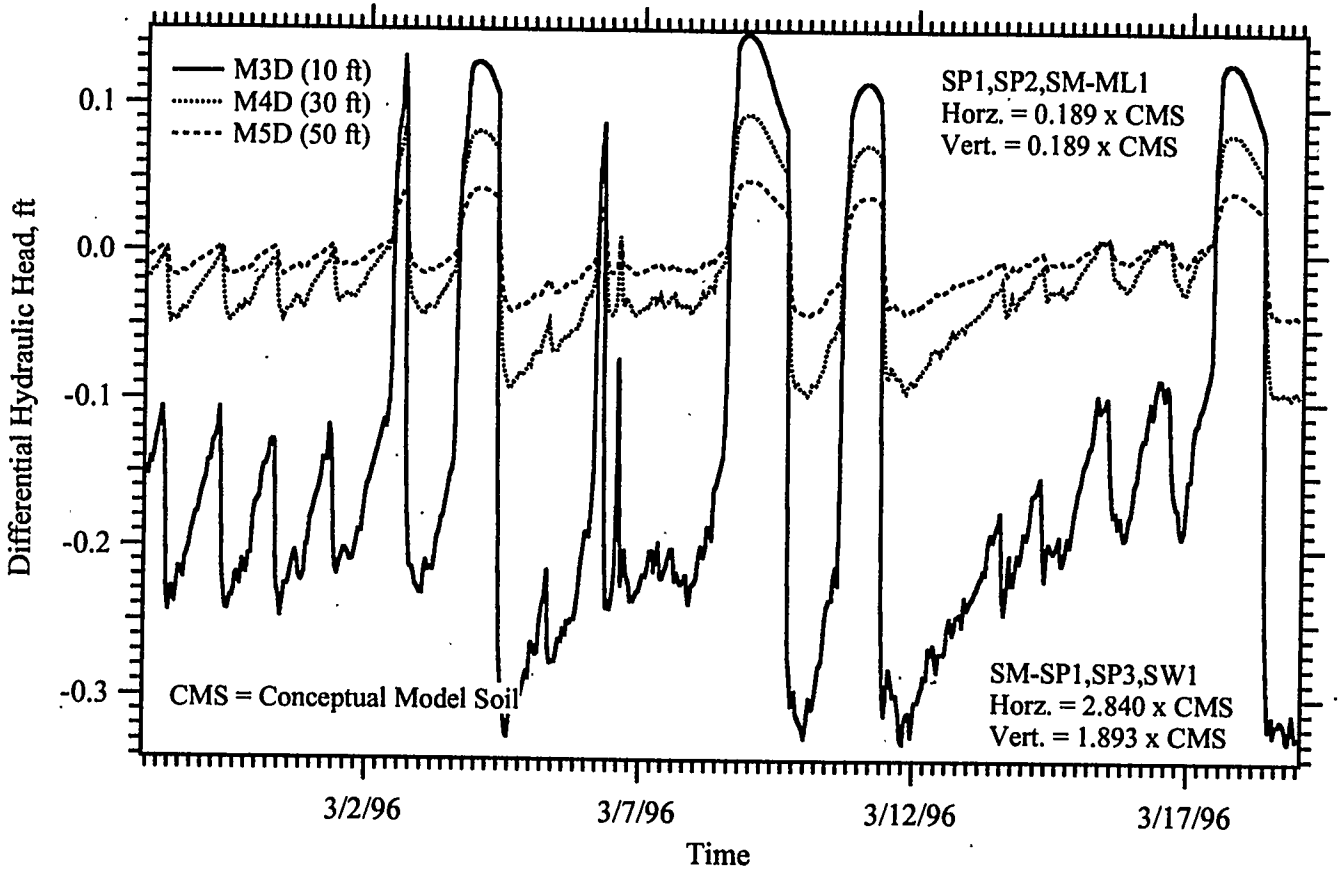

Figure D.16 Differential Hydraulic Pressure Versus Time, Simulation LPI
(Operational Field Test #13, February 27, 1996 - March 19, 1996)

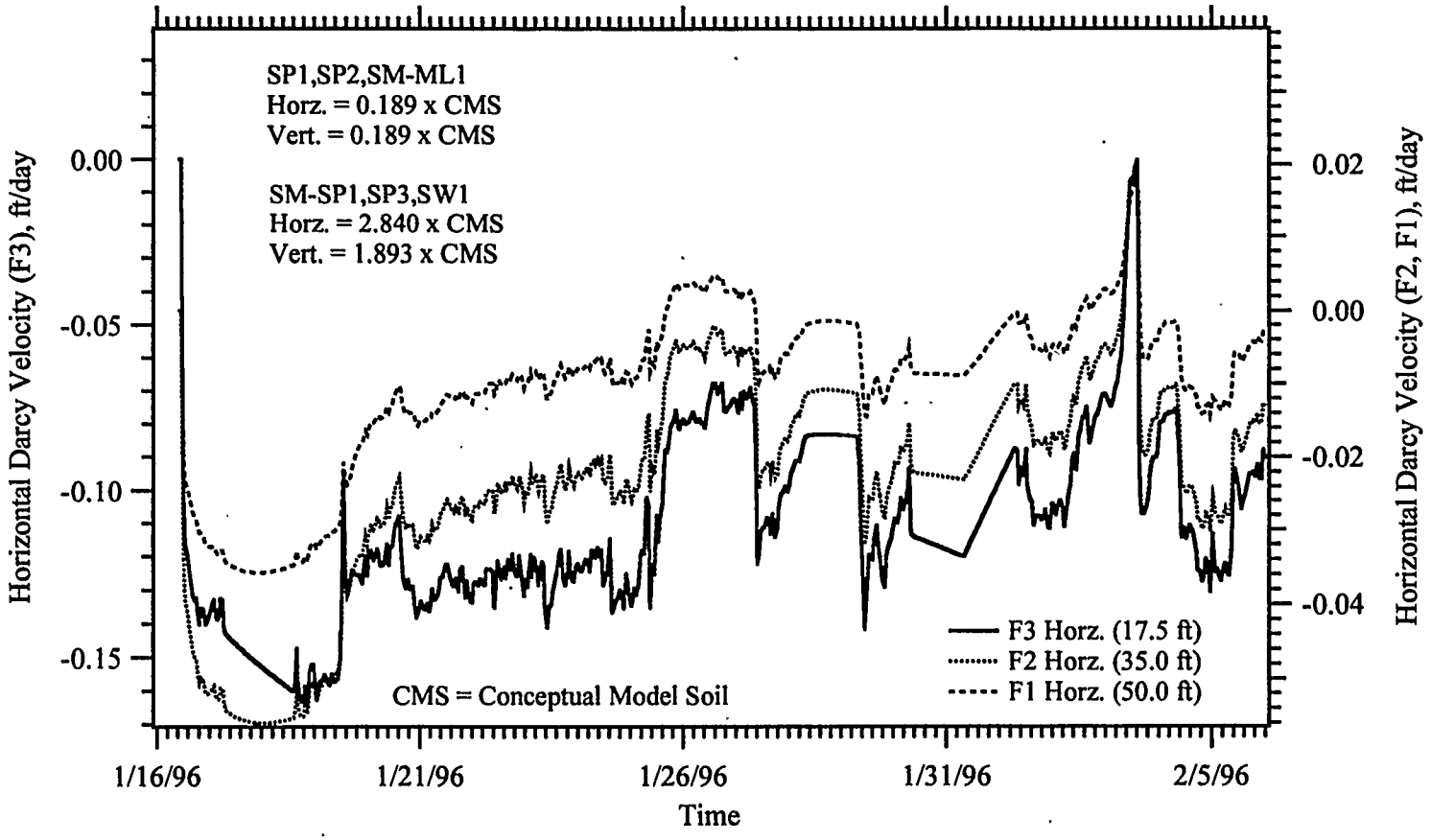

Figure D.17 Horizontal Darcy Velocity Versus Time, Simulation LPI
(Operational Field Test #13, January 16, 1996 - February 6, 1996)

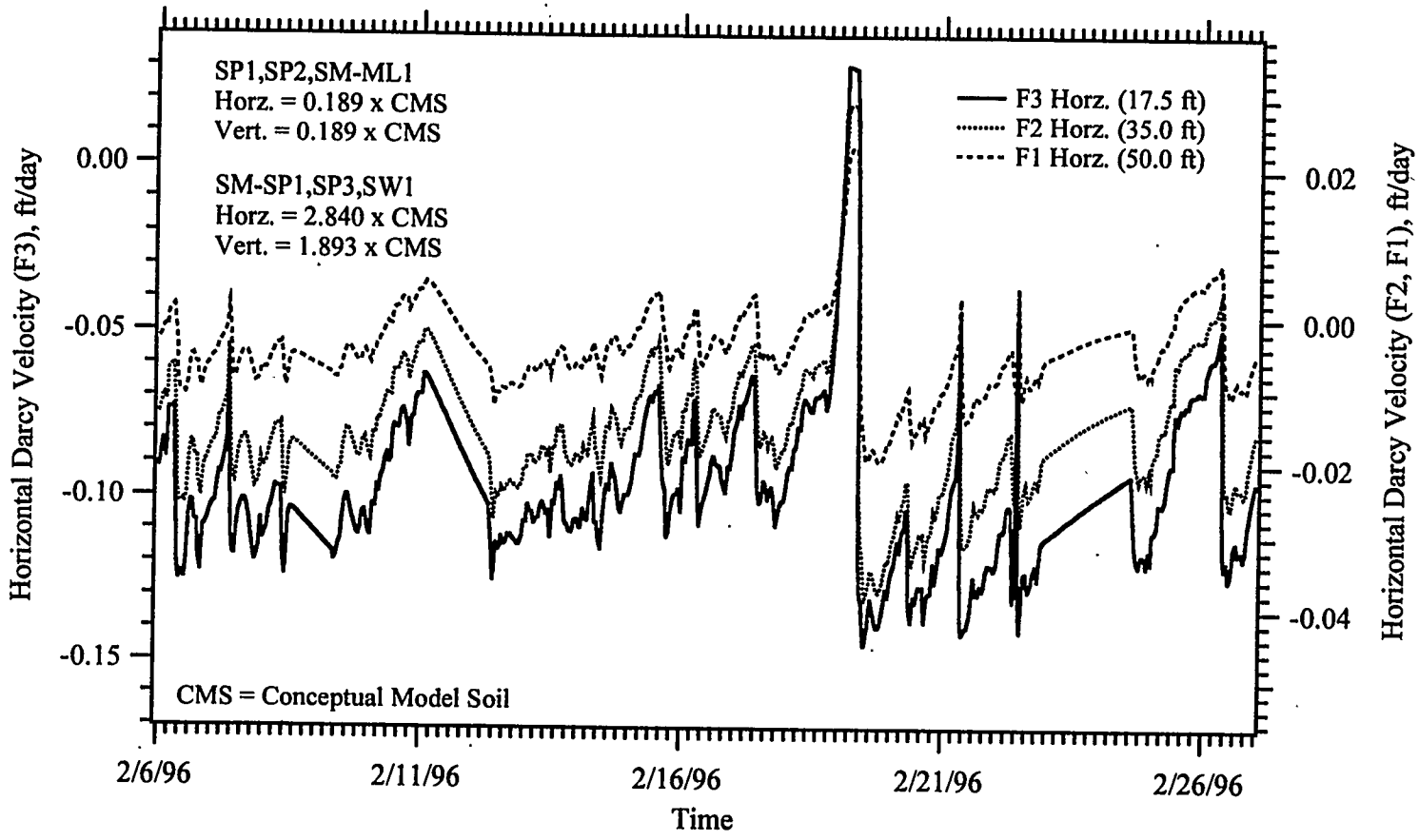

Figure D.18 Horizontal Darcy Velocity Versus Time, Simulation LPI
(Operational Field Test #13, February 6, 1996 - February 27, 1996)

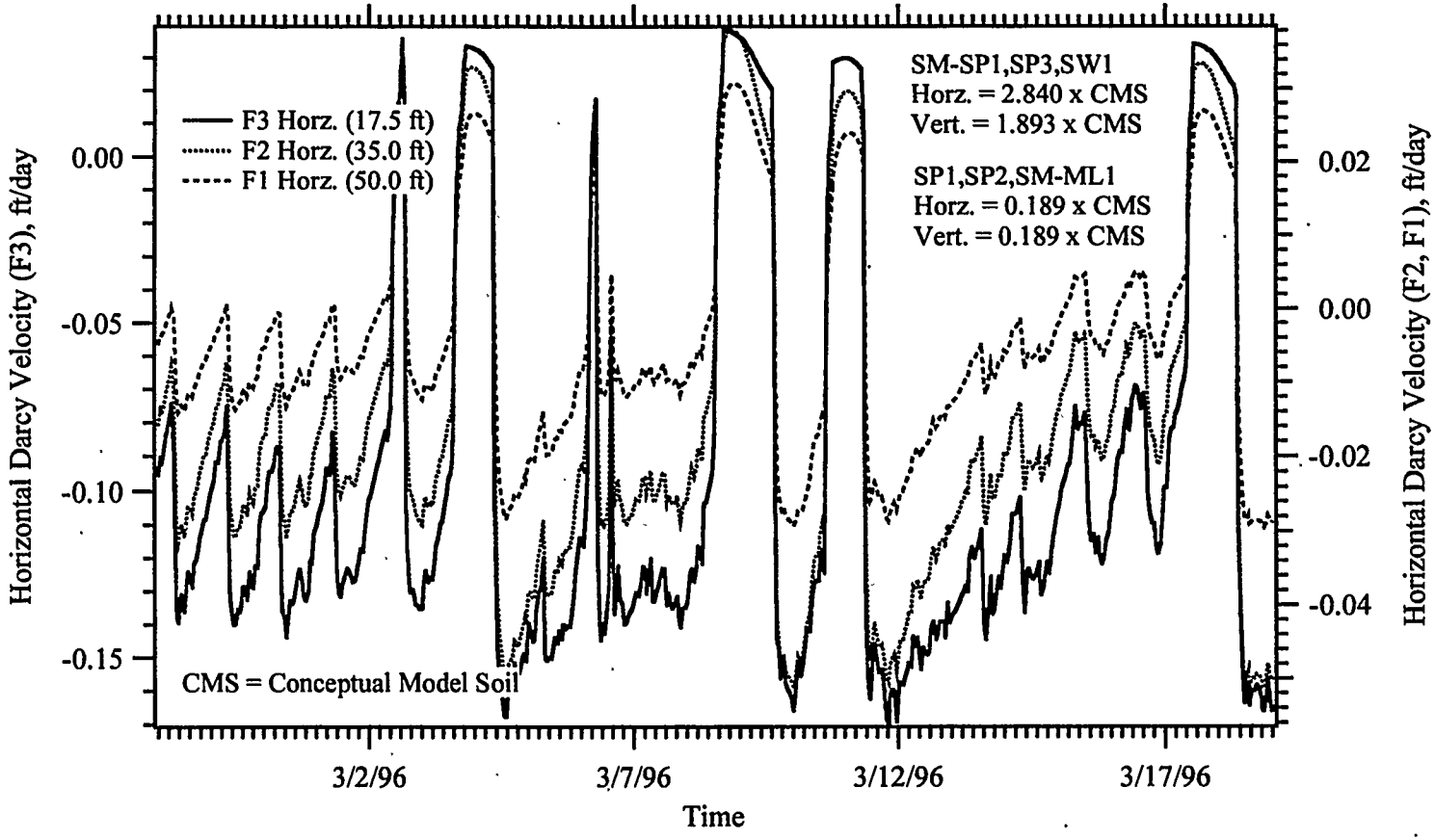

Figure D.19 Horizontal Darcy Velocity Versus Time, Simulation LPI
(Operational Field Test #13, February 27, 1996 - March 19, 1996)

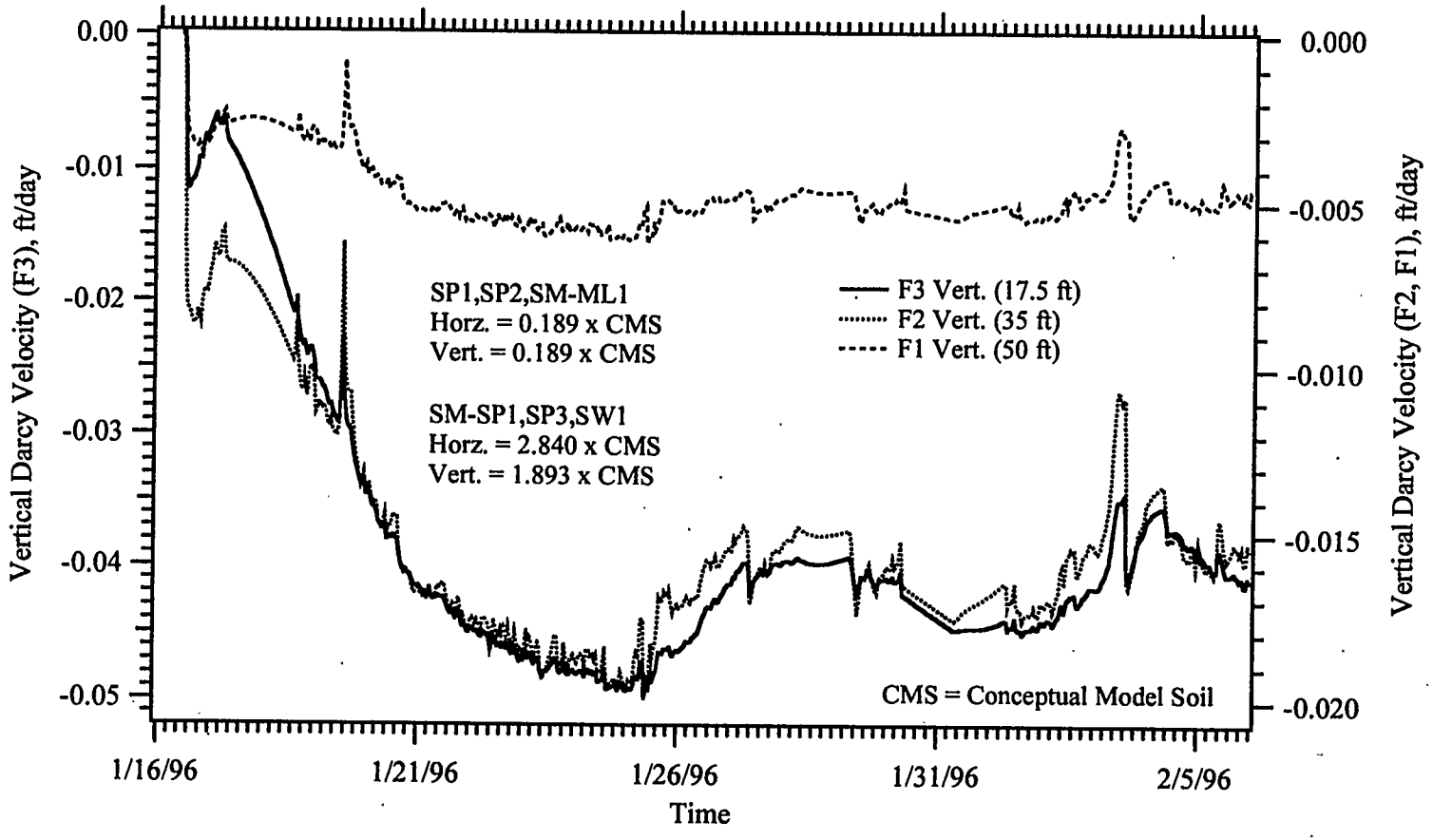

Figure D.20 Vertical Darcy Velocity Versus Time, Simulation LPI
(Operational Field Test #13, January 16, 1996 - February 6, 1996)

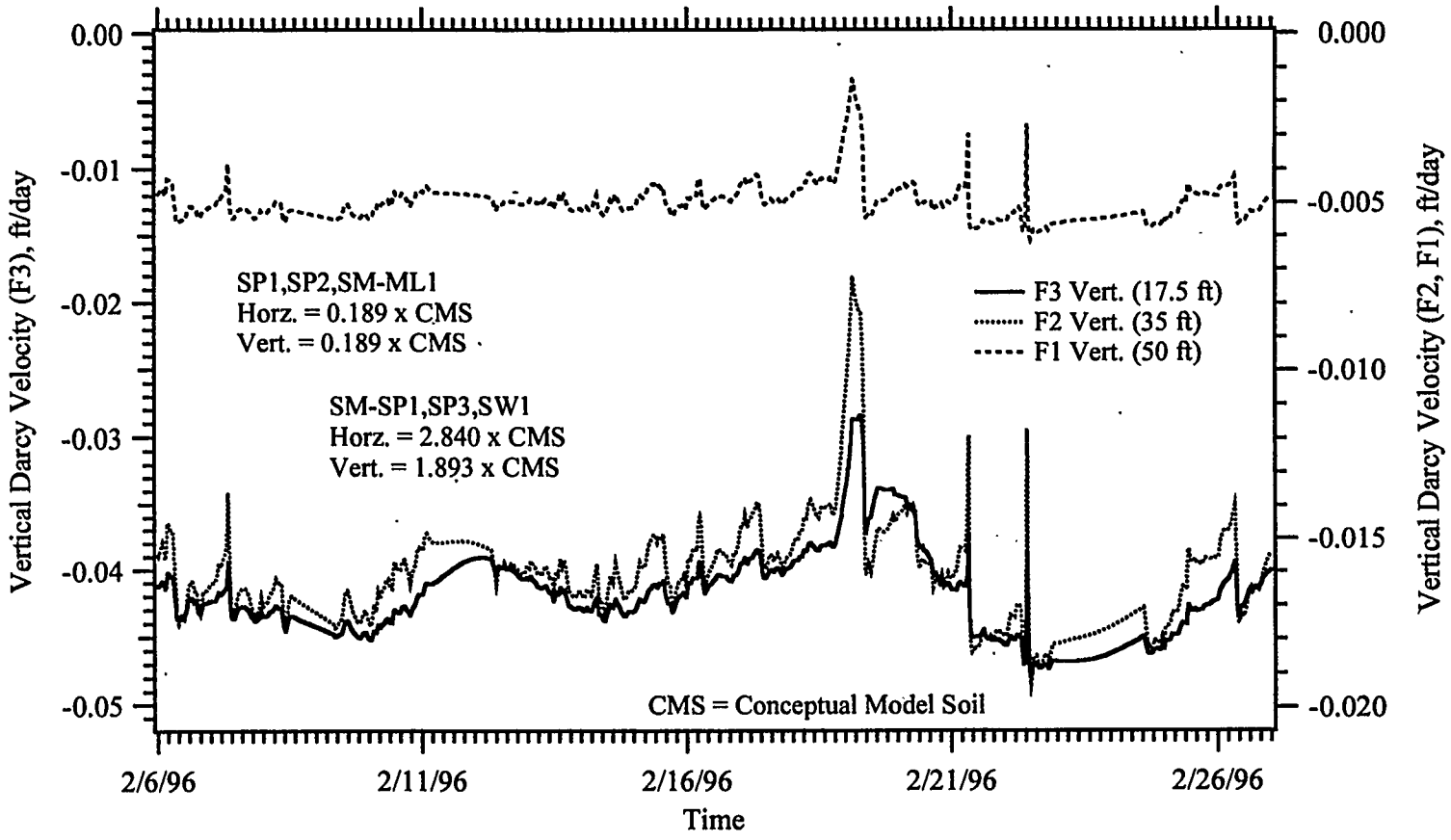

Figure D.21 Vertical Darcy Velocity Versus Time, Simulation LPI
(Operational Field Test #13, February 6, 1996 - February 27, 1996)

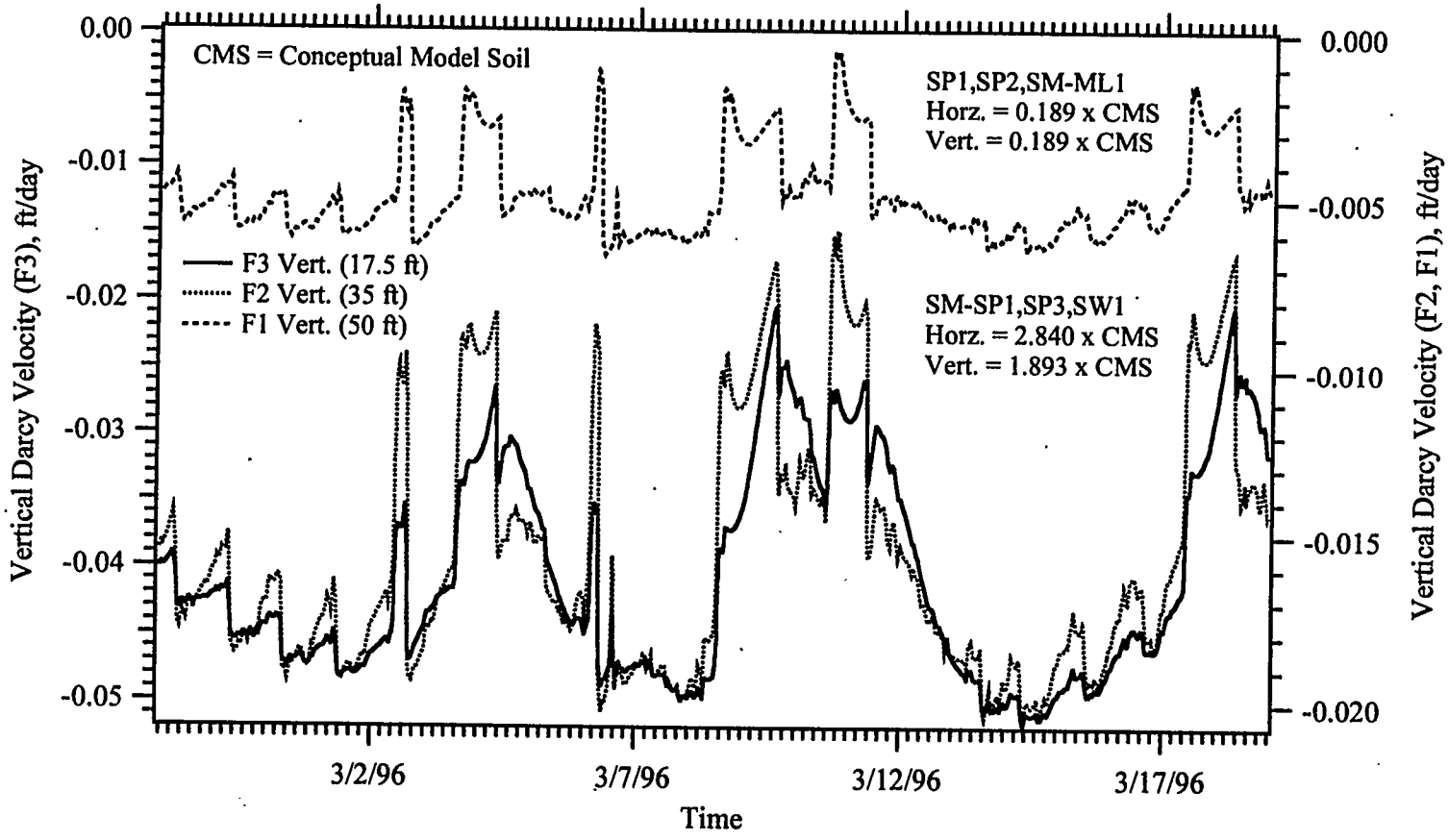

Figure D.22 Vertical Darcy Velocity Versus Time, Simulation LPI
(Operational Field Test #13, February 27, 1996 - March 19, 1996)

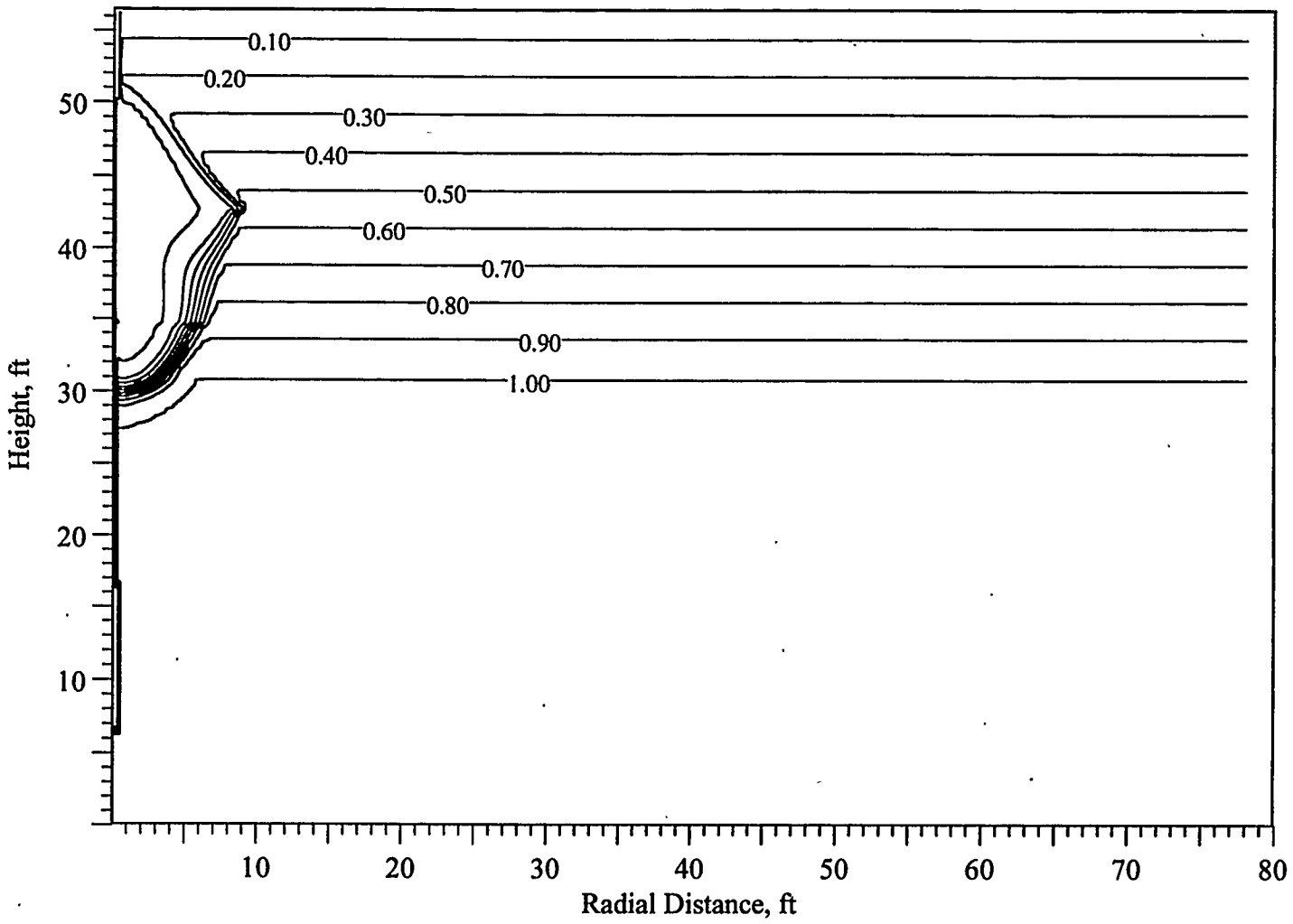

Figure D.23 TCE Concentration Profile at 1 Day, Simulation LPI
(Operational Field Test #13, January 17, 1996)

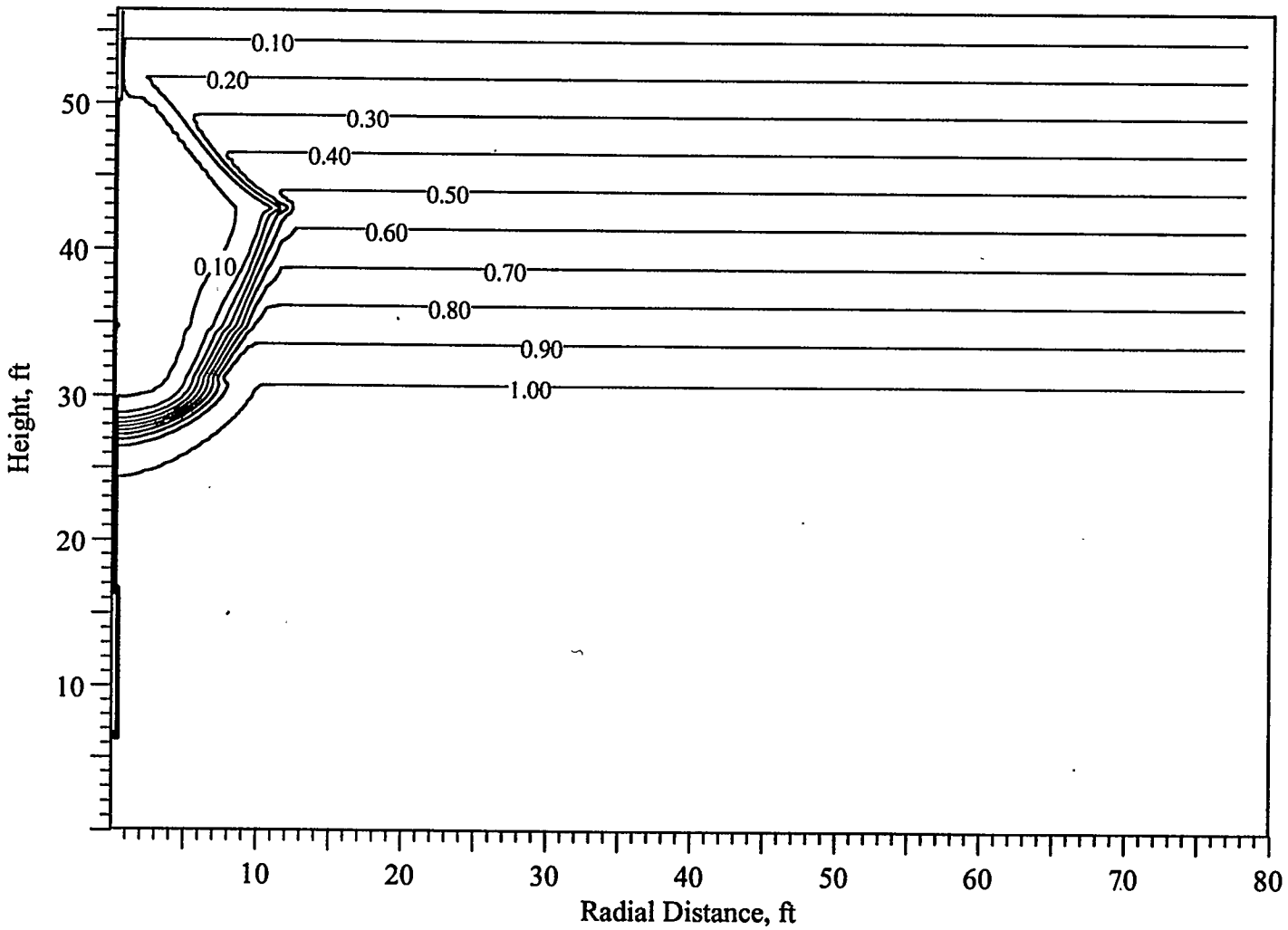

Figure D.24 TCE Concentration Profile at 2 Days, Simulation LPI
(Operational Field Test #13, January 18, 1996)

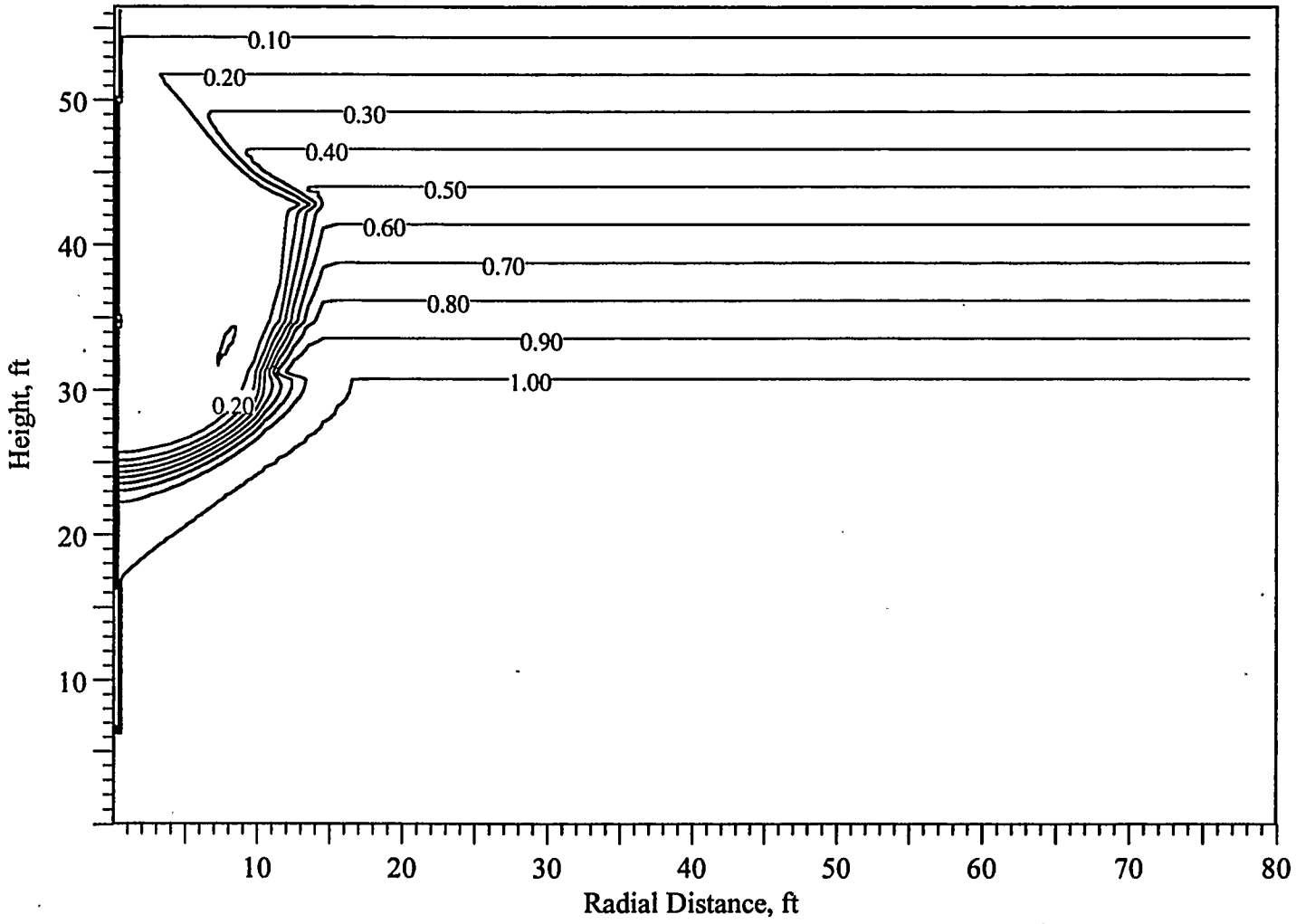

Figure D.25 TCE Concentration Profile at 4 Days, Simulation LPI
(Operational Field Test #13, January 20, 1996)

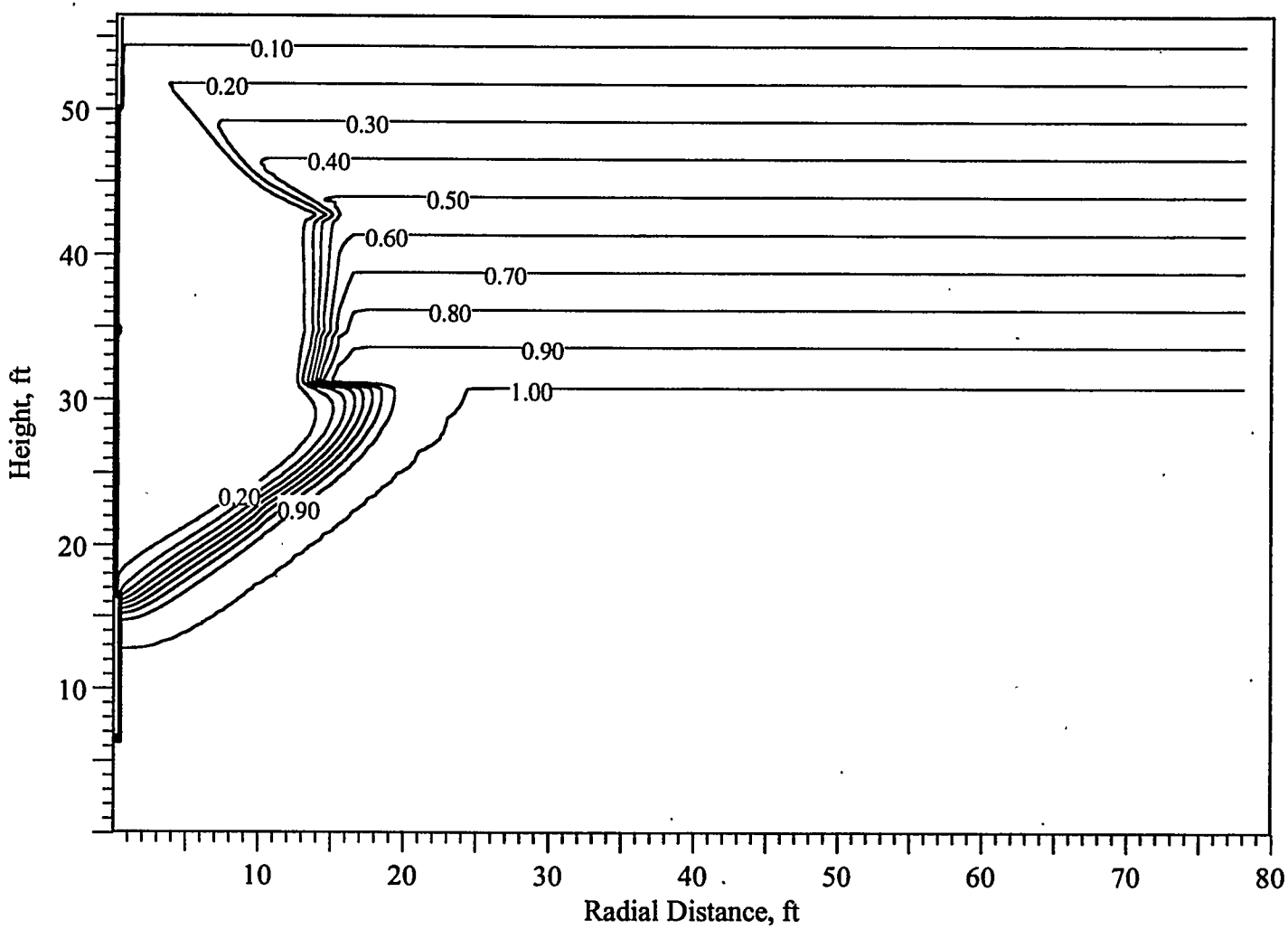

Figure D.26 TCE Concentration Profile at 8 Days, Simulation LPI
(Operational Field Test #13, January 24, 1996)

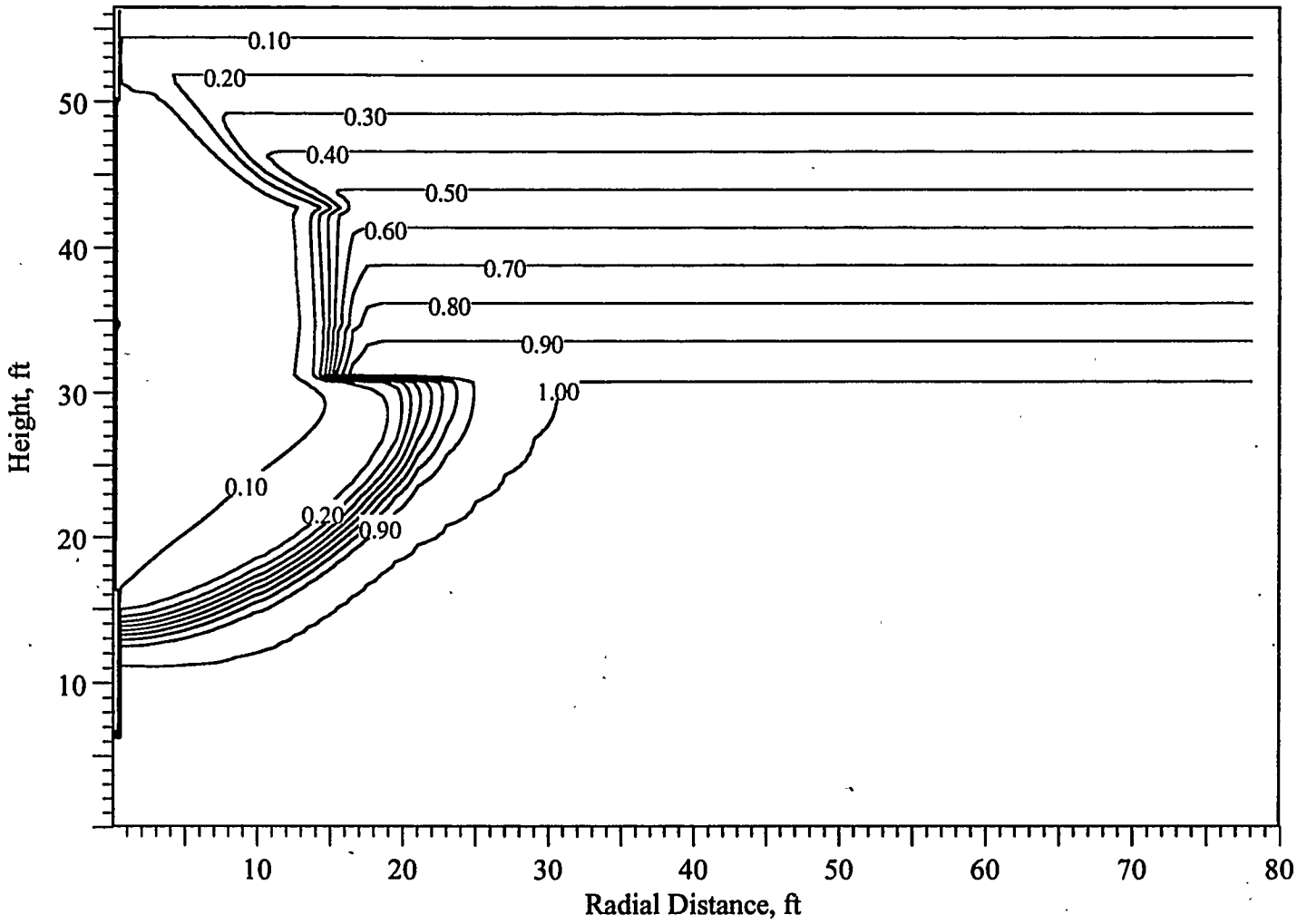

Figure D.27 TCE Concentration Profile at 16 Days, Simulation LPI
(Operational Field Test #13, February 1, 1996)

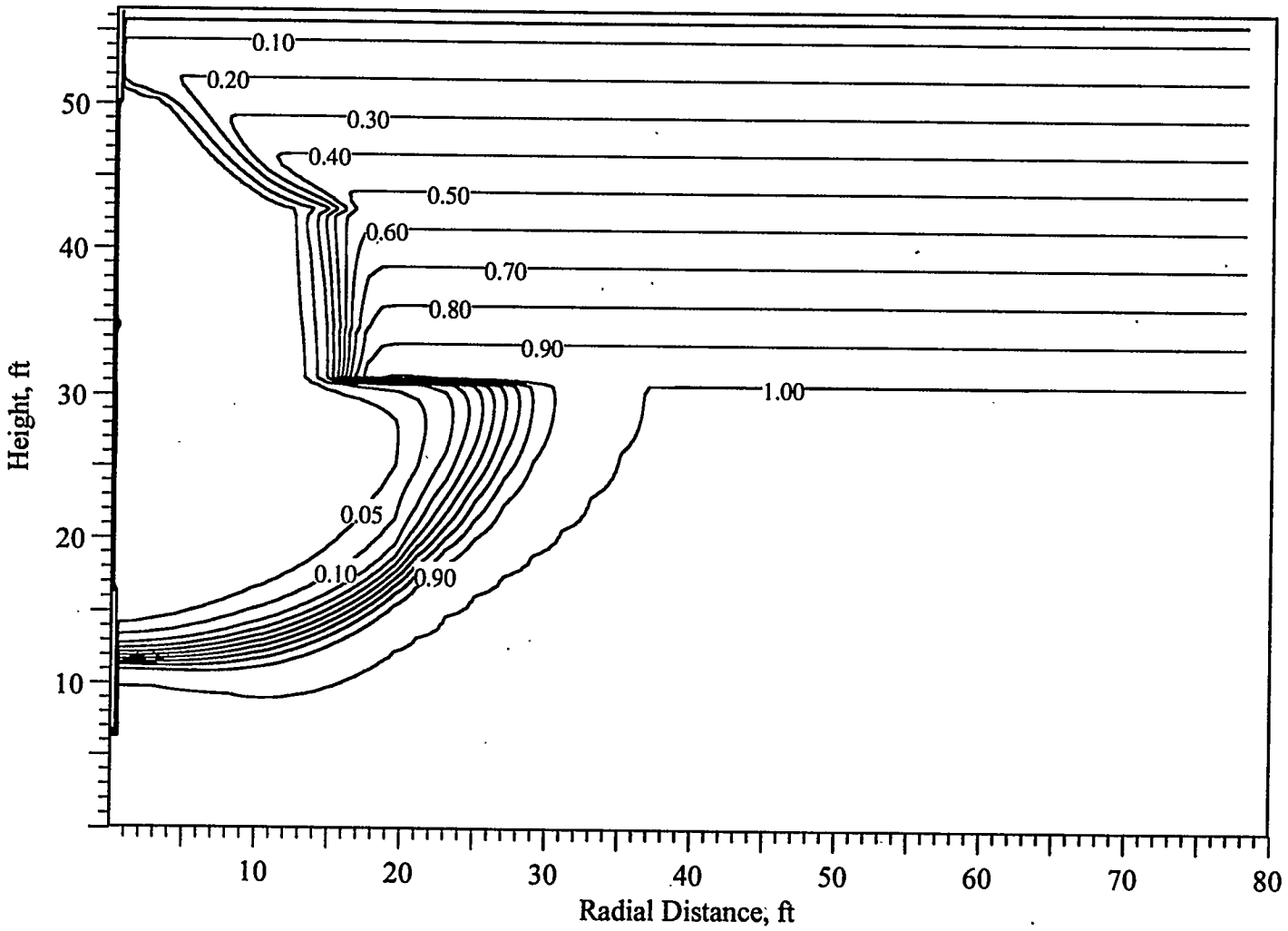

Figure D.28 TCE Concentration Profile at 32 Days, Simulation LPI
(Operational Field Test #13, February 17, 1996)

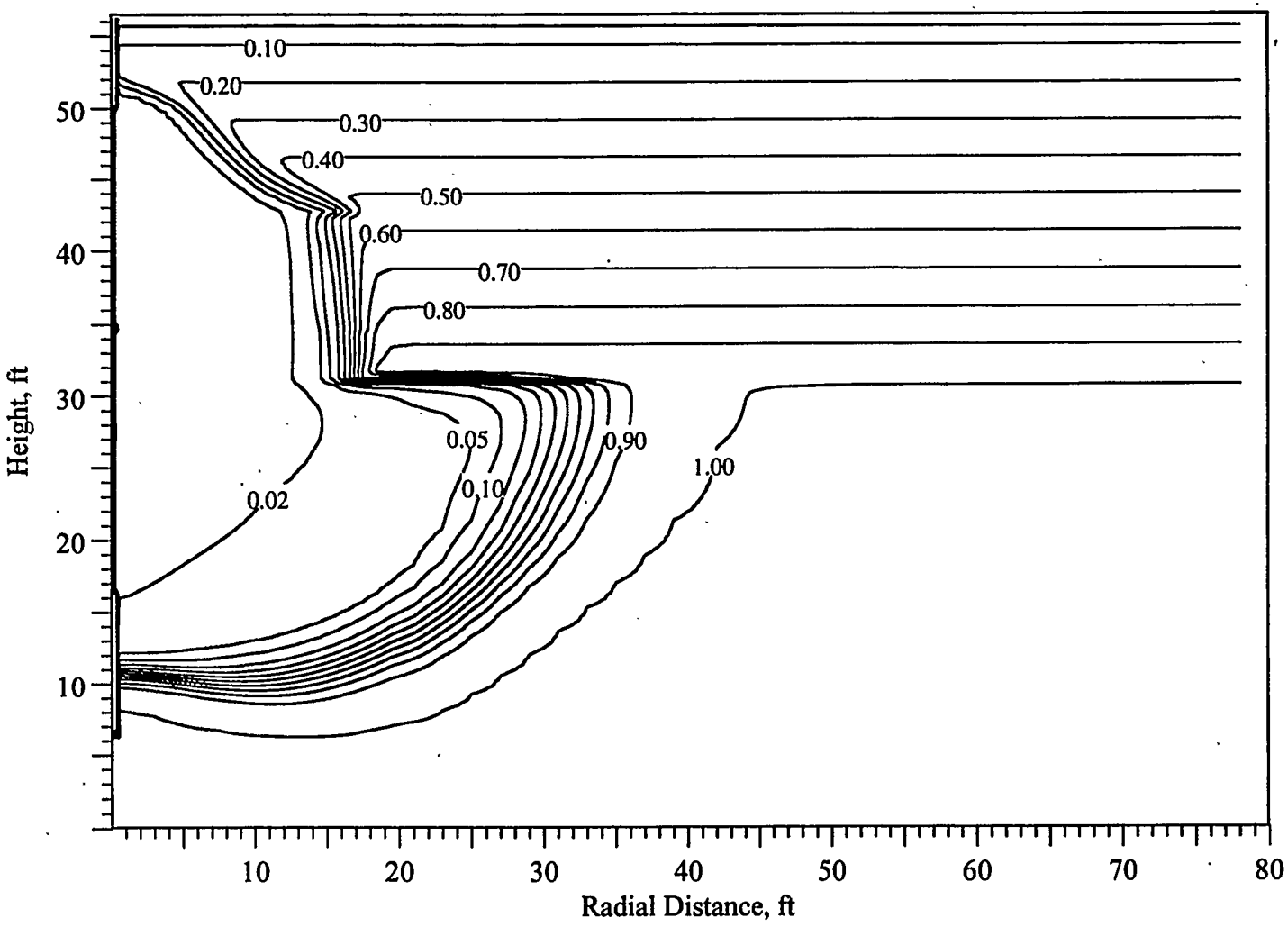

Figure D.29 TCE Concentration Profile at 63 Days, Simulation LPI
(Operational Field Test #13, March 19, 1996)

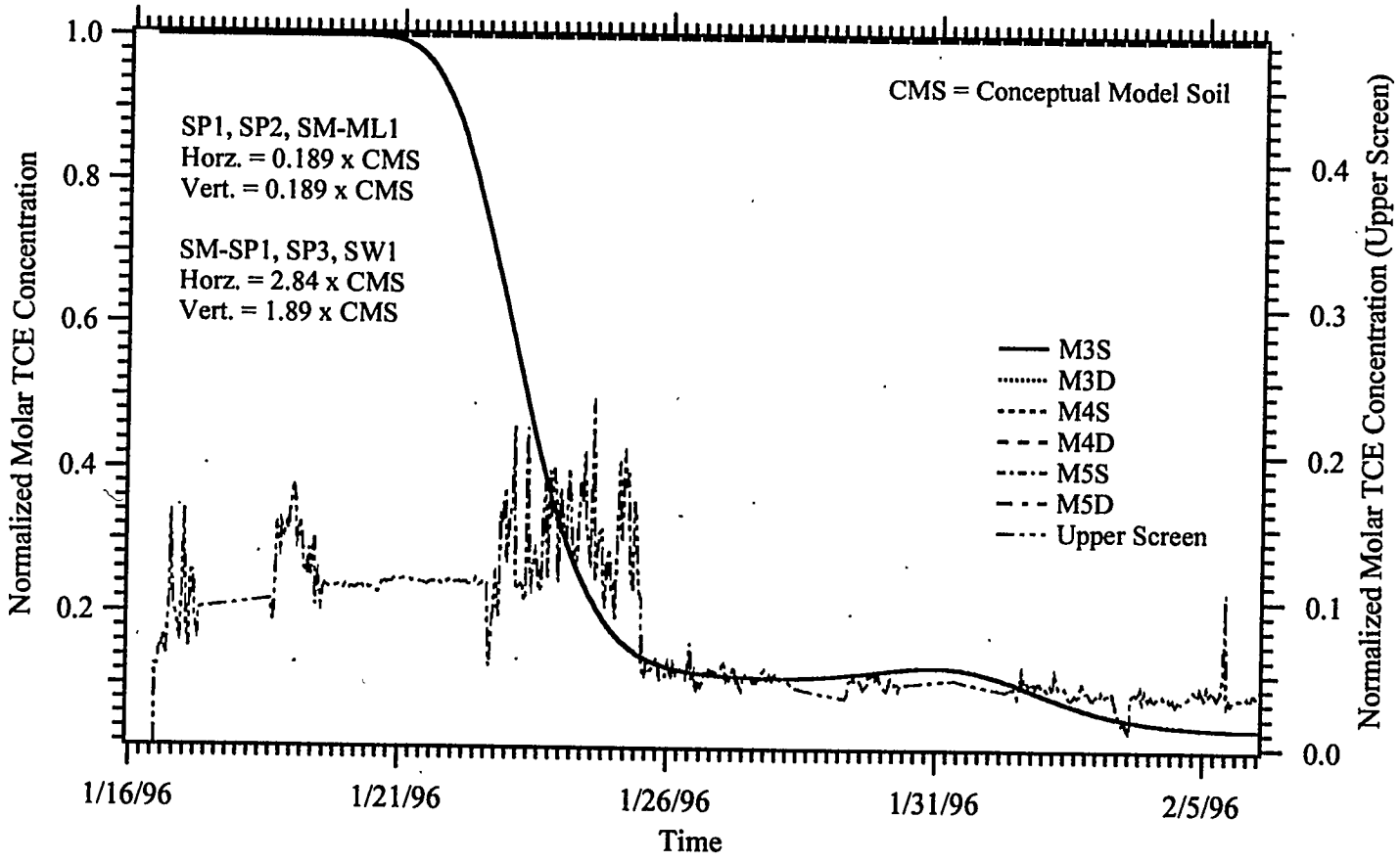

Figure D.30 Dissolved TCE Concentration Versus Time, Simulation LPI
(Operational Field Test #13, January 16, 1996 - February 6, 1996)

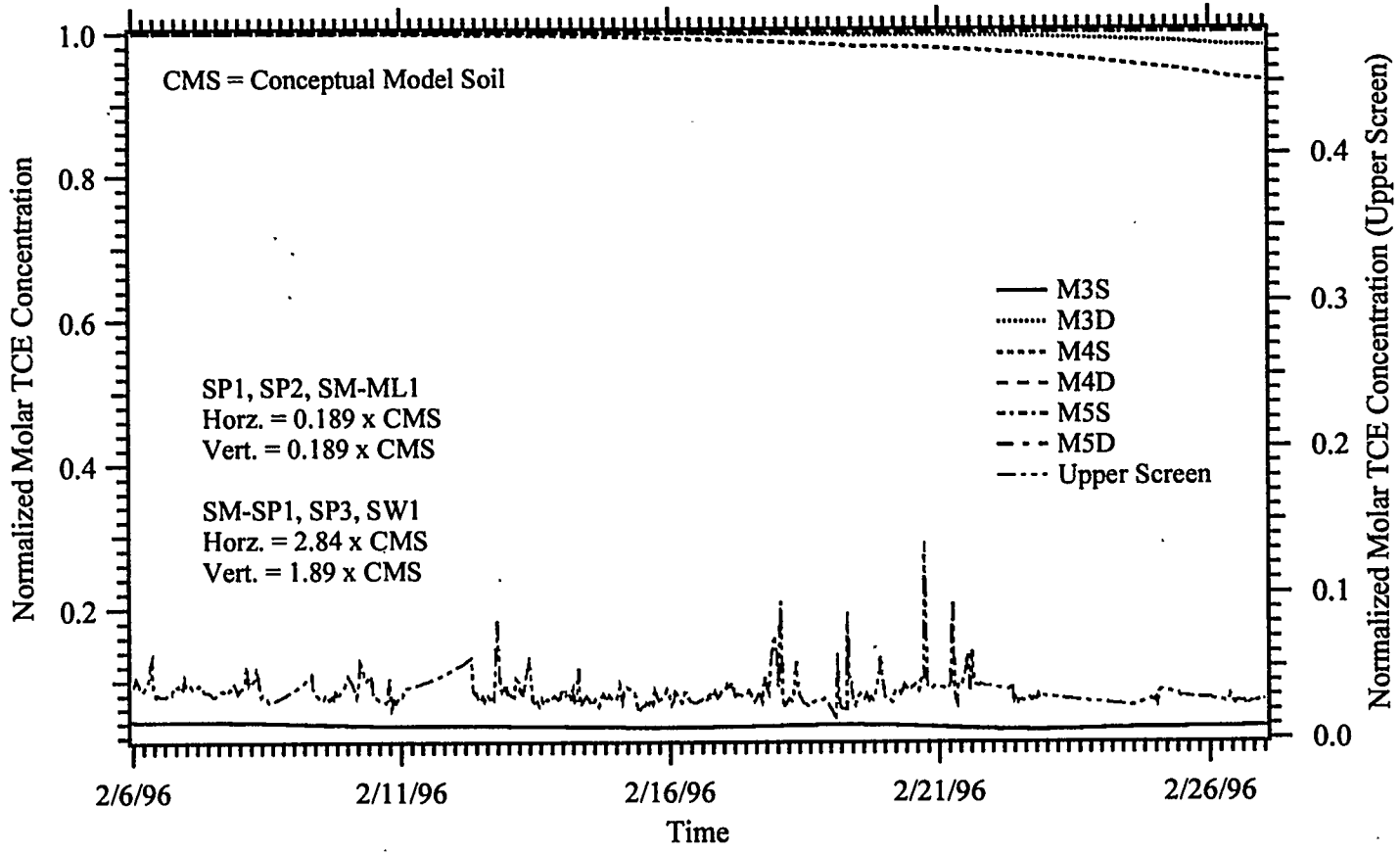

Figure D.31 Dissolved TCE Concentration Versus Time, Simulation LPI
(Operational Field Test #13, February 6, 1996 - February 27, 1996)

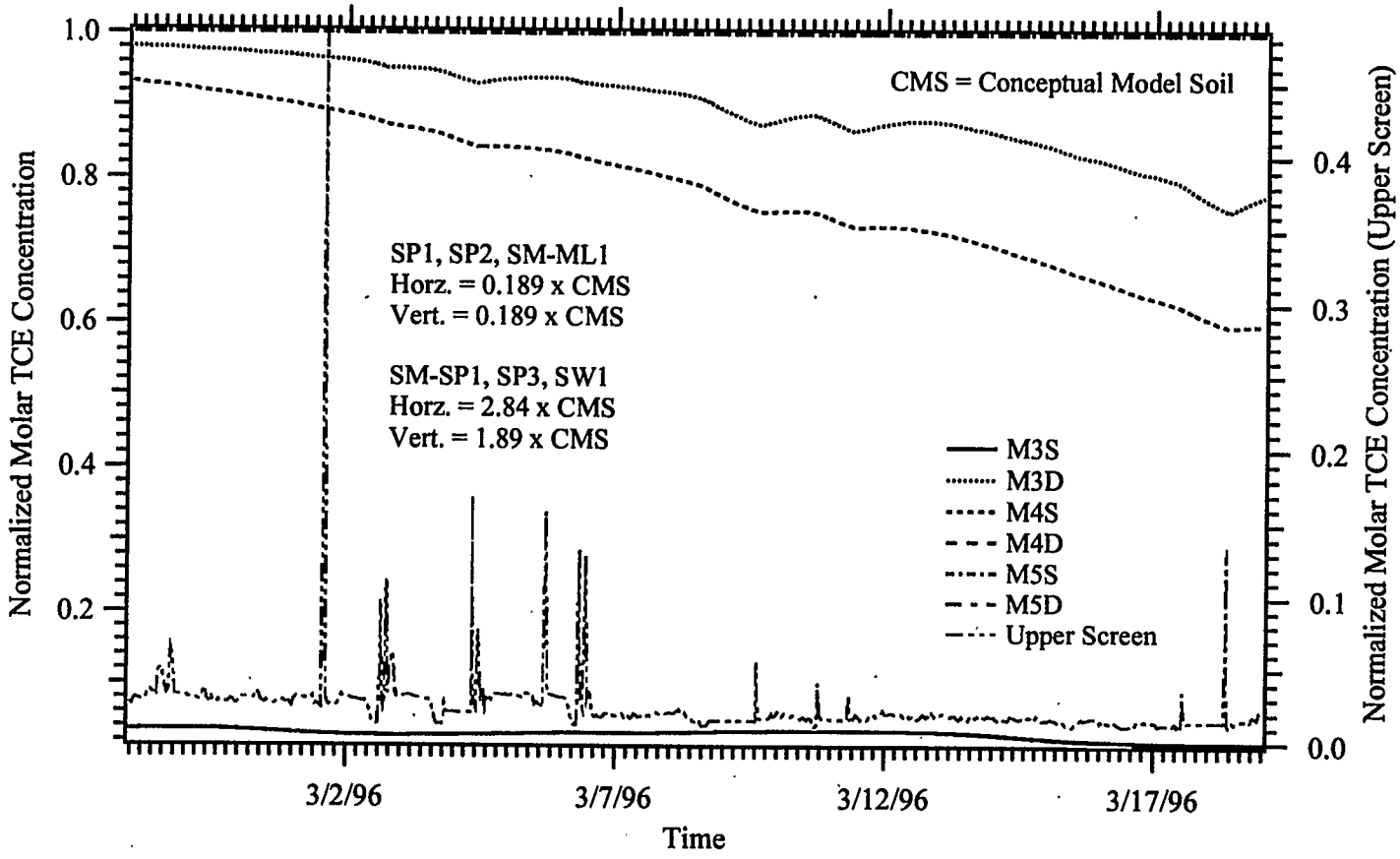

Figure D.32 Dissolved TCE Concentration Versus Time, Simulation LPI
(Operational Field Test #13, February 27, 1996 - March 19, 1996)

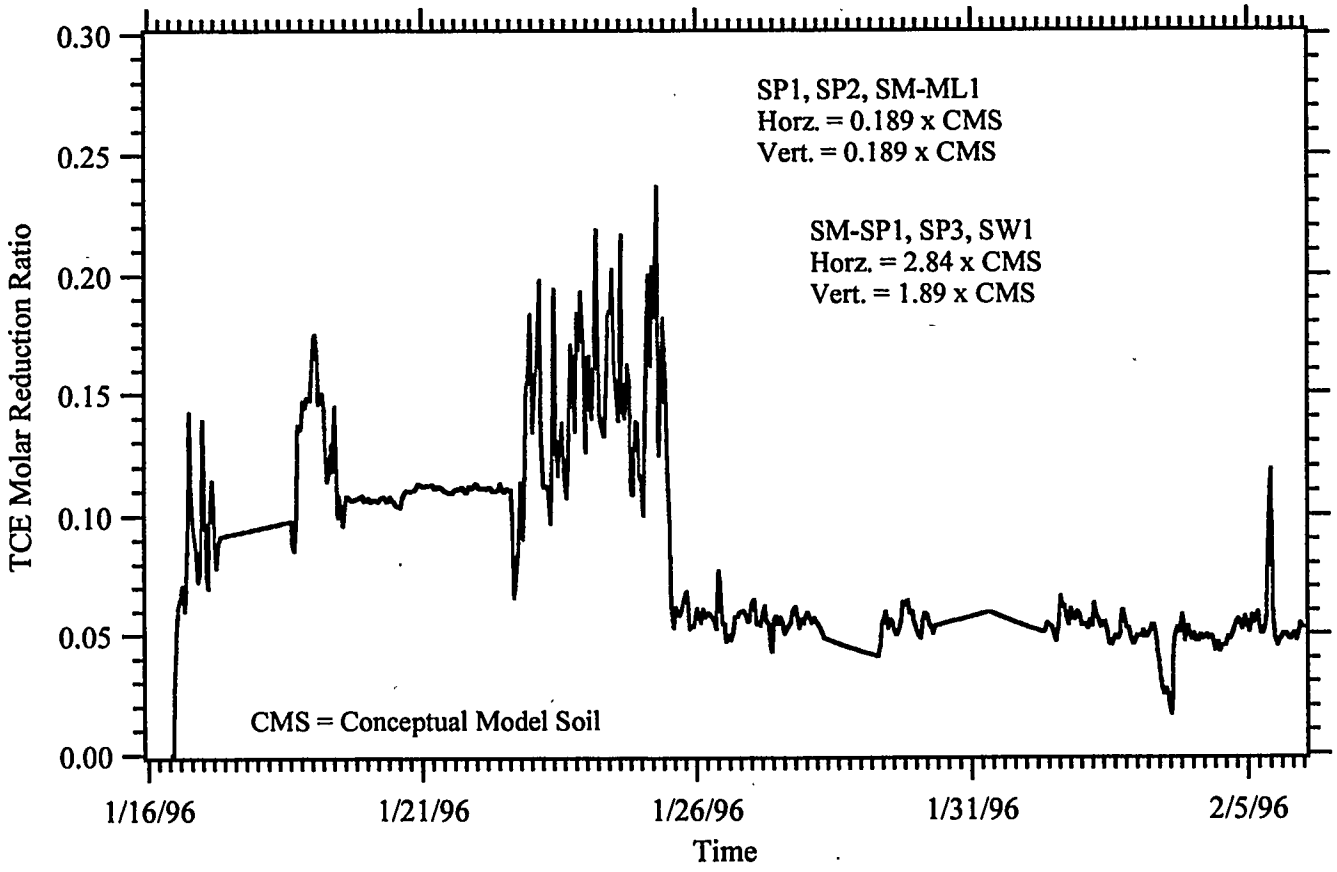

Figure D.33 TCE Molar Reduction Ratio Versus Time, Simulation LPI
(Operational Field Test #13, January 16, 1996 - February 6, 1996)

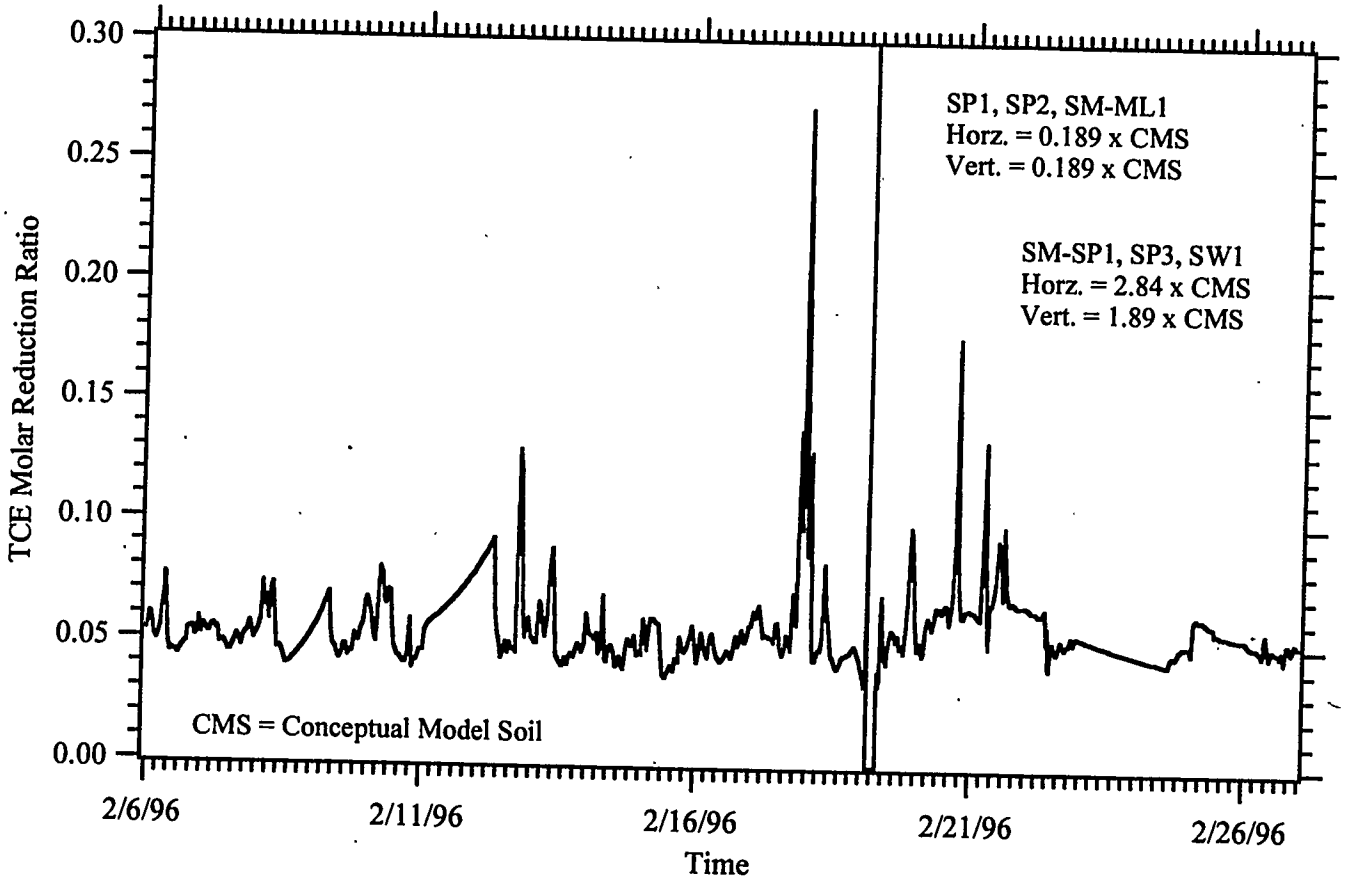

Figure D.34 TCE Molar Reduction Ratio Versus Time, Simulation LPI
(Operational Field Test #13, February 6, 1996 - February 27, 1996)

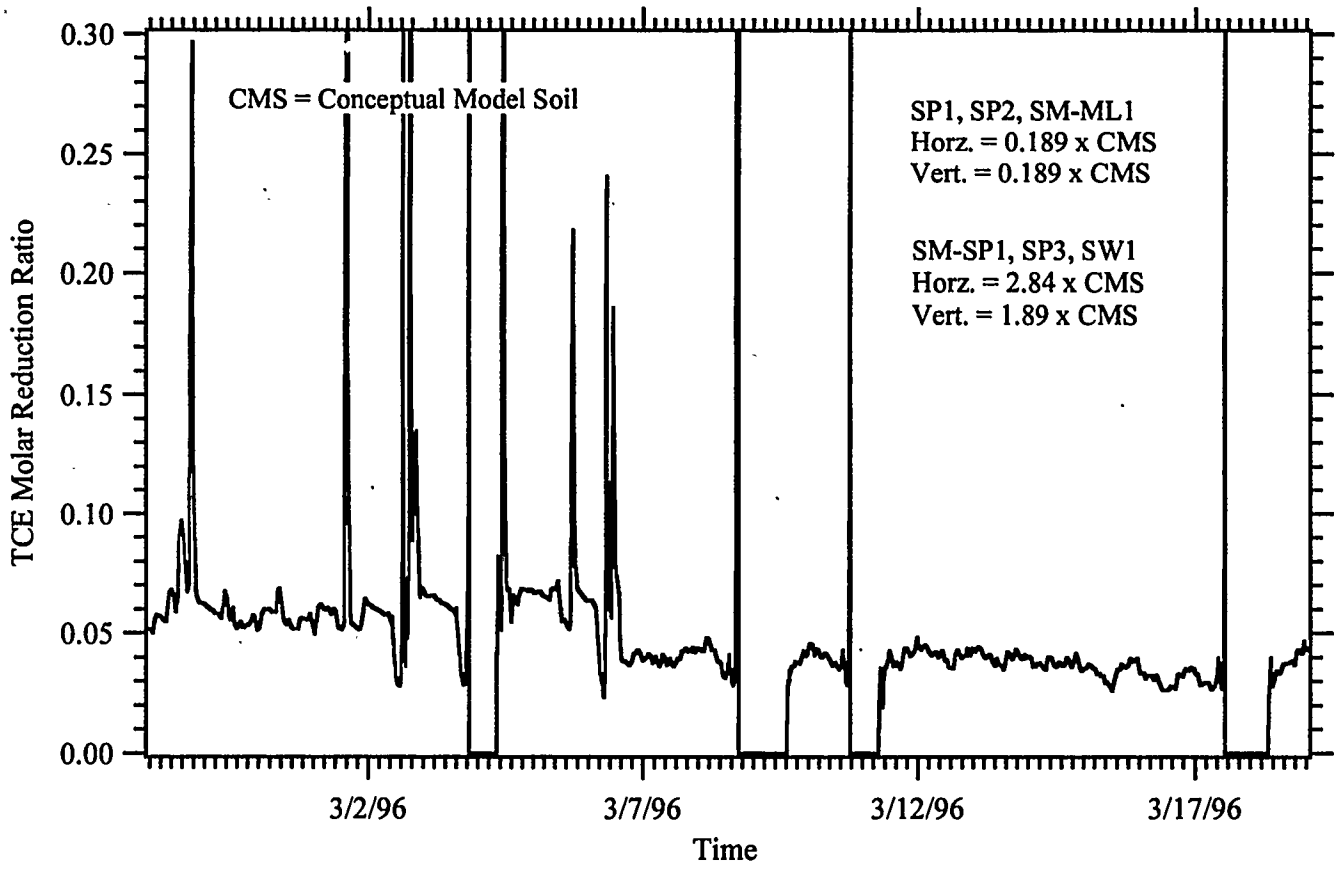

Figure D.35 TCE Molar Reduction Ratio Versus Time, Simulation LPI
(Operational Field Test #13, February 27, 1996 - March 19, 1996)

APPENDIX E

HIGH-PERMEABILITY ISOTROPIC SIMULATION RESULTS

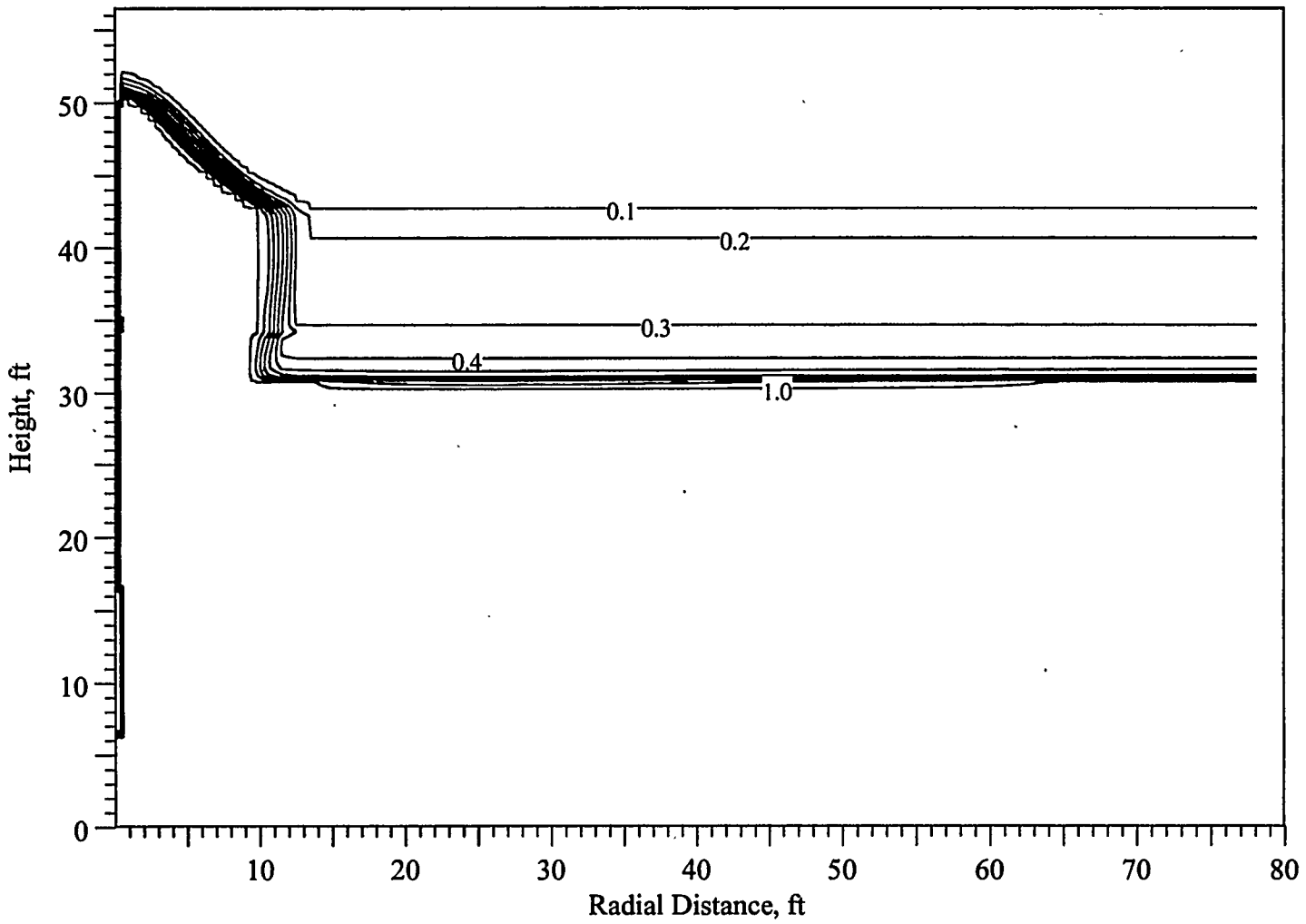

Figure E.1 Saturation Profile at 1 Day, Simulation HPI
(Operational Field Test #13, January 17, 1996)

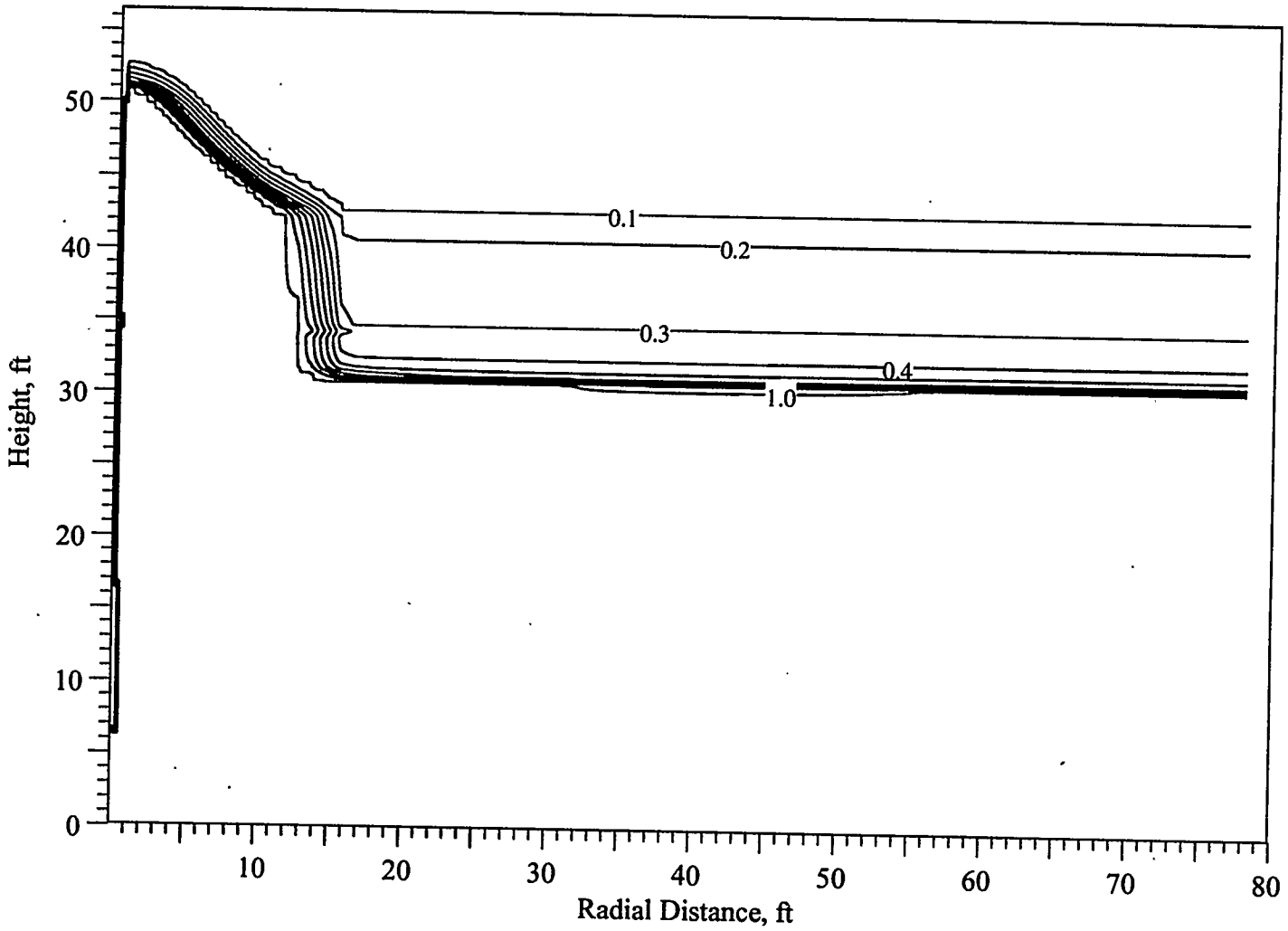

Figure E.2 Saturation Profile at 2 Days, Simulation HPI
(Operational Field Test #13, January 18, 1996)

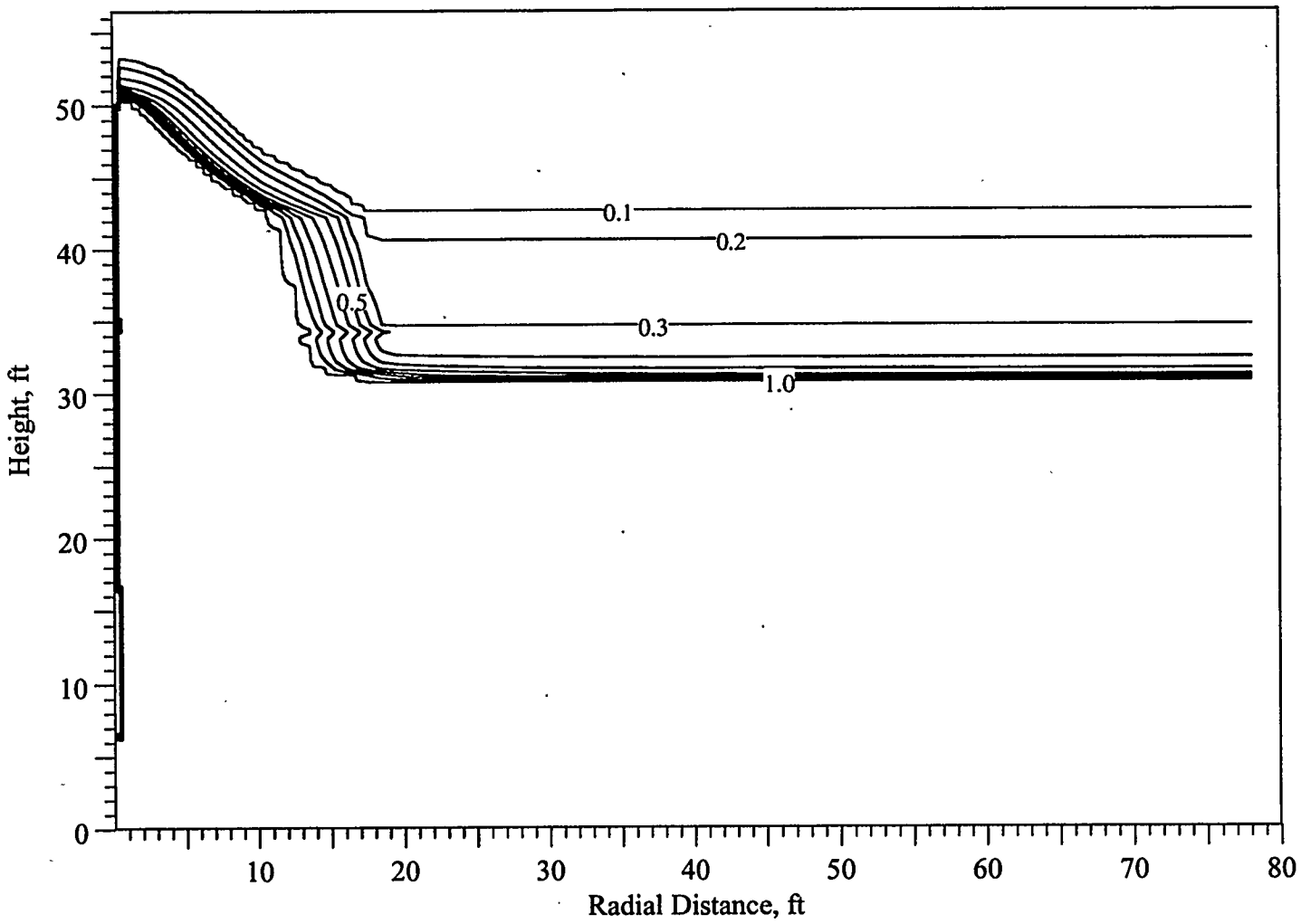

Figure E.3 Saturation Profile at 4 Days, Simulation HPI
(Operational Field Test #13, January 20, 1996)

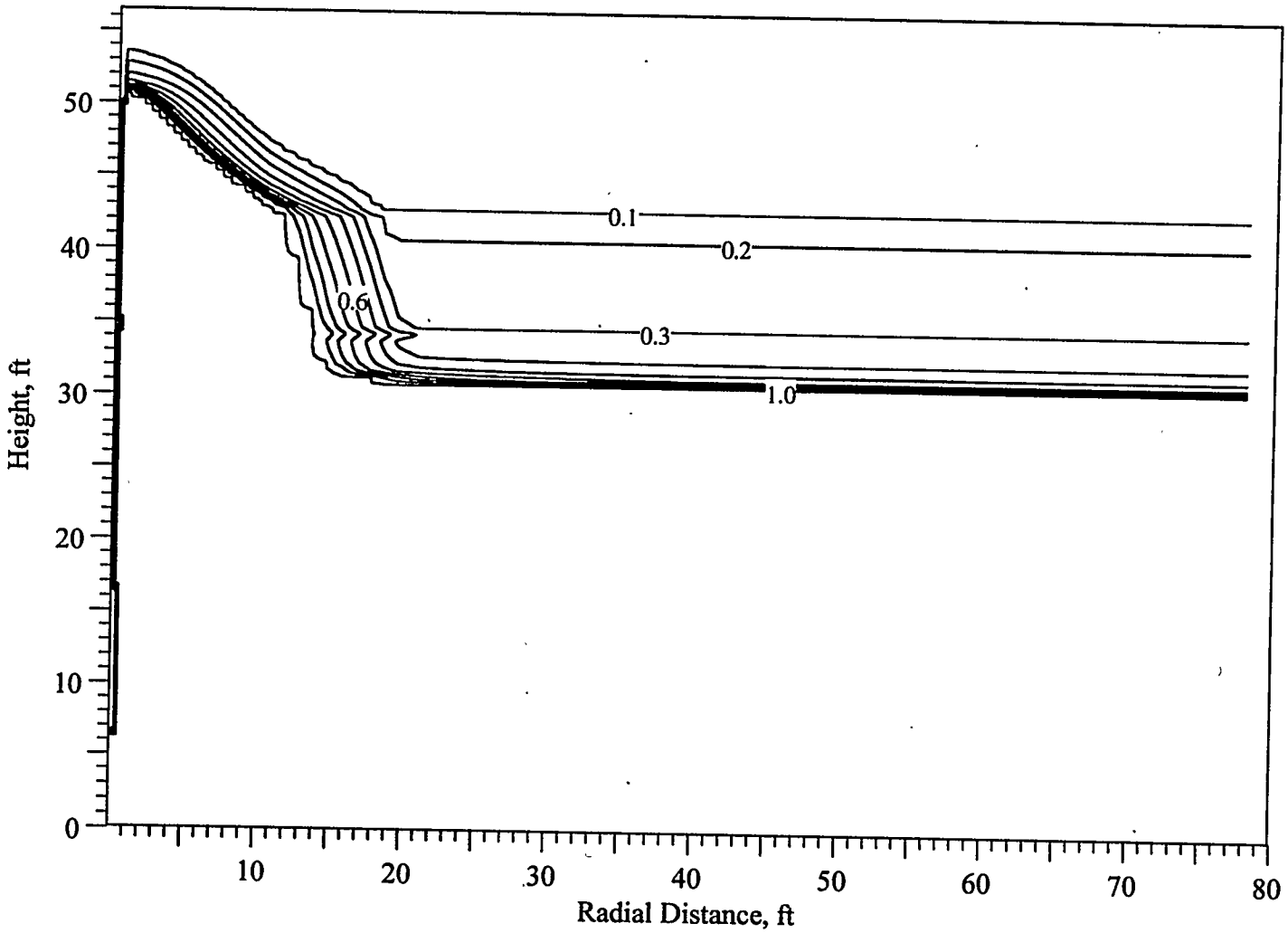

Figure E.4 Saturation Profile at 8 Days, Simulation HPI
(Operational Field Test #13, January 24, 1996)

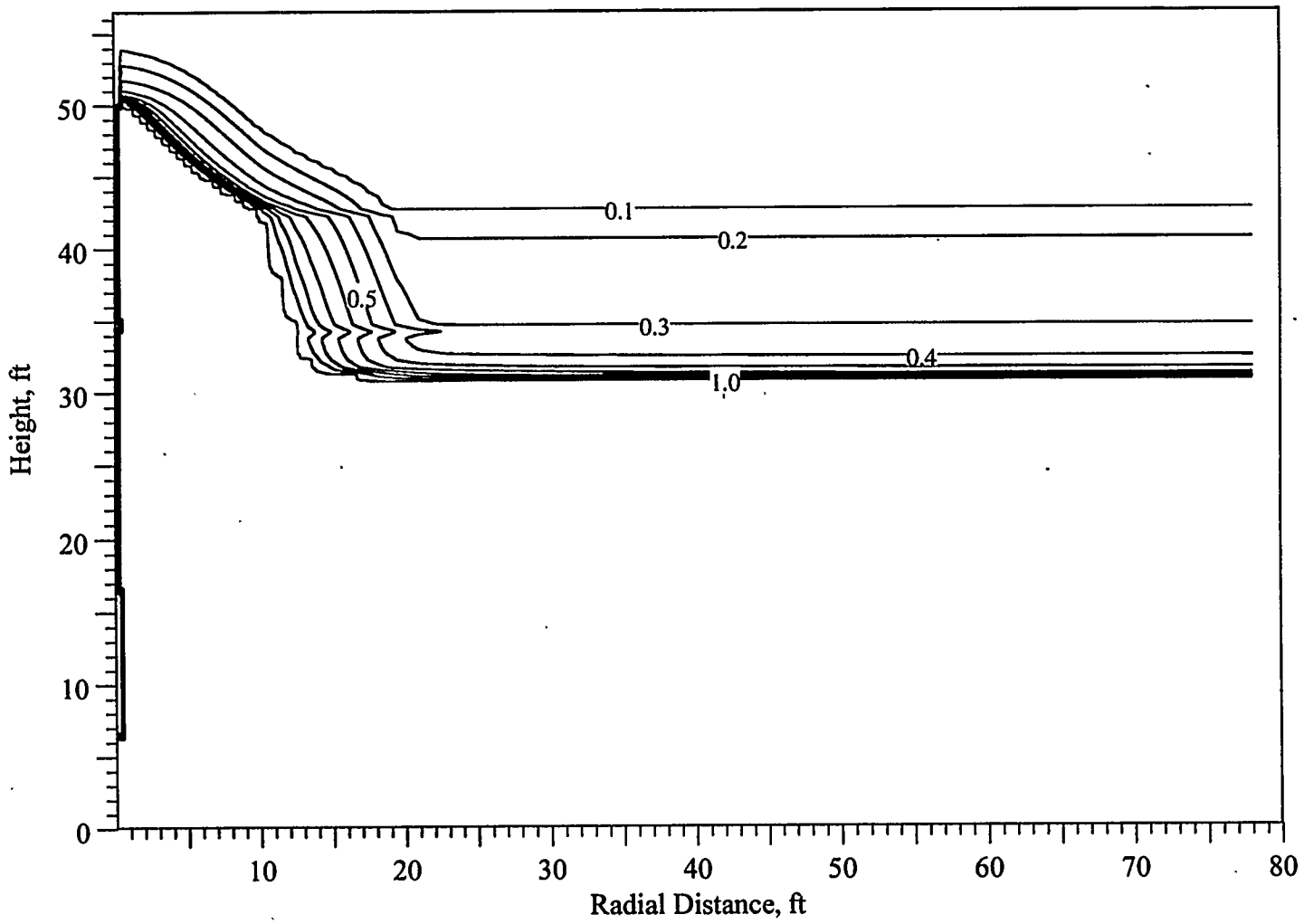

Figure E.5 Saturation Profile at 16 Days, Simulation HPI
(Operational Field Test #13, February 1, 1996)

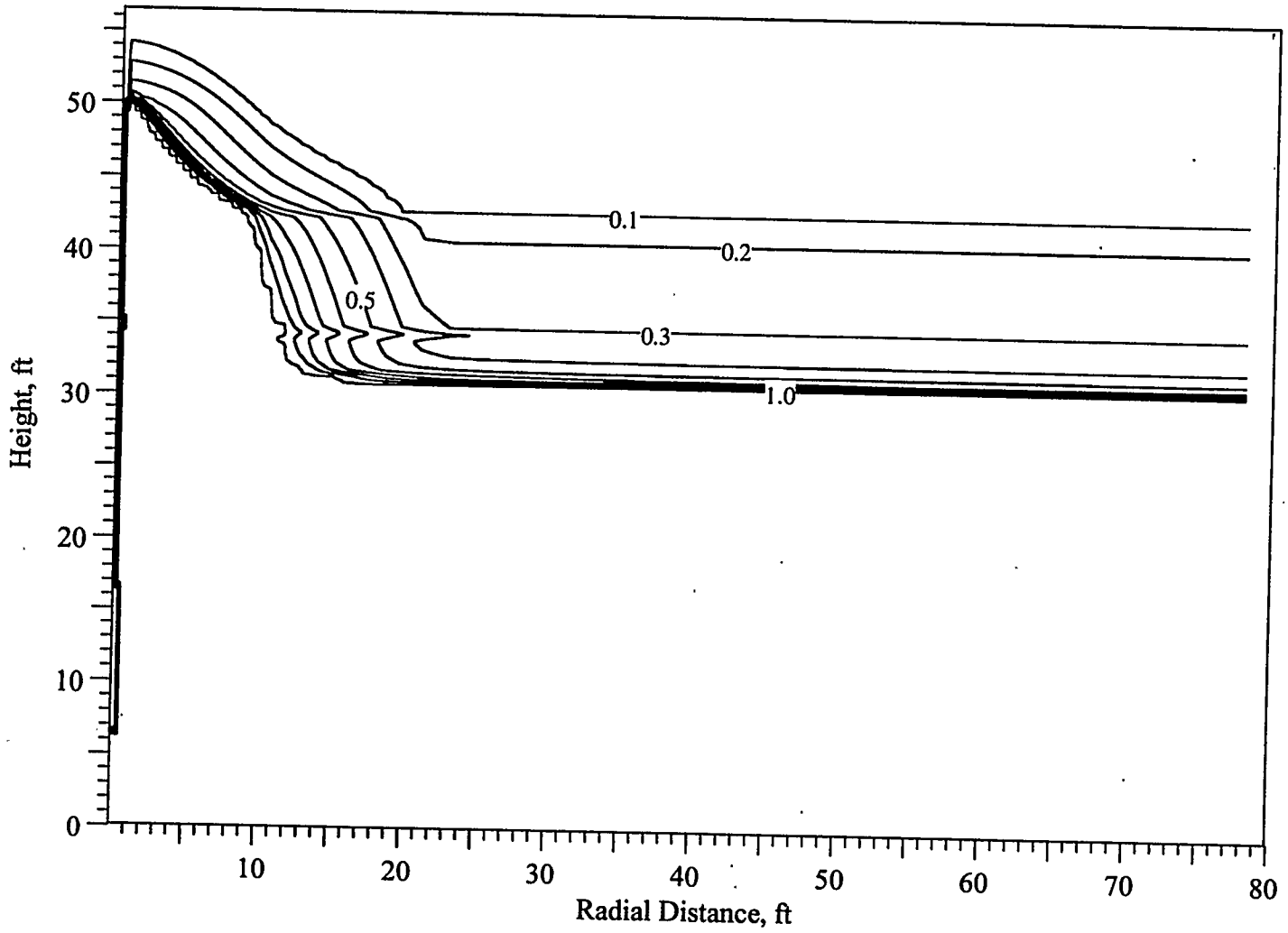

Figure E.6 Saturation Profile at 32 Days, Simulation HPI
(Operational Field Test #13, February 17, 1996)

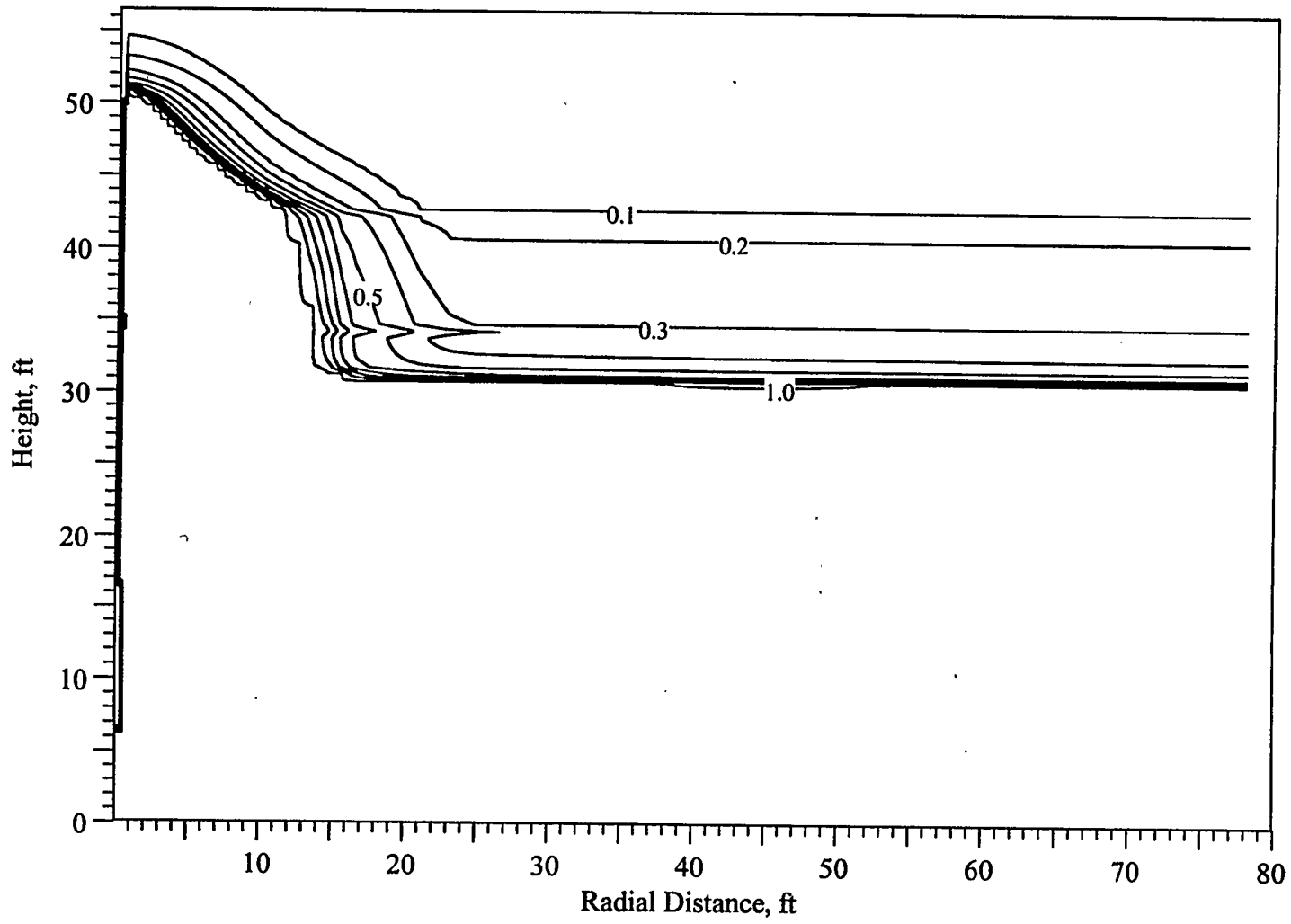

Figure E.7 Saturation Profile at 63 Days, Simulation HPI
(Operational Field Test #13, March 19, 1996)

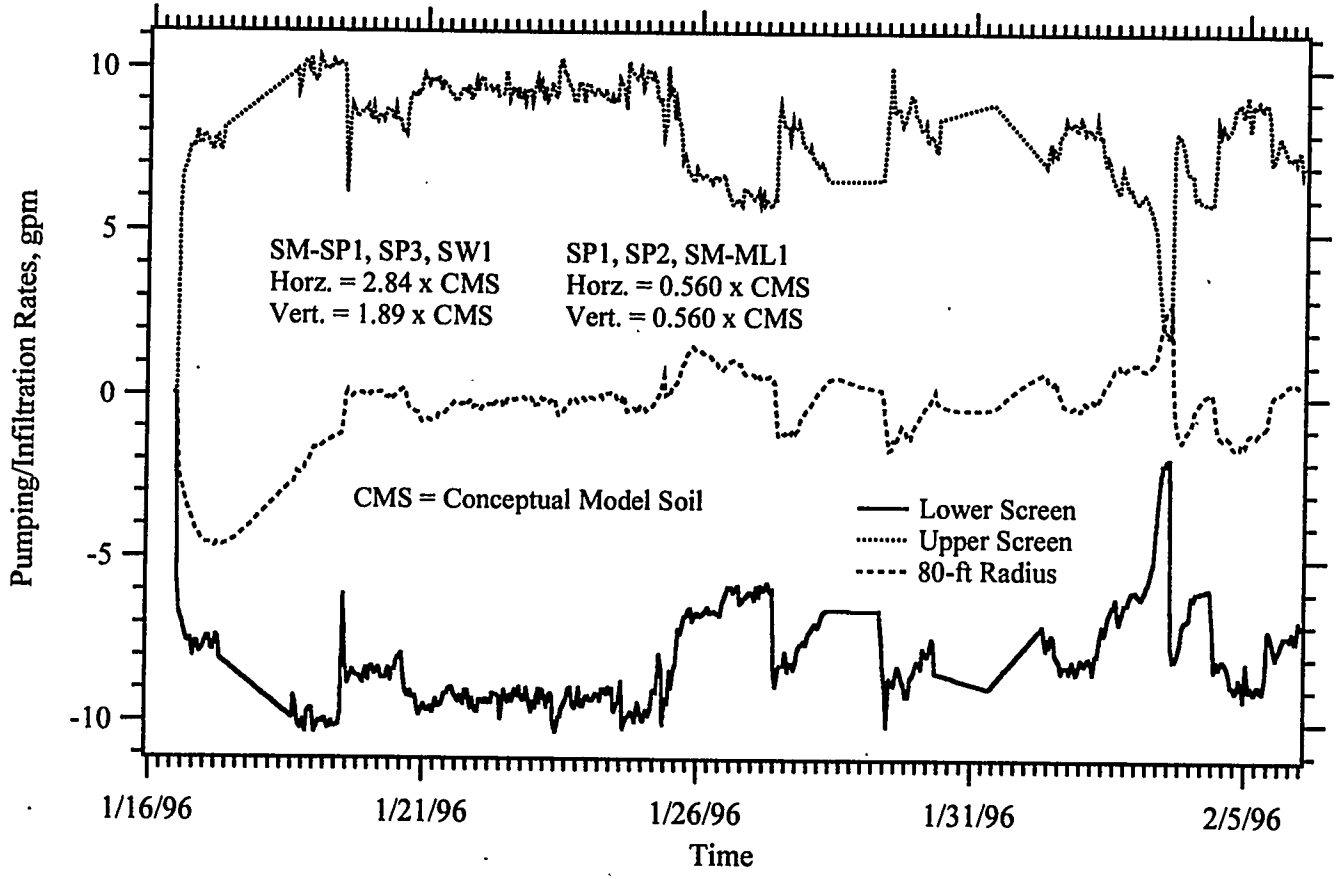

Figure E.8 Pumping/Infiltration Rates Versus Time, Simulation HPI
(Operational Field Test #13, January 16, 1996 - February 6, 1996)

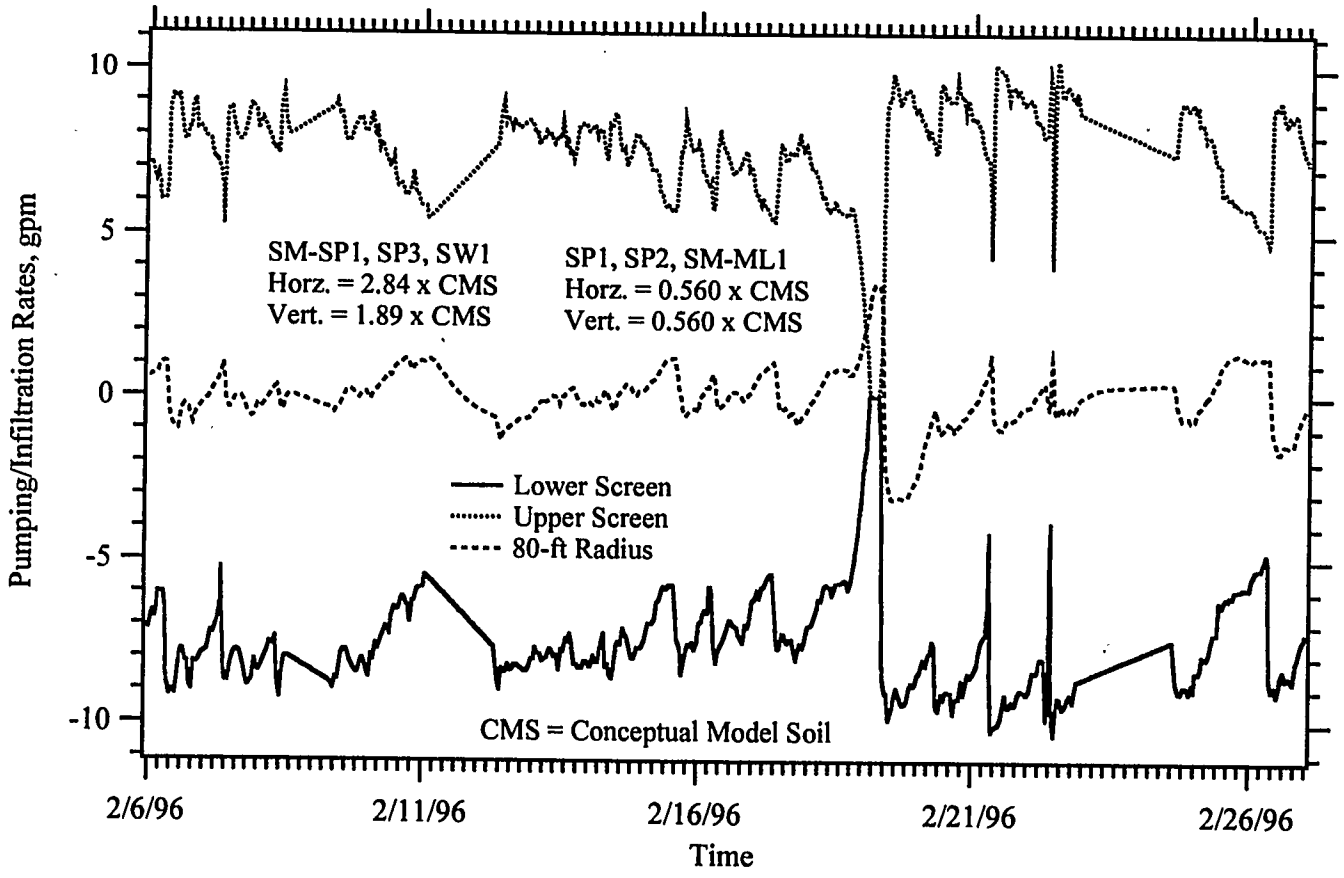

Figure E.9 Pumping/Infiltration Rates Versus Time, Simulation HPI
(Operational Field Test #13, February 6, 1996 - February 27, 1996)

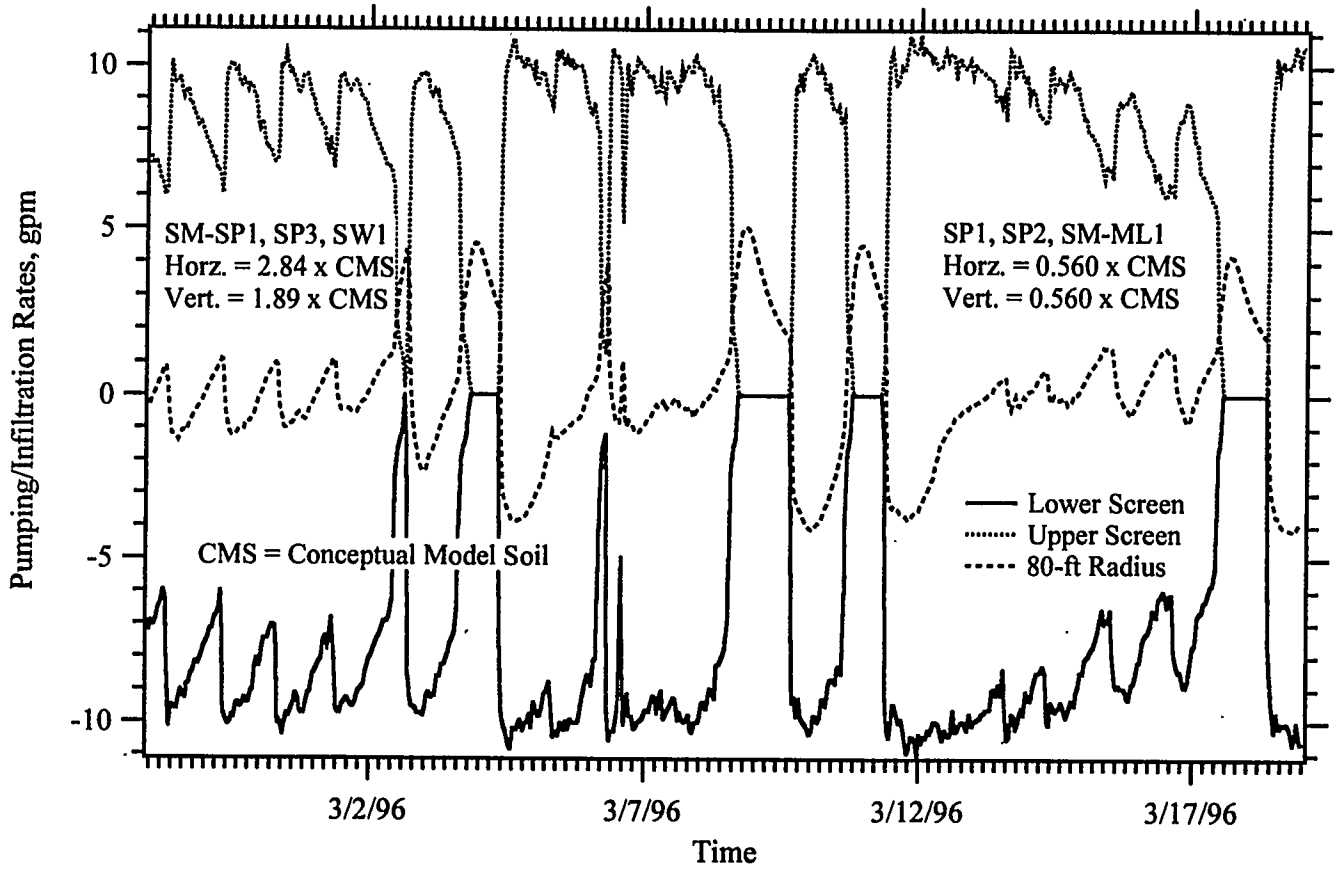

Figure E.10 Pumping/Infiltration Rates Versus Time, Simulation HPI
(Operational Field Test #13, February 27, 1996 - March 19, 1996)

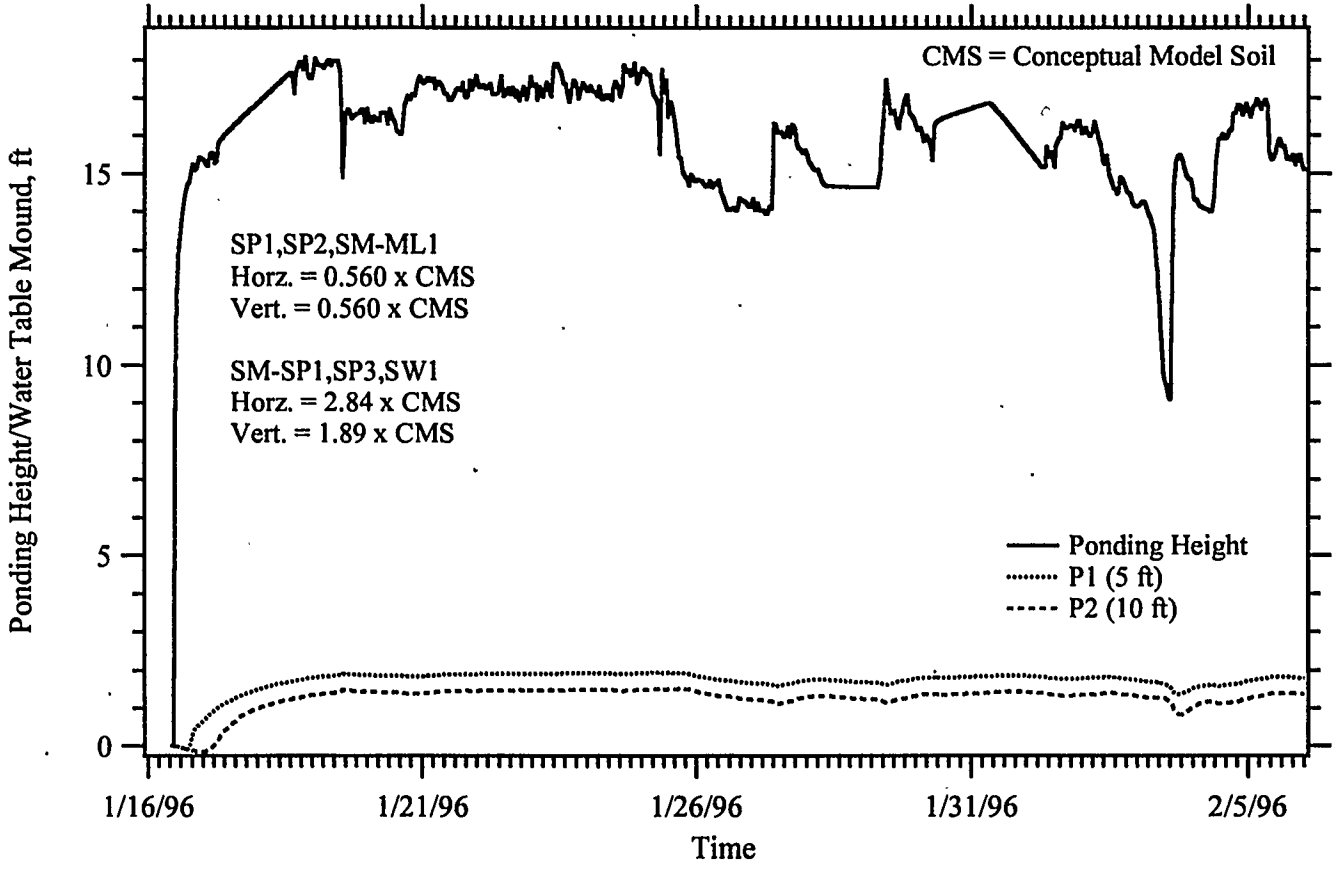

Figure E.11 Ponding Height/Water Table Mound Versus Time, Simulation HPI
(Operational Field Test #13, January 16, 1996 - February 6, 1996)

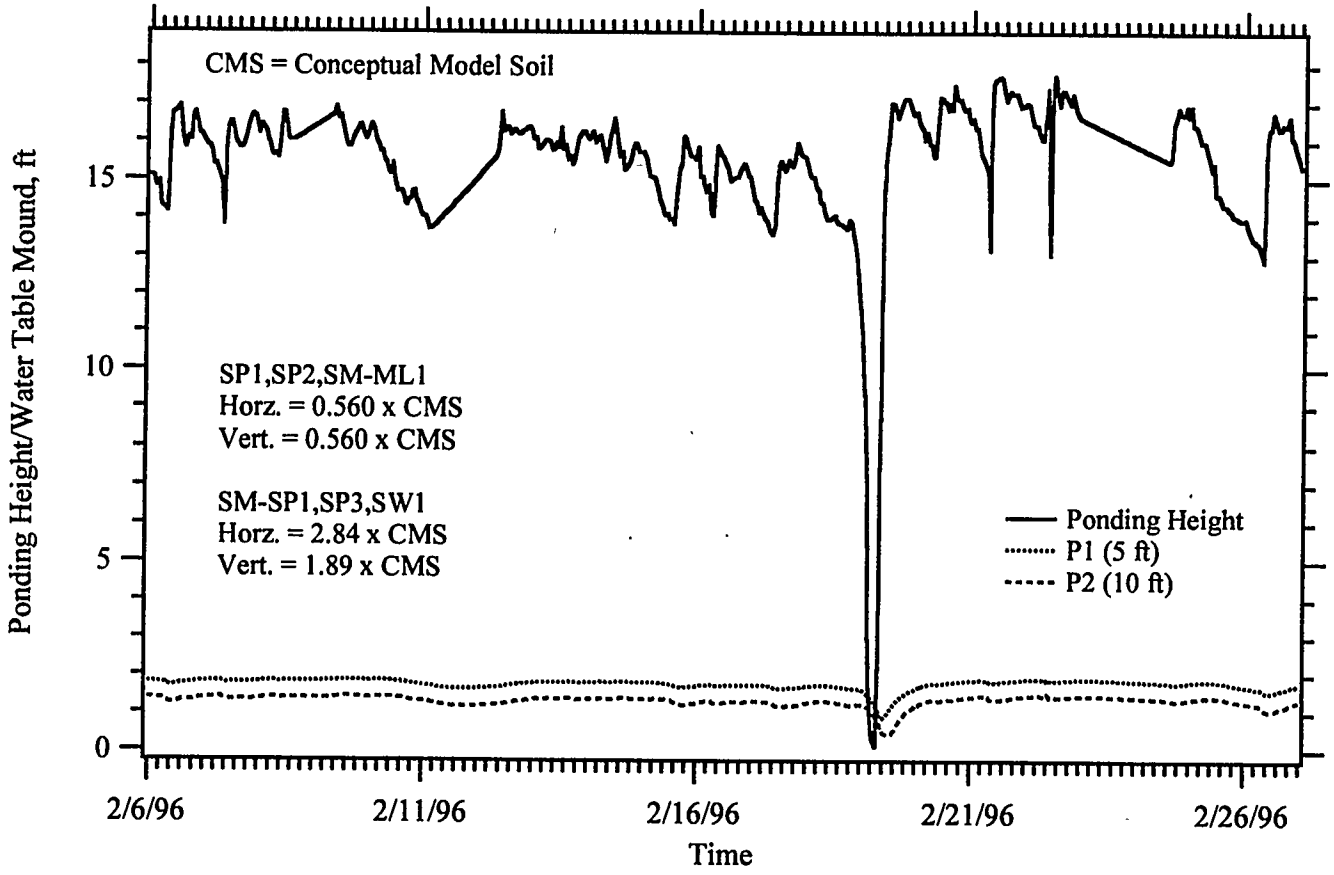

Figure E.12 Ponding Height/Water Table Mound Versus Time, Simulation HPI
(Operational Field Test #13, February 6, 1996 - February 27, 1996)

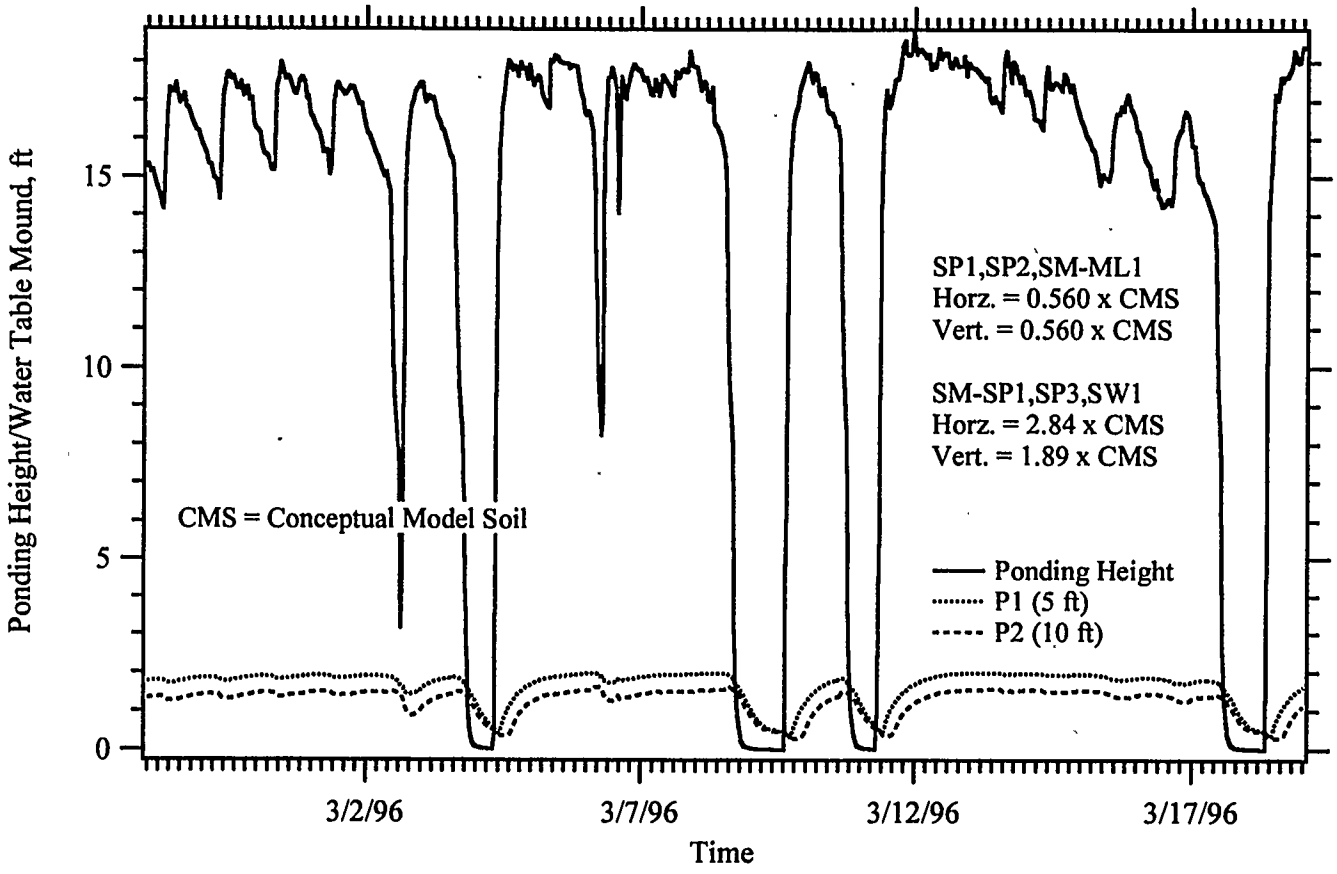

Figure E.13 Ponding Height/Water Table Mound Versus Time, Simulation HPI
(Operational Field Test #13, February 27, 1996 - March 19, 1996)

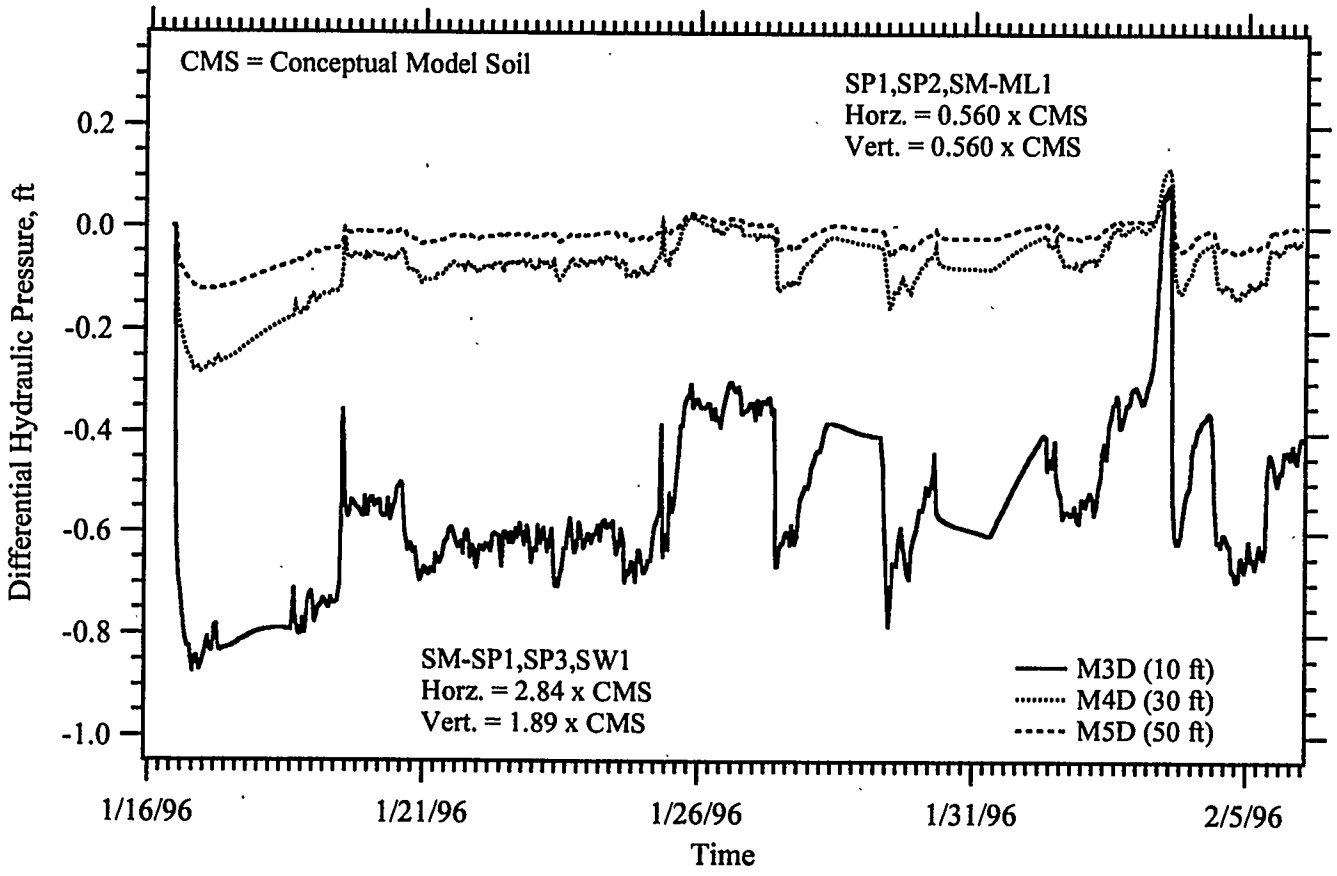

Figure E.14 Differential Hydraulic Pressure Versus Time, Simulation HPI
(Operational Field Test #13, January 16, 1996 - February 6, 1996)

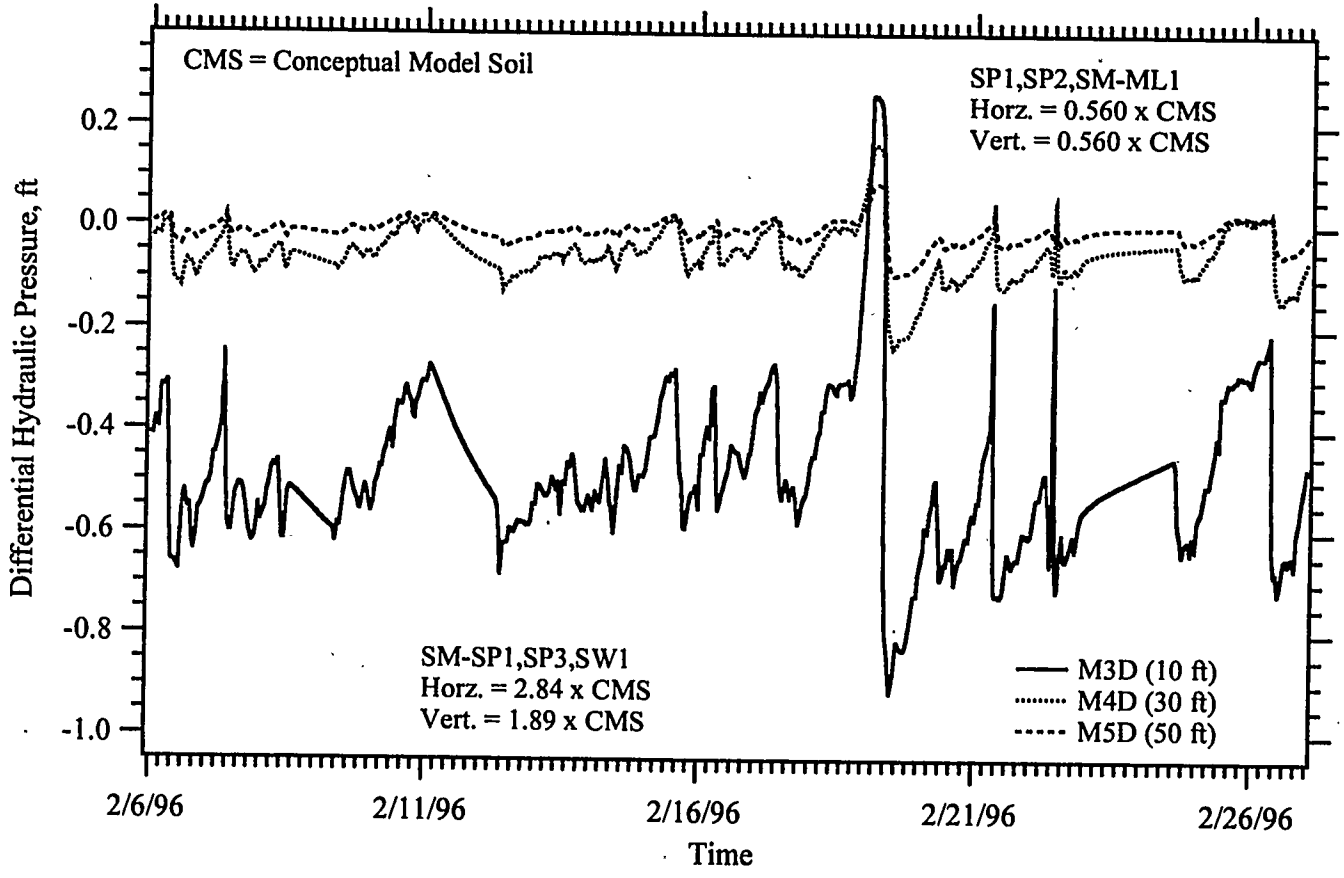

Figure E.15 Differential Hydraulic Pressure Versus Time, Simulation HPI
(Operational Field Test #13, February 6, 1996 - February 27, 1996)

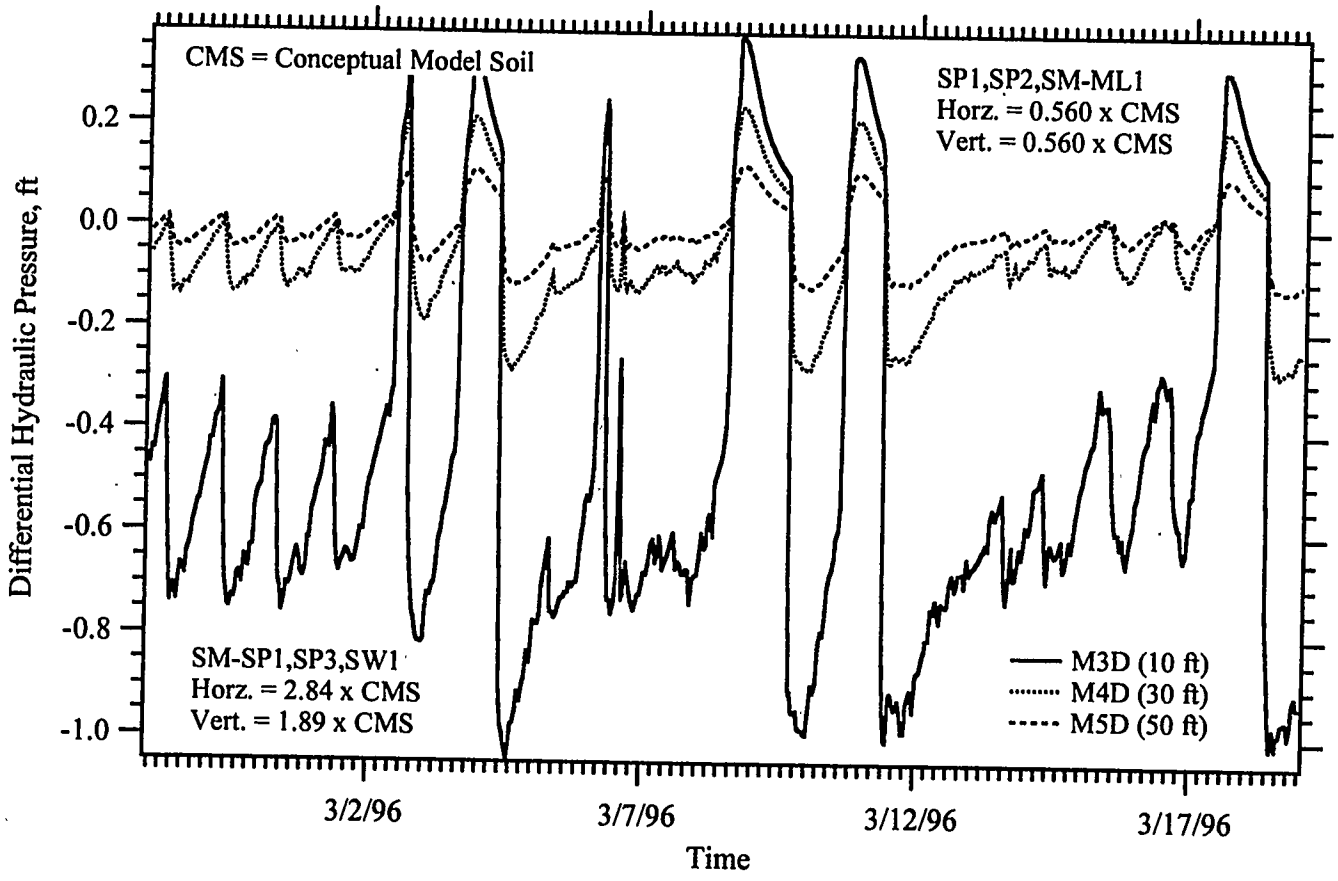

Figure E.16 Differential Hydraulic Pressure Versus Time, Simulation HPI
(Operational Field Test #13, February 27, 1996 - March 19, 1996)

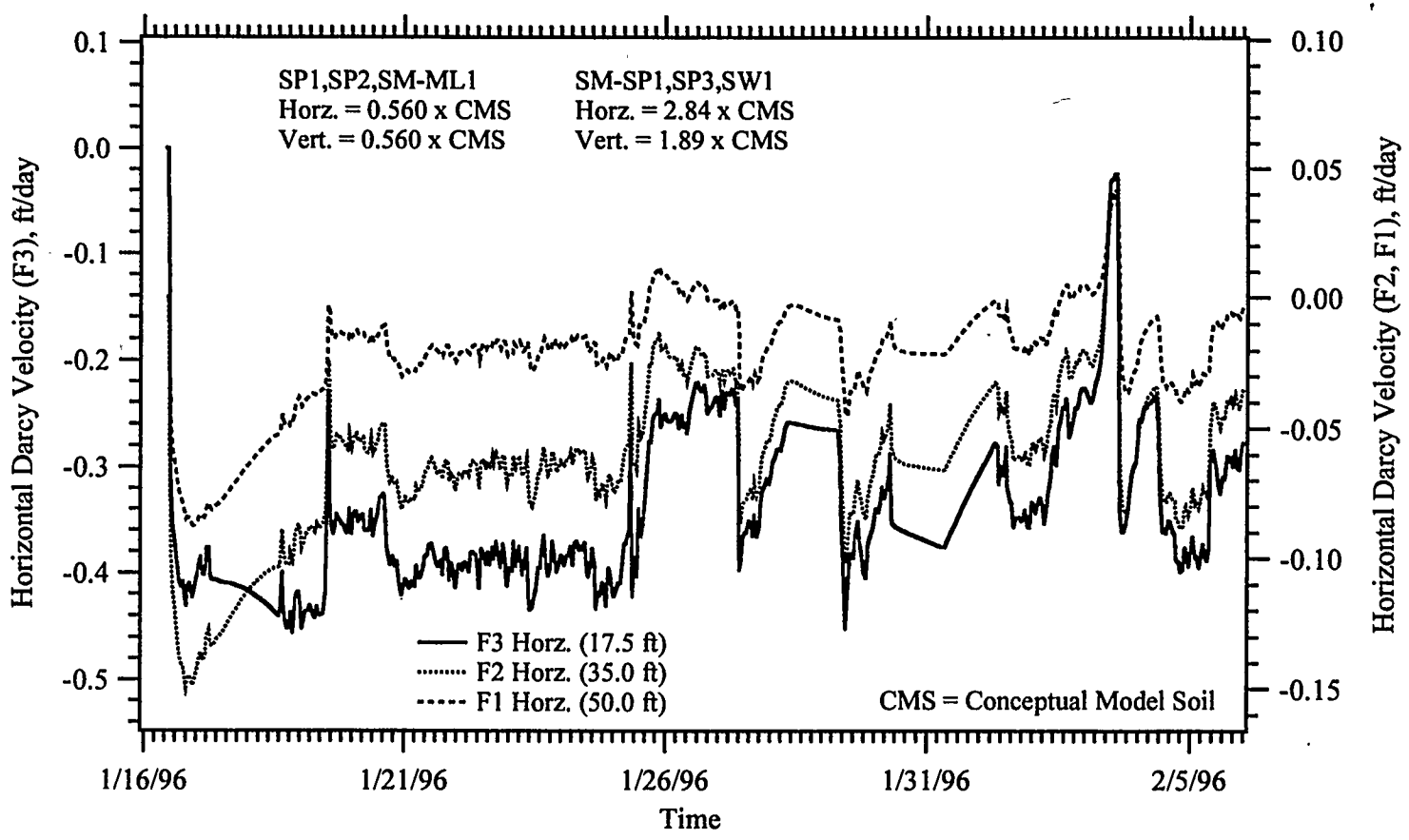

Figure E.17 Horizontal Darcy Velocity Versus Time, Simulation HPI
(Operational Field Test #13, January 16, 1996 - February 6, 1996)

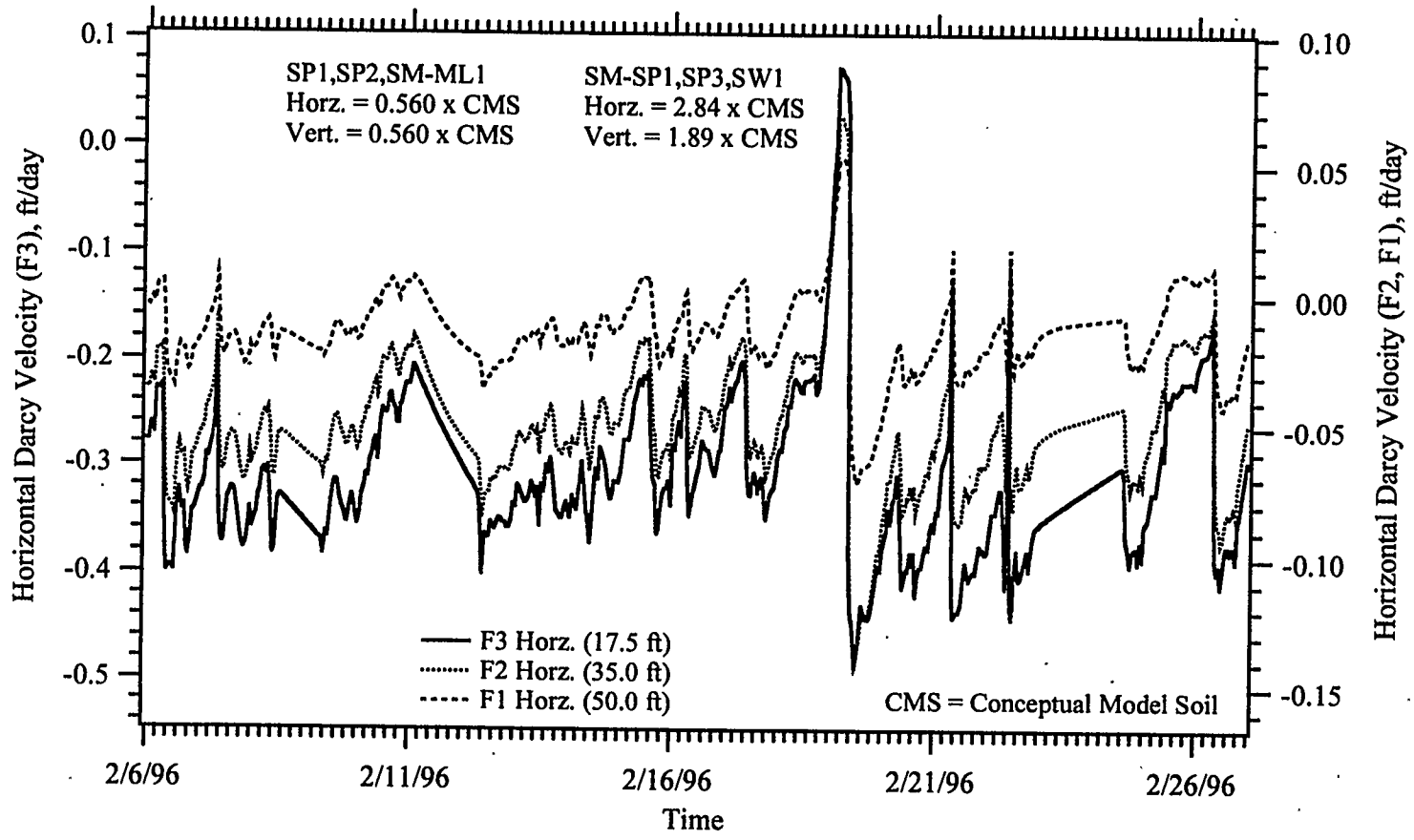

Figure E.18 Horizontal Darcy Velocity Versus Time, Simulation HPI
(Operational Field Test #13, February 6, 1996 - February 27, 1996)

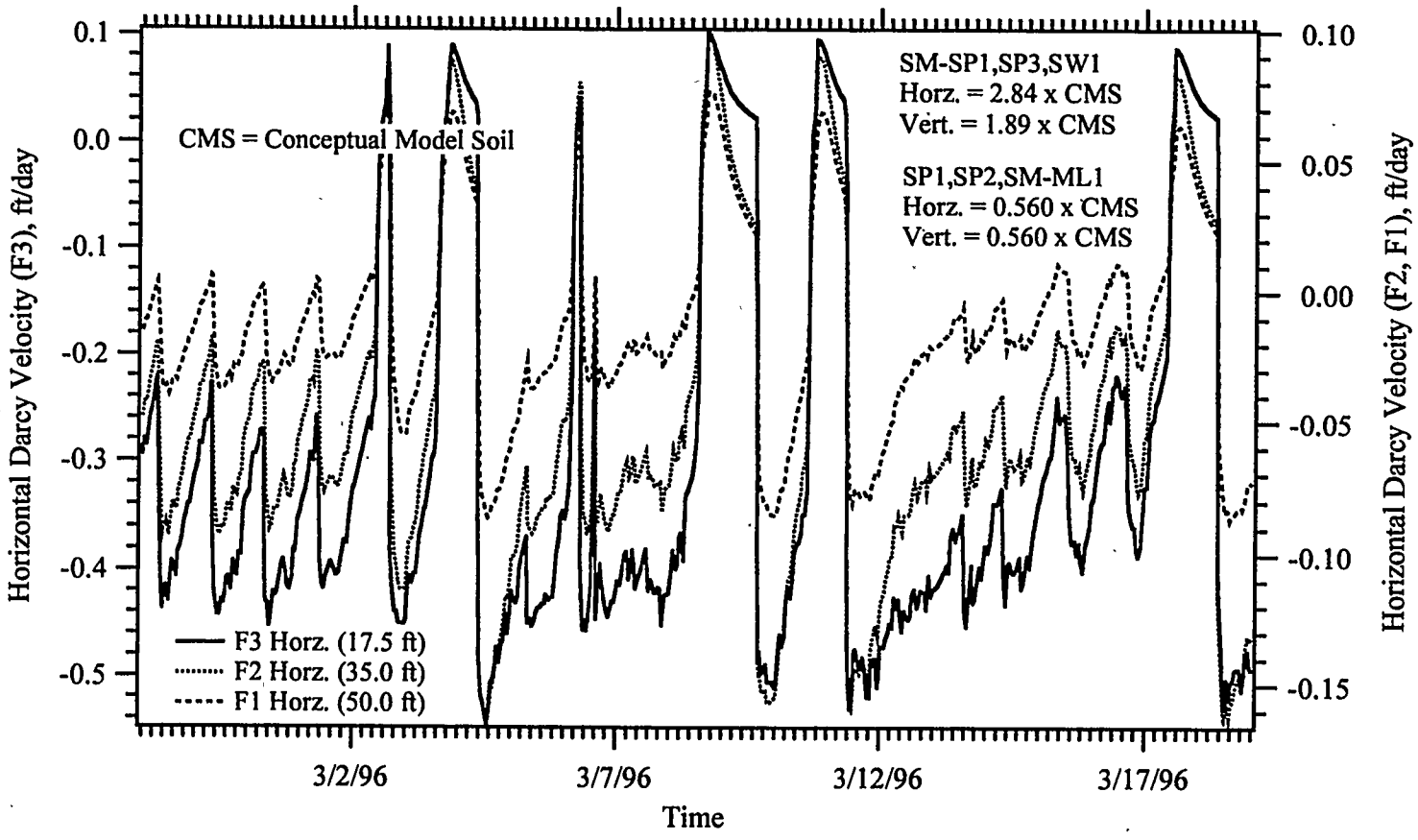

Figure E.19 Horizontal Darcy Velocity Versus Time, Simulation HPI
(Operational Field Test #13, February 27, 1996 - March 19, 1996)

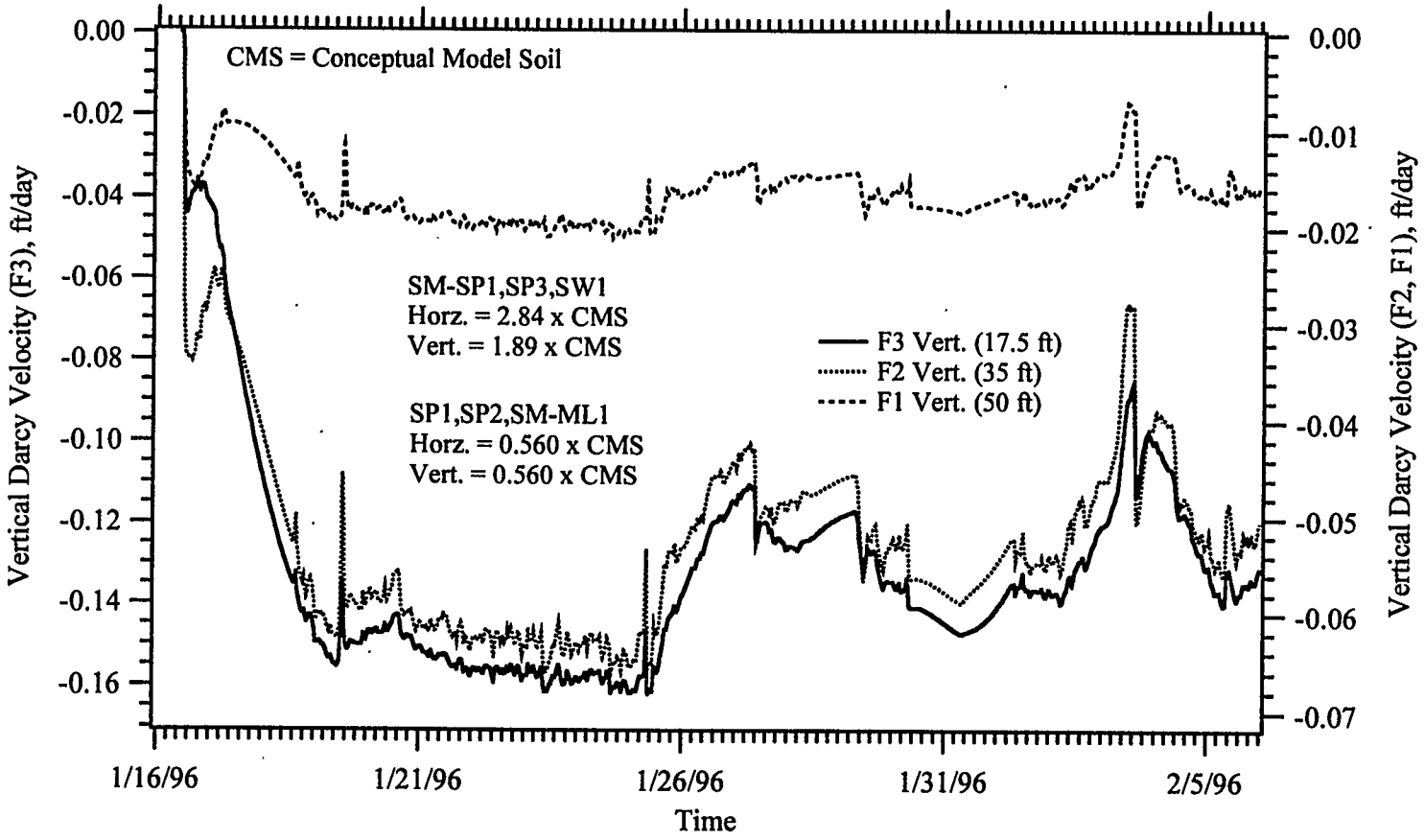

Figure E.20 Vertical Darcy Velocity Versus Time, Simulation HPI
(Operational Field Test #13, January 16, 1996 - February 6, 1996)

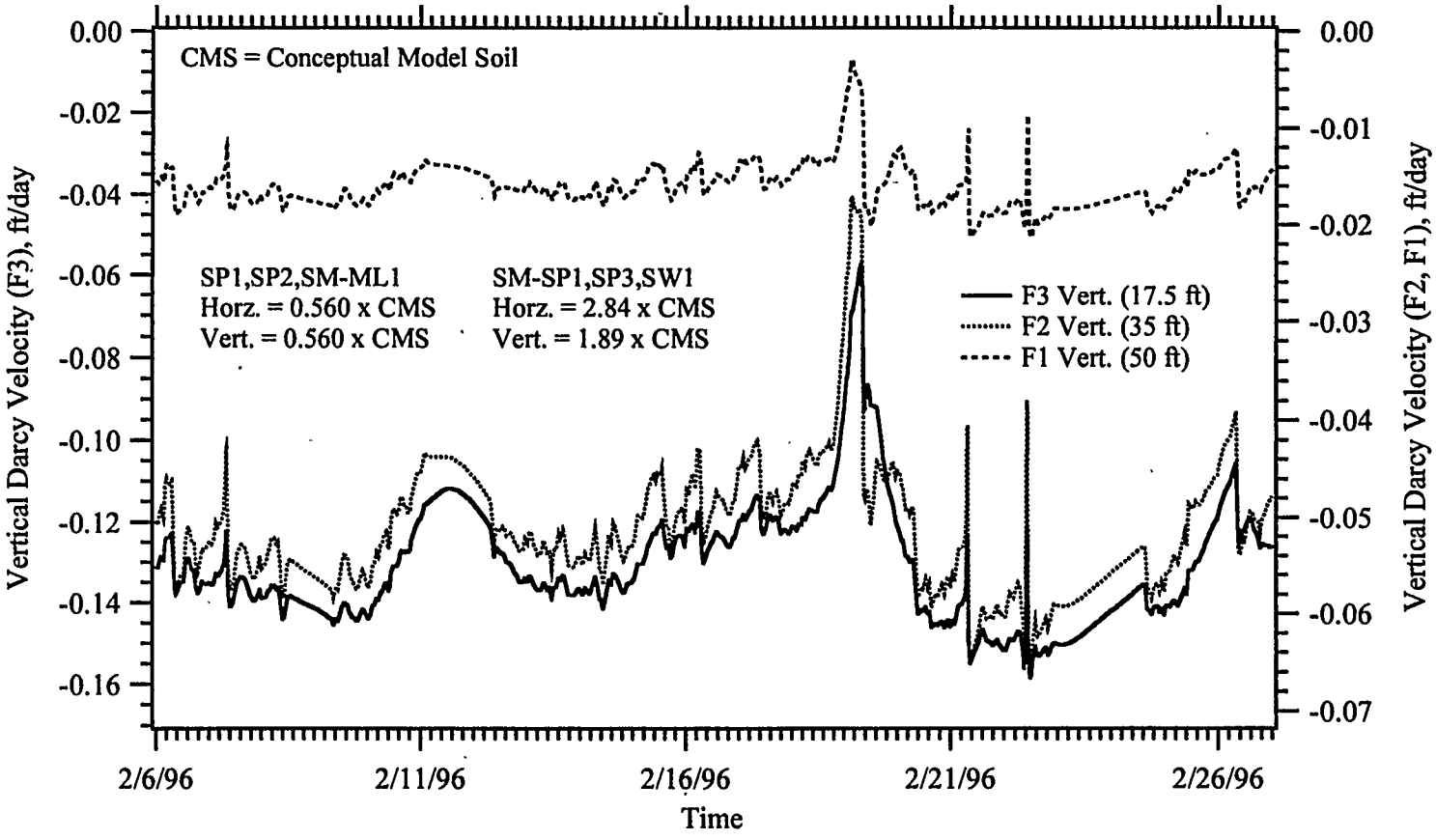

Figure E.21 Vertical Darcy Velocity Versus Time, Simulation HPI
(Operational Field Test #13, February 6, 1996 - February 27, 1996)

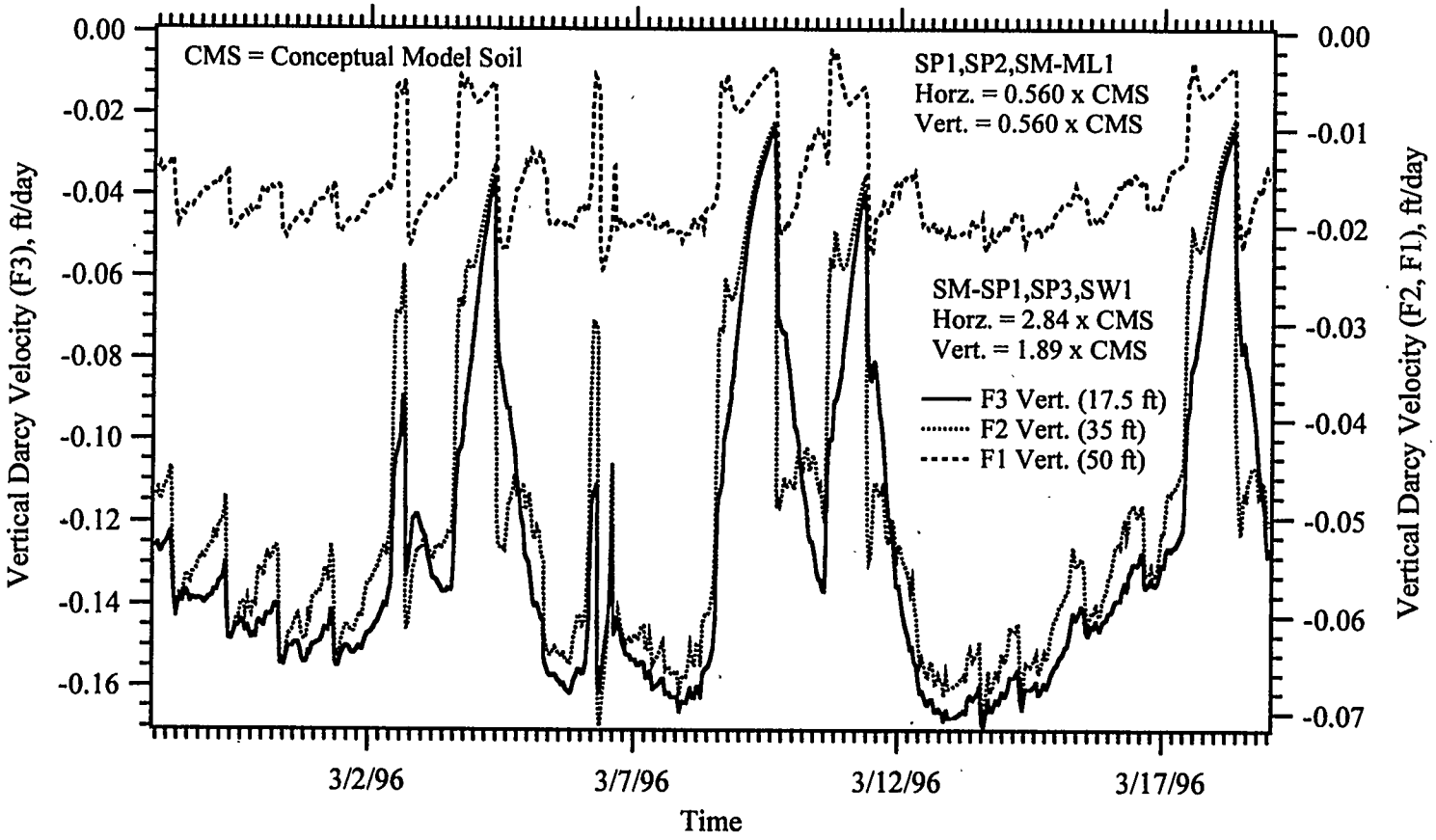

Figure E.22 Vertical Darcy Velocity Versus Time, Simulation HPI
(Operational Field Test #13, February 27, 1996 - March 19, 1996)

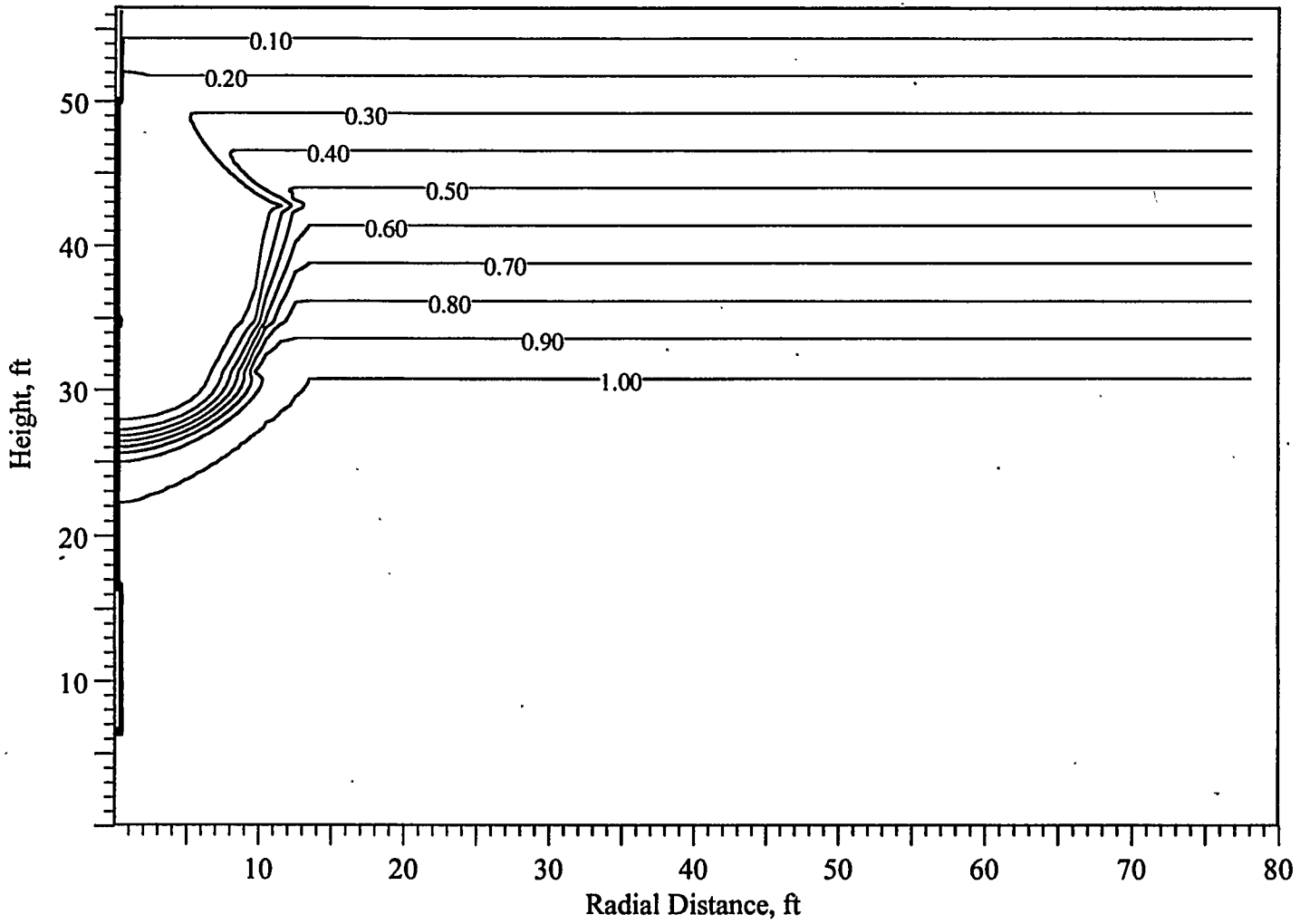

Figure E.23 TCE Concentration Profile at 1 Day, Simulation HPI
(Operational Field Test #13, January 17, 1996)

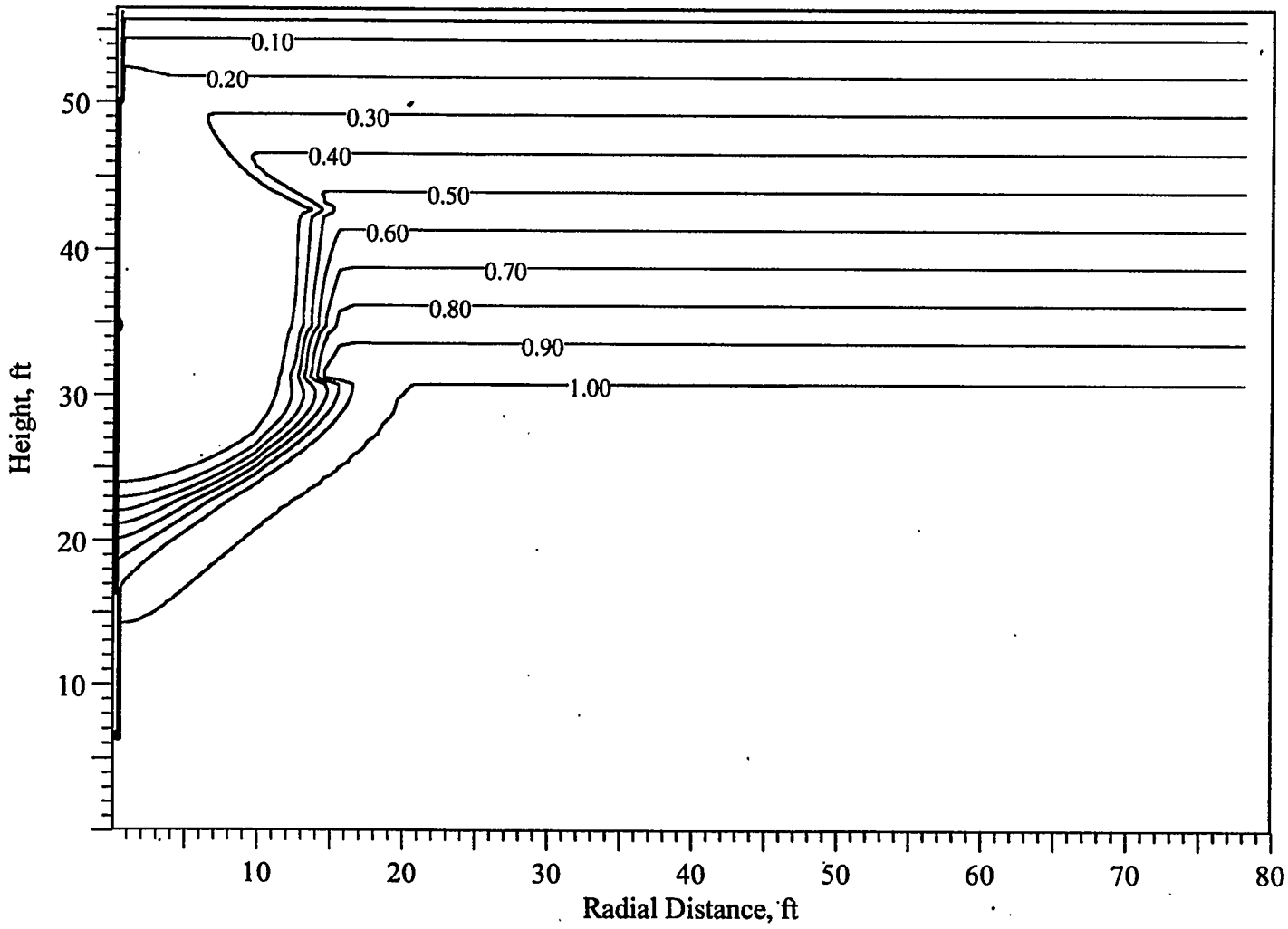

Figure E.24 TCE Concentration Profile at 2 Days, Simulation HPI
(Operational Field Test #13, January 18, 1996)

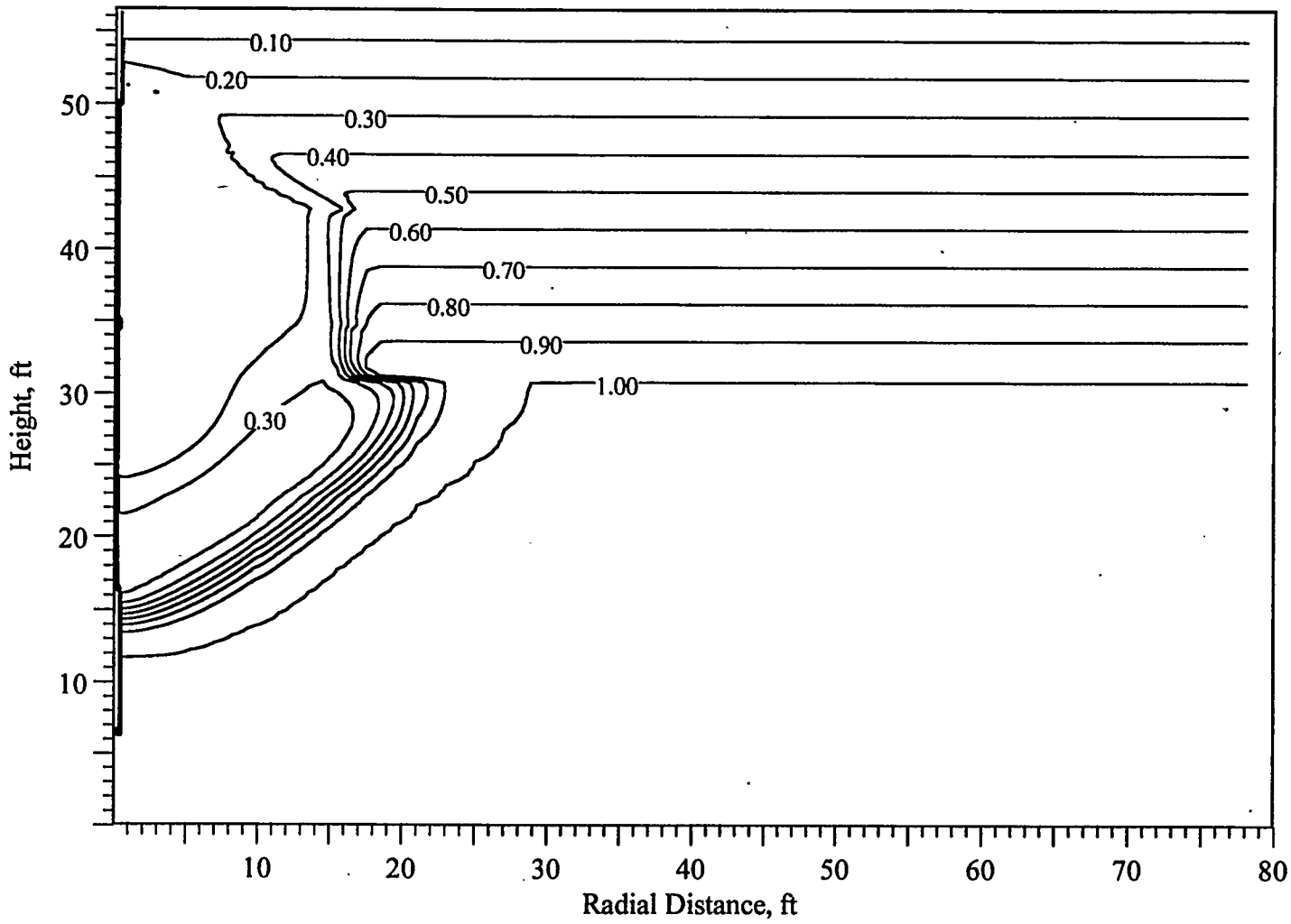

Figure E.25 TCE Concentration Profile at 4 Days, Simulation HPI
(Operational Field Test #13, January 20, 1996)

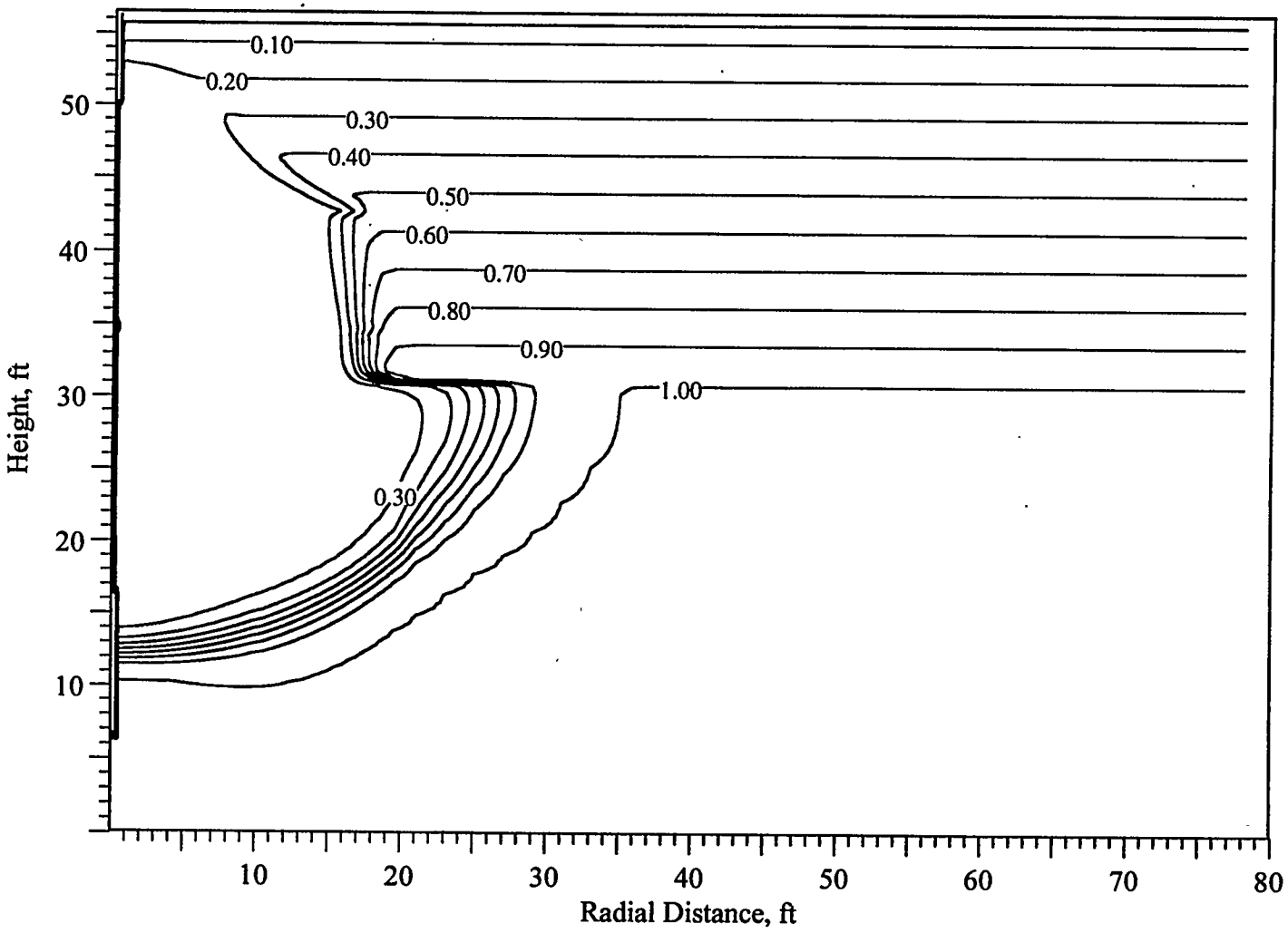

Figure E.26 TCE Concentration Profile at 8 Days, Simulation HPI
(Operational Field Test #13, January 24, 1996)

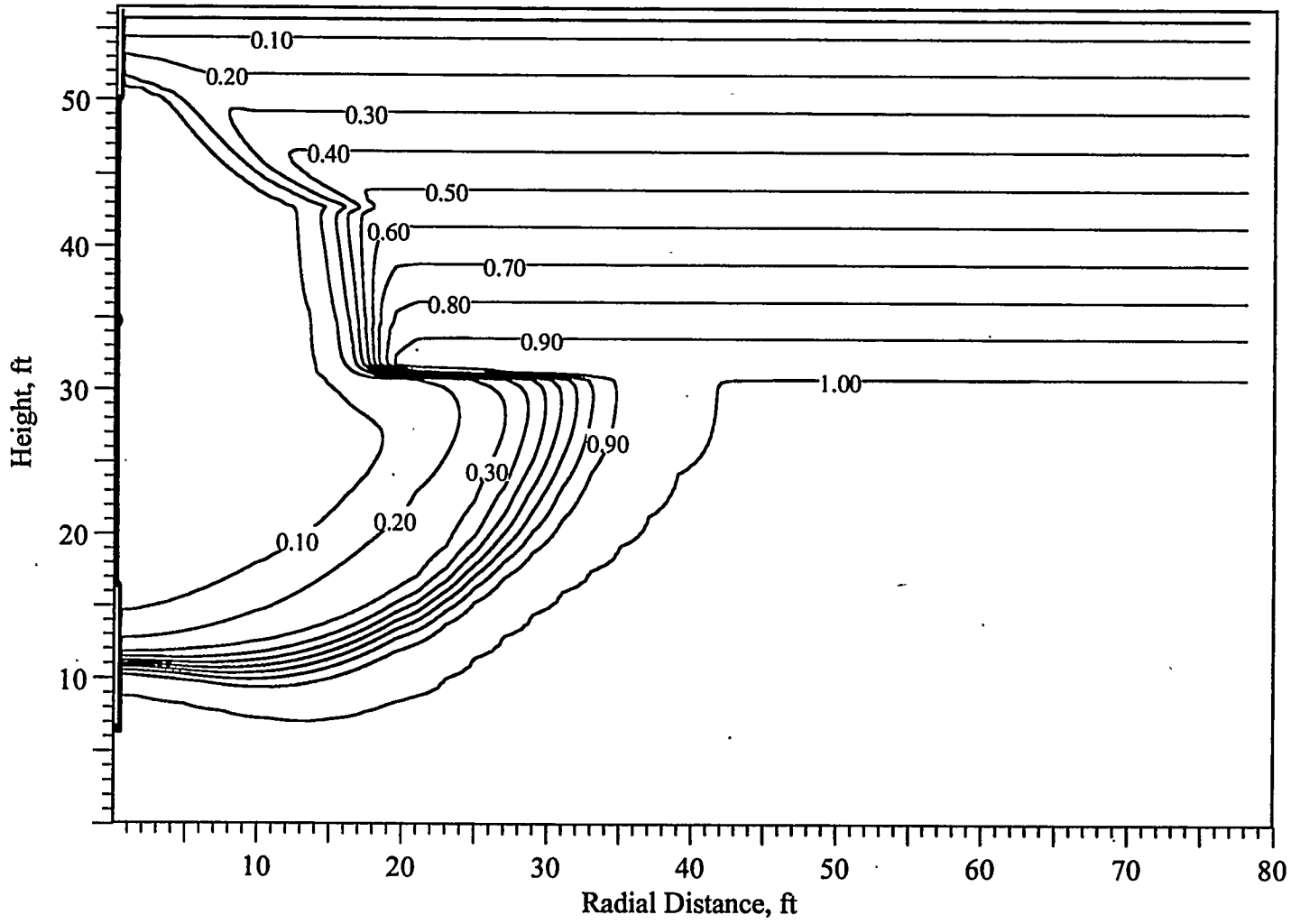

Figure E.27 TCE Concentration Profile at 16 Days, Simulation HPI
(Operational Field Test #13, February 1, 1996)

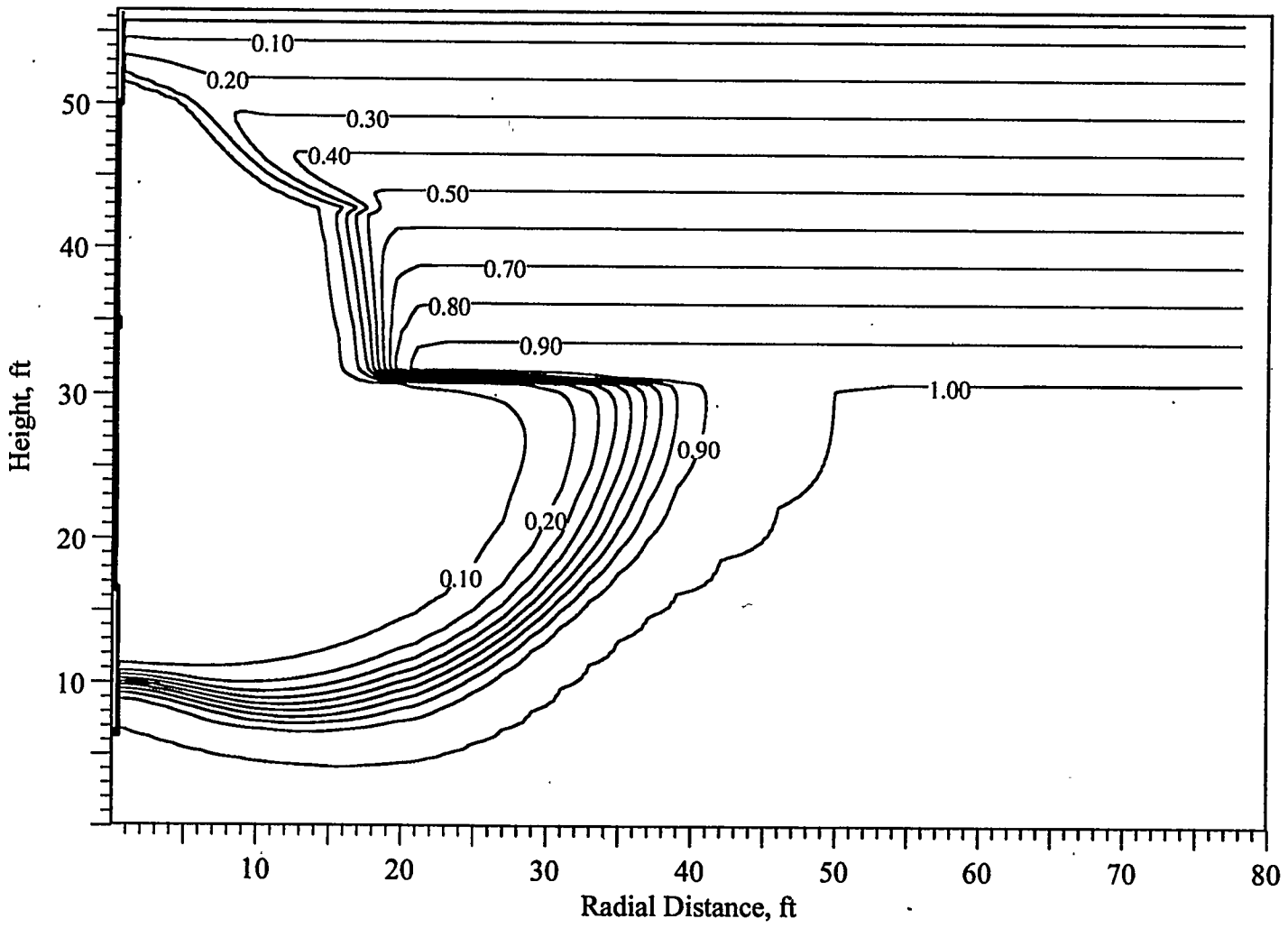

Figure E.28 TCE Concentration Profile at 32 Days, Simulation HPI
(Operational Field Test #13, February 17, 1996)

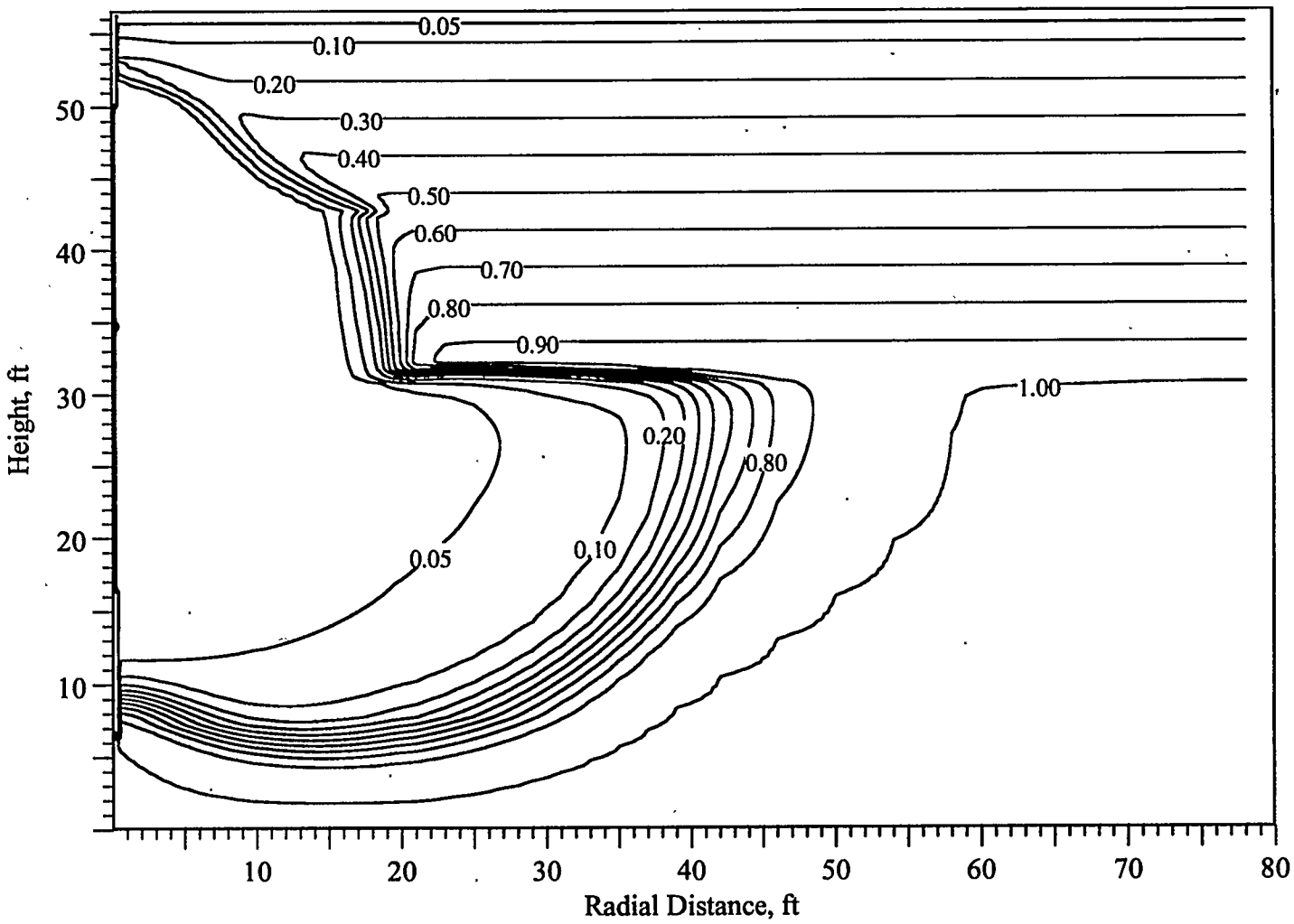

Figure E.29 TCE Concentration Profile at 63 Days, Simulation HPI
(Operational Field Test #13, March 19, 1996)

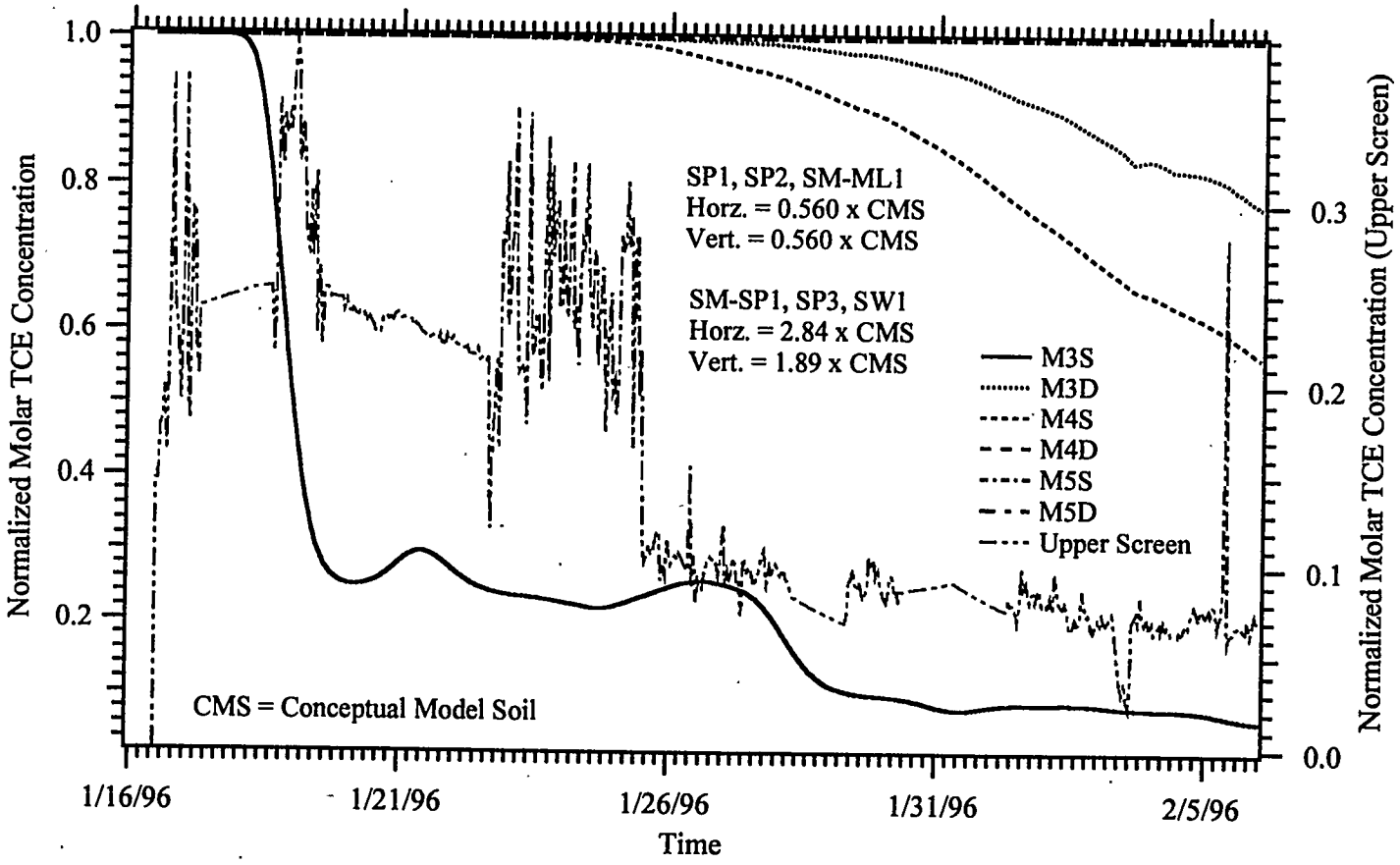

Figure E.30 Dissolved TCE Concentration Versus Time, Simulation HPI
(Operational Field Test #13, January 16, 1996 - February 6, 1996)

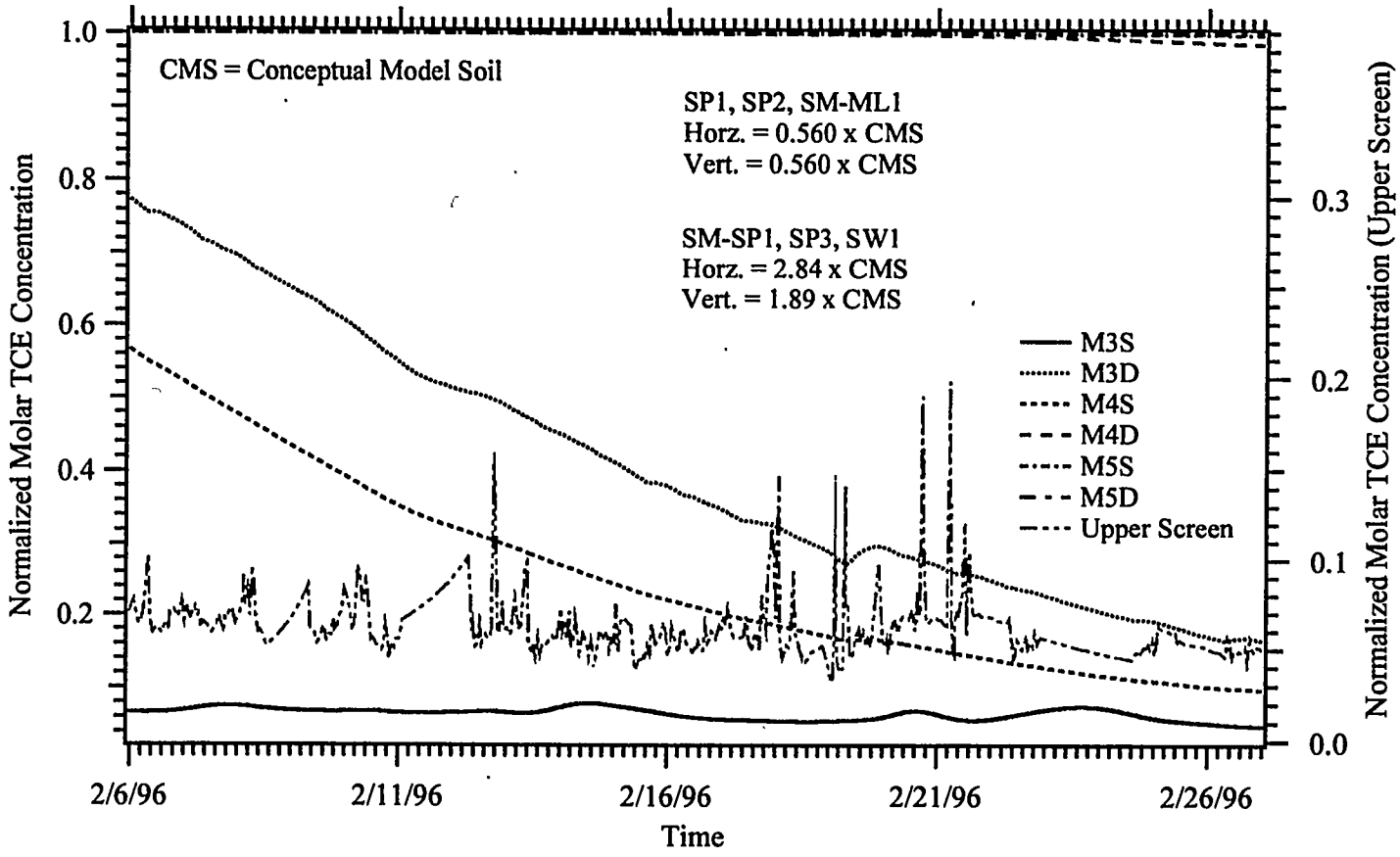

Figure E.31 Dissolved TCE Concentration Versus Time, Simulation HPI
(Operational Field Test #13, February 6, 1996 - February 27, 1996)

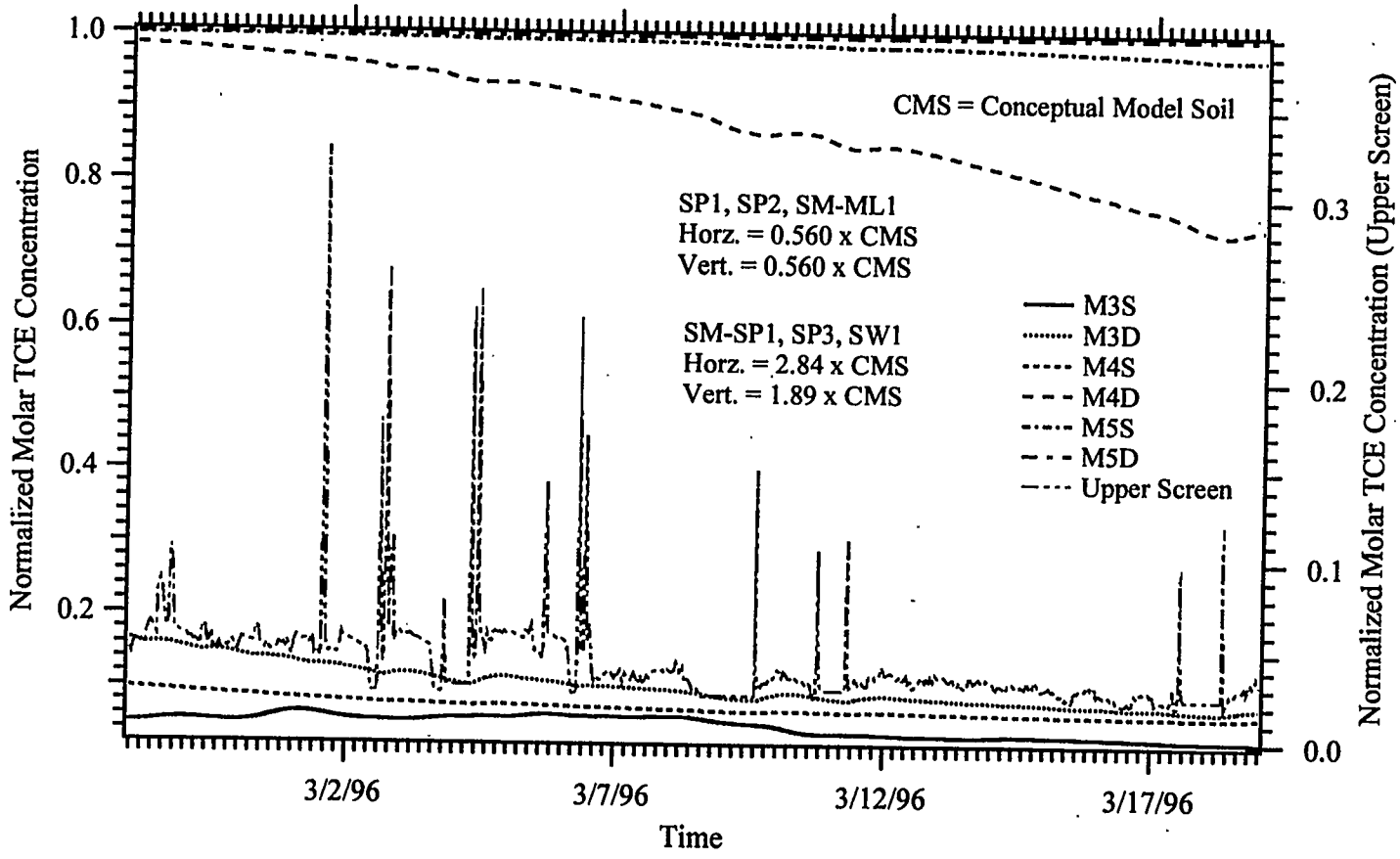

Figure E.32 Dissolved TCE Concentration Versus Time, Simulation HPI
(Operational Field Test #13, February 27, 1996 - March 19, 1996)

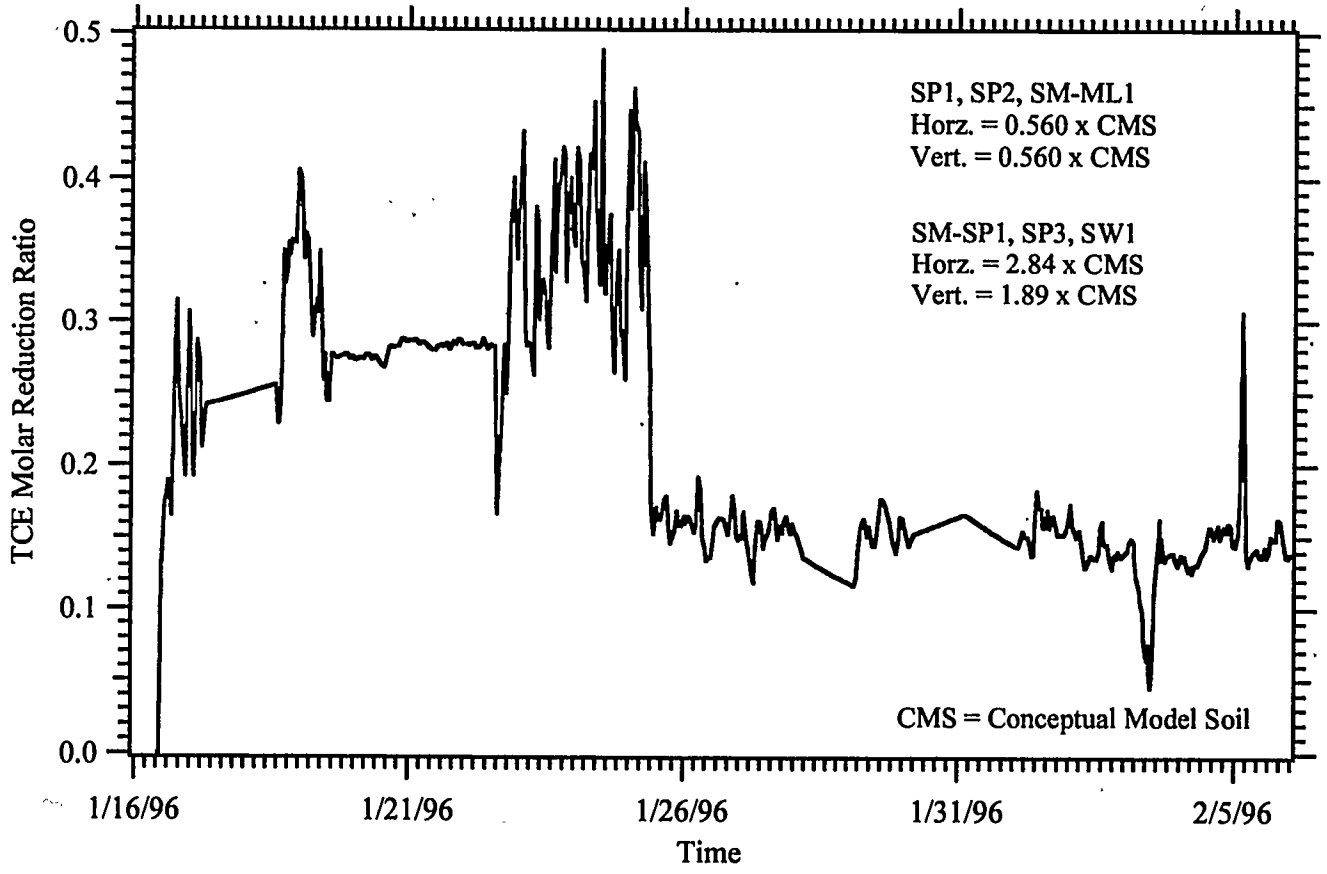

Figure E.33 TCE Molar Reduction Ratio Versus Time, Simulation HPI
(Operational Field Test #13, January 16, 1996 - February 6, 1996)

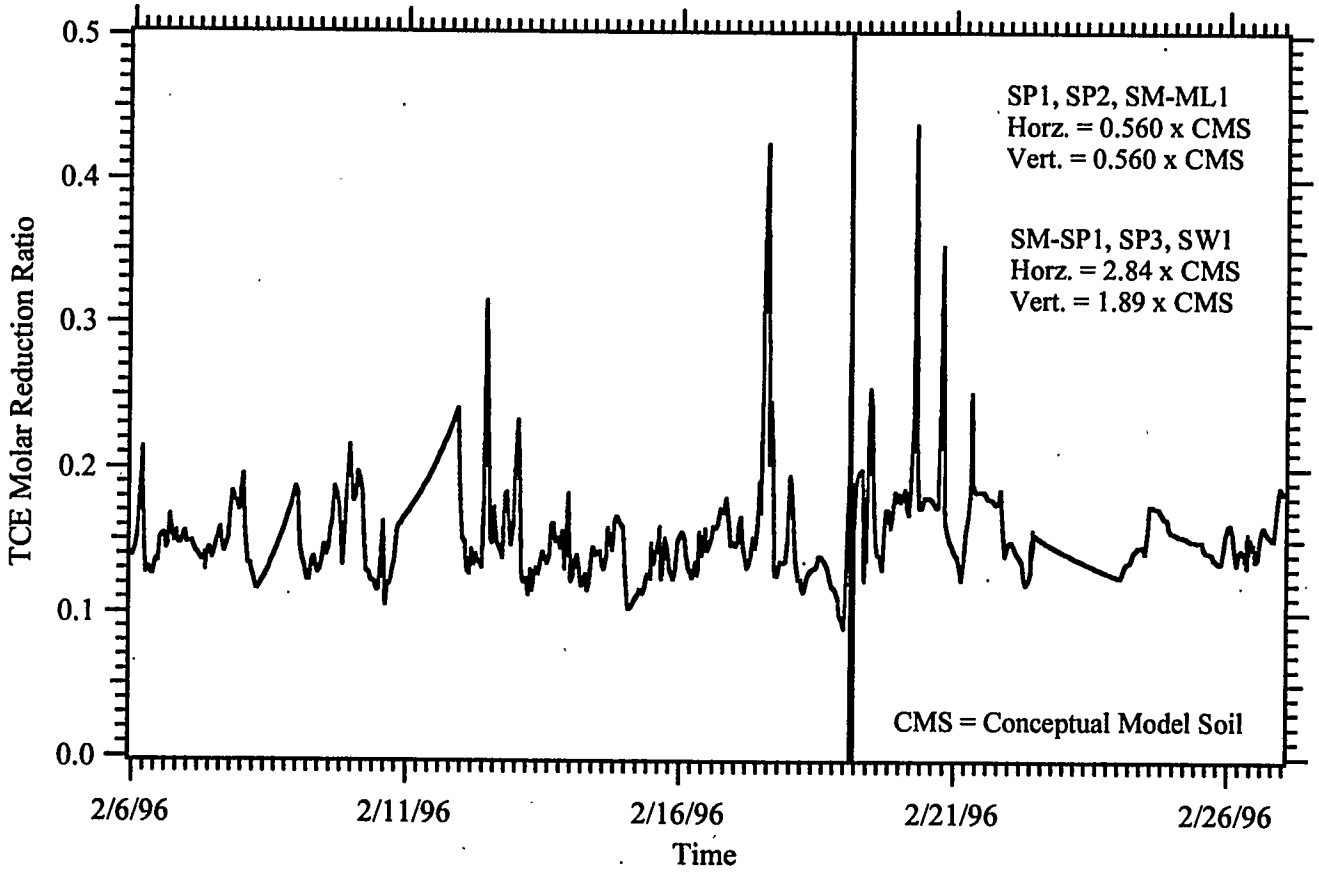

Figure E.34 TCE Molar Reduction Ratio Versus Time, Simulation HPI
(Operational Field Test #13, February 6, 1996 - February 27, 1996)

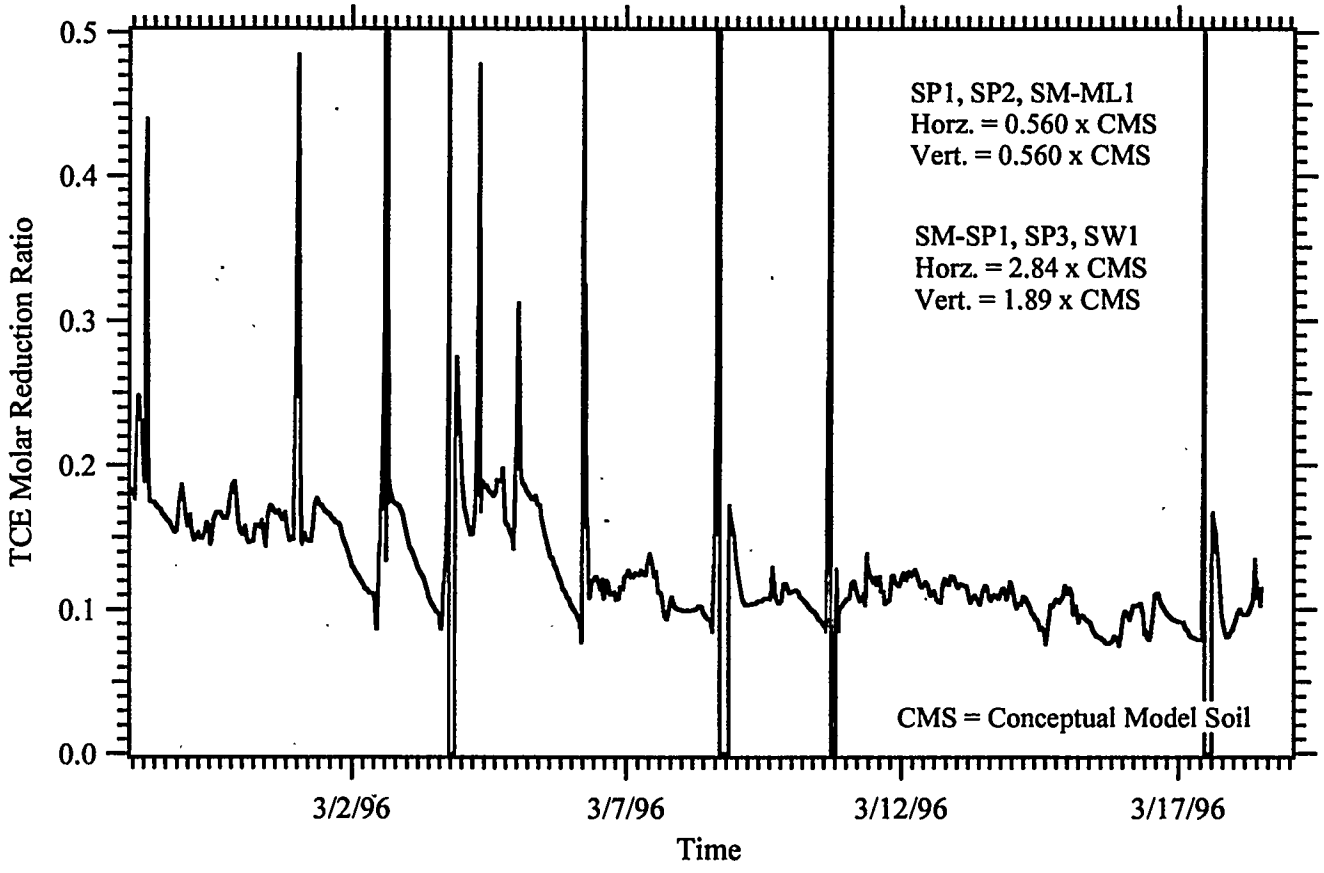

Figure E.35 TCE Molar Reduction Ratio Versus Time, Simulation HPI
(Operational Field Test #13, February 27, 1996 - March 19, 1996)

APPENDIX F

HIGH-PERMEABILITY ANISOTROPIC SIMULATION RESULTS

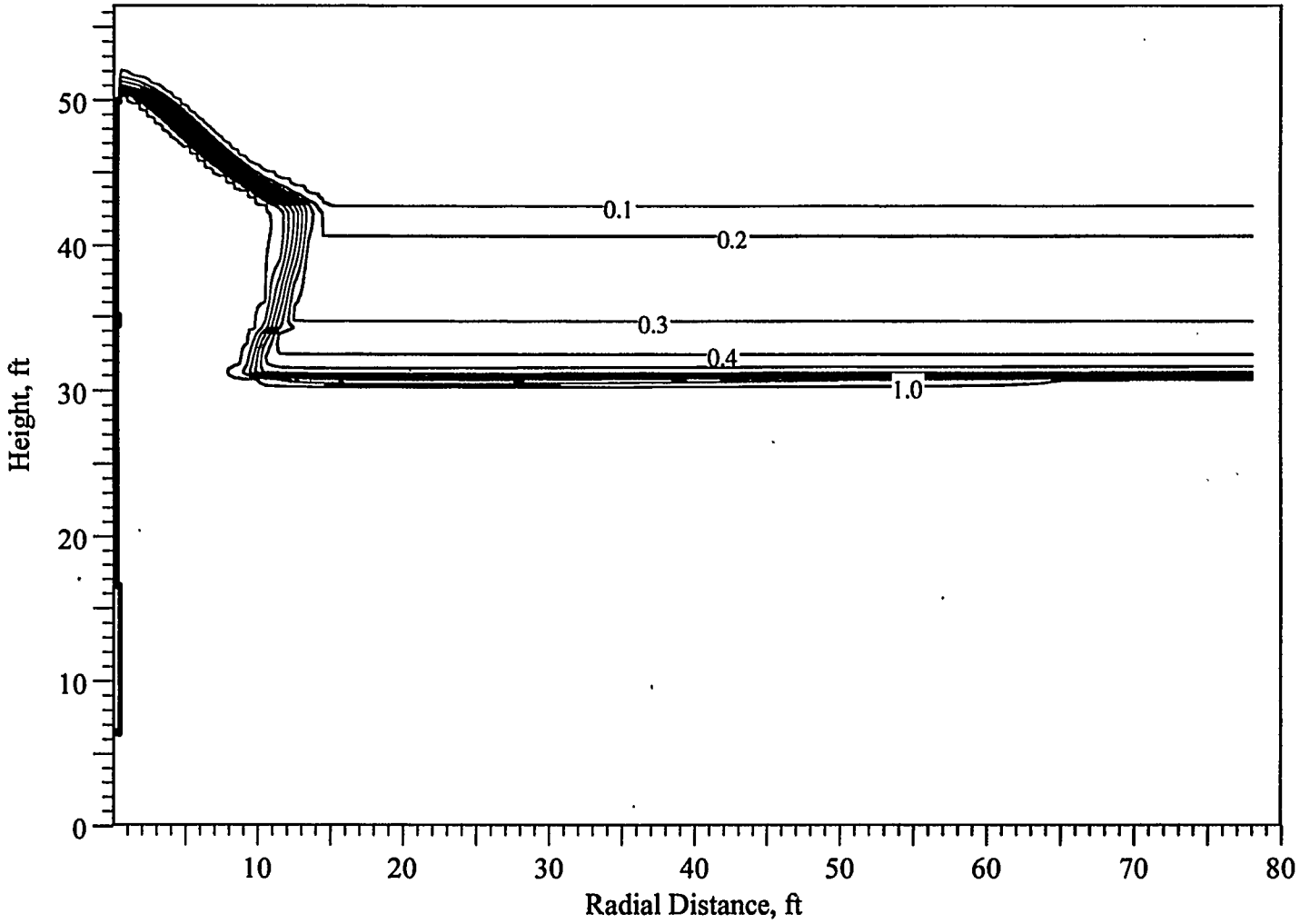

Figure F.1 Saturation Profile at 1 Day, Simulation HPA
(Operational Field Test #13, January 17, 1996)

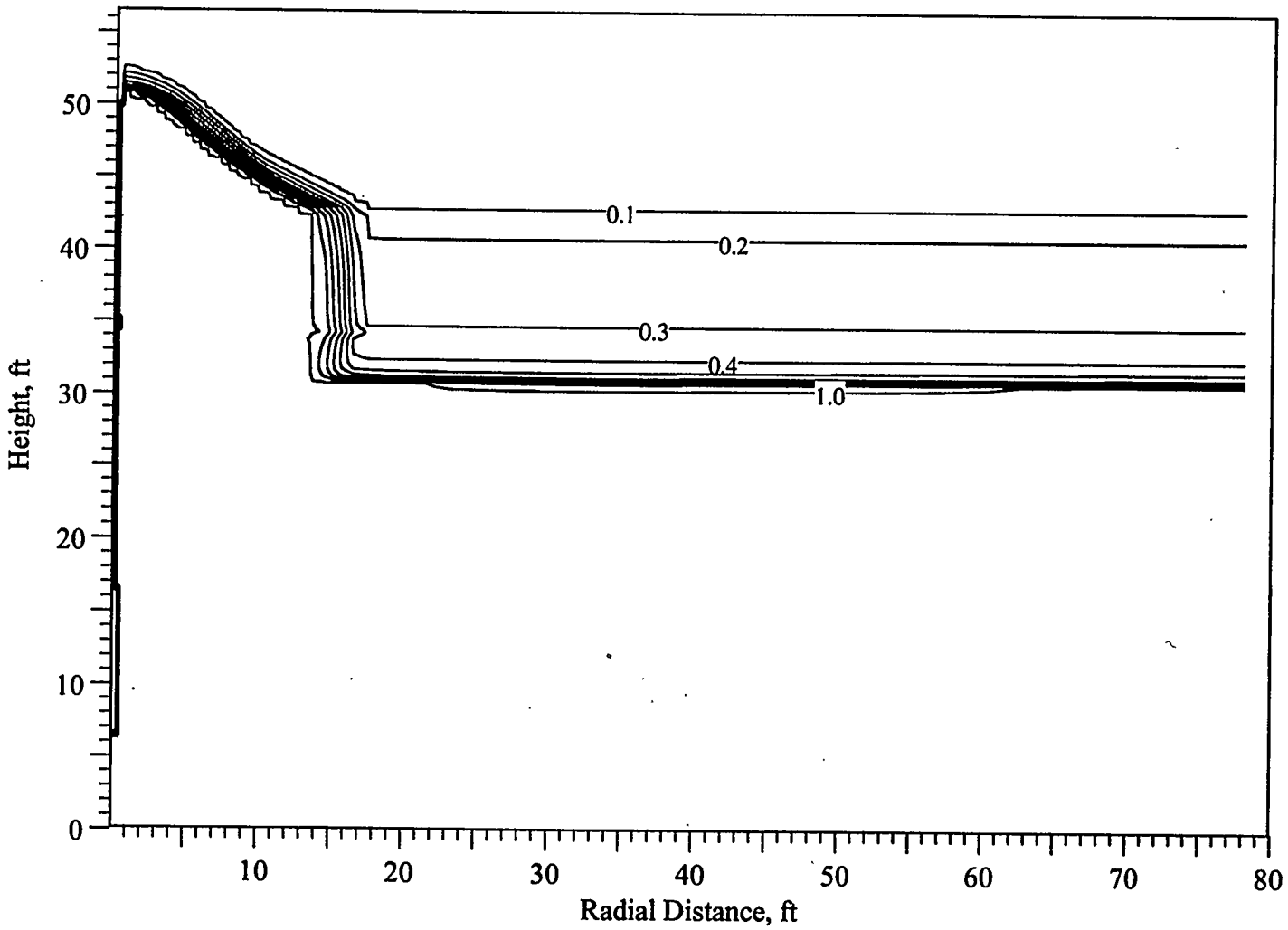

Figure F.2 Saturation Profile at 2 Days, Simulation HPA
(Operational Field Test #13, January 18, 1996)

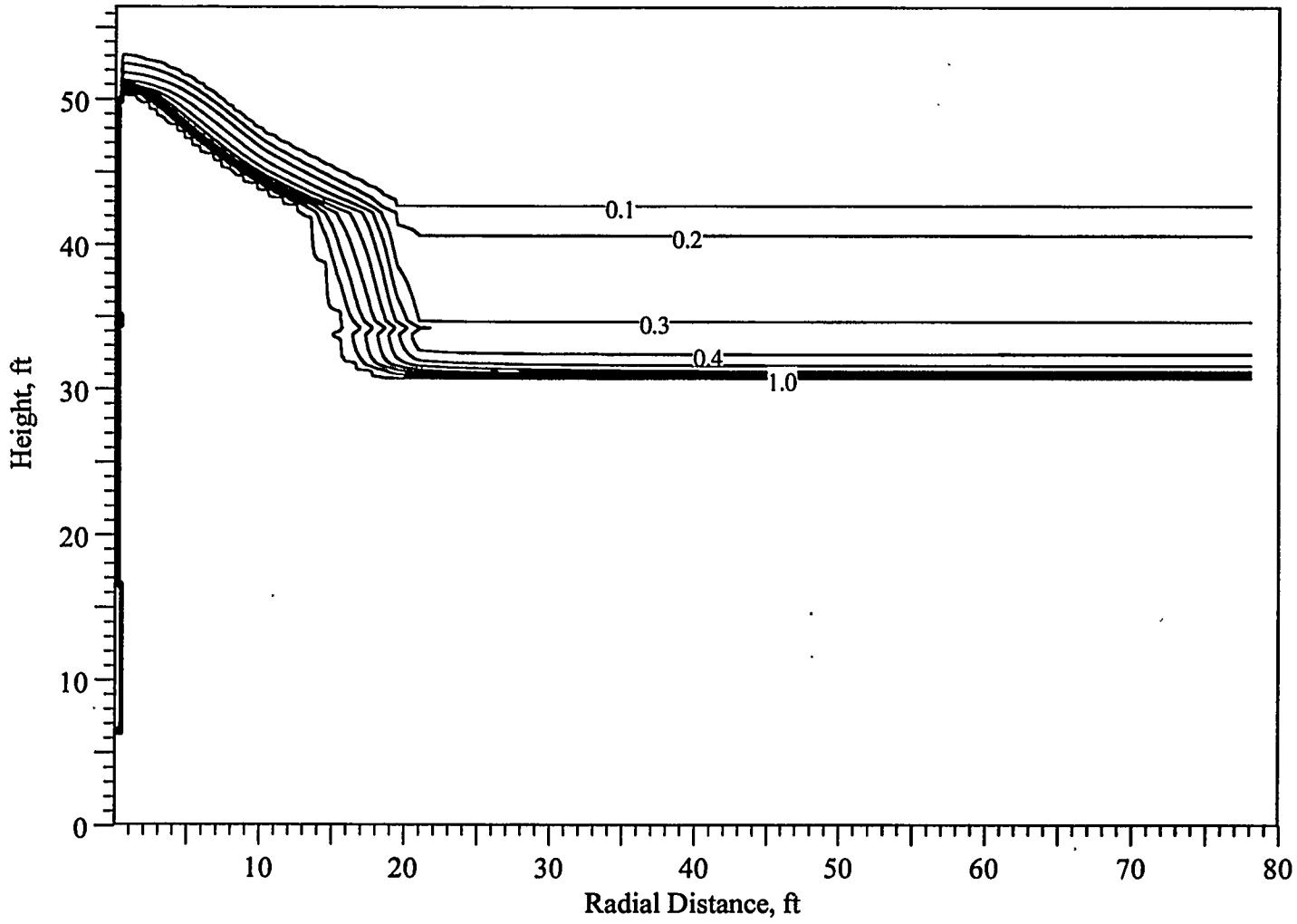

Figure F.3 Saturation Profile at 4 Days, Simulation HPA
(Operational Field Test #13, January 20, 1996)

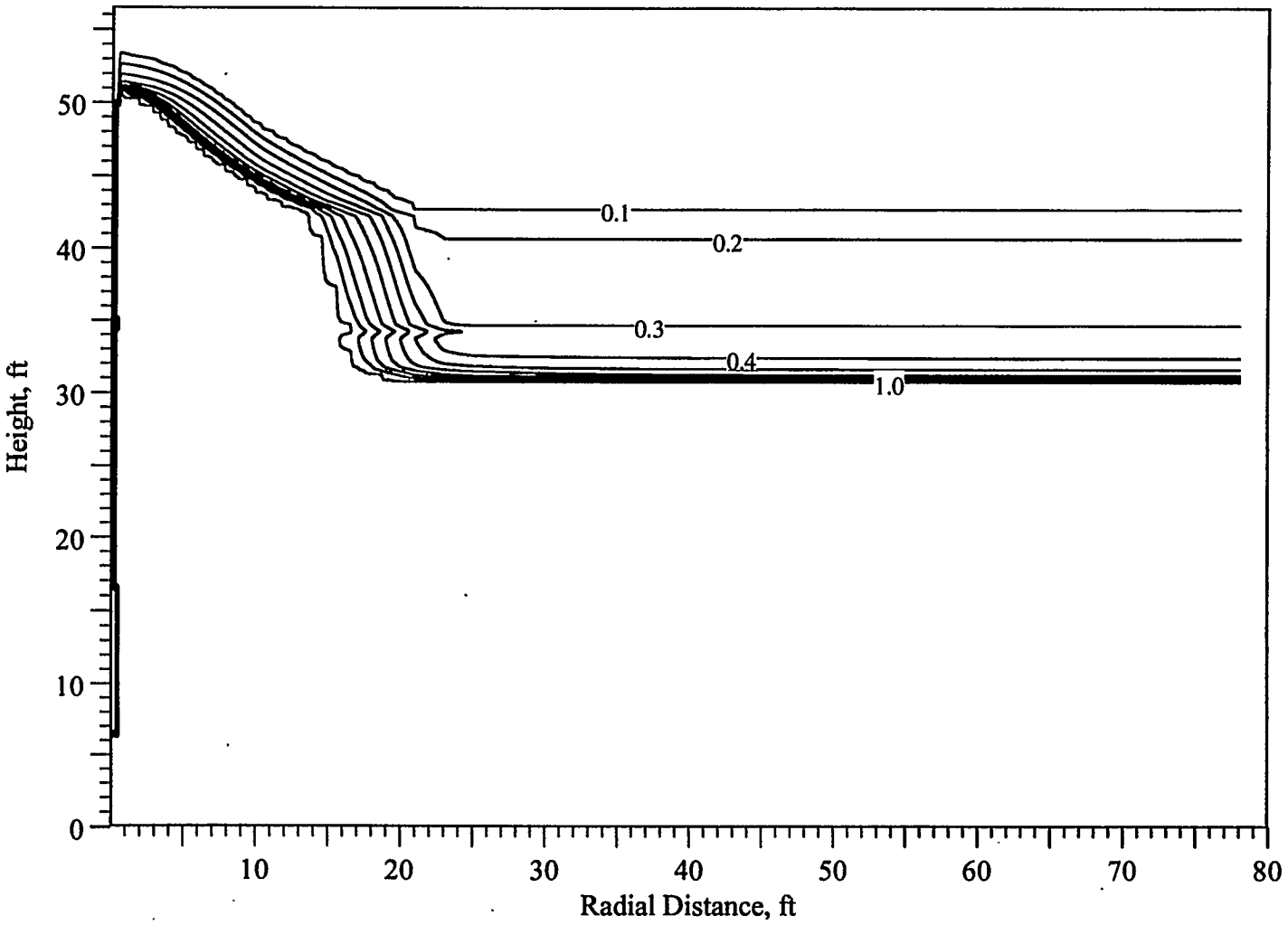

Figure F.4 Saturation Profile at 8 Days, Simulation HPA
(Operational Field Test #13, January 24, 1996)

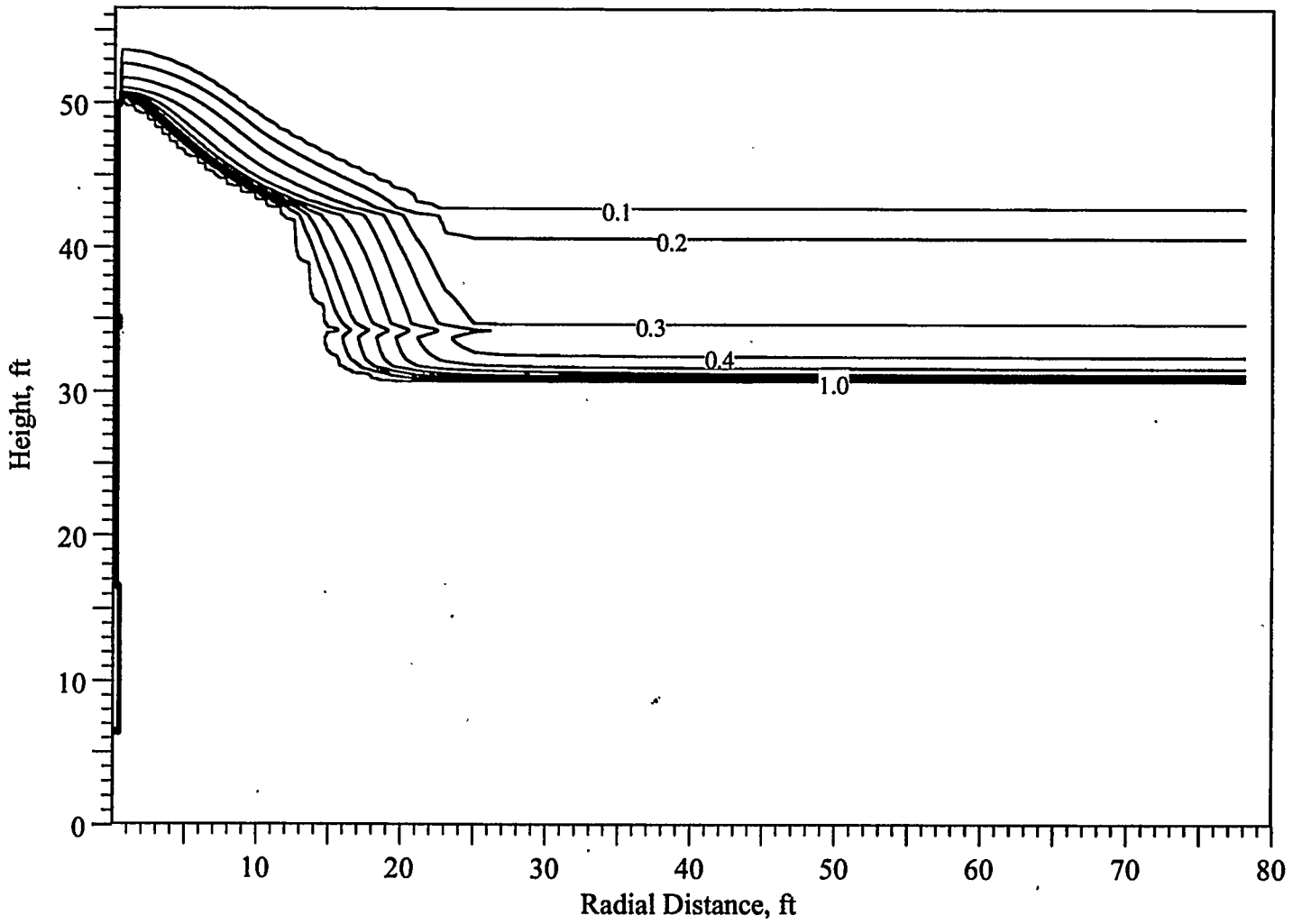

Figure F.5 Saturation Profile at 16 Days, Simulation HPA
(Operational Field Test #13, February 1, 1996)

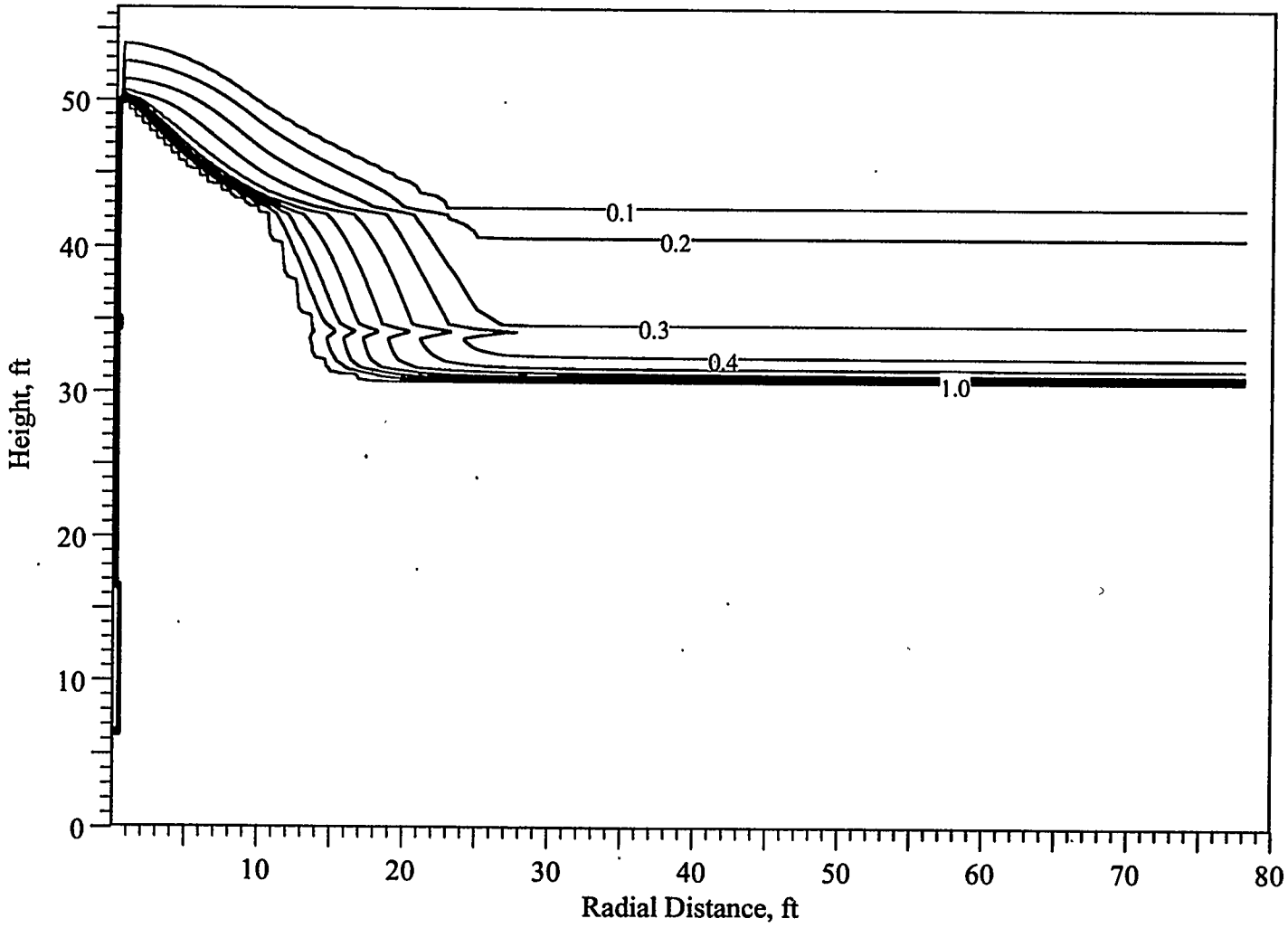

Figure F.6 Saturation Profile at 32 Days, Simulation HPA
(Operational Field Test #13, February 17, 1996)

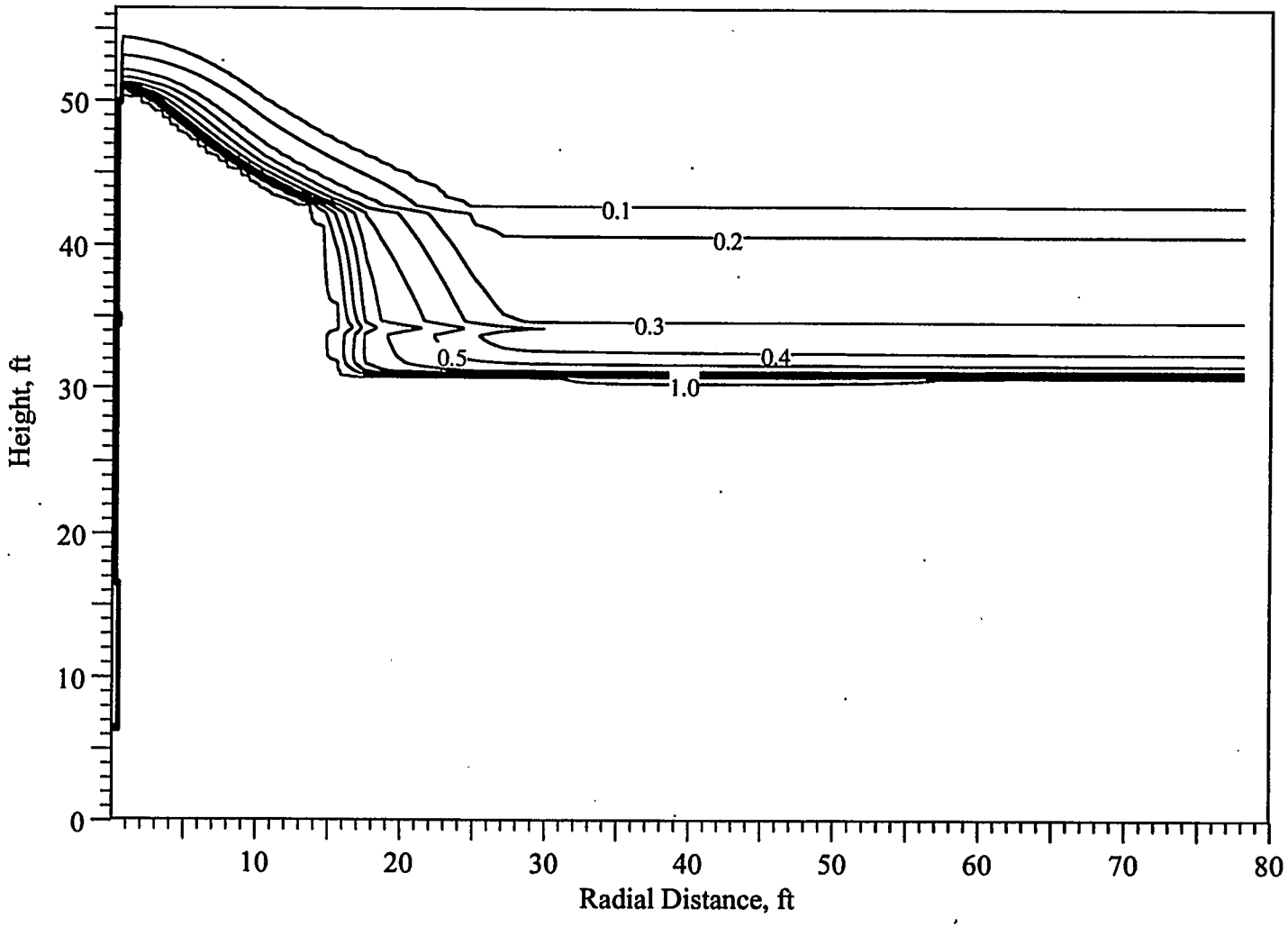

Figure F.7 Saturation Profile at 63 Days, Simulation HPA
(Operational Field Test #13, March 19, 1996)

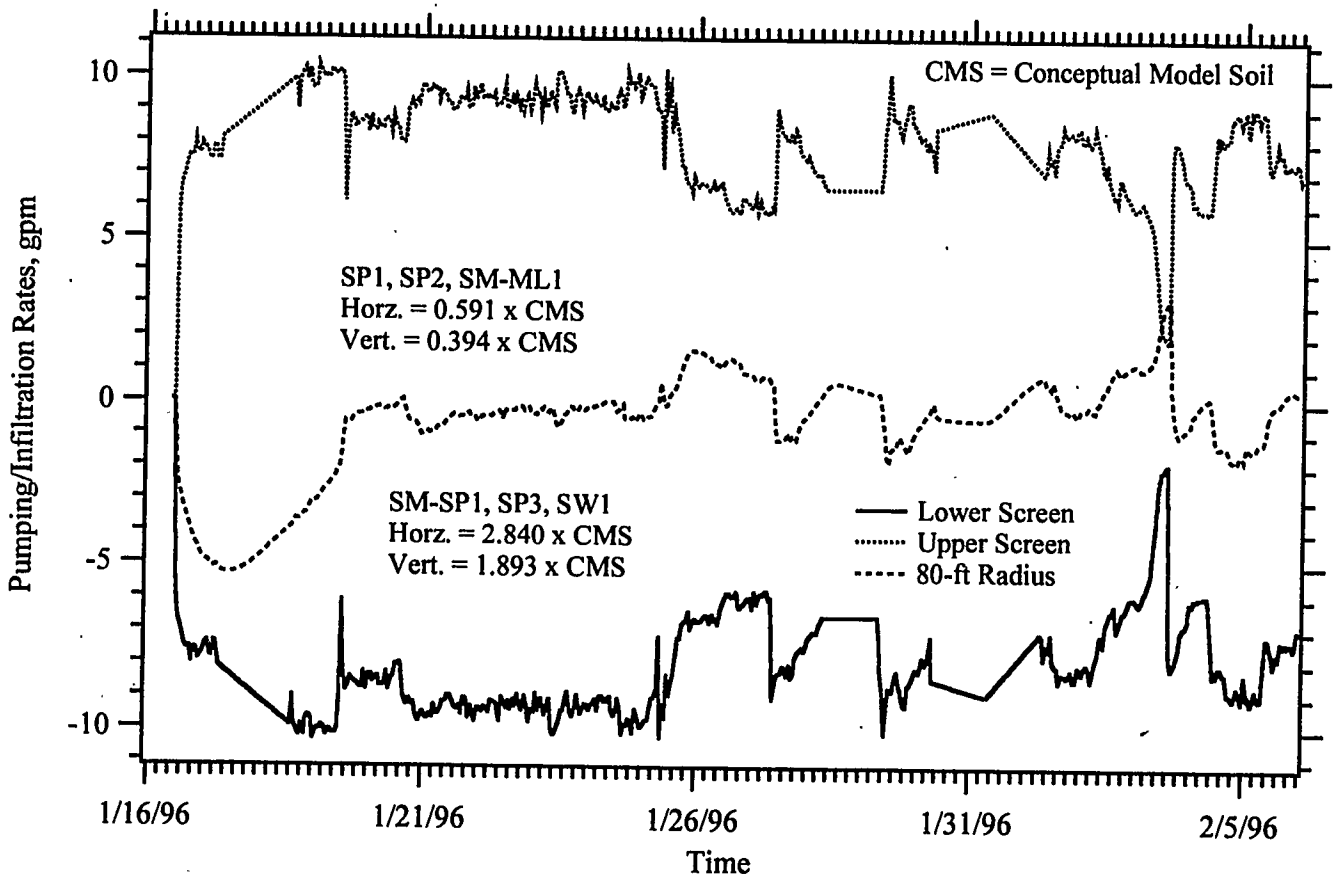

Figure F.8 Pumping/Infiltration Rates Versus Time, Simulation HPA
(Operational Field Test #13, January 16, 1996 - February 6, 1996)

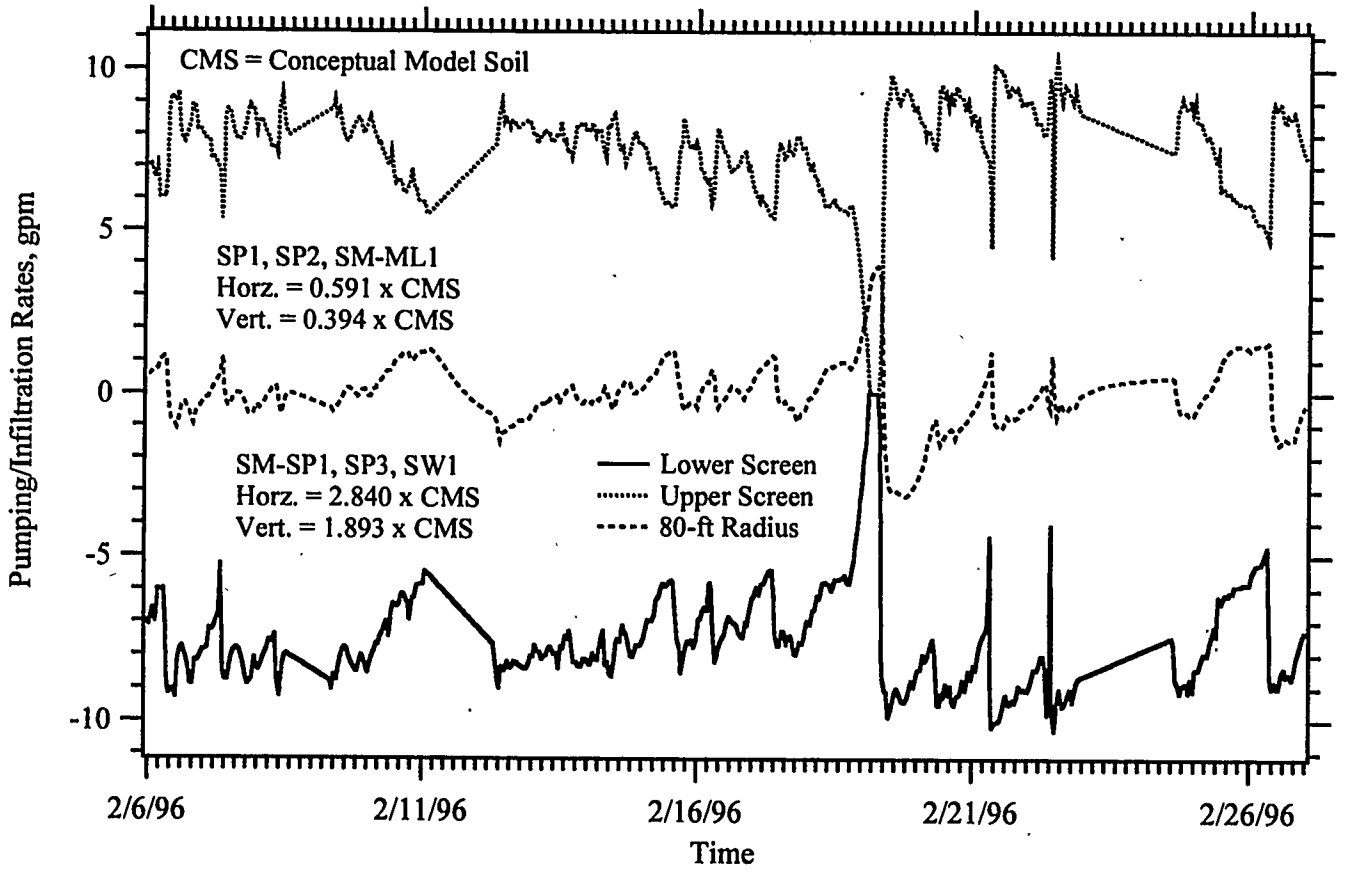

Figure F.9 Pumping/Infiltration Rates Versus Time, Simulation HPA
(Operational Field Test #13, February 6, 1996 - February 27, 1996)

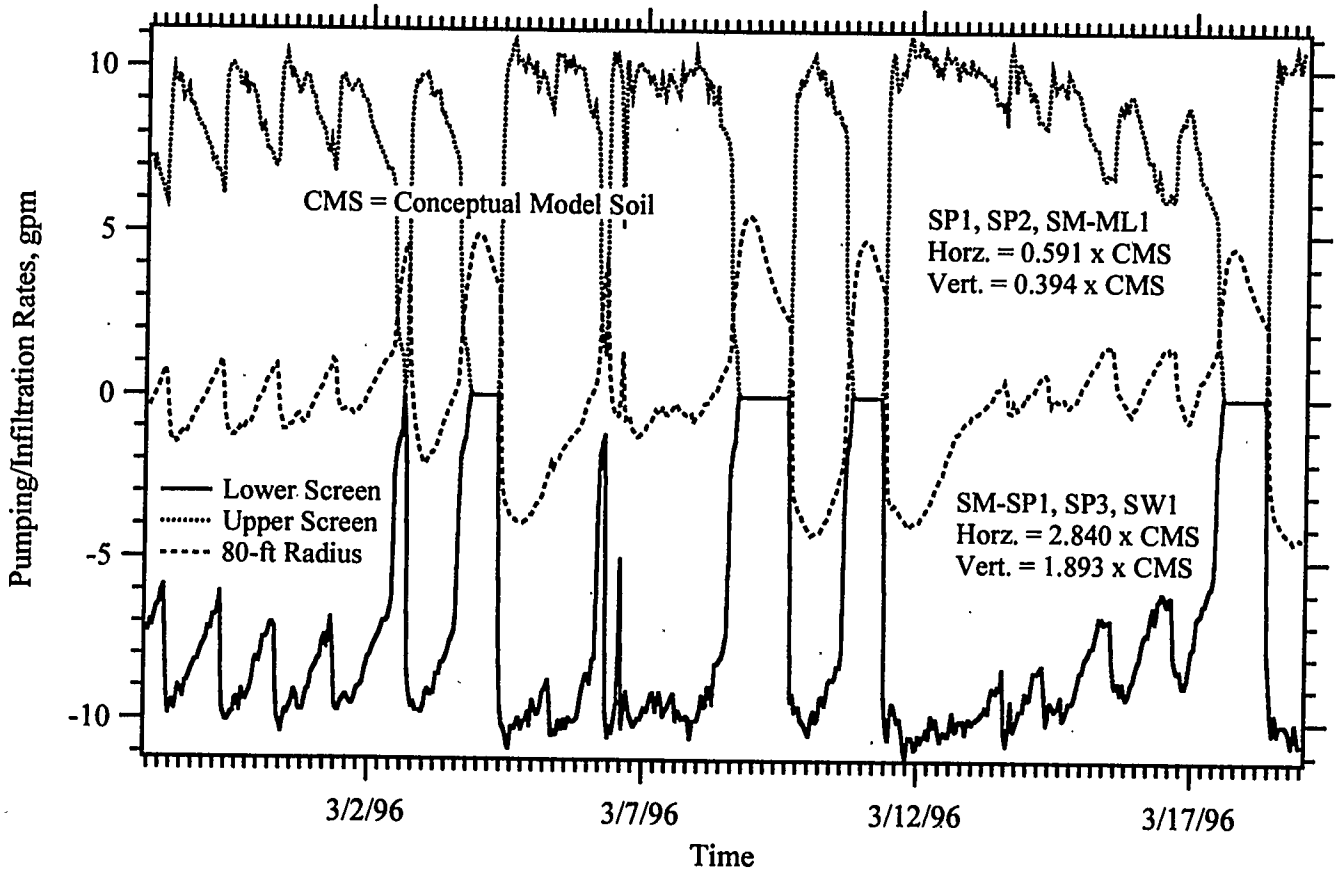

Figure F.10 Pumping/Infiltration Rates Versus Time, Simulation HPA
(Operational Field Test #13, February 27, 1996 - March 19, 1996)

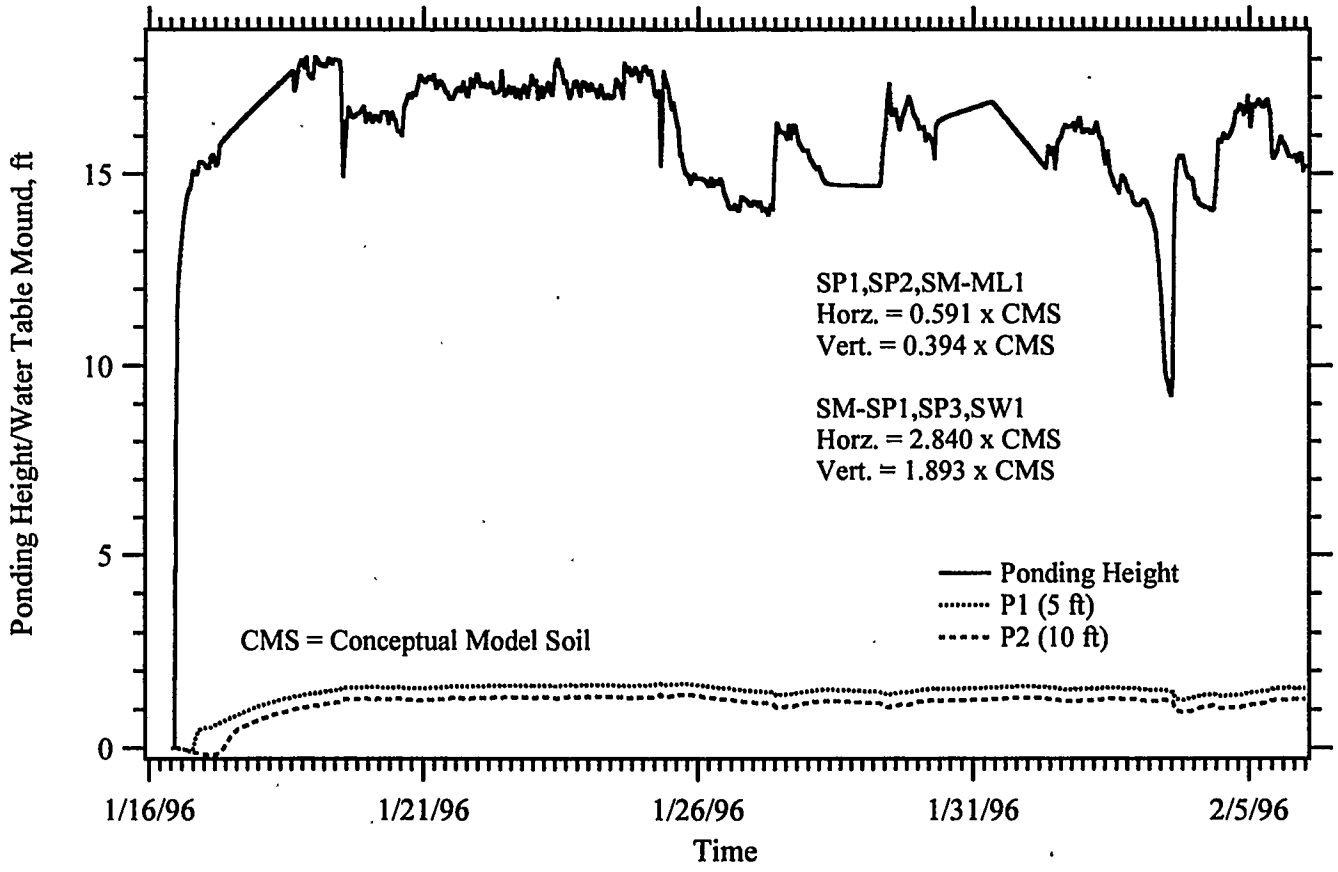

Figure F.11 Ponding Height/Water Table Mound Versus Time, Simulation HPA
(Operational Field Test #13, January 16, 1996 - February 6, 1996)

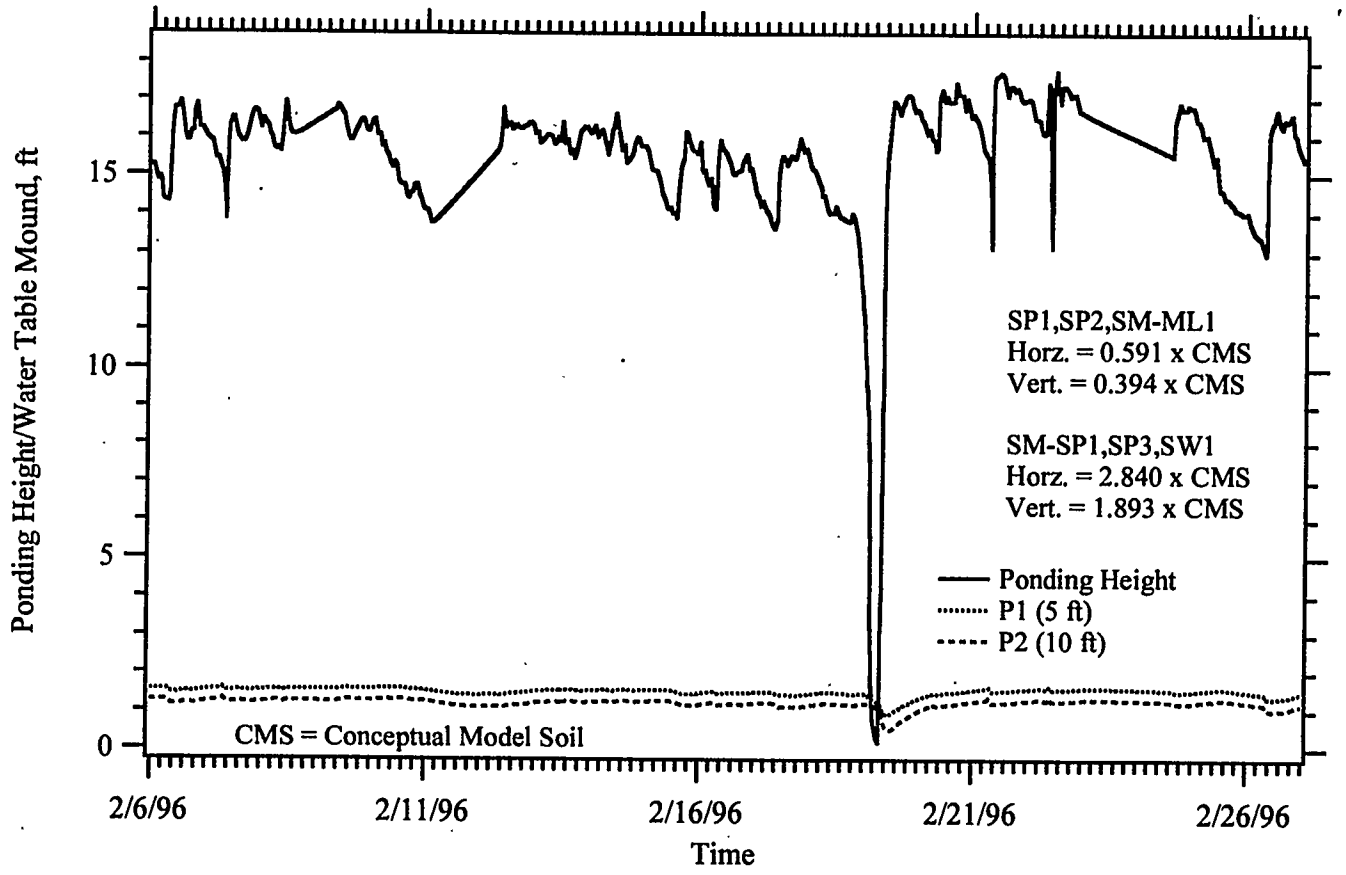

Figure F.12 Ponding Height/Water Table Mound Versus Time, Simulation HPA
(Operational Field Test #13, February 6, 1996 - February 27, 1996)

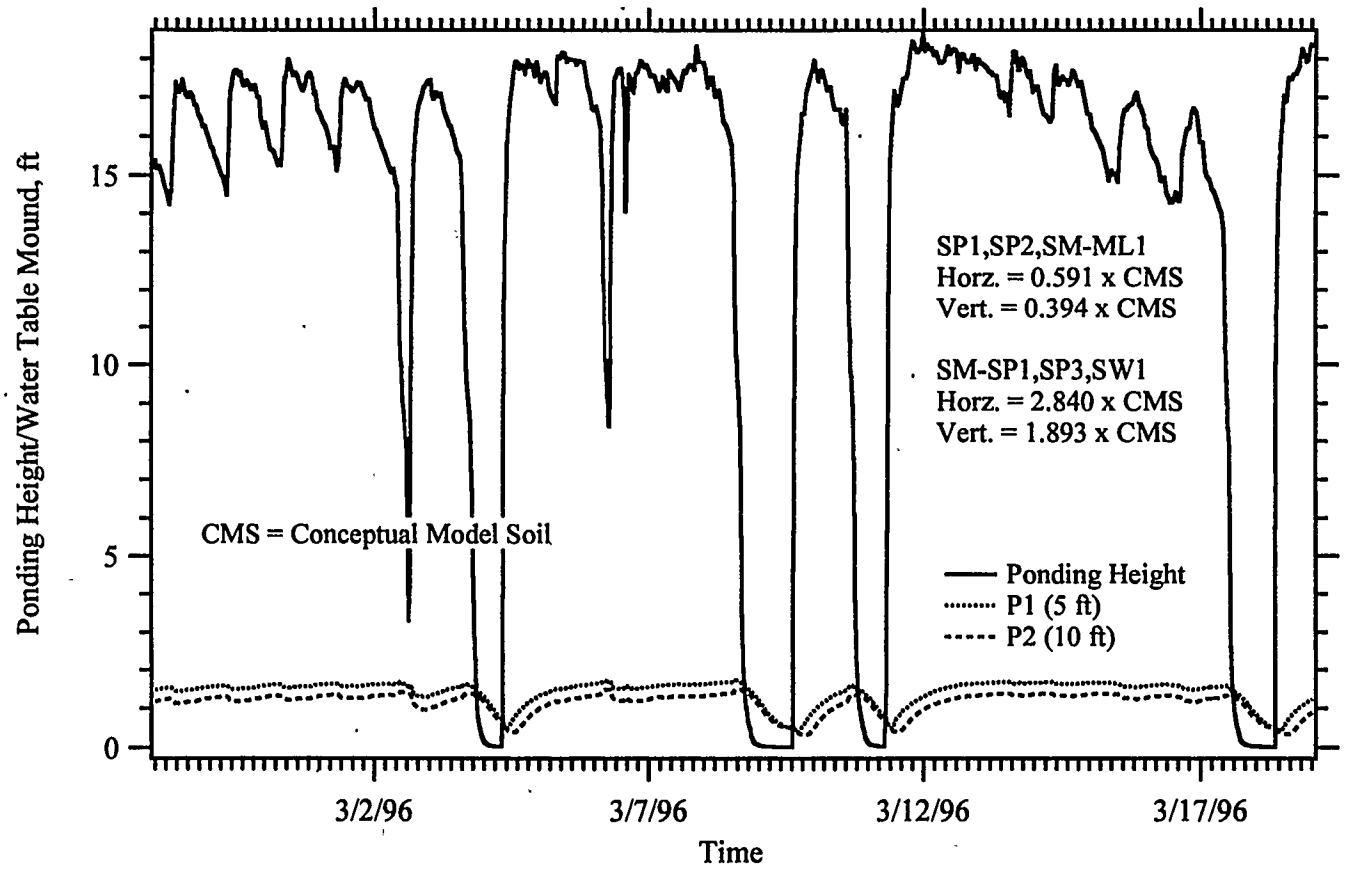

Figure F.13 Ponding Height/Water Table Mound Versus Time, Simulation HPA
(Operational Field Test #13, February 27, 1996 - March 19, 1996)

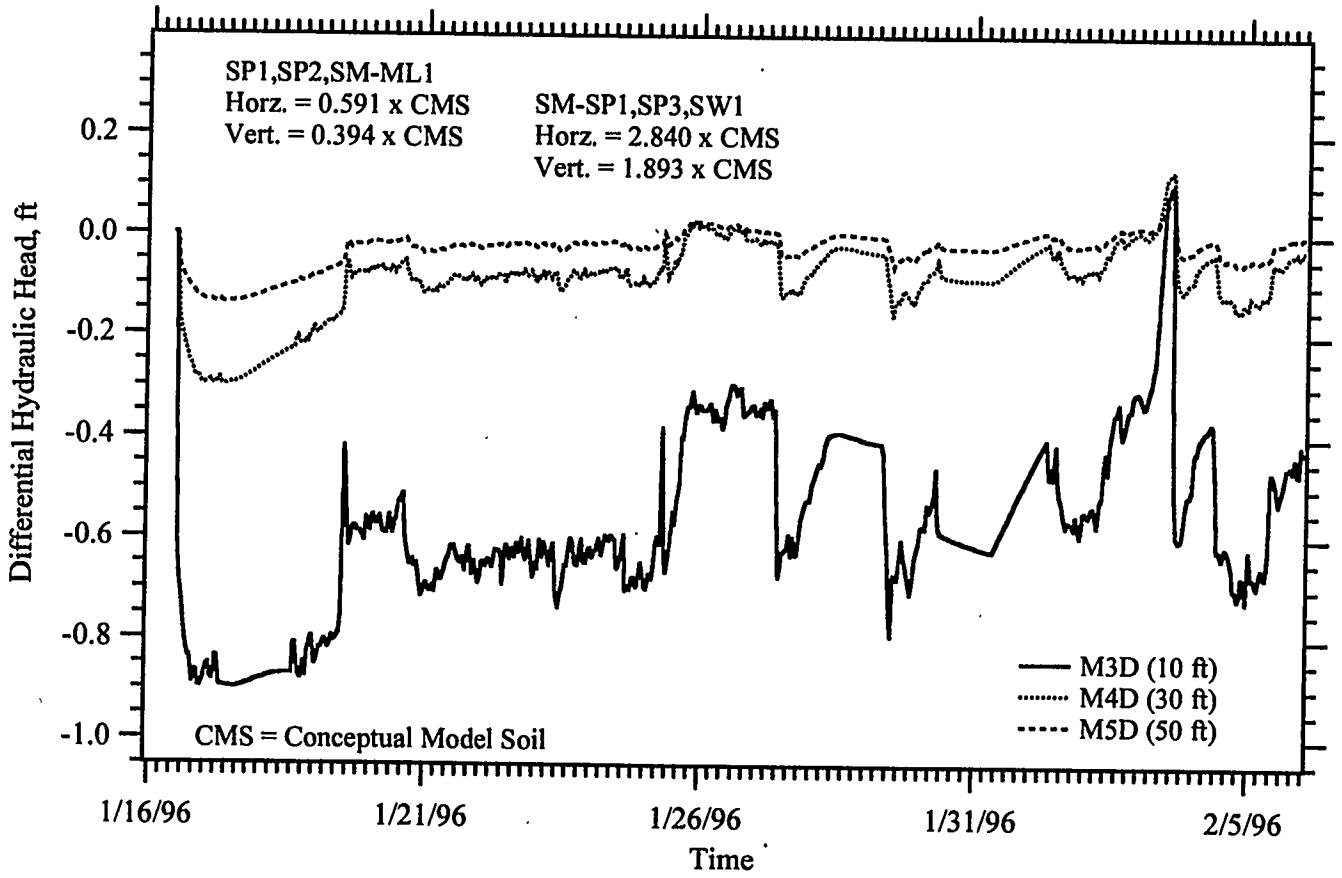

Figure F.14 Differential Hydraulic Pressure Versus Time, Simulation HPA
(Operational Field Test #13, January 16, 1996 - February 6, 1996)

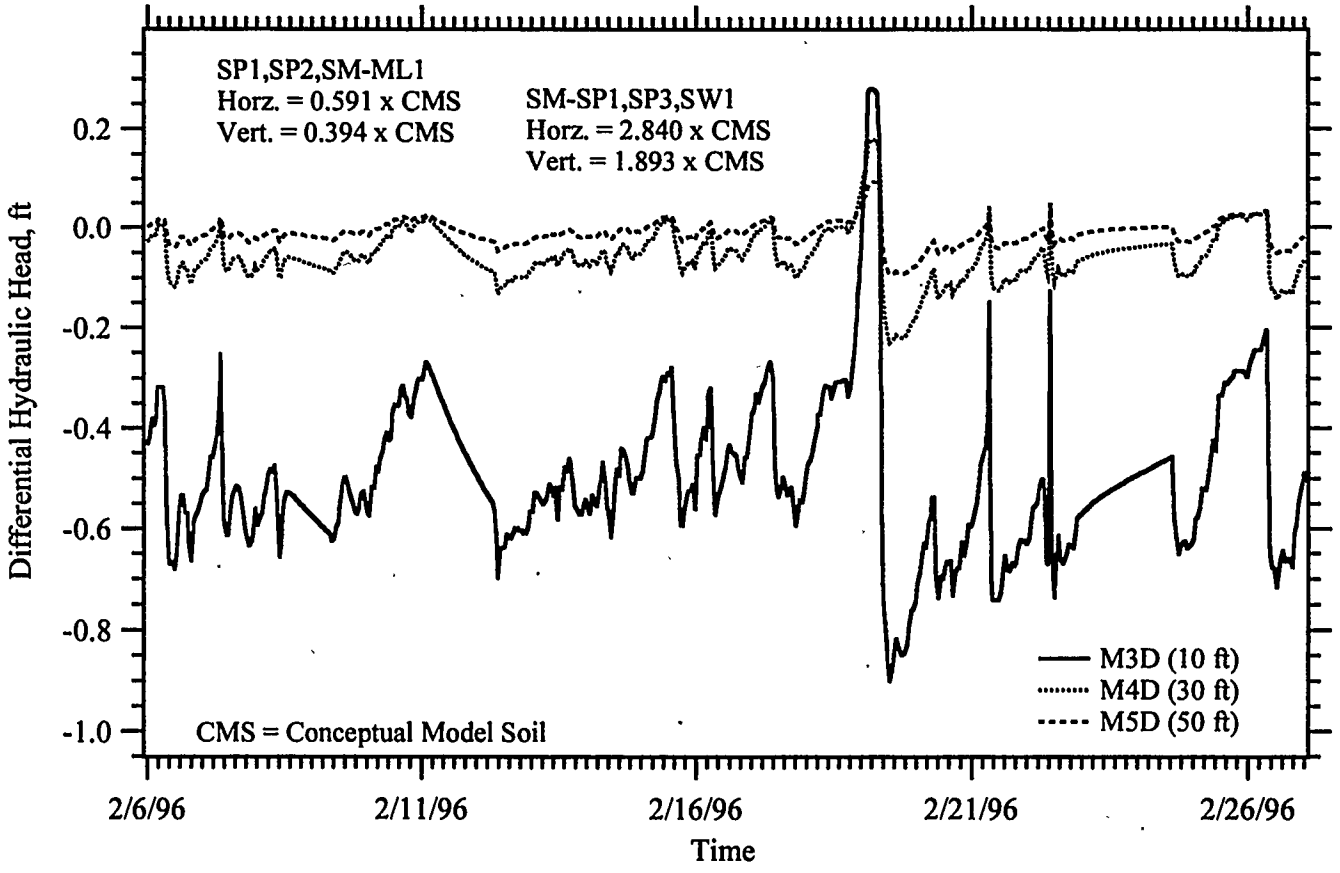

Figure F.15 Differential Hydraulic Pressure Versus Time, Simulation HPA
(Operational Field Test #13, February 6, 1996 - February 27, 1996)

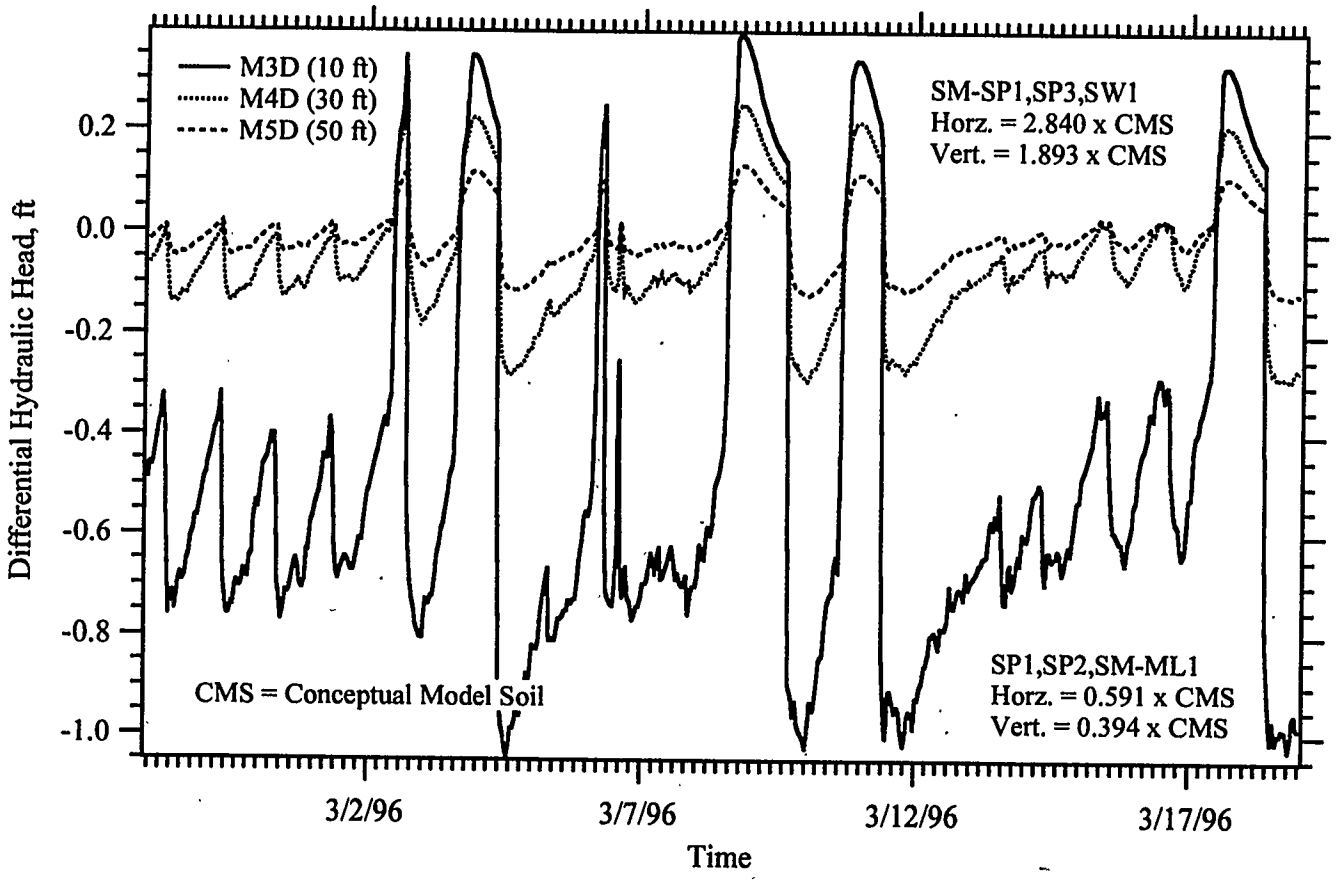

Figure F.16 Differential Hydraulic Pressure Versus Time, Simulation HPA
(Operational Field Test #13, February 27, 1996 - March 19, 1996)

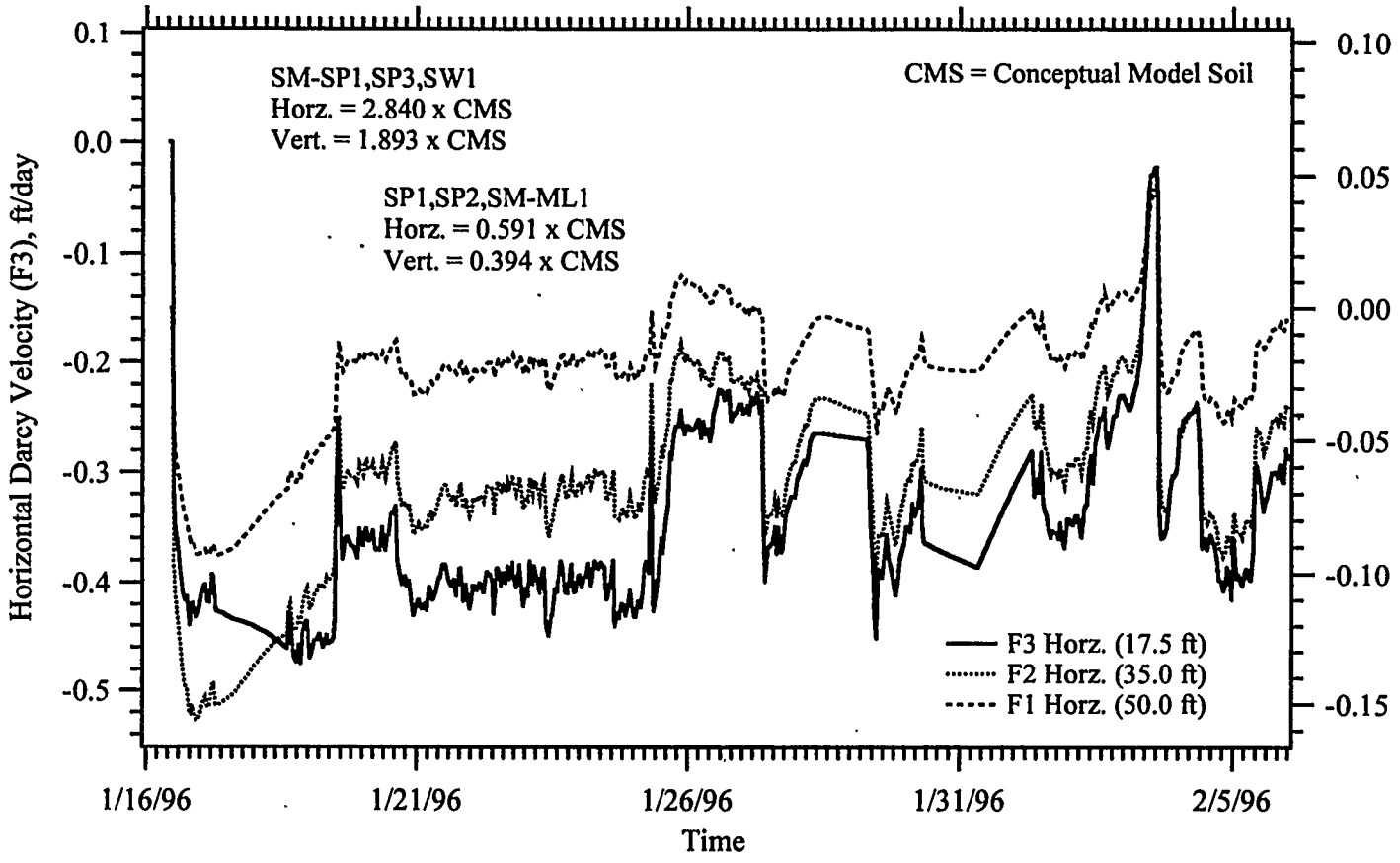

Figure F.17 Horizontal Darcy Velocity Versus Time, Simulation HPA
(Operational Field Test #13, January 16, 1996 - February 6, 1996)

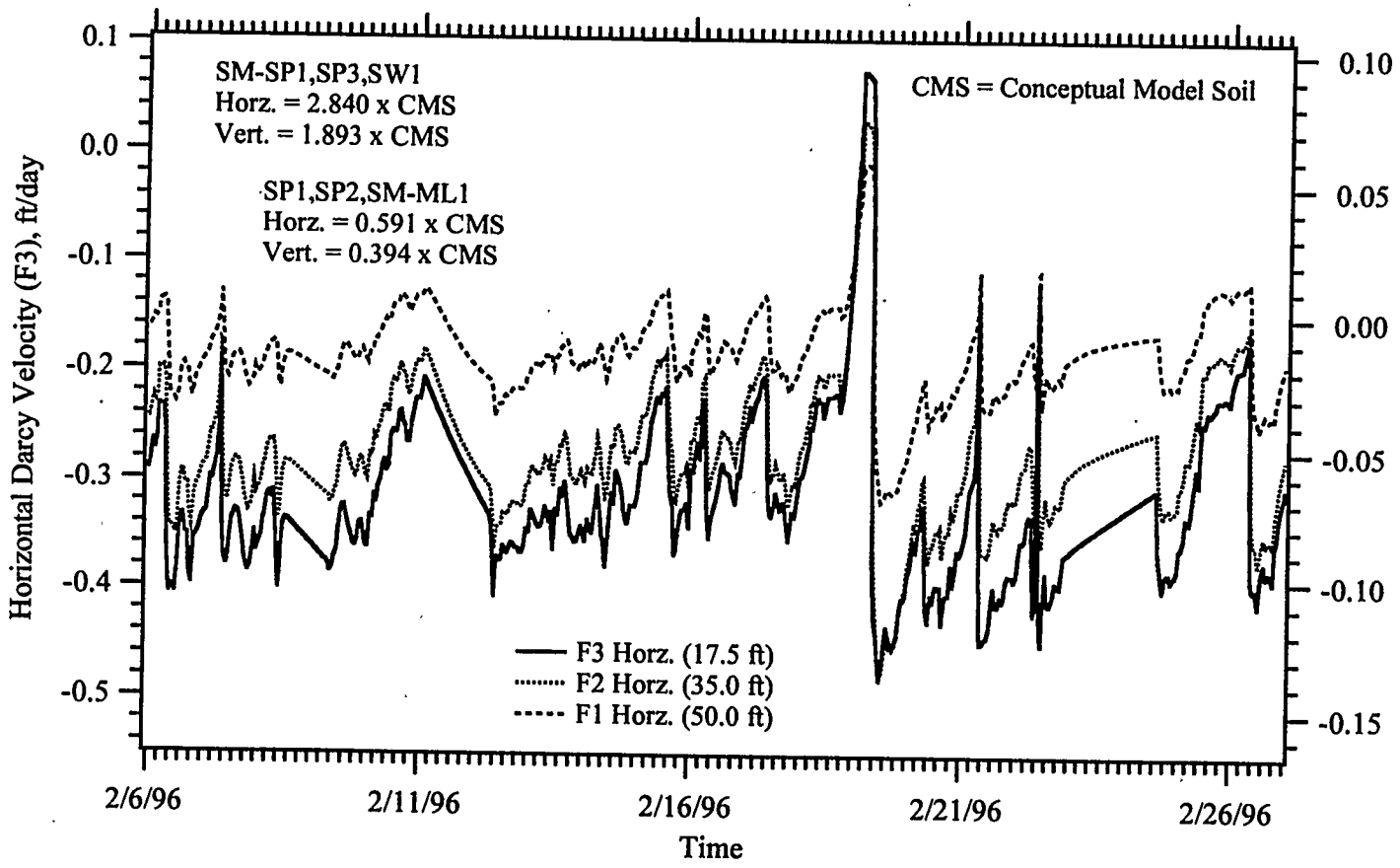

Figure F.18 Horizontal Darcy Velocity Versus Time, Simulation HPA
(Operational Field Test #13, February 6, 1996 - February 27, 1996)

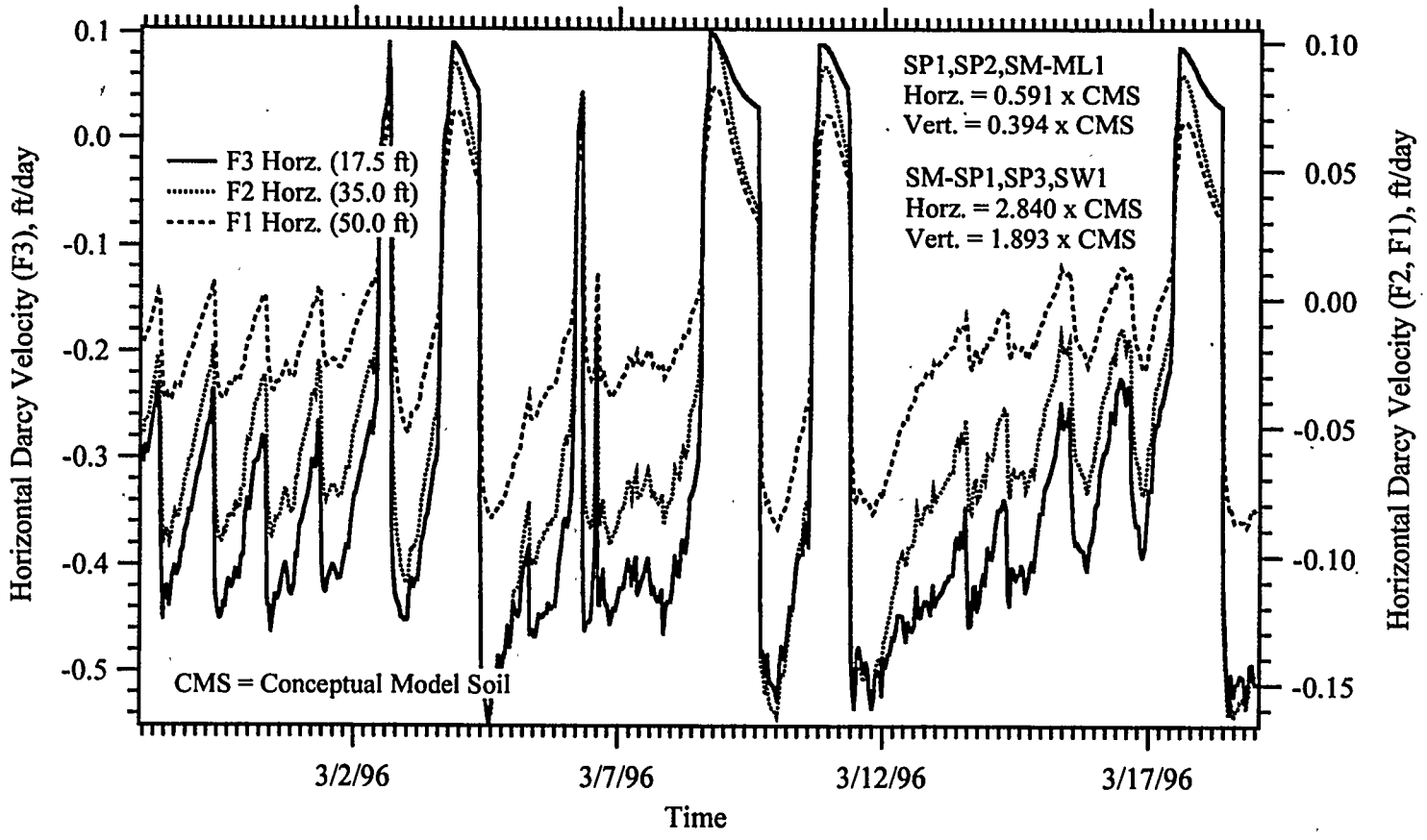

Figure F.19 Horizontal Darcy Velocity Versus Time, Simulation HPA
(Operational Field Test #13, February 27, 1996 - March 19, 1996)

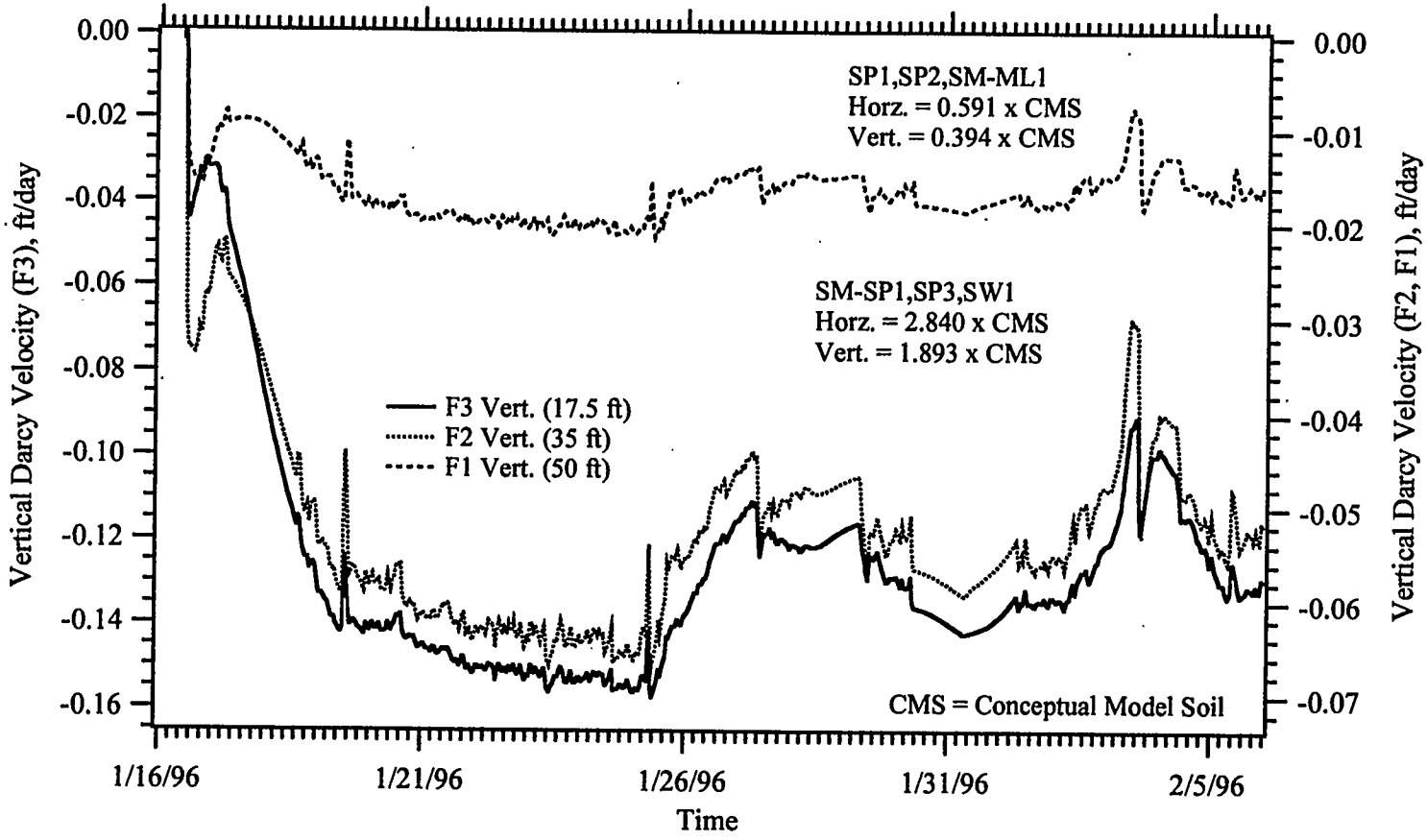

Figure F.20 Vertical Darcy Velocity Versus Time, Simulation HPA
(Operational Field Test #13, January 16, 1996 - February 6, 1996)

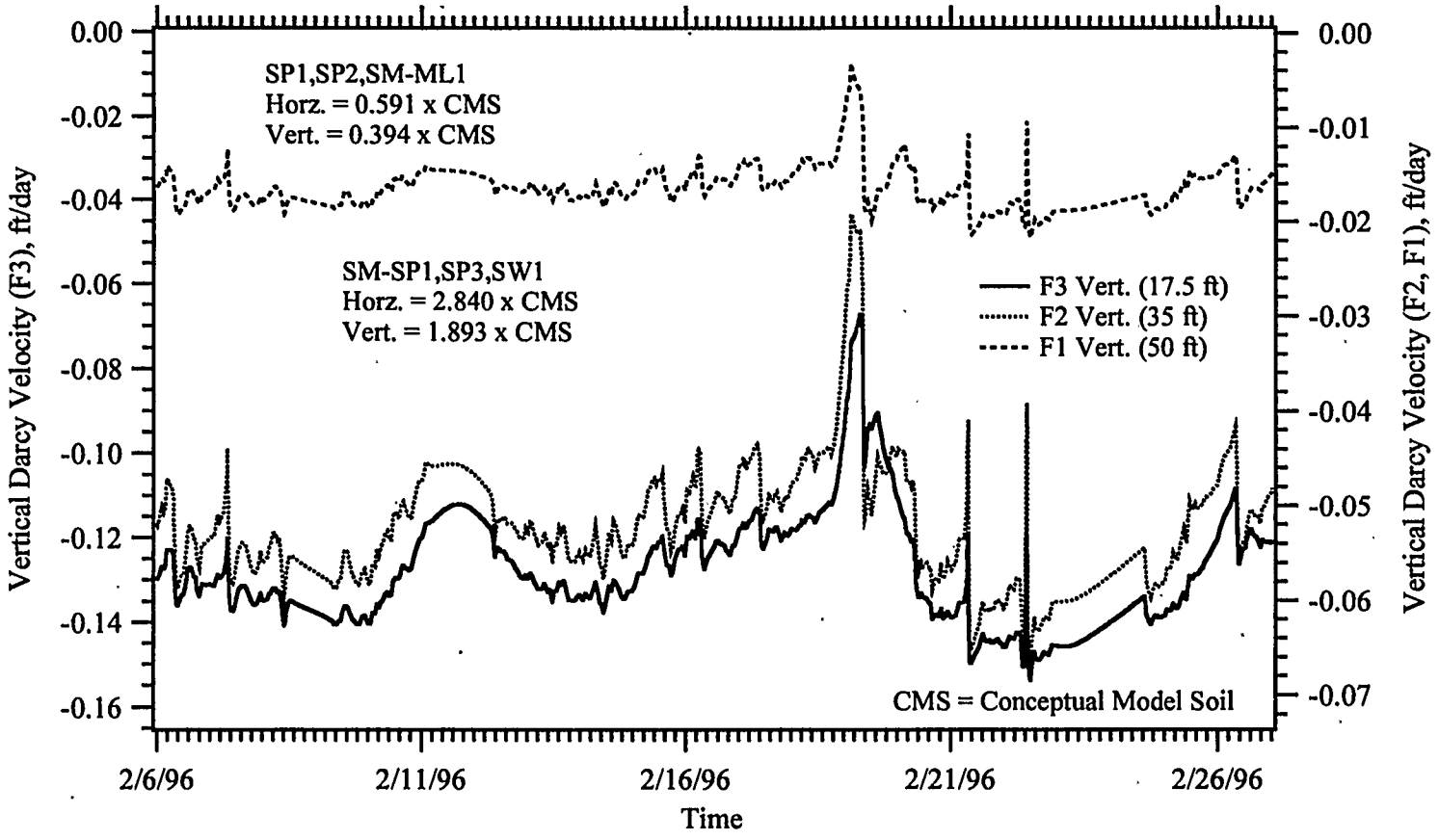

Figure F.21 Vertical Darcy Velocity Versus Time, Simulation HPA
(Operational Field Test #13, February 6, 1996 - February 27, 1996)

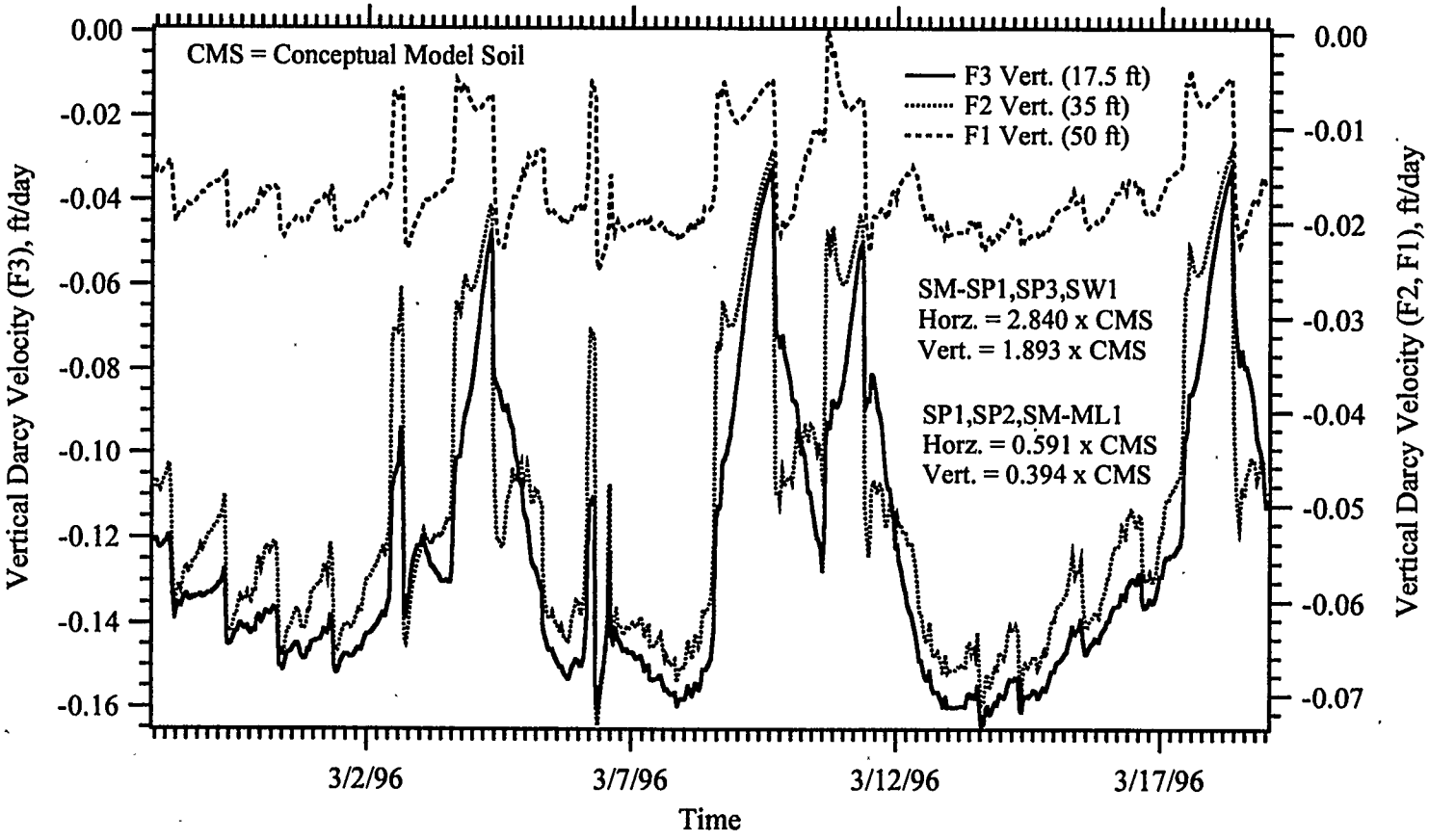

Figure F.22 Vertical Darcy Velocity Versus Time, Simulation HPA
(Operational Field Test #13, February 27, 1996 - March 19, 1996)

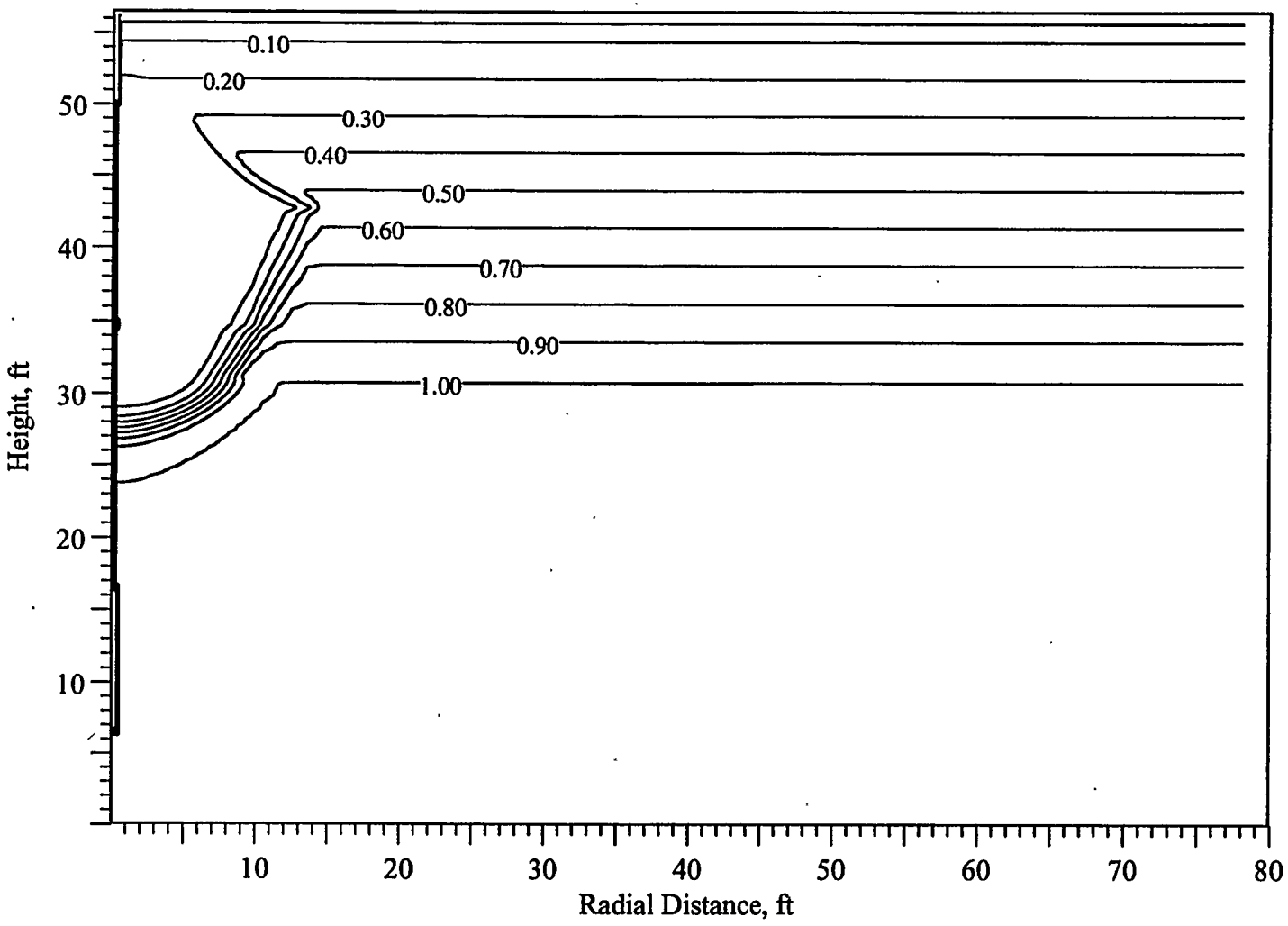

Figure F.23 TCE Concentration Profile at 1 Day, Simulation HPA
(Operational Field Test #13, January 17, 1996)

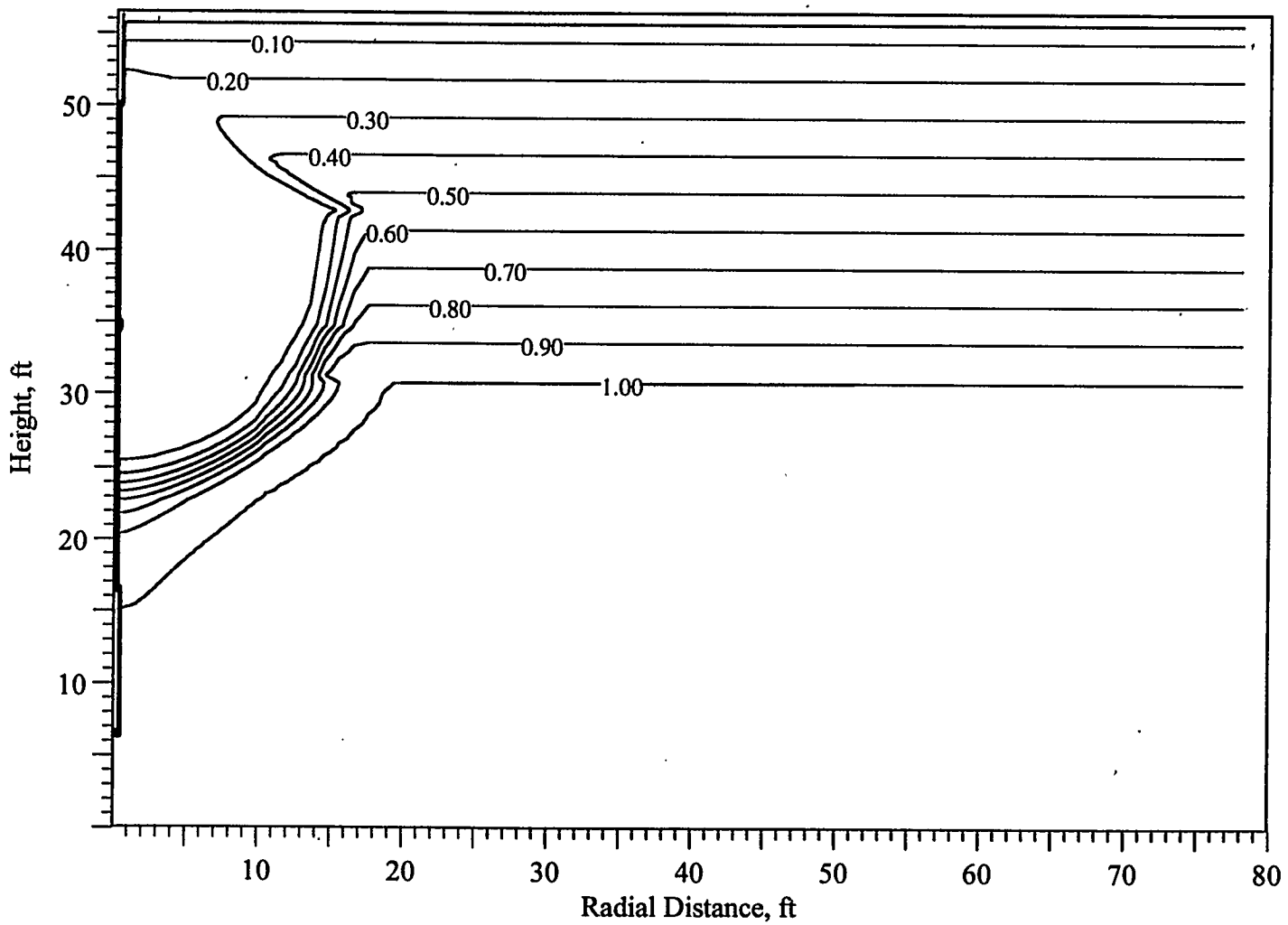

Figure F.24 TCE Concentration Profile at 2 Days, Simulation HPA
(Operational Field Test #13, January 18, 1996)

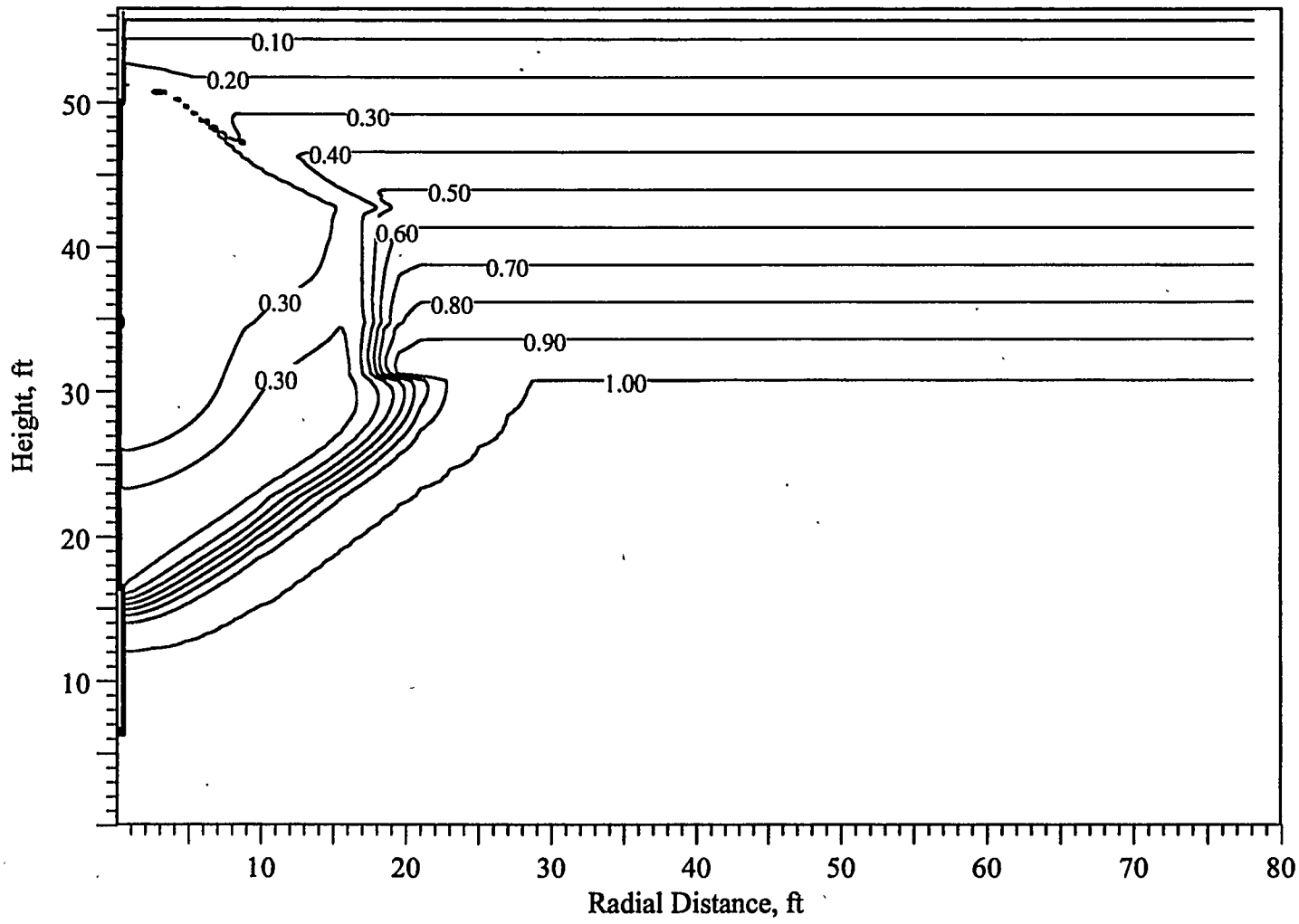

Figure F.25 TCE Concentration Profile at 4 Days, Simulation HPA
(Operational Field Test #13, January 20, 1996)

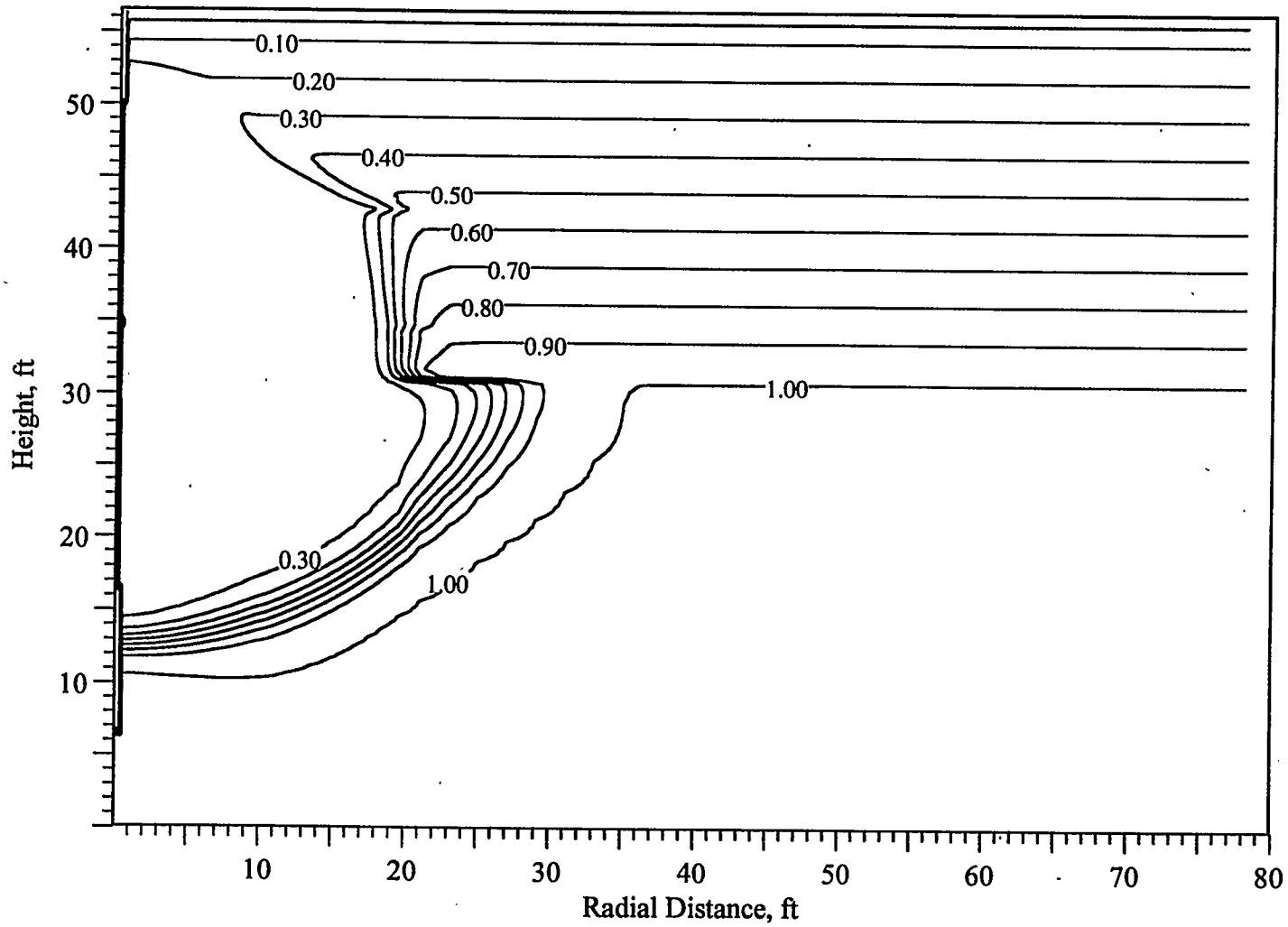

Figure F.26 TCE Concentration Profile at 8 Days, Simulation HPA
(Operational Field Test #13, January 24, 1996)

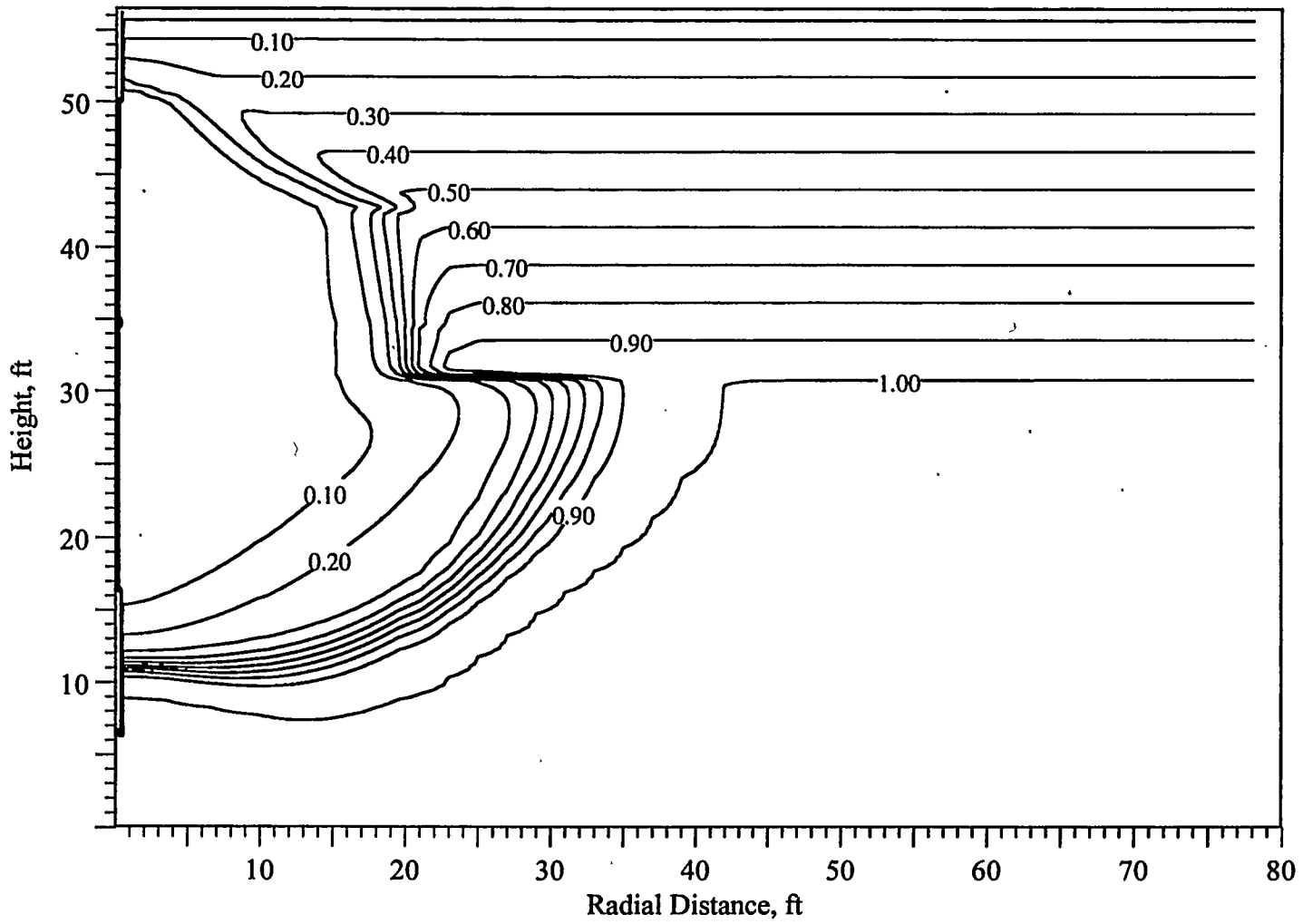

Figure F.27 TCE Concentration Profile at 16 Days, Simulation HPA
(Operational Field Test #13, February 1, 1996)

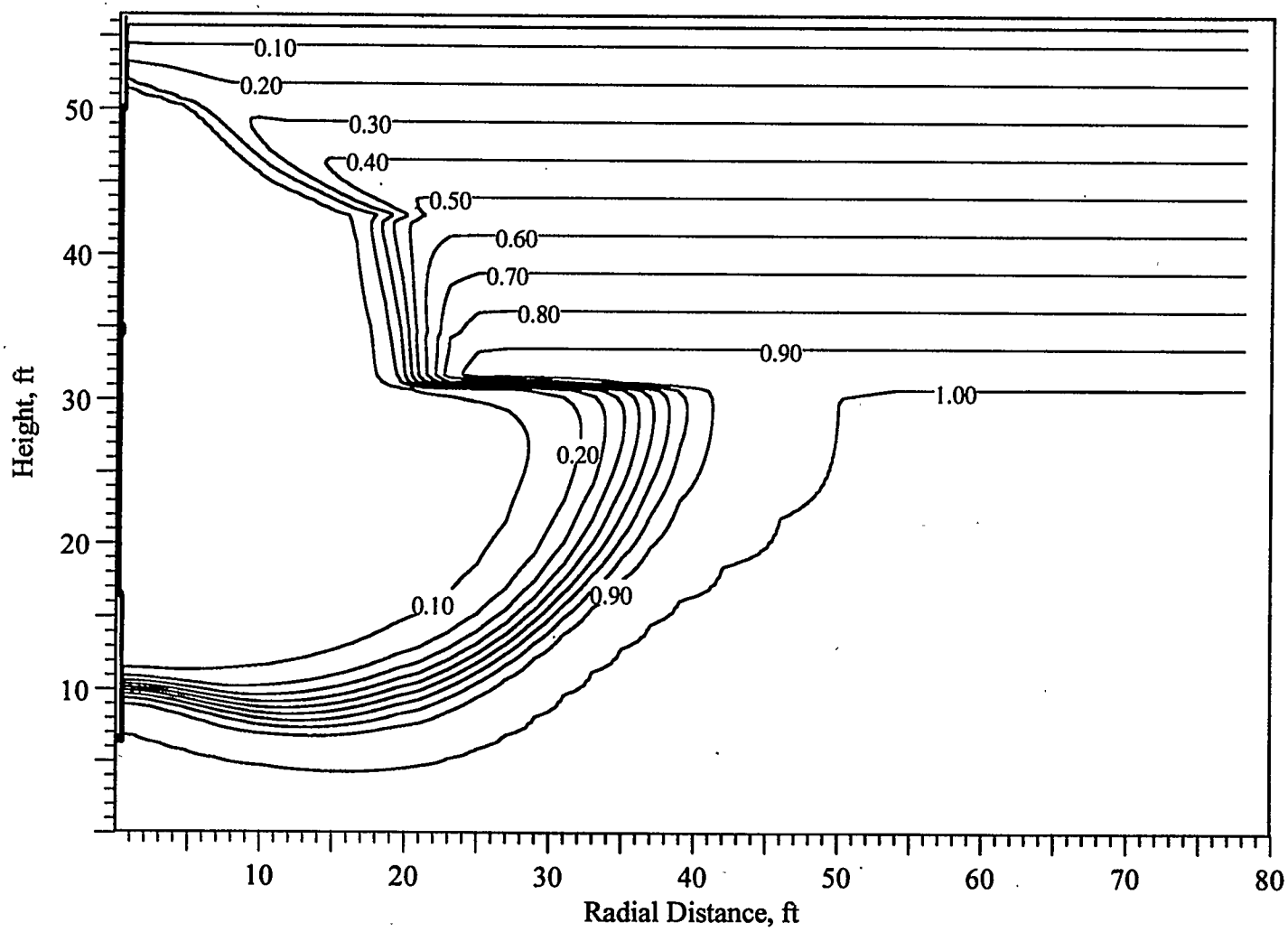

Figure F.28 TCE Concentration Profile at 32 Days, Simulation HPA
(Operational Field Test #13, February 17, 1996)

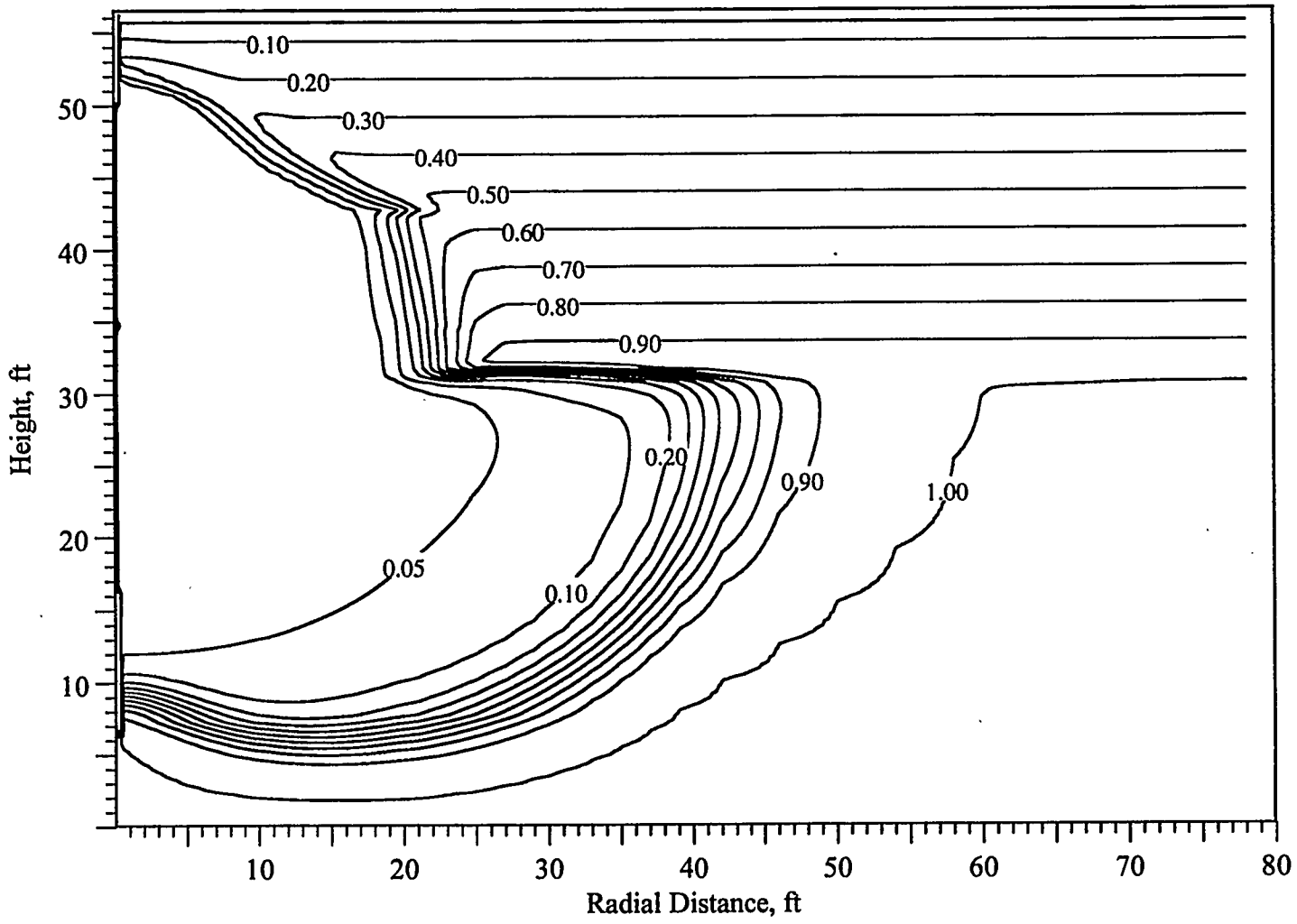

Figure F.29 TCE Concentration Profile at 63 Days, Simulation HPA
(Operational Field Test #13, March 19, 1996)

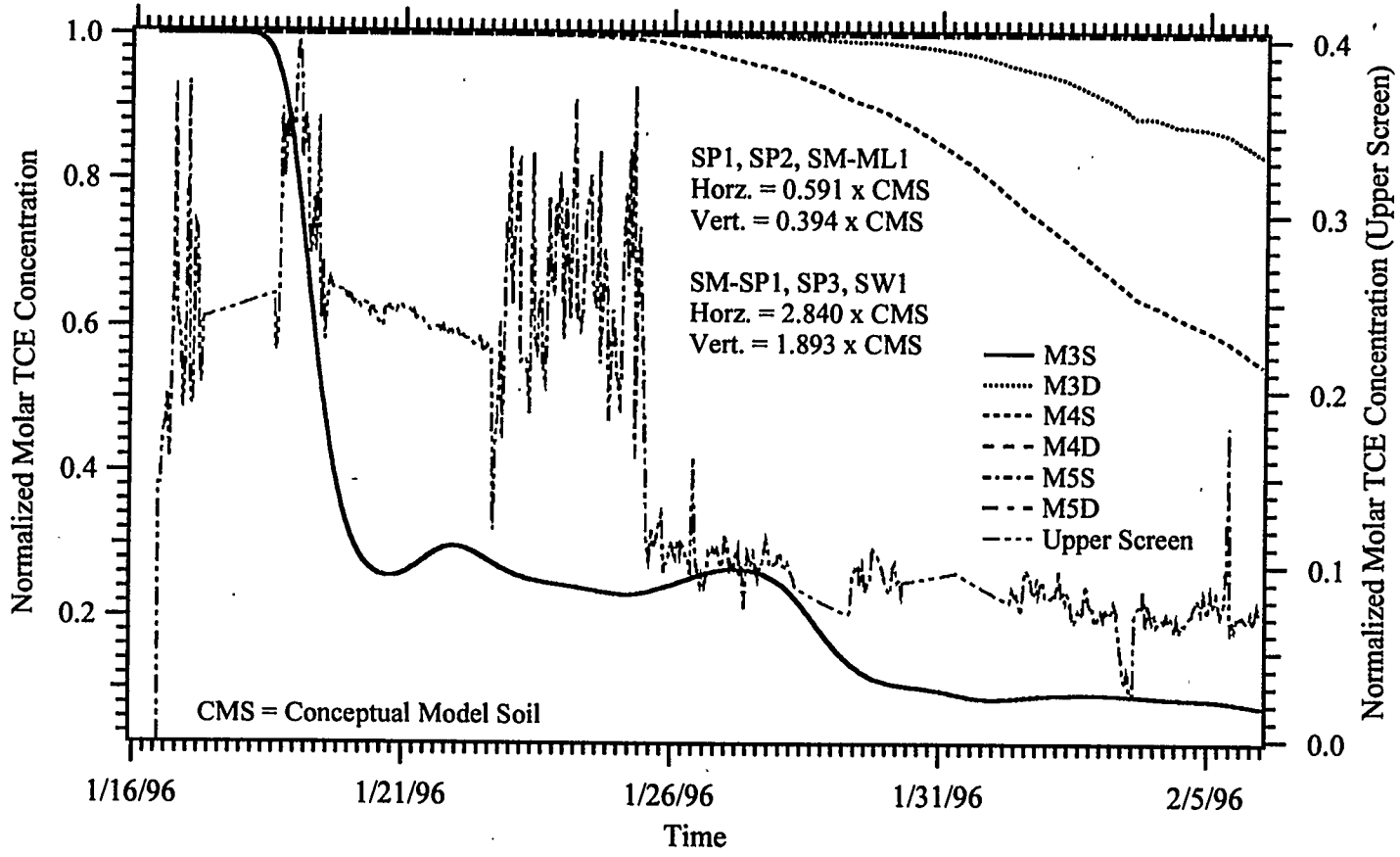

Figure F.30 Dissolved TCE Concentration Versus Time, Simulation HPA
(Operational Field Test #13, January 16, 1996 - February 6, 1996)

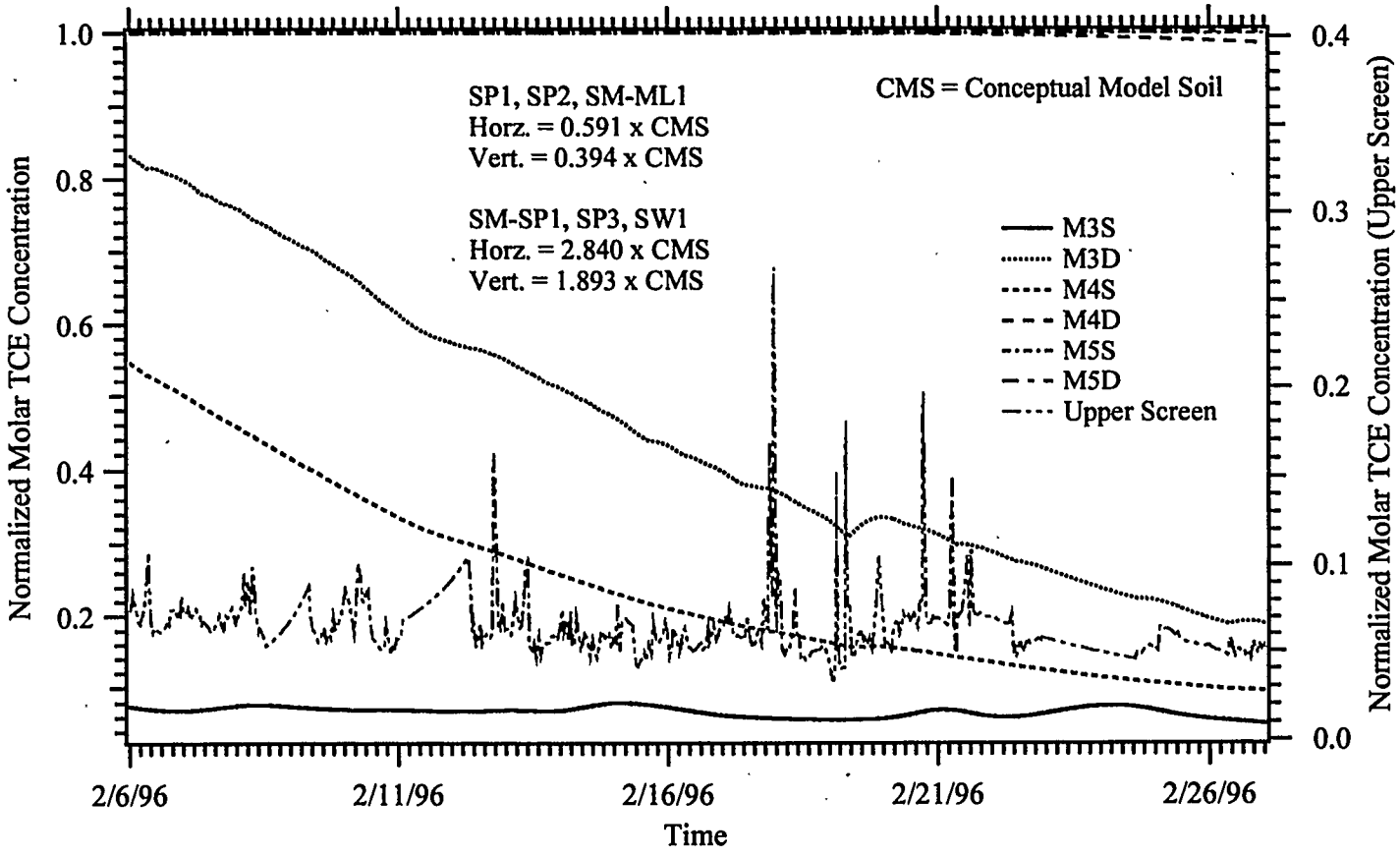

Figure F.31 Dissolved TCE Concentration Versus Time, Simulation HPA
(Operational Field Test #13, February 6, 1996 - February 27, 1996)

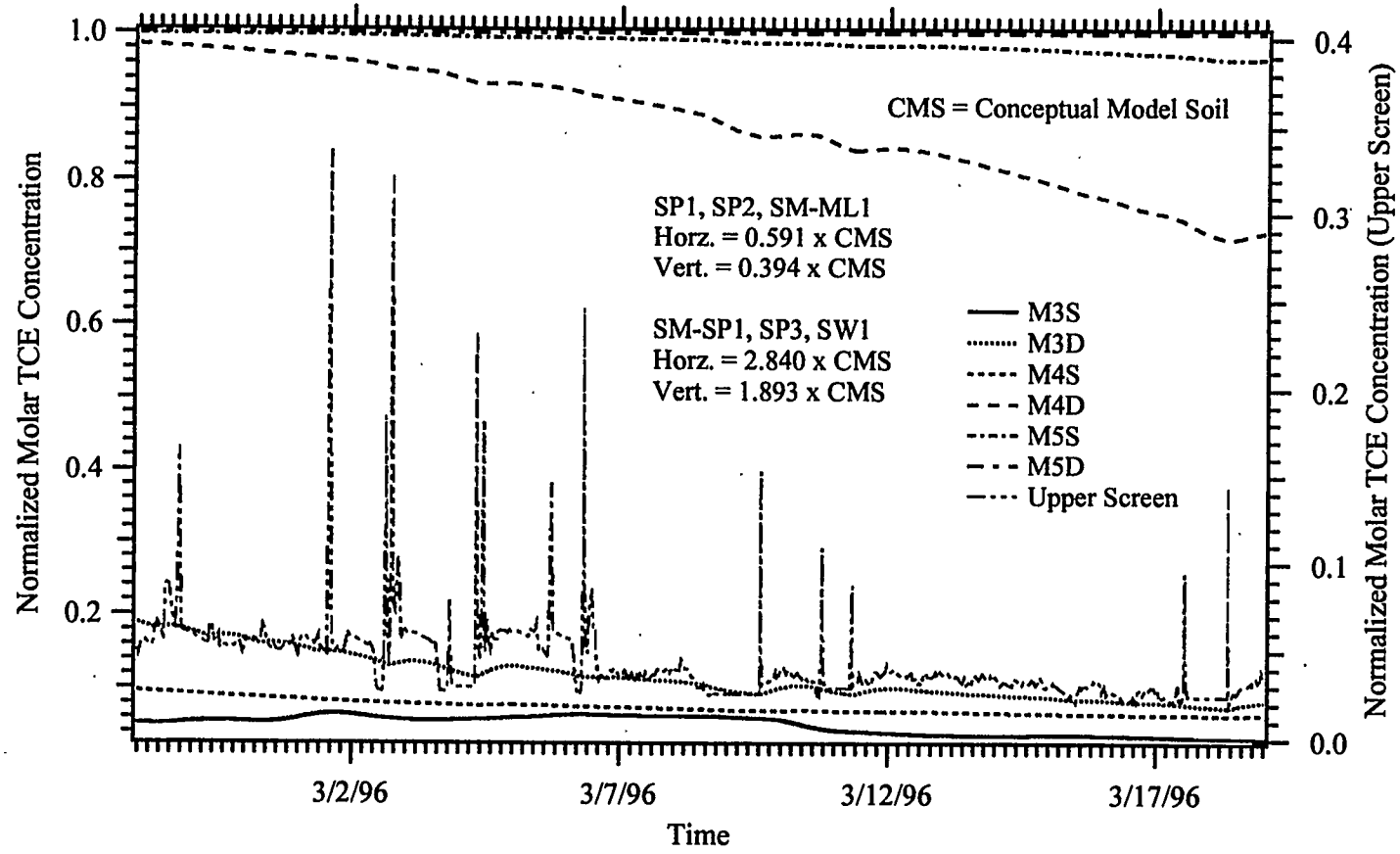

Figure F.32 Dissolved TCE Concentration Versus Time, Simulation HPA
(Operational Field Test #13, February 27, 1996 - March 19, 1996)

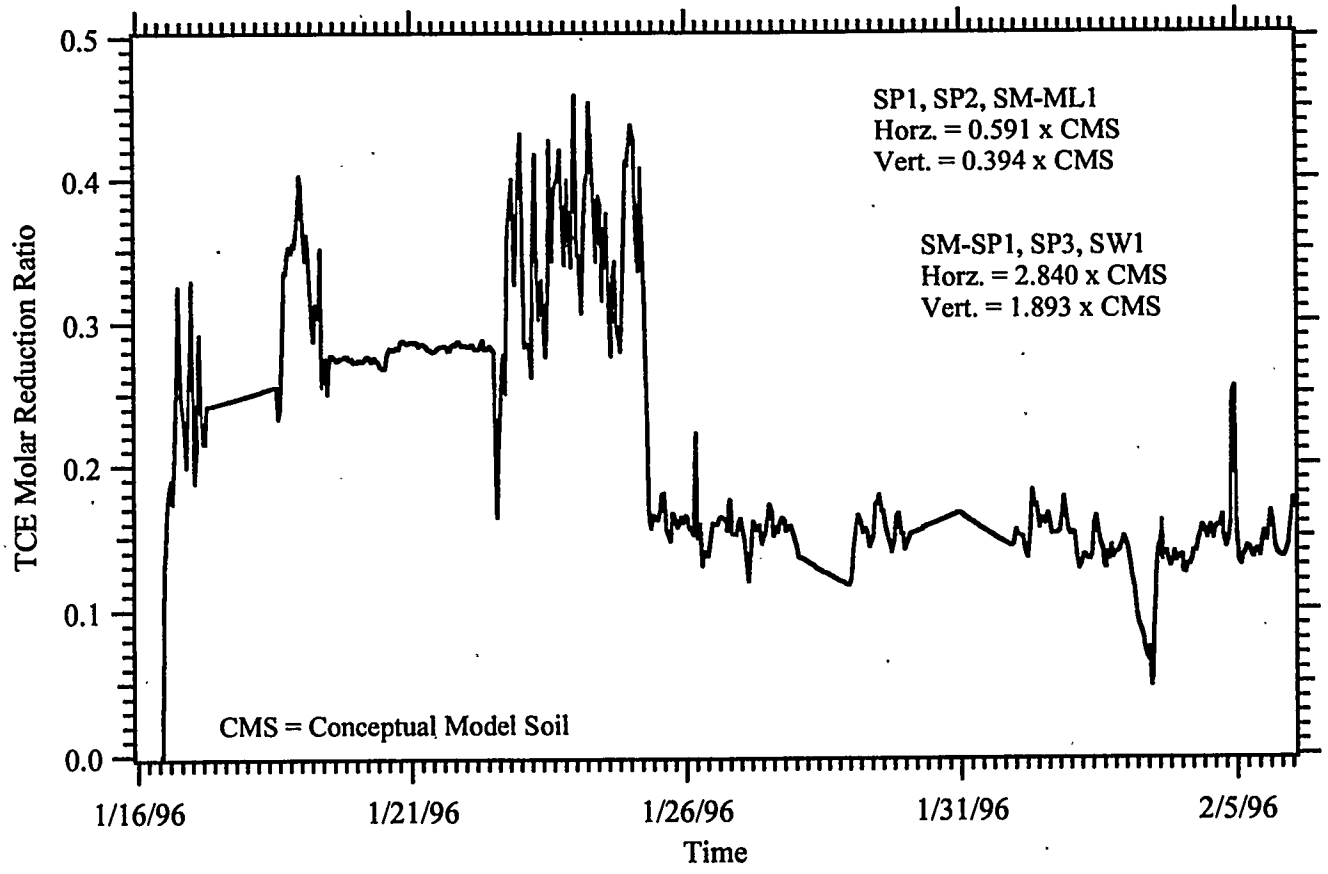

Figure F.33 TCE Molar Reduction Ratio Versus Time, Simulation HPA
(Operational Field Test #13, January 16, 1996 - February 6, 1996)

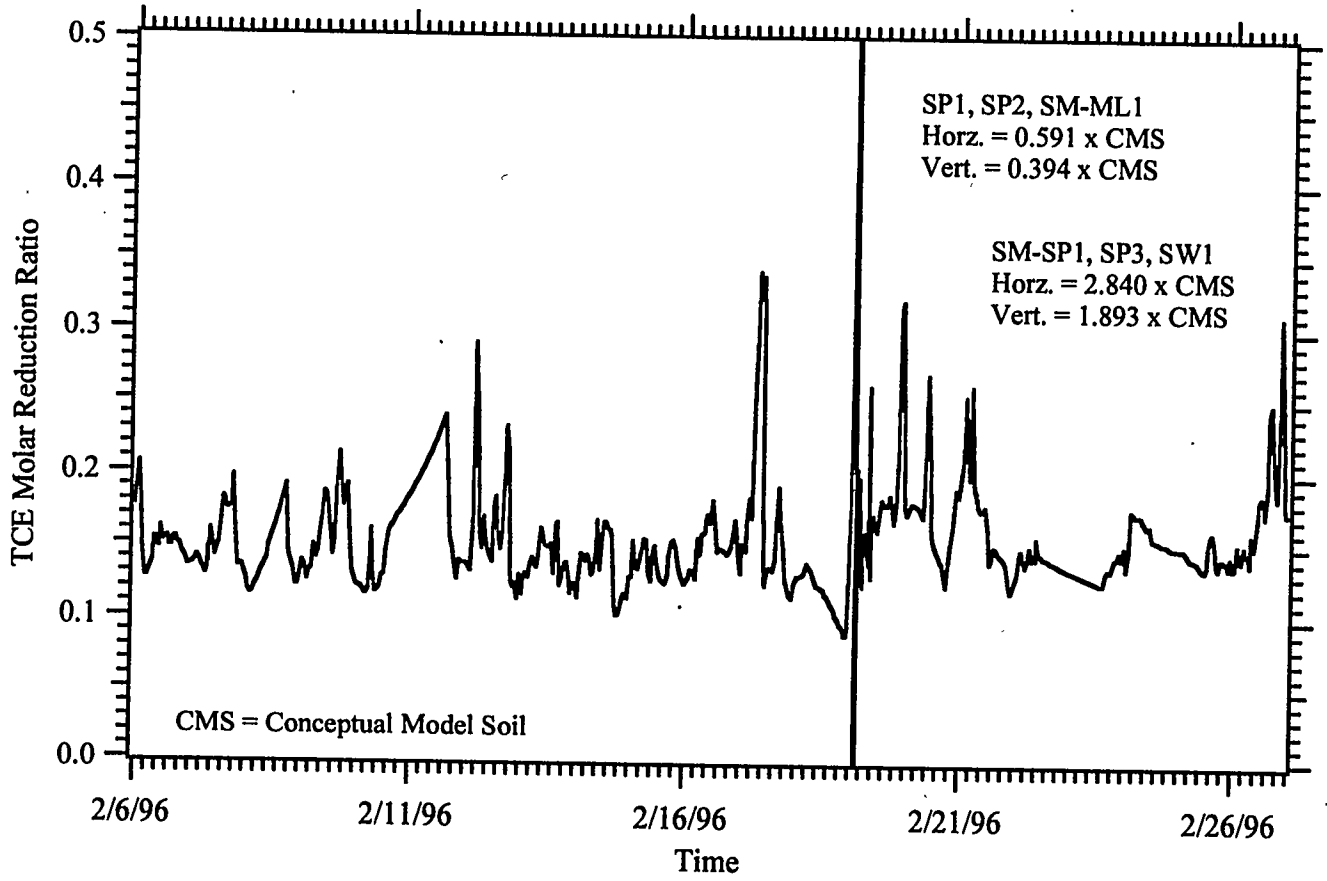

Figure F.34 TCE Molar Reduction Ratio Versus Time, Simulation HPA
(Operational Field Test #13, February 6, 1996 - February 27, 1996)

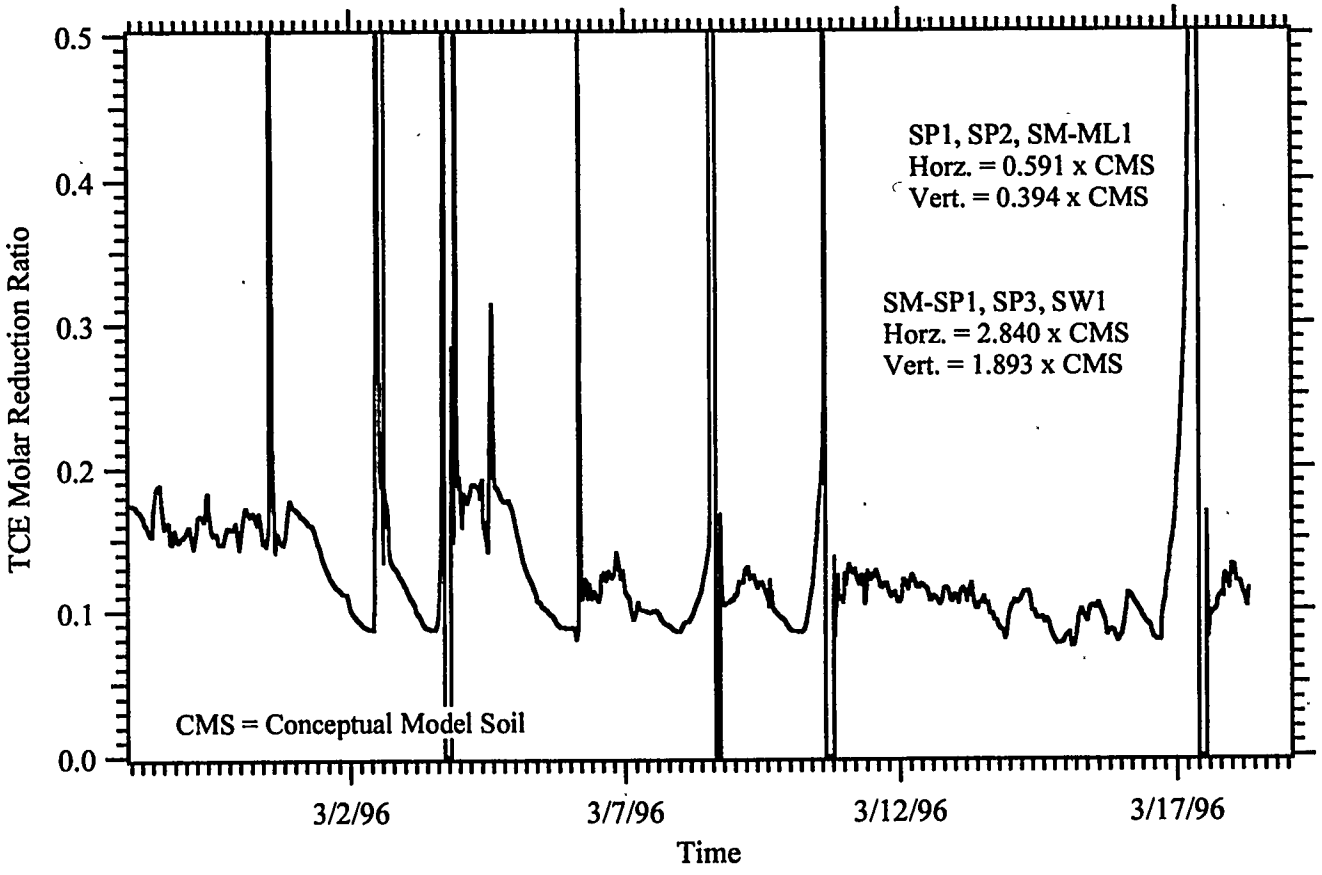

Figure F.35 TCE Molar Reduction Ratio Versus Time, Simulation HPA
(Operational Field Test #13, 2/27/96-3/19/96)

Distribution

No. of Copies

Offsite

S. Ballard, MS 0750
Sandia National Laboratories
1515 Eubank S.E.
Albuquerque, NM 87123

T. Hicks
U.S. Department of Energy
Subsurface Contaminant Focus Area
P.O. Box A
Aiken, SC 29808

R. Johnson
Oregon Graduate Institute
Department of Environmental Science and Engineering
P.O. Box 91000
Portland, OR 97291

2 Stanford University
Building 320, Room 118
Stanford, CA 94305-2115
ATTN: S. M. Gorelick
M. J. Pinto

No. of Copies

D. Steckel
Air Force Flight Test Center/EMR
70 N. Wolfe Avenue
Edwards AFB, CA 93524-1032

A. Thomas
Armstrong Laboratory
AL/EQM
139 Barnes Drive, Suite 2
Tyndall AFB, FL 32043-5323

Onsite

32 **Pacific Northwest National Laboratory**

B. Allewan	BCO
J. L. Devary	K6-96
R. M. Ecker	K6-91
M. D. Freshley	K6-96
T. J Gilmore (10)	K6-81
F. A. Spane, Jr.	K6-96
M. D. White (10)	K9-36
Information Release Office (7)	K1-06